Development of Composite Biomaterials with Self-Healing Properties

Mani Diba

Colophon

The research presented in this thesis was financially supported by the Netherlands Enterprise Agency through Project No. SHM012014 in the theme IOP Self Healing Materials.

Netherlands Enterprise Agency

Publication of this thesis was financially supported by the Netherlands Society for Biomaterials and Tissue Engineering (NBTE), Radboud University Medical Center (Radboudumc), and Radboud Institute for Molecular Life Sciences (RIMLS).

NBTE Netherlands society for Biomaterials and Tissue Engineering

Radboudumc

RIMLS

Thesis Radboud University Medical Center, Nijmegen, the Netherlands, with Summary in English and Dutch.

Development of Composite Biomaterials with Self-Healing Properties

ISBN: 978-94-028-0749-3

Cover design: Dr. Matilde Bongio and Mani Diba

Layout: Mani Diba

Printed by: Ipskamp Printing, Enschede

Development of Composite Biomaterials with Self-Healing Properties

Proefschrift

ter verkrijging van de graad van doctor
aan de Radboud Universiteit Nijmegen
op gezag van de rector magnificus prof. dr. J.H.J.M. van Krieken,
volgens besluit van het college van decanen
in het openbaar te verdedigen op dinsdag 9 januari 2018
om 14:30 uur precies

door

Mani Diba

geboren op 5 september 1986
te Teheran (Iran)

Promotor
Prof. dr. John A. Jansen

Copromotor
Dr. ir. Sander C.G. Leeuwenburgh

Manuscriptcommissie
Prof. dr. Daniela A. Wilson (voorzitter)
Prof. dr. Sybrand van der Zwaag (Technische Universiteit Delft)
Prof. dr. Patricia Y.W. Dankers (Technische Universiteit Eindhoven)

Paranimfen
Antonio Castro
Dr. Kambiz Farbod

Development of Composite Biomaterials with Self-Healing Properties

Doctoral Thesis

to obtain the degree of doctor
from Radboud University Nijmegen
on the authority of the Rector Magnificus Prof. Dr. J.H.J.M. van Krieken,
according to the decision of the Council of Deans
to be defended in public on Tuesday, January 9, 2018
at 14:30 hours

by

Mani Diba

born on September 5, 1986
in Tehran (Iran)

Supervisor
Prof. dr. John A. Jansen

Co-supervisor
Dr. ir. Sander C.G. Leeuwenburgh

Doctoral Thesis Committee
Prof. dr. Daniela A. Wilson (Chair)
Prof. dr. Sybrand van der Zwaag (Delft University of Technology)
Prof. dr. Patricia Y.W. Dankers (Eindhoven University of Technology)

Paranymphs
Antonio Castro
Dr. Kambiz Farbod

To my parents and all the people who helped me to expand and realize my imagination

Contents

Chapter 1	General introduction	11
Chapter 2	Highly elastic and self-healing composite colloidal gels	23
Chapter 3	Composite colloidal gels made of bisphosphonate-functionalized gelatin and bioactive glass particles for regeneration of osteoporotic bone defects	55
Chapter 4	Exploiting bisphosphonate-bioactive glass interactions for the development of self-healing and bioactive composite hydrogels	93
Chapter 5	Hybrid alendronate-bioactive glass particles for treatment of osteoporotic bone defects	123
Chapter 6	Fiber-reinforced colloidal gels as injectable and moldable biomaterials for regenerative medicine	153
Chapter 7	Nanostructured raspberry-like gelatin microspheres for local delivery of multiple biomolecules	173
Chapter 8	Summary, closing remarks and future perspectives	207
Chapter 9	Samenvatting, slotopmerkingen en toekomstperspectieven	221
	Acknowledgments	237
	List of publications	245
	Awards and honors	249
	Vitae	251

Chapter 1

General introduction

1. Biomaterials: from replacement to regeneration

Throughout history, the strive for longer and healthier life has urged mankind to search for materials that can restore function of lost or damaged body parts. Initially, these materials were selected "off-the-shelf" based on the ingenuity of the surgeons [1]. During the last century, medical and technological progress has led to the rise of the new field of biomaterials research and the emergence of a biomaterials industry. Consequently, a wide range of synthetic or natural biomaterials have been developed to augment or replace tissues, organs or function of our body parts. The first generation of biomaterials were bioinert implants, which were designed to replace lost or damaged body parts with a minimal immune response upon their implantation [2]. In the 1970s, the field of biomaterials expanded with the introduction of bioactive materials that could elicit desired physiological reactions in the body and bond to living tissues [3, 4]. Another important breakthrough in the field was the development of bioresorbable materials which could be resorbed by the body after implantation [5]. Since the 1990s, the focus of biomaterials research has shifted to regeneration rather than replacement of tissues and organs [6, 7]. Tissue engineering and regenerative medicine began to emerge as separate research fields, which increased the requirements for biomaterials considerably [8]. Consequently, new solutions are needed to overcome major challenges in biomaterials research such as improved control over the mechanical properties of biomaterials.

2. Self-healing: nature's ultimate adaptive solution

While synthetic biomaterials generally do not recover from mechanical damage, nature displays an exceptional capacity for self-healing, as evidenced for instance by bone fractures or ruptured skin. This self-healing ability is the ultimate solution of nature for continued survival which is achieved by adaptation and remodeling of damaged tissues [9, 10]. Recently, a new generation of man-made materials has evolved with the capacity to self-heal [9]. These self-healing materials are characterized by their ability to recover their original properties after damage, particularly in term of mechanical properties [11]. Several strategies have been explored so far for the development of such material systems. Depending on the self-healing mechanism, the self-healing capacity of these materials can be "extrinsic" or "intrinsic". Materials with extrinsic self-healing capacity are not able to heal themselves without external aids [11, 12] such as microcapsules that

contain healing agents. These capsules can be incorporated into a material so that mechanical damage would break the capsules and release their healing agent, thereby enabling the material to repair itself [13]. Bacteria have also been identified as external aids that can be embedded in concrete material to heal potential cracks following precipitation of calcite [14]. In contrast to extrinsic self-healing materials, intrinsically self-healing materials do not require external aids to achieve self-healing. Materials with intrinsic self-healing can be prepared by exploiting reversible rather than conventional irreversible crosslinks. Upon damage, such physical or chemical bonds break, but their reversible nature allows reformation of these bonds leading to recovery after damage [11, 12]. From the late 1990s onward, research on self-healing materials initially focused on development of new self-healing concepts for construction materials such as concrete [15-17] and asphalt [18, 19]. Recently, however, self-healing materials are increasingly developed for biomedical applications such as regenerative medicine [20, 21].

Self-healing biomaterials would be more durable, injectable/moldable, and cohesive than conventional non-self-healing biomaterials, while enabling tissue ingrowth and remodeling due to their adaptive nature [22, 23]. Accordingly, dynamic, self-healing biomaterials have the potential to define the next generation of biomaterials with strong advantages over conventional, static and non-self-healing biomaterials including:

- Increased load-bearing capacity by improving damage tolerance;
- Increased durability by hampering microcrack propagation;
- Improved injectability/moldability by facilitating recovery after destructive shearing;
- Improved *in vivo* cohesion by reversible attractive interactions between building blocks;
- Improved tissue ingrowth by facilitating cell migration due to their adaptive nature.

3. Composites: the power of synergy

"The whole is other than the sum of the parts", stated by psychologist Kurt Koffka, describes the attractiveness of composite materials. Biological composites such as bone or nacre exhibit exceptional mechanical properties owing to the synergetic combination of their organic and inorganic phases [24]. In materials science, this

concept has been employed for decades to manufacture high performance materials [25]. In the biomedical sector, composites are an increasingly important class of biomaterials which outperform their individual constituents [26]. The composite approach can not only create biomaterials with enhanced mechanical properties, but can also render them multifunctional [27]. For instance, while one constituent can impart therapeutic efficacy to a composite biomaterial, another constituent can induce the capacity to mineralize [28]. Accordingly, in view of the complexity of tissue regeneration processes, composite biomaterials offer promising solutions to overcome complex challenges in tissue regeneration [8].

4. Particulate biomaterials: building from the bottom up

As compared to the conventional top-down approach, bottom-up synthesis of materials offers a tremendous potential to control their properties and produce materials with remarkable features [29, 30]. Recently, bottom-up strategies have gained interest for the development of biomaterials with novel and improved properties [31], for instance by using micro- or nanosize particles as building blocks to synthesize bulk biomaterials [32]. Such biomaterials can obtain unique properties by combining size-, shape-, and chemistry-dependent properties of individual organic and/or inorganic particles. By controlling the interparticle interactions, these building blocks can be assembled into three-dimensional structures [33]. Colloidal gels are materials prepared by bottom-up synthesis which are composed of a continuous network of assembled particles dispersed in a liquid. Unlike monolithic polymeric gels, colloidal gels exhibit a heterogeneous structure characterized by assembly of colloidal particles into strands which form a mechanically stable particulate network due to attractive interparticle forces [34]. Various particle types and combinations thereof can be used as building blocks for the development of colloidal gels. These building blocks can also be loaded or functionalized with different types of drugs or biomolecules [35, 36]. By employing reversible, non-covalent interparticle bonds, injectable colloidal gels can be prepared with an intrinsic capacity for self-healing, enabling them to recover their mechanical properties after destructive shearing upon extrusion through needles [9]. Such capability is highly advantageous for applications such as minimally invasive treatments, three-dimensional printing and injection molding, since it allows their use without requiring post-injection cross-linking steps [37, 38]. Furthermore, the dynamic and adaptive nature of colloidal gel

networks can provide a suitable microenvironment for tissue ingrowth and cellular activity [22], potentially leading to improved tissue regeneration.

5. Objectives of this thesis

Bottom-up synthesis of biomaterials based on assembly from particulate building blocks can offer tremendous advantages for biomedical applications. More specifically, injectable and self-healing colloidal gels have recently shown a great potential for applications in regenerative medicine [37, 39]. Nevertheless, currently available polymeric colloidal gels are mechanically weak, which restricts their applicability [37, 39, 40]. The mechanical properties of colloidal gels can be improved by reinforcement with inorganic nanoparticles [38], but composite colloidal gels that resist substantial compressive and/or tensile loads have not yet been reported. Due to the weak mechanical properties of colloidal gels, their self-healing ability has only been demonstrated by means of rheological characterizations so far. Moreover, mechanical reinforcement of colloidal gels with inorganic fillers compromised the self-healing capacity of the resulting composites [38]. Since both mechanical robustness and self-healing ability are required for practical application of self-healing biomaterials [20], it remains a major challenge to develop a colloidal gel which combines mechanical robustness with self-healing capacity.

Generally, the bulk properties of colloidal gels are determined by their microstructure, the properties of each colloidal particle, and the interactions between these particles within a colloidal gel network [34]. Accordingly, a crucial and often challenging task for the synthesis of colloidal gels is to control and adjust their interparticle interactions.

Bisphosphonates (BPs) are a class of drugs commonly used for treatment of osteoporosis. Besides their medicinal efficacy, BP groups exhibit a strong binding affinity for the mineral phase of bone, i.e., hydroxyapatite (HAp) [41]. The physical bonds that are formed between BPs and HAp are not only strong but also reversible, which facilitates the development of self-healing biomaterials [42]. The binding affinity of BP groups for HAp has been attributed to their interaction with Ca ions as present on HAp surfaces [43], which might indicate that BP groups can also bind to other Ca-containing phases. However, although the interactions between BPs and calcium phosphates (e.g., HAp) have been widely studied [43, 44], the interaction of BPs with other Ca-containing inorganic phases such as calcium

silicates has not yet been extensively explored. Bioactive glasses are typically Ca-containing silicate glasses with applications in a wide range of biomedical areas [45, 46]. Specific compositions of these materials (e.g., 45S5 Bioglass®) have been reported to exhibit a superior bone-bonding and tissue regenerative capability as compared to other bioactive ceramics such as HAp [47, 48]. Nevertheless, it is unknown (i) to which extent BPs bind to bioactive glasses as compared to HAp, and (ii) if this interaction can be exploited for the development of self-healing and bioactive composite biomaterials.

At last, although organic-inorganic composites can be considered as ideal biomaterials for bone tissue regeneration [27], various biomedical applications such as soft tissue regeneration require biomaterials that are fully organic and biodegradable, but are also mechanically robust [49, 50]. Such fully organic colloidal gels might be synthesized by combining organic particles with different aspect ratios or a hierarchical assembly of organic nanoparticles into complex structures.

To address all the above-mentioned challenges, this PhD thesis focused on the following research questions:

1) Can composite colloidal gels be developed from silica and gelatin particles which can withstand compressive and tensile loads as well as recover completely from shear- or cutting-induced failure? (Chapter 2)

2) Can self-healing composites with bone regenerative capability be synthesized by combining bisphosphonate-functionalized gelatin particles with bioactive glass particles? (Chapter 3)

3) Can self-healing composites be formed by means of bridging flocculation between bisphosphonate-functionalized polymers and bioactive glass particles? (Chapter 4)

4) Can the interactions between bisphosphonates and bioactive glasses be exploited to synthesize hybrid bisphosphonate-bioactive glass particles? (Chapter 5)

5) Can organic colloidal gels be reinforced mechanically with discrete organic nanofibers instead of inorganic particles? (Chapter 6)

6) Can complex gelatin microparticles be formed though assembly from gelatin sub-micron particles? (Chapter 7)

References

[1] B.D. Ratner, A history of biomaterials, Biomaterials science: an introduction to materials in medicine, Academic press, 2004.

[2] L. Hench, Biomaterials, Science 208 (1980) 826-831.

[3] L. Hench, J. Wilson, Surface-active biomaterials, Science 226 (1984) 630-636.

[4] L.L. Hench, R.J. Splinter, W.C. Allen, T.K. Greenlee, Bonding mechanisms at the interface of ceramic prosthetic materials, Journal of Biomedical Materials Research 5 (1971) 117-141.

[5] J.W. Leenslag, A.J. Pennings, Synthesis of high-molecular-weight poly(L-lactide) initiated with tin 2-ethylhexanoate, Die Makromolekulare Chemie 188 (1987) 1809-1814.

[6] L.L. Hench, J.M. Polak, Third-Generation Biomedical Materials, Science 295 (2002) 1014-1017.

[7] R. Langer, J. Vacanti, Tissue engineering, Science 260 (1993) 920-926.

[8] E.S. Place, N.D. Evans, M.M. Stevens, Complexity in biomaterials for tissue engineering, Nature Materials 8 (2009) 457-470.

[9] T. Speck, G. Bauer, F. Flues, K. Oelker, M. Rampf, A.C. Schussele, M. von Tapavicza, J. Bertling, R. Luchsinger, A. Nellesen, A.M. Schmidt, R. Mulhaupt, O. Speck, CHAPTER 16 Bio-inspired Self-healing Materials, Materials Design Inspired by Nature: Function Through Inner Architecture, The Royal Society of Chemistry, 2013, pp. 359-389.

[10] C.E. Diesendruck, N.R. Sottos, J.S. Moore, S.R. White, Biomimetic Self-Healing, Angewandte Chemie International Edition 54 (2015) 10428-10447.

[11] M.D. Hager, P. Greil, C. Leyens, S. van der Zwaag, U.S. Schubert, Self-Healing Materials, Advanced Materials 22 (2010) 5424-5430.

[12] S.K. Ghosh, Self-healing materials: fundamentals, design strategies, and applications, John Wiley & Sons, 2009.

[13] S.R. White, N.R. Sottos, P.H. Geubelle, J.S. Moore, M.R. Kessler, S.R. Sriram, E.N. Brown, S. Viswanathan, Autonomic healing of polymer composites, Nature 409 (2001) 794-797.

[14] H.M. Jonkers, E. Schlangen, Development of a bacteria-based self healing concrete, Proc. int. FIB symposium, 2008, pp. 425-430.

[15] W.H. Zhong, W. Yao, Influence of damage degree on self-healing of concrete, Construction and Building Materials 22 (2008) 1137-1142.

[16] C. Edvardsen, Water permeability and autogenous healing of cracks in concrete, Aci Materials Journal 96 (1999) 448-454.

[17] H.M. Jonkers, A. Thijssen, G. Muyzer, O. Copuroglu, E. Schlangen, Application of bacteria as self-healing agent for the development of sustainable

concrete, Ecological Engineering 36 (2010) 230-235.
[18] A. Bhasin, R. Bommavaram, M.L. Greenfield, D.N. Little, Use of Molecular Dynamics to Investigate Self-Healing Mechanisms in Asphalt Binders, Journal of Materials in Civil Engineering 23 (2011) 485-492.
[19] Q.T. Liu, A. Garcia, E. Schlangen, M. van de Ven, Induction healing of asphalt mastic and porous asphalt concrete, Construction and Building Materials 25 (2011) 3746-3752.
[20] D.L. Taylor, M.I.H. Panhuis, Self-Healing Hydrogels, Advanced Materials 28 (2016) 9060-9093.
[21] X.E. Ma, N.Z. Zhou, T.Z. Zhang, W.J. Hu, N. Gu, Self-healing pH-sensitive poly (methyl vinyl ether)-alt-(maleic acid) -based supramolecular hydrogels formed by inclusion complexation between cyclodextrin and adamantane, Materials Science & Engineering C-Materials for Biological Applications 73 (2017) 357-365.
[22] H. Wang, S.C. Heilshorn, Adaptable Hydrogel Networks with Reversible Linkages for Tissue Engineering, Advanced Materials 27 (2015) 3717-3736.
[23] C.M. Kirschner, K.S. Anseth, Hydrogels in healthcare: From static to dynamic material microenvironments, Acta Materialia 61 (2013) 931-944.
[24] J.W.C. Dunlop, P. Fratzl, Biological Composites, in: D.R. Clarke, M. Ruhle, F. Zok (Eds.), Annual Review of Materials Research, Vol 40, Annual Reviews, Palo Alto, 2010, pp. 1-24.
[25] A.R. Studart, Towards High-Performance Bioinspired Composites, Advanced Materials 24 (2012) 5024-5044.
[26] S. Ramakrishna, J. Mayer, E. Wintermantel, K.W. Leong, Biomedical applications of polymer-composite materials: a review, Composites Science and Technology 61 (2001) 1189-1224.
[27] K. Rezwan, Q.Z. Chen, J.J. Blaker, A.R. Boccaccini, Biodegradable and bioactive porous polymer/inorganic composite scaffolds for bone tissue engineering, Biomaterials 27 (2006) 3413-3431.
[28] V. Mourino, J.P. Cattalini, J.A. Roether, P. Dubey, I. Roy, A.R. Boccaccini, Composite polymer-bioceramic scaffolds with drug delivery capability for bone tissue engineering, Expert Opinion on Drug Delivery 10 (2013) 1353-1365.
[29] M. Shimomura, T. Sawadaishi, Bottom-up strategy of materials fabrication: a new trend in nanotechnology of soft materials, Current Opinion in Colloid & Interface Science 6 (2001) 11-16.
[30] K. Ariga, J.P. Hill, M.V. Lee, A. Vinu, R. Charvet, S. Acharya, Challenges and breakthroughs in recent research on self-assembly, Science and Technology of Advanced Materials 9 (2008) 96.
[31] S.G. Zhang, Fabrication of novel biomaterials through molecular self-assembly,

Nature Biotechnology 21 (2003) 1171-1178.
[32] H. Wang, S.C. Leeuwenburgh, Y. Li, J.A. Jansen, The use of micro-and nanospheres as functional components for bone tissue regeneration, Tissue Engineering Part B: Reviews 18 (2011) 24-39.
[33] R. Shenhar, V.M. Rotello, Nanoparticles: Scaffolds and Building Blocks, Accounts of Chemical Research 36 (2003) 549-561.
[34] P.J. Lu, D.A. Weitz, Colloidal Particles: Crystals, Glasses, and Gels, in: J.S. Langer (Ed.), Annual Review of Condensed Matter Physics, Vol 4, Annual Reviews, Palo Alto, 2013, pp. 217-233.
[35] J. Song, J.C. Odekerken, D.W. Löwik, P.M. López-Pérez, T.J. Welting, F. Yang, J.A. Jansen, S.C. Leeuwenburgh, Influence of the Molecular Weight and Charge of Antibiotics on Their Release Kinetics From Gelatin Nanospheres, Macromolecular bioscience 15 (2015) 901-911.
[36] H. Wang, Q. Zou, O.C. Boerman, A.W. Nijhuis, J.A. Jansen, Y. Li, S.C. Leeuwenburgh, Combined delivery of BMP-2 and bFGF from nanostructured colloidal gelatin gels and its effect on bone regeneration in vivo, Journal of Controlled Release 166 (2013) 172-181.
[37] Q. Wang, L. Wang, M.S. Detamore, C. Berkland, Biodegradable Colloidal Gels as Moldable Tissue Engineering Scaffolds, Advanced Materials 20 (2008) 236-239.
[38] H. Wang, M. Bongio, K. Farbod, A.W.G. Nijhuis, J. van den Beucken, O.C. Boerman, J.C.M. van Hest, Y. Li, J.A. Jansen, S.C.G. Leeuwenburgh, Development of injectable organic/inorganic colloidal composite gels made of self-assembling gelatin nanospheres and calcium phosphate nanocrystals, Acta Biomaterialia 10 (2014) 508-519.
[39] H. Wang, M.B. Hansen, D.W.P.M. Löwik, J.C.M. van Hest, Y. Li, J.A. Jansen, S.C.G. Leeuwenburgh, Oppositely Charged Gelatin Nanospheres as Building Blocks for Injectable and Biodegradable Gels, Advanced Materials 23 (2011) H119-H124.
[40] S.R. Van Tomme, M.J. van Steenbergen, S.C. De Smedt, C.F. van Nostrum, W.E. Hennink, Self-gelling hydrogels based on oppositely charged dextran microspheres, Biomaterials 26 (2005) 2129-2135.
[41] G.A. Rodan, H.A. Fleisch, Bisphosphonates: mechanisms of action, The Journal of Clinical Investigation 97 (1996) 2692-2696.
[42] M.R. Nejadnik, X. Yang, M. Bongio, H.S. Alghamdi, J.J.J.P. van den Beucken, M.C. Huysmans, J.A. Jansen, J. Hilborn, D. Ossipov, S.C.G. Leeuwenburgh, Self-healing hybrid nanocomposites consisting of bisphosphonated hyaluronan and calcium phosphate nanoparticles, Biomaterials 35 (2014) 6918-6929.
[43] F. Errassifi, S. Sarda, A. Barroug, A. Legrouri, H. Sfihi, C. Rey, Infrared, Raman and NMR investigations of risedronate adsorption on nanocrystalline

apatites, Journal of Colloid and Interface Science 420 (2014) 101-111.
[44] M.A. Lawson, Z. Xia, B.L. Barnett, J.T. Triffitt, R.J. Phipps, J.E. Dunford, R.M. Locklin, F.H. Ebetino, R.G.G. Russell, Differences between bisphosphonates in binding affinities for hydroxyapatite, Journal of Biomedical Materials Research Part B: Applied Biomaterials 92B (2010) 149-155.
[45] V. Miguez-Pacheco, L.L. Hench, A.R. Boccaccini, Bioactive glasses beyond bone and teeth: Emerging applications in contact with soft tissues, Acta Biomaterialia 13 (2015) 1-15.
[46] J.R. Jones, Review of bioactive glass: From Hench to hybrids, Acta Biomaterialia 9 (2013) 4457-4486.
[47] Y. Fujishiro, L.L. Hench, H. Oonishi, Quantitative rates of in vivo bone generation for Bioglass(R) and hydroxyapatite particles as bone graft substitute, Journal of Materials Science-Materials in Medicine 8 (1997) 649-652.
[48] A. Hoppe, N.S. Güldal, A.R. Boccaccini, A review of the biological response to ionic dissolution products from bioactive glasses and glass-ceramics, Biomaterials 32 (2011) 2757-2774.
[49] Q.-Z. Chen, S.E. Harding, N.N. Ali, A.R. Lyon, A.R. Boccaccini, Biomaterials in cardiac tissue engineering: Ten years of research survey, Materials Science and Engineering: R: Reports 59 (2008) 1-37.
[50] S. MacNeil, Biomaterials for tissue engineering of skin, Materials Today 11 (2008) 26-35.

Chapter 2

Highly elastic and self-healing composite colloidal gels

This chapter is based on:

M. Diba*, H. Wang*, T.E. Kodger, S. Parsa, and S.C.G. Leeuwenburgh, *Advanced Materials*, 29 (2017) 1604672.

*These authors contributed equaly to this work.

Colloidal gels are composed of a continuous network of assembled particles dispersed in a liquid [1]. They are frequently used in applications such as ceramic and glass processing [2], paint and coating production [3], food products [4], cosmetics [5] and biomedical engineering [6]. Unlike monolithic polymeric gels, colloidal gels exhibit a heterogeneous structure characterized by assembly of colloidal particles into strands which form a mechanically stable particulate network due to attractive interparticle forces [7]. Colloidal gels are particularly appealing in view of their fascinating viscoelastic properties [8]. By exploiting the reversibility of non-covalent interparticle interactions, colloidal gels can be rendered self-healing [6, 9]. However, current self-healing colloidal gels consist of polymeric particles and are mechanically weak, which restrict their applicability [6, 9]. The mechanical properties of colloidal gels can be improved by reinforcement with inorganic nanoparticles [10], but such composite colloidal gels that resist substantial compressive and/or tensile loads have not yet been reported. Due to the weak mechanical properties of colloidal gels, their self-healing ability has only been demonstrated by rheological tests so far. Moreover, mechanical reinforcement of colloidal gels with inorganic fillers compromised the self-healing capacity of the resulting composites [10]. Since both mechanical robustness and self-healing ability are required for practical application of self-healing gels [11], it remains a major challenge to develop a colloidal gel which combines mechanical robustness with self-healing capacity.

Here, we developed a novel nanocomposite colloidal gel with an unprecedented combination of mechanical properties and self-healing capacity by i) careful control of particle assembly, ii) fundamental understanding of the mechanism of gel network formation, and iii) precise tuning of composition and structure of the resulting gel networks. We used amphoteric soft gelatin nanoparticles and negatively charged hard silica nanoparticles as the organic and inorganic colloidal building blocks, respectively. To prevent uncontrollable aggregation resulting from direct mixing of attractive binary colloids, electrostatic assembly of the nanoparticles into homogeneous binary networks was facilitated by controlling the pH of the colloidal system. These homogeneous gels exhibit a remarkable self-healing capacity, as evidenced by immediate recovery of gel elasticity upon destructive shearing to values which even exceed initial gel elasticity. In addition, we show - for the

first time - that colloidal gels can be prepared which not only resist substantial compressive and tensile loads, but also are able of complete self-healing upon shear- or cutting-induced failure. Our study provides new, critical insight into the structural and mechanical properties of composite colloidal gels and, more importantly, opens up a new horizon for applications of colloidal gel systems.

Colloidal gels formed by direct mixing of attractive colloids are often characterized by uncontrollable, non-uniform aggregation and phase separation [6, 10] which compromise their structural integrity and mechanical strength [12]. Furthermore, pre-shear resulting from sample mixing and loading substantially alters the structural and mechanical properties of colloidal gels, thereby hampering analysis of the relationship between their structure and mechanical properties. Therefore, we mixed basic aqueous suspensions (20 mM NaOH; pH~11) of gelatin nanoparticles (diameter~400 nm) and silica (diameter~80 nm) nanoparticles to ensure that all particles were negatively charged and homogeneously mixed. We then introduced glucono delta-lactone (GDL) [13] as an acidifier which upon decomposition decreased the pH gradually from ~11 to below the isoelectric point (IEP) of gelatin nanoparticles (pH<8). As a consequence, the net charge of gelatin nanoparticles changed from negative to positive, thereby triggering self-assembly between oppositely charged silica and gelatin nanoparticles. Scheme 1 shows a general overview of the gel formation method used in our study.

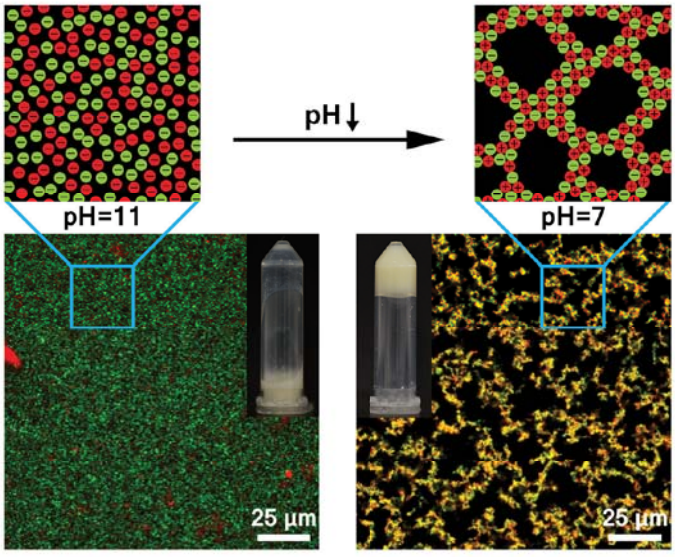

Scheme 1. Schematic illustration of the gel network formation, and representative confocal and macroscopic images before and after gel formation. Red and green particles represent gelatin and silica, respectively.

To monitor the pH-induced assembly and network formation resulting from the decomposition of GDL, we labeled silica and gelatin nanoparticles with different fluorescent dyes. This fluorescent labeling allowed real-time, two-dimensional imaging of gel network formation using confocal microscopy of a mixed suspension with a particle volume fraction φ of 0.05 and silica-to-gelatin particle number ratio R of 5 (Figure 1a; Movie S1, Supporting Information). This imaging modality facilitated additional analysis of the particle mobility defined as average displacement of particles between consecutive images using particle image velocimetry (PIV, see Experimental Section in Supporting Information) [14]. In addition, we measured the zeta potential of the particles as well as the pH change and viscoelasticity of the colloidal suspension as a function of time.

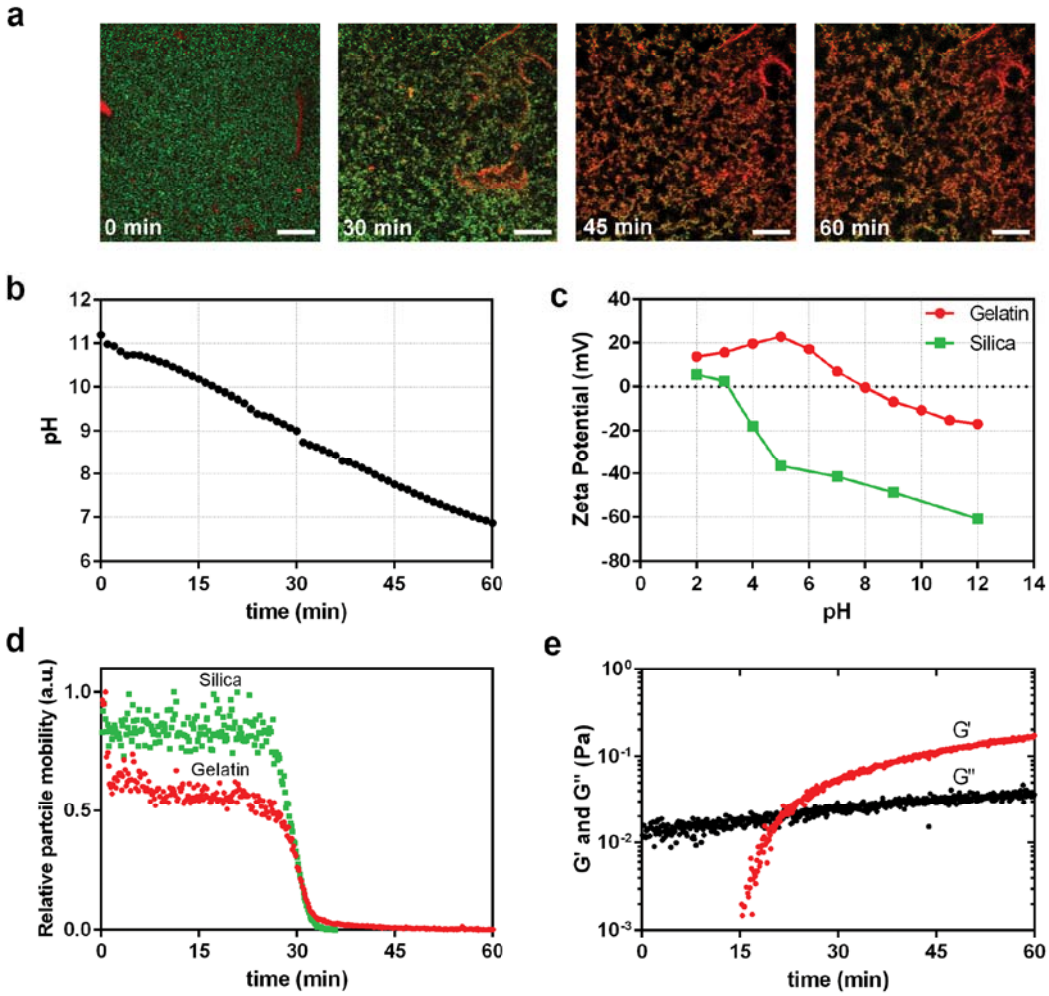

Figure 1. Colloidal network formation by pH-induced electrostatic assembly of oppositely charged silica and gelatin nanoparticles (R=5 and φ=0.05). a) Confocal micrographs at different time points during the gelation of colloidal composite gels composed of silica (green) and gelatin (red) nanoparticles. b) pH change during decomposition of glucono delta-lactone

(80 mM). c) Zeta potential of silica and gelatin nanoparticles as a function of pH. d) Relative particle mobility of silica and gelatin nanoparticles during the gel formation calculated using PIV. e) Evolution of storage (G') and loss (G") moduli during the gel formation process. Scale bars in images represent 25 µm.

We found that the gelation of the binary colloidal gels is driven by the pH of the colloidal system. At the basic starting condition (pH~11, Figure 1b), interparticle interactions were repulsive (Figure 1c), resulting in a homogeneous suspension showing high particle mobility driven by Brownian motion (Figure 1d). At this stage, the storage modulus G' was too low to be measurable using a rheometer and much lower than the loss modulus G", corresponding to liquid-like behavior (Figure 1e). Clusters of gelatin nanoparticles were occasionally formed at the early stage of process at pH>9 (Figure 1a). This phenomenon may be due to the formation of stable bonds between dangling gelatin chains [15], which were not formed between gelatin and silica nanoparticles. When the pH decreased below the IEP of gelatin (~8), repulsive interactions were no longer strong enough to prevent nanoparticle collisions. Consequently, attractive interparticle potentials between silica and gelatin nanoparticles ($U_{Si\text{-}Gel}$) and gelatin nanoparticles ($U_{Gel\text{-}Gel}$) were dominant. Pair potential $U_{Si\text{-}Gel}$ gradually increased and dominated $U_{Gel\text{-}Gel}$ with decreasing pH due to the enhanced electrostatic attraction between silica and gelatin nanoparticles. Consequently, the number of silica-gelatin bonds increased, eventually inducing the formation of an interconnected particulate network. This transient response occurred within several minutes as evidenced by a sudden and simultaneous drop of the mobility of both gelatin and silica nanoparticles after ~30 min (Figure 1d), indicating that the nanoparticles were arrested (Figure 1a; Movie S1, Supporting Information). Gel formation was also confirmed macroscopically using rheometry which revealed a gradual transition from liquid- to solid-like behavior (G' exceeding G") with decreasing pH (Figure 1e). We observed that this composite gel network - once formed at pH values below 8 - could not be broken by subsequent increase of the pH to the basic starting condition upon addition of an excess of 100 mM NaOH solution (Figure S3, Supporting Information). While gel network formation was induced by long-range attractive electrostatic interactions, additional short-range interparticle interactions such as van der Waals and hydrogen bonds [16] which exceeded repulsive electrostatic forces at basic pH were formed thereafter, thereby retaining gel network integrity. In contrast, mixed suspensions

of silica and gelatin nanoparticles (pH~11) remained liquid-like without forming particulate networks, confirming the role of electrostatic forces in the self-assembly process and the effectiveness of pH-induced assembly (Figure S4 and Movie S2, Supporting Information).

We also observed gel formation for purely organic gelatin colloidal suspensions (R=0), indicating that the attractive potential between gelatin particles ($U_{Gel-Gel}$) was sufficient to trigger gel network formation (Movie S3, Supporting Information). Nevertheless, the gelation of gelatin colloidal suspension proceeded much slower, and the resulting gels stored less elastic energy (indicated by lower G' values) as compared to the composite gels (Figure S5, Supporting Information). In contrast, purely inorganic silica colloidal suspensions (R=∞) did not form gels and displayed liquid-like behavior only (Figure S5 and Movie S4, Supporting Information).

The viscoelastic properties of colloidal gels are strongly determined by their gel network structure [7, 17]. To understand the relationship between composition, structure and mechanical properties for the composite colloidal gels, we investigated the effect of the silica-to-gelatin ratio, R, on the topology and connectivity of the gel networks. To this end, we used confocal microscopy to quantify the average strand thickness r, average strand length ξ, and node density ν (see Experimental Section in Supporting Information). For R ranging from 0 to 10, we observed the formation of uniform, interconnected particulate networks, similar to diffusion-limited cluster aggregation typically formed by fast flocculation (Figure 2a) [1]. Within this compositional range, gel network structure was similar as strand thickness r and length ξ (Figure S6, Supporting Information) did not vary considerably. As R increased to 50, a percolated network with significantly thicker and longer strands but lower connectivity was assembled similar to reaction-limited cluster aggregation typically formed by slow flocculation, as indicated by a lower node density ν in Figure S6 (Supporting Information) [18]. At higher R values, i.e. R=100, no gel network was formed due to an excess of similarly charged silica nanoparticles (Movie S5, Supporting Information). As shown in Figure 2b, the storage modulus of gels with particle volume fractions (φ=0.05) similar to the ones used in the above-described confocal microscopy studies increased with increasing R from 0 to 5, whereas a further increase of R compromised gel elasticity. For this specific composition (R=5), the storage modulus of gelatin-silica composite gels

was more than ten-fold higher than purely organic gelatin colloidal gels. Increasing the silica content to R=50 resulted into lower G' and much higher damping factor tan(δ) values (Figure S7, Supporting Information) than gels of R≤10, corresponding to reduced gel elasticity.

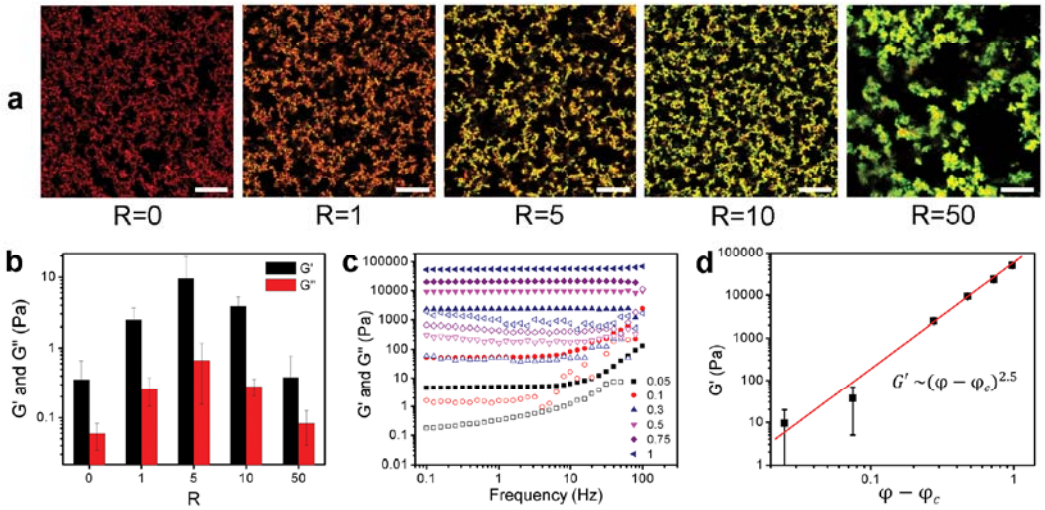

Figure 2. a) Representative confocal microscopy images demonstrating the microstructure of colloidal networks at different silica-to-gelatin ratios (R); red and green pixels represent gelatin and silica nanoparticles, respectively (φ=0.05). Viscoelastic properties of colloidal gels: b) Storage (G') and loss (G") moduli of colloidal gels as a function of silica-to-gelatin ratio (R) (φ=0.05). c) Frequency dependence of storage (solid symbols, G') and loss (open symbols, G") moduli of colloidal composite gels with different particle volume fractions φ (at R=5). d) Storage modulus G' of colloidal gels with R=5 as a function of the difference between their volume fraction φ and the critical volume fraction φ_c; the red line corresponds to the power-law fit. Scale bars in images represent 25 μm.

Generally, the elasticity of the colloidal gel networks can be described by $G' \sim \kappa(\xi)/\xi$, where κ(ξ) is the spring constant of a strand of length ξ [17, 19]. κ(ξ) is related to the dimension of the strand as well as the stiffness and interparticle potential of the particulate building blocks [19], while ξ is directly affected by composition and volume fraction [17]. We suggest that the elastic modulus of the gels with lower R value (R≤10) is dominated by the local spring constant κ(ξ) of the composite strands, since no significant difference was observed with respect to strand dimensions (Figure S6, Supporting Information). Thus, by increasing R through addition of stiff silica nanoparticles, κ(ξ) is enhanced and stronger networks are formed. The low storage modulus for composite gels with R=50 can be attributed to the substantially longer strands (larger ξ) and reduced connectivity of the strands (Figure 2a), which

apparently plays a more dominant role over κ(ξ) in determining gel elasticity at this composition (Figure 2b).

The effect of volume fraction φ on the viscoelastic properties of the composite colloidal gels was further investigated at an optimal composition (R=5). We observed experimentally that the critical volume fraction φc to allow gel formation was φ~0.025. Above φ_c, the colloidal gels exhibited frequency-independent behavior, corresponding to the formation of elastic gels (Figure 2c). The difference in size between gelatin and silica nanoparticles [20] and deformability of soft gelatin nanoparticles allowed the preparation of highly jammed colloidal dispersions with particle volume fractions much higher than random close packing (RCP) of monodisperse hard spheres (φ~0.64) [21]. Therefore, we were able to produce highly elastic composite gels with volume fractions up to 1, most likely by deformation of swollen gelatin nanoparticles into interparticle voids. These highly jammed gels were cohesive and very stiff as characterized by a large storage modulus of ~50 kPa. Moreover, the storage modulus showed a power-law behavior as a function of φ, $G' \sim (\varphi - \varphi_c)^{2.5}$, as shown in Figure 2d. This behavior corresponds to attractive colloidal systems formed by interparticle potentials such as electrostatic forces [22], and allows precise control over the elasticity of colloidal gels in a predictable manner for G' values ranging from 10 Pa to 50 kPa. Strikingly, the composite gels were not only injectable and moldable (Figures S10 and S11, Supporting Information), but also displayed a highly elastic behavior as reflected by repeated bouncing (Movie S6, Supporting Information).

We hypothesized that the reversibility of the non-covalent interparticle bonds endows these composite colloidal gels with self-healing properties. Therefore, we quantified the recovery of their storage modulus after multiple cycles of shear-induced gel network destruction (0.1–1000 % strain). Remarkably, the composite colloidal gels revealed an exceptional self-healing capacity since gel elasticity recovered repeatedly after network destruction, up to levels that exceeded their initial gel elasticity (self-healing>100%) (Figure 3a). The storage modulus increased for six consecutive cycles of network destruction and recovery, whereafter recovered G' values reached a plateau value (Figure 3b). Importantly, we observed that the gels prepared by the direct mixing of oppositely charged nanoparticles at pH 7 exhibited a significantly lower stiffness and poor self-healing capacity (Figure 3a).

These observations imply that uniform mixing of the nanoparticles and controlled assembly of the composite gels were crucial to obtain composite colloidal gels of high elasticity and self-healing capacity.

In order to explain why self-healing efficiencies of more than 100% were observed, we visualized the microstructure of the respective composite colloidal gels using confocal microscopy before and after destructive shearing up to 1000% strain (see Supporting Information for the experimental details). As shown in Figure 3c, the self-healed network revealed a different microstructure compared to the virgin one; the strands composed of silica and gelatin nanoparticles became considerably thicker and longer while the node density decreased considerably as compared to the virgin network structure. We suggest that this strand thickening effect results from the high shear forces which destroy the virgin network and form a new structure of higher packing density out of ruptured particles and clusters [23]. Apparently, this newly formed colloidal network leads to a higher storage modulus, most likely due to the increased spring constant of the strands ($\kappa(\xi)$). From Figure 3b we conclude that this strand thickening effect occurs for up to six cycles of destruction and recovery. We propose that gel destruction occurs by separation of highly packed clusters after more than six consecutive cycles of network destruction and recovery. After shear removal, these clusters form gel networks with similar morphology and rheological properties to the gels before shearing. This type of destruction and subsequent recovery of network properties has been reported previously for peptide hydrogels [24]. Moreover, the self-healing efficiency of gels does not exceed 100% at particle volume fractions higher than the RCP (Figure 3d). Under these conditions, the particles are highly jammed which hampers shear-induced structural changes. It should be emphasized, however, that dry gelatin-silica colloidal composites are not able to self-heal after mechanical damage, which is in line with the previously reported self-healing behavior of polyelectrolyte-based materials [25]. In both systems, self-healing is mainly based on the reversibility of electrostatic interactions under aqueous conditions.

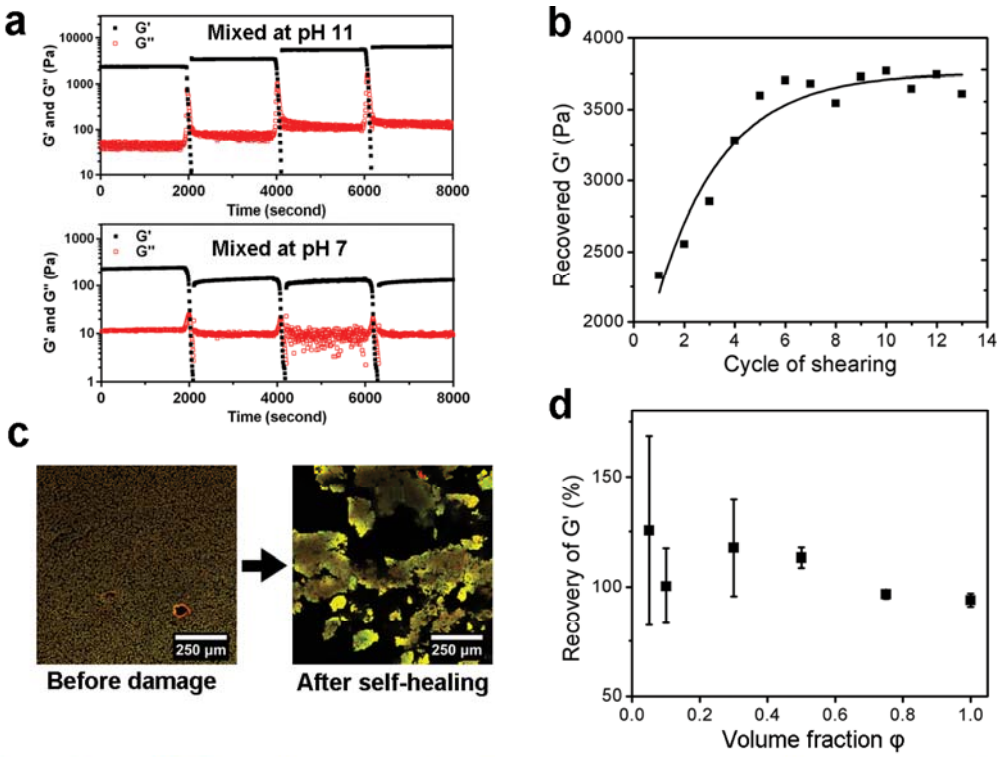

Figure 3. Self-healing behavior of colloidal gels upon destructive shearing. a) Evolution of storage (blue symbols, G') and loss (red symbols, G'') moduli of colloidal composite gels (R=5, and φ=0.3) during 3 cycles of destructive shearing (oscillatory strain sweep with increasing strain from 0.1% to 1000% with a fixed frequency of 1Hz) and recovery (oscillatory time sweep at 0.5% strain and a frequency of 1Hz for 30min). b) Evolution of storage modulus G' and yield strain as a function of the number of destructive shear and recovery cycles (R=5, φ=0.3). c) Representative confocal images showing the microstructure of gel networks before damage and after self-healing (R=5, φ=0.05). d) Recovery of storage modulus (G') 30 min after gel network destruction as a function of volume fraction φ (at R=5).

Since composite gels with φ=1 exhibited superior mechanical properties and complete self-healing upon shearing, we evaluated their mechanical properties and self-healing capability in more detail using conventional compression and tensile tests, which has not been reported previously for colloidal gels. The composite gels showed a linear-elastic response followed by a brittle fracture mode upon compressive loading (Figure 4a; Movie S7, Supporting Information). The compressive modulus (E) and strength (σ_c) of the tested gels were 93.8±6.8 and 43.9±2.8 kPa, respectively, whereas pure gelatin colloidal gels were considerably less stiff (E = 26.1±1.3 kPa) and strong (σ_c = 15.2±1.6 kPa). To our surprise, the tensile tests also revealed a purely elastic response for the composite colloidal gels, as evidenced by the linear stress-strain curve and the absence of any plastic deformation. The composite gels fractured at ~23% elastic strain (Figure 4b;

Movies S8, Supporting Information). The tensile modulus (E) and strength (σ_t) of the colloidal composite gel were 40.6±6.7 kPa and 8.4±1.8 kPa, respectively. In comparison, silica-free colloidal gelatin gels were significantly less stiff (E = 27.2±2.7 kPa) but stronger (σ_t of 14.8±2.4 kPa) and more stretchable as reflected by a fracture strain of ~54%. The higher stretchability of the pure gelatin gels might be caused by attractive interactions between dangling gelatin chains as well as the more flexible nature of gelatin nanoparticles as compared to rigid silica nanoparticles.

To evaluate the self-healing ability of the composite gels upon cutting, we cut the composite gels into small pieces and put these pieces (stained with purple and pink dyes) into direct contact at their freshly-cut interfaces. The cracks self-healed within a few minutes at room temperature by re-establishment of the interparticle bonds at the cut interfaces, and the gel sections formed one stable gel piece that could withstand its own weight in both horizontal (Figure 4c) and vertical (Figure 4d) directions.

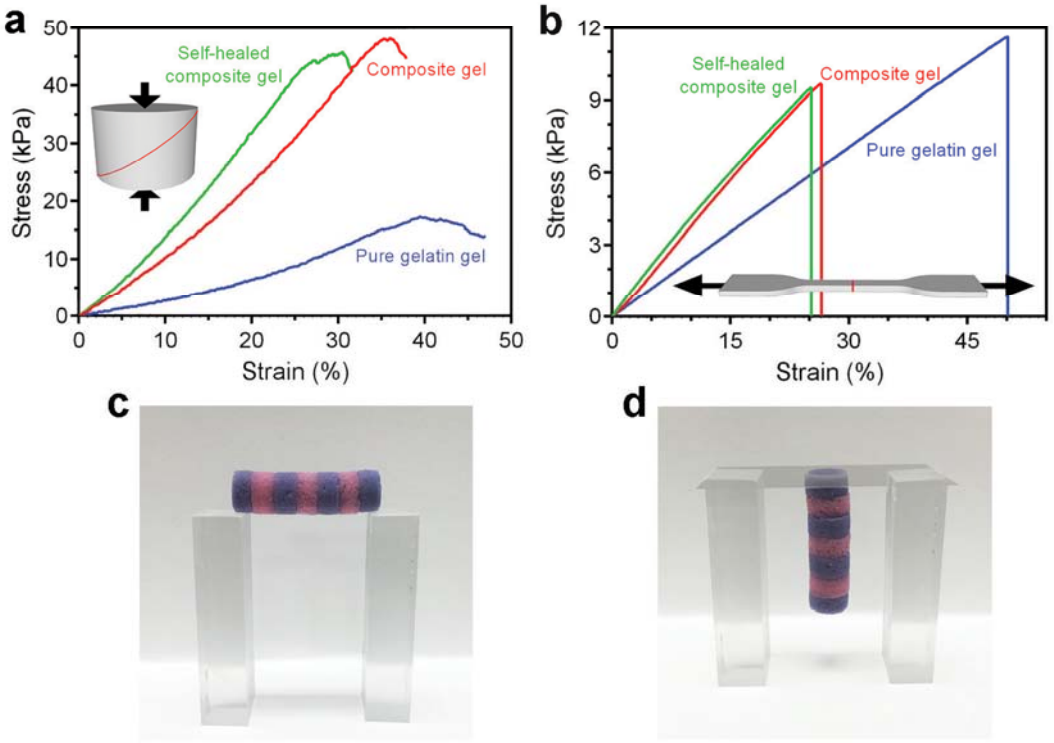

Figure 4. Stress-strain curves of virgin and self-healed gels upon a) compressive and b) tensile loading. The red lines and black arrows in the schematics indicate the cut/self-healed interfaces and the direction of applied forces, respectively. Macroscopic photographs showing self-healing of composite gel after putting freshly-cut gels (pink and purple) together to form (c) a horizontal bridge between two columns, or (d) a vertical pillar glued to a horizontally positioned cover glass.

To confirm the self-healing capability of the composite gels also quantitatively, the specimens used for compression and tensile testing were cut diagonally and vertically, respectively, after which the separate parts were put together and stored overnight. Upon compressive loading, we observed complete self-healing (Figure 4a) of the gels as evidenced by the fact that the compressive modulus ($E = 119.0 \pm 18.5$ kPa) and strength ($\sigma_c = 40.6 \pm 5.6$ kPa) were statistically similar ($P > 0.1$) to the virgin gels. Strikingly, the self-healing capacity of the composite gels was even confirmed upon tensile loading (Figure 4b), since the tensile modulus ($E = 39.6 \pm 3.8$) and strength ($\sigma_t = 8.0 \pm 1.5$ kPa) were statistically similar ($P > 0.1$) to the virgin samples before cutting.

The composite gels were cytocompatible by supporting attachment and continuous proliferation of mammalian cells (NIH 3T3 fibroblast cells) in both 2D and 3D *in vitro* culture conditions (Figure S15 and S16, Supporting Information). Consequently, applications in the biomedical field such as bioprinting and regenerative medicine may benefit from the dynamic, adaptive nature as well as excellent mechanical and handling properties of these composite gels [26].

In conclusion, we have developed a novel class of highly elastic and self-healing composite colloidal gels by pH-controlled assembly of oppositely charged gelatin and silica nanoparticles. The composite design and controlled assembly of these building blocks resulted in significantly improved mechanical properties of the composite gels in comparison with previous polymeric colloidal gels.

Mechanically robust colloidal gels were produced which were able to withstand substantial compressive and tensile loads, which was not reported previously in literature. In addition, these composite colloidal gels were able to self-heal upon both shear-induced and cutting-induced failure. These properties render these gels as ideal candidates for a wide range of applications including emerging fields such as 3D-printing. Our study strongly contributes to a deeper understanding of the structural and mechanical properties of binary colloidal systems, and opens up new avenues for practical application of colloidal gels.

Experimental section

Synthesis of gelatin nanoparticles: Gelatin nanoparticles were synthesized by a two-step desolvation method using water and acetone. Fluorescent particles were prepared by rhodamine B labeling.

Synthesis of silica nanoparticles: Silica nanoparticles were synthesized by a Stöber method through the base-catalyzed hydrolysis of tetraethyl orthosilicate. Fluorescent particles were synthesized by preparing fluorescein-labeled silica cores coated with pure silica shells.

Gel preparation: Colloidal gels were prepared by mixing basic suspensions (20 mM NaOH; pH~11) of silica and gelatin nanoparticles followed by the addition of GDL powder (at 80 mM). For gels with particle volume fractions higher than 0.3, the mixed suspensions were freeze-dried at basic pH and further gel preparation was performed by subsequent addition of water and GDL.

Confocal microscopy: A Leica TCS SP5 confocal microscope was used to visualize the gel formation process and the structure of gel networks. To monitor the gel formation process, a square-shaped chamber was used and the imaging was started immediately after mixing the suspension with GDL. For the structural evaluations, the chambers were closed and imaging was performed after overnight equilibration of gels.

Rheological tests: Rheological characterizations of samples with volume fractions of $\varphi \leq 0.05$ or $\varphi > 0.05$ were performed using either a discovery hybrid rheometer (TA instruments, with a double gap concentric cylinder geometry) or an AR2000ex rheometer (TA instruments, with a flat steel plate geometry), respectively.

Compression and tensile tests: Compression and tensile tests were performed using universal testing machines with crosshead displacement rates of 0.5 and 1 mm/min on cylindrical and dumbbell shaped specimens, respectively.

References

[1] P.J. Lu , D.A. Weitz, Colloidal Particles: Crystals, Glasses, and Gels, Annual Review of Condensed Matter Physics 4 (2013) 217-233.

[2] L.L. Hench, J.K. West, The sol-gel process, Chemical Reviews 90(1) (1990) 33-72.

[3] T. F. Tadros, in Colloids in Paints: Colloids and Interface Science, Vol. 6, (Eds: T. F. Tadros) Wiley-VCH, Weinheim, Germany, 2011, Ch.1.

[4] P. Walstra, T. van Vliet, L. G. B. Bremer, in Food polymers, gels and colloids (Eds: E. Dickinson), The Royal Society of Chemistry, Cambridge, UK, 1991, Ch. 30.

[5] T. F. Tadros, in Colloids in Cosmetics and Personal Care, Vol. 4, (Eds: T. F. Tadros) Wiley-VCH, Weinheim, Germany 2008, Ch. 1.

[6] H. Wang, M.B. Hansen, D.W.P.M. Löwik, J.C.M. van Hest, Y. Li, J.A. Jansen, S.C.G. Leeuwenburgh, Oppositely Charged Gelatin Nanospheres as Building Blocks for Injectable and Biodegradable Gels, Advanced Materials 23 (2011) H119-H124.

[7] J. Sprakel, S.B. Lindström, T.E. Kodger, D.A. Weitz, Stress Enhancement in the Delayed Yielding of Colloidal Gels, Physical Review Letters 106 (2011) 248303.

[8] J.R. Stokes, W.J. Frith, Rheology of gelling and yielding soft matter systems, Soft Matter 4 (2008) 1133-1140.

[9] a) Q. Wang, L. Wang, M.S. Detamore, C. Berkland, Biodegradable Colloidal Gels as Moldable Tissue Engineering Scaffolds, Advanced Materials 20 (2008) 236-239.; b) Z. Shao, A.S. Negi, C.O. Osuji, Role of interparticle attraction in the yielding response of microgel suspensions, Soft Matter 9 (2013) 5492-5500.

[10] H. Wang, M. Bongio, K. Farbod, A.W.G. Nijhuis, J. van den Beucken, O.C. Boerman, J.C.M. van Hest, Y. Li, J.A. Jansen, S.C.G. Leeuwenburgh, Development of injectable organic/inorganic colloidal composite gels made of self-assembling gelatin nanospheres and calcium phosphate nanocrystals, Acta Biomaterialia 10 (2014) 508-519.

[11] D.L. Taylor, M. in het Panhuis, Self-Healing Hydrogels, Advanced Materials 28 (2016) 9060-9093.

[12] a) S.B. Lindstrom, T.E. Kodger, J. Sprakel, D.A. Weitz, Structures, stresses, and fluctuations in the delayed failure of colloidal gels, Soft Matter 8 (2012) 3657-3664.; b) F. Varrato, L. Di Michele, M. Belushkin, N. Dorsaz, S.H. Nathan, E. Eiser, G. Foffi, Arrested demixing opens route to bigels, Proceedings of the National Academy of Sciences 109 (2012) 19155-19160.

[13] D. Go, T.E. Kodger, J. Sprakel, A.J.C. Kuehne, Programmable co-assembly of oppositely charged microgels, Soft Matter 10 (2014) 8060-8065.

[14] C.E. Willert, M. Gharib, Digital particle image velocimetry, Experiments in

Fluids 10 (1991) 181-193.
[15] a) E.B. Stukalin, L.-H. Cai, N.A. Kumar, L. Leibler, M. Rubinstein, Self-Healing of Unentangled Polymer Networks with Reversible Bonds, Macromolecules 46 (2013) 7525-7541.; b) R. Tadmor, J. Janik, J. Klein, L.J. Fetters, Sliding Friction with Polymer Brushes, Physical Review Letters 91 (2003) 115503.
[16] T. Coradin, O. Durupthy, J. Livage, Interactions of Amino-Containing Peptides with Sodium Silicate and Colloidal Silica: A Biomimetic Approach of Silicification, Langmuir 18 (2002) 2331-2336.
[17] A.D. Dinsmore, V. Prasad, I.Y. Wong, D.A. Weitz, Microscopic Structure and Elasticity of Weakly Aggregated Colloidal Gels, Physical Review Letters 96 (2006) 185502.
[18] R. G. Larson, The structure and rheology of complex fluids, Oxford University Press, New York, NY, USA 1999.
[19] A.D. Dinsmore, D.A. Weitz, Direct imaging of three-dimensional structure and topology of colloidal gels, Journal of Physics: Condensed Matter 14 (2002) 7581.
[20] A.B. Hopkins, F.H. Stillinger, S. Torquato, Densest binary sphere packings, Physical Review E 85 (2012) 021130.
[21] V. Baranau, U. Tallarek, Random-close packing limits for monodisperse and polydisperse hard spheres, Soft Matter 10 (2014) 3826-3841.
[22] a) M.C. Grant, W.B. Russel, Volume-fraction dependence of elastic moduli and transition temperatures for colloidal silica gels, Physical Review E 47 (1993) 2606-2614.; b) V. Trappe, V. Prasad, L. Cipelletti, P.N. Segre, D.A. Weitz, Jamming phase diagram for attractive particles, Nature 411 (2001) 772-775.
[23] D.T.N. Chen, Q. Wen, P.A. Janmey, J.C. Crocker, A.G. Yodh, Rheology of Soft Materials, Annual Review of Condensed Matter Physics 1 (2010) 301-322.
[24] C. Yan, A. Altunbas, T. Yucel, R.P. Nagarkar, J.P. Schneider, D.J. Pochan, Injectable solid hydrogel: mechanism of shear-thinning and immediate recovery of injectable β-hairpin peptide hydrogels, Soft Matter 6 (2010) 5143-5156.
[25] a) X. Wang, F. Liu, X. Zheng, J. Sun, Water-Enabled Self-Healing of Polyelectrolyte Multilayer Coatings, Angewandte Chemie International Edition 50 (2011) 11378-11381.; b) D. Chen, M. Wu, B. Li, K. Ren, Z. Cheng, J. Ji, Y. Li, J. Sun, Layer-by-Layer-Assembled Healable Antifouling Films, Advanced Materials 27 (2015) 5882-5888.; c) H. Zhang, C. Wang, G. Zhu, N.S. Zacharia, Self-Healing of Bulk Polyelectrolyte Complex Material as a Function of pH and Salt, ACS Applied Materials & Interfaces 8 (2016) 26258-26265.
[26] H. Wang, S.C. Heilshorn, Adaptable Hydrogel Networks with Reversible Linkages for Tissue Engineering, Advanced Materials 27 (2015) 3717-3736.

Supporting Information

1. Experimental section

1.1. Materials

Gelatin A (from porcine skin, 300 Bloom), tetraethyl orthosilicate (TEOS; reagent grade, 98%), 3-Aminopropyl triethoxysilane (APTES; 99%), rhodamine B isothiocyanate (RBITC; mixed isomers), fluorescein isothiocyanate (FITC; isomer I), D-(+)-gluconic acid δ-lactone (GDL; ≥99.0%) were purchased from Sigma–Aldrich. GDL powder was grinded using a mortar and pestle before usage. All other chemicals were of reagent grade and were used without any purification.

1.2. Synthesis of gelatin nanoparticles

Spherical gelatin nanoparticles were prepared by a two-step desolvation method. In the first step, 50 g of gelatin powder was dissolved in 1 L of distilled water at 50 °C. Afterward, 1 L of acetone was added to the gelatin solution and the mixture was left at room temperature for 1h to precipitate high molecular- weight gelatin. Thereafter, the supernatant was discarded and the gelatin precipitates were dissolved in distilled water and freeze-dried until further usage. In the second step, 3.75 g of the freeze-dried gelatin was dissolved in 75 mL of distilled water and the pH of solution was set to 2.5 by adding hydrochloric acid. Thereafter, 225 mL of acetone was added to the gelatin solution at 40 °C using a syringe pump with a dripping rate of 12 mL/min during vigorous stirring of the solution at 1200 rpm. To stabilize the gelatin nanoparticles by cross-linking, 495 µL of glutaraldehyde solution (25 wt%) was added to the gelatin dispersion at room temperature and left to react overnight while stirring at 600 rpm. In the next day, 300 mL of a 100mM aqueous solution of guanidine hydrochloride was added to the gelatin dispersion to block unreacted aldehyde groups and render the gelatin nanoparticles positively charged. After 1 h of stirring, the dispersion was filtered with a nylon mesh (100 µm mesh size). Subsequently, the dispersion was washed with distilled water through four centrifugation and redispersion steps.

1.3. Synthesis of fluorescent gelatin nanoparticles

To modify the gelatin nanoparticles with fluorescent rhodamine molecules, an aqueous solution of RBITC (1 mg/mL) was added to a dispersion of gelatin nanoparticle (30 mg/mL) to reach a RITC/gelatin ratio of 0.1w/w% and left to react

for 3 h while stirring with 600 rpm. Afterward, the dispersion was washed with distilled water through four centrifugation and redispersion steps

1.4. Synthesis of silica nanoparticles

Spherical silica nanoparticles were synthesized by a Stöber method. Briefly, 6.1 mL of ammonia solution (25%) and 100 mL of EtOH were mixed. Thereafter, during stirring at 600rpm, 3.3 mL of TEOS was added to the EtOH-ammonia solution and left to react at room temperature for 30 min. The solution was kept at 4 °C overnight. In the next day, the nanoparticles were washed with ethanol (1 time), ethanol-water (1 time), and distilled water (3 times) through six centrifugation and redispersion steps.

1.5. Synthesis of fluorescent silica nanoparticles

Fluorescent silica nanoparticles were prepared in three steps:

Step 1 (preparation of FITC-APTES conjugate): 27.5 µmol of FITC was dissolved in 5 mL of dimethylsulfoxide. 33 µmol APTES was added to the solution and left to stir for 1 h at room temperature.

Step 2 (preparation of fluorescent silica cores): 167.5 mL of EtOH and 12.75 mL of ammonia solution (25%) were mixed. The solution of FITC-APTES conjugate (prepared in step 1) was added to this solution and left to stir for 1 h. Thereafter, 7.1 mL of TEOS was added to the solution and left to react overnight.

Step 3 (preparation of silica shells): In the next day, 3.55 mL of TEOS was added to the suspension of fluorescent silica cores (prepared in the step 2) and left to react overnight.

During all the synthesis steps, the samples were covered with aluminum foils. After synthesis steps 1-3, the nanoparticles were washed with ethanol (1 time), ethanol-water (1 time), and distilled water (3 times) through six centrifugation and redispersion steps.

1.6. Particle size measurement

The size of nanoparticles at dry state was measured using ImageJ software (NIH) based on scanning electron microscopy (SEM; JEOL 6301) images of at least 50 dry nanoparticles. The size of swollen gelatin nanoparticles in water was measured by Nanoparticle Tracking Analysis (NTA) using a NanoSight LM10 instrument (NanoSight Ltd., UK).

1.7. Zeta potential measurement

The zeta potential of nanoparticles was measured using a Zetasizer® Nano-S instrument (Malvern Instruments Ltd.) at 25 °C by dispersion of nanoparticles in HEPES buffer (5 mM) with adjusted pH (using HCl or NaOH). Each zeta potential value represents an average of three measurements which were calculated by the Malvern software based on the measured mobility of nanoparticles according to the Smoluchowski equation.

1.8. Calculation of volume fraction and number of particles in suspensions

Suspensions of silica nanoparticles:

The volume fraction of silica in suspension was calculated based on the mass concentration of silica (obtained by air-drying) and a silica bulk density value of 2.07 mg/mL. The total number of silica nanoparticles in the suspension was calculated by dividing the total silica volume to the volume of a single silica particle.

Suspensions of gelatin nanoparticles:

To calculate the number of gelatin nanoparticles in suspension, first the total volume of dry gelatin (V_{dry} gelatin) in suspension was calculated based on the dry gelatin mass concentration in the suspension and a bulk density of 1.4 g/mL for dry gelatin. Thereafter, the total number of particles (N) was calculated by dividing V_{dry} gelatin to the volume of a single dry gelatin particle (based on the size of dry gelatin nanoparticles measured using scanning electron microscopy). Thereafter, the following equation was used to calculate the volume fraction of gelatin suspensions:

$$\varphi = \frac{4}{3}\pi r^3 \left(\frac{N}{V}\right)$$

where φ is the total volume fraction of swollen gelatin nanoparticles in the suspension, r is the radius of swollen gelatin nanoparticles (measured by NTA), N is the total number of nanoparticles in the suspension (explained above) and V is the total volume of the suspension.

1.9. Preparation of colloidal gels

Volume fraction $\varphi \leq 0.3$:

Gelatin and silica suspensions of similar volume fraction were prepared that contained 20 mM of NaOH. Thereafter, depending on the required silica-to-

gelatin ratio R, specific volumes of the silica suspension were added to the gelatin suspension and mixed by vortexing. To initiate gel formation, 80mM of GDL powder was added to the mixed suspension at pH~11.

Volume fraction $\varphi > 0.3$:

Mixed suspensions of silica and gelatin nanoparticles (pH~11 and φ=0.05) were freeze-dried. Depending on the desired volume fraction, a specific volume of distilled water was added to the freeze-dried nanoparticles. The amount of added water included the volume of the water required for complete swelling of dry gelatin nanoparticles (radius expansion from ~200 nm in dry state to ~400 nm in fully swollen state). Gelation was initiated by adding 80mM of GDL powder.

1.10. pH measurements

The pH measurements were performed using a VWR symphony pH meter. For the real-time measurements of pH of mixed dispersions as a function of the decomposition time of GDL, 5 mL of dispersion was used and the GDL powder (80mM) was added just before the measurement.

1.11. Confocal microscopy

A Leica TCS SP5 confocal microscope was used to visualize the process of gel formation and the structure of the resulting gel networks. To prepare a sample chamber, a square-shaped cavity (~1.5×1.5 cm) was removed from the middle of a plastic cover slip (0.16 mm thick) using a razor blade. The plastic cover slip, covered with a commercial sealant, was placed on top of a cover glass. For GDL-containing samples, GDL powder was applied close to the edges of the chamber. The colloidal dispersion was placed in the middle of the chamber. Finally, another cover glass was placed on top to close the chamber. For gel formation studies, the measurement was started immediately after closing the chamber.

For gel structure evaluation, the measurement was performed after overnight equilibration of the samples. The detection wavelengths for fluorescent silica (FITC-labeled) and gelatin (RBITC-labeled) nanoparticles were set to 500–530 nm and 575–700 nm, respectively. The silica and gelatin nanoparticles with different fluorescence excitation profiles were imaged by separate detectors and their corresponding excitation laser lines through sequential excitation to minimize fluorescence bleed-through.

1.12. Confocal microscopy of self-healed gels

To evaluate the microstructure of self-healed gels after shear-induced gel network destruction, a mixed suspension of silica and gelatin (φ =5; R=5; 80mM NaOH) was prepared. A rectangular cover glass was fixed on the rheometer Peltier plate using adhesive tapes (Figure S12, Supporting Information). GDL powder was distributed on the cover glass surface after which the mixed suspension was added onto the cover glass. The rheometer gap was set to 500 µm. 1 h of equilibration at room temperature was carried out to form the gel under the geometry. A strain sweep from 0.5 to 1000 strain % was performed to shear the gel network destructively. Immediately after the strain sweep the gap distance was increased and the cover glass carrying the sheared gel sample was placed under the confocal microscope to perform tile scans in order to obtain an overview image of the structure.

1.13. Particle mobility analysis

A particle image velocimetry (PIV) method [1] was used to measure the relative mobility of each set of particles. This method divides the images into smaller windows and calculates the displacement of fluorescent particles by cross-correlating the image intensities in these windows in pairs of consecutive frames. The relative mobility was obtained from the measured average displacement field normalized by the largest displacement. The spatial resolution for the relative mobility was 1.12 µm.

1.14. Gel structure analysis

The topology and connectivity of the gel structures were evaluated quantitatively with an image processing method using an ImageJ software plugin (DiameterJ) [2]. In this method, firstly, confocal images were transformed to binary black and white images using a thresholding process. The intersection density of strands (node density) was determined by skeletonization of the gel network using a strand thinning algorithm which determines the centerlines of strands. The average thickness of strands was determined using a Euclidian distance transformation algorithm which determines the distance of each strand pixel to its nearest void pixel. The strand thickness values at intersections were excluded from the strand thickness calculations. The average strand length (node-to-node distance) was calculated by dividing the total length of centerlines (strands) by the total number of nodes (intersection of strands). For each composition of gels, 50 confocal images

from random areas of 2 samples were analyzed.

1.15. Rheological tests

For rheological characterization of samples with low volume fractions ($\varphi \leq 0.05$), a discovery hybrid rheometer (TA instruments) with a double gap concentric cylinder geometry (a cup radius of 15 mm, a rotor radius of 14 mm, and a rotor height of 42 mm) was used. The extensive shearing surface of this geometry provides a high sensitivity for rheological measurement of weak gels, but requires a high volume of sample. For each measurement, 6 mL of dispersion was used. The measurements were performed at 25 °C and with an operating gap of 2000 μm.

For rheological characterization of samples with volume fractions higher than 0.05, an AR2000ex rheometer (TA instruments) with a flat steel plate geometry (40 mm diameter) was used. The measurements were performed at 25 °C and with an operating gap of 500 μm.

All the measurements started with a time sweep of 3 h as the sample equilibration step. The initial and subsequent time sweep measurements were performed at a frequency and strain of 1 Hz and 0.5%, respectively. Frequency sweep measurements were performed with frequencies ranging from 0.1 to 100 Hz at a constant strain of 0.5%. Strain sweep measurements were performed at a constant frequency of 1 Hz with strains ranging from 0.1 to 1000%. Self-healing properties of the samples were studied quantitatively by performing multiple cycles of consecutive strain and time sweeps (30 min). The self-healing ability of the gels was quantified based on the recovery (%) of the storage modulus (G') of the gels after each step of strain sweep-induced gel network destruction relative to their initial storage modulus before strain sweeps. The shear-thinning behavior of the gels was determined by measuring their viscosity while varying the shear rate from 0 to 1000 s^{-1}.

1.16. Compression tests

Compression tests were performed using an LS1 (Lloyd Instruments, UK) universal testing machine equipped with a 100 N load cell. Cylindrical hydrogel specimens (Figure S13a) were prepared by pressing the hydrogels into cylindrical Teflon molds (diameter: 8 mm, height: 5 mm) and keeping them at 4 °C overnight. Self-healed samples were prepared by diagonal cutting of the cylindrical hydrogels into two parts using a surgical blade after which the two sections were put back together to close their cut interfaces (Figure S14). Thereafter, the samples were kept at 4 °C

overnight inside cylindrical Teflon molds, with the same dimensions as the samples, in order to ensure physical contact between the two sections. The compression tests were carried out at a loading rate of 0.5 mm/min. The elastic modulus of the samples was calculated from the average slope of the initial part (0 to 10 % strain) of their stress-strain curves. The compressive strength was calculated from the maximum load reached during the fracture of samples divided by their original cross-sectional area. Three samples were measured for each experimental condition (n=3).

1.17. Tensile tests

Tensile tests were performed using a Z2.5 (Zwick Roell, Germany) universal testing machine equipped with a 20 N load cell. Dumbbell shaped hydrogel specimens (Figure S13b) were prepared by pressing the hydrogels into 3D-printed plastic molds (designed according to type 5B of ISO 527-2 standard) and keeping them at 4 °C overnight. Self-healed samples were prepared by cutting the hydrogel specimens into two parts using a surgical blade after which the two sections were put back together to close their cut interfaces (Figure S14). Thereafter, the samples were kept at 4 °C overnight inside the dumbbell shaped Teflon molds, with the same dimensions as the samples, in order to ensure physical contact between the two sections. The tensile tests were carried out at a crosshead displacement rate of 1 mm/min. To avoid potential slipping between the hydrogel surfaces and the tensile grips, each end of the hydrogel specimens was glued to plastic holders which were fixed with grips. The tensile modulus of the samples was calculated from the average slope of their stress-strain curves. The tensile strength was calculated as the maximum load before breakage of the samples divided by their original cross-sectional area. Three samples were measured for each experimental condition (n=3).

1.18. Statistics

Statistical analysis for the results obtained from compression and tensile tests was carried out using an unpaired Student's t-test, with $P < 0.1$ being considered as statistically different.

1.19. Cell culture

NIH3T3 (ATCC® CRL-1658™) fibroblasts cells were cultured for 7 days in proliferation medium (Dulbecco's modified Eagle medium, DMEM, Sigma-Aldrich) supplemented with 10% v/v fetal bovine serum (FBS, Gibco) at 37 °C,

95% relative humidity and 5% CO_2. The medium was changed after 1 day to remove non-adherent cells, and it was refreshed after every three days of culture. At confluence, cells were washed twice with Phosphate-Buffered Saline (PBS), detached using trypsin/EDTA (0.25 % w/v trypsin/0.02 % EDTA) for 5 min and resuspended in medium.

Gelatin and silica nanoparticles were sterilized by washing first with 75% v/v ethanol solution and then with sterile distilled water for several times before being combined at various number ratios (R=0, 1, 5) in dilute NaOH (20mM) solutions (pH~11). After freeze-drying for at least 48 hours, these nanoparticle mixtures were mixed with DMEM cell culture medium in a Luer-lock dual syringe system (two 1 ml syringes connected with a female-female adaptor) to form composite colloidal gels with a volume fraction of 0.75. The resulting composite gels were injected into polydimethylsiloxane molds (5mm diameter, 2mm depth) and incubated in 6-well plates (Greiner-Bio One). The gel-loaded molds were soaked in culture medium and incubated at 37°C overnight, in which the media were refreshed before cell seeding. Subsequently, NIH3T3 cells were seeded on top of the gels at 5000 cells/cm² and allowed to attach for 1 hour, and then 2 ml of culture media were added to submerge the gels. The media were changed after 1 day to prevent nutrient exhaustion. Gels were removed at 24, 48 and 72 hours for qualitative assessment of cell viability.

Cell survival was determined using a LIVE/DEAD Viability/Cytotoxicity Kit (Molecular Probes). To this end, gels were washed in sterile PBS for 30 min at 37 °C prior to incubation for 30 min at room temperature with 2 mM calcein-AM (red-fluorescent dye for dead cells) and 4 mM ethidium homodimer (green-fluorescent dye for live cells) in PBS solution. After incubation, gels were rinsed in PBS and examined using confocal laser scanning microscopy.

2. Supplemental figures

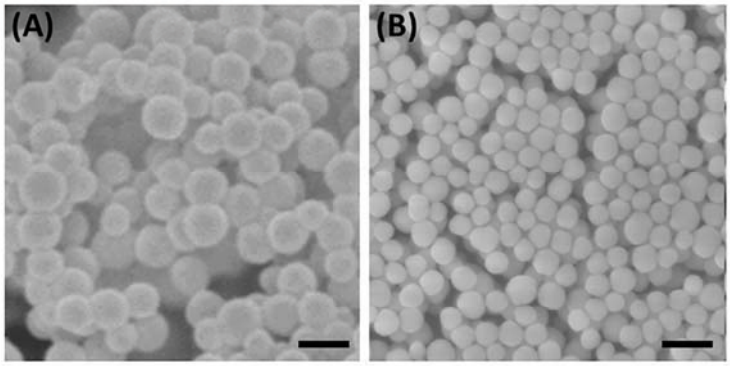

Figure S1. Scanning electron micrographs of (A) freeze-dried gelatin and (B) air-dried silica nanoparticles. Scale bars represent 200 nm.

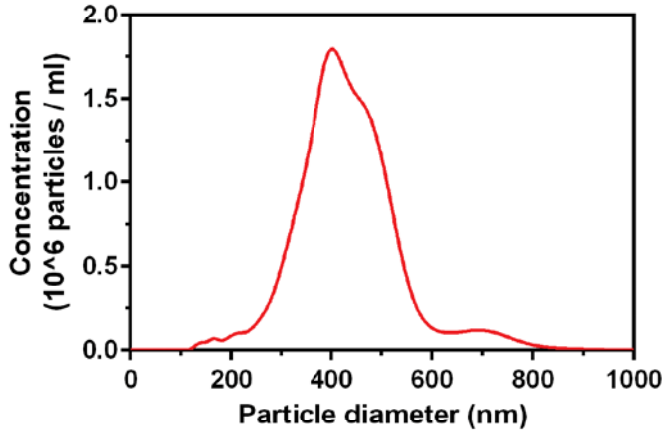

Figure S2. Particle size distribution profile of swollen gelatin nanoparticles in water.

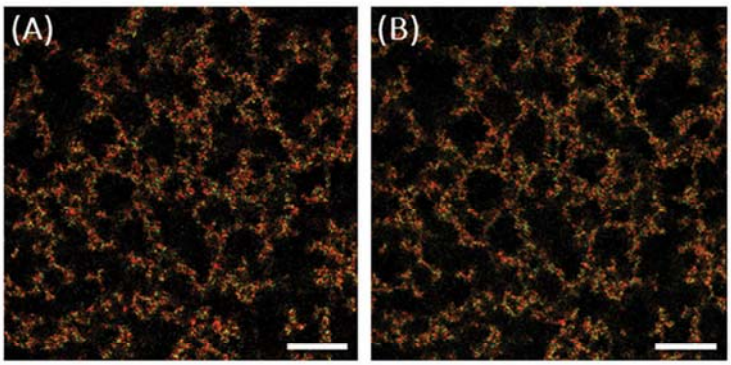

Figure S3. Confocal images of a colloidal gel with R=5 and φ=0.05 (A) before and (B) after addition of an excessive amount 100mM NaOH solution. Scale bars represent 25 μm.

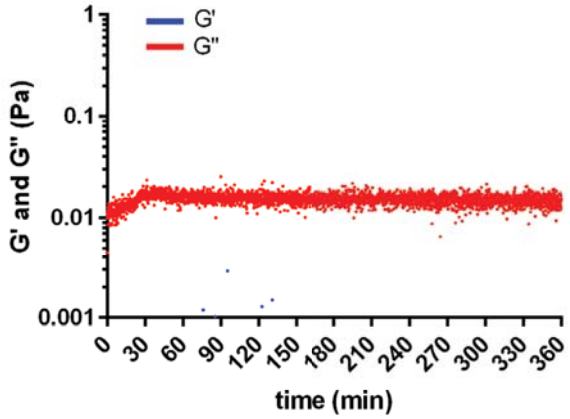

Figure S4. Storage and loss moduli of a colloidal dispersion with R=5 and φ=0.05 (without GDL) as a function of time.

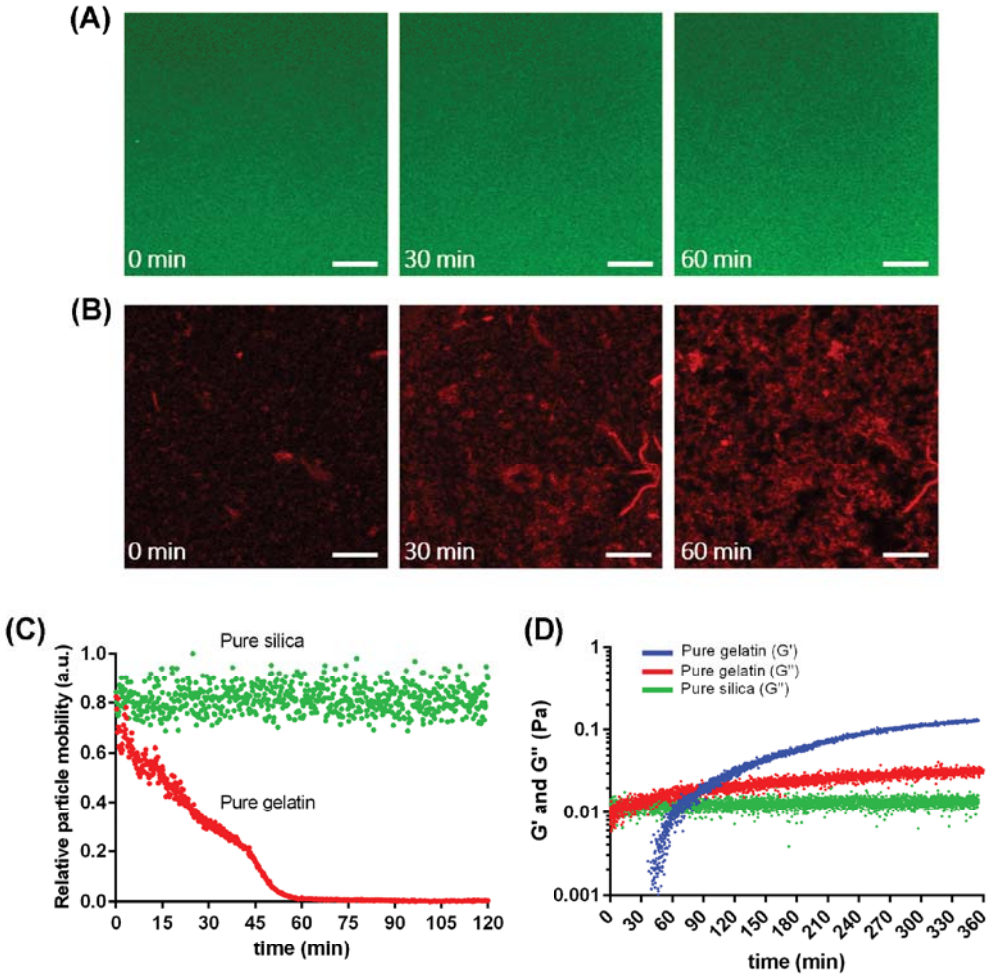

Figure S5. Confocal images showing (A) pure silica (R=∞) and (B) pure gelatin (R=0) samples at different time points during GDL decomposition. (C) Mobility of particles in pure silica and pure gelatin samples as a function of time. (D) Rheological characterization of pure silica and pure gelatin samples during GDL decomposition. φ=0.05 for all the samples. Scale bars in images represent 25 μm.

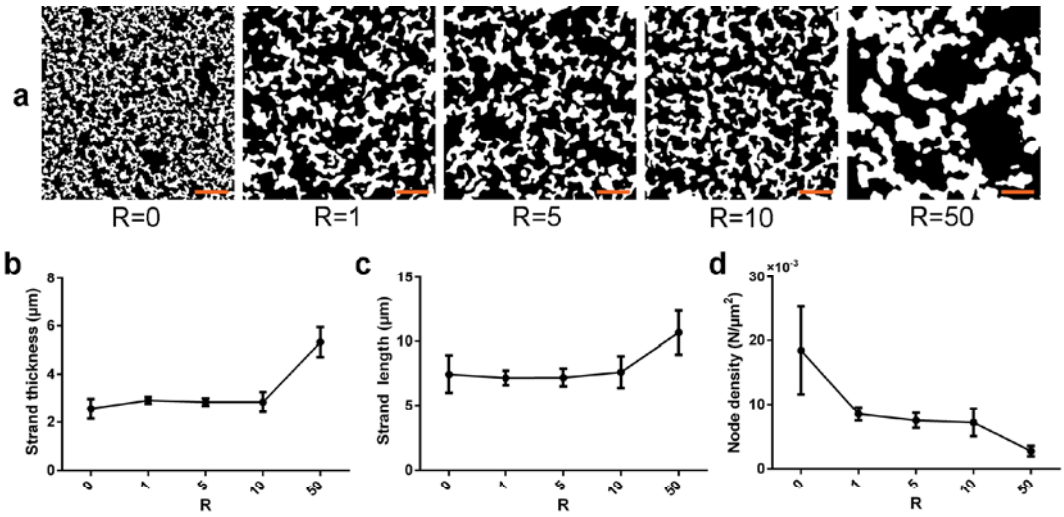

Figure S6. Microstructural features of colloidal gel networks. a) Representative binary images of colloidal gels with various silica-to-gelatin number ratio ratios R. b) Mean strand thickness, c) average strand length (node-to-node distance), and d) node density of colloidal networks as a function of silica-to-gelatin ratio R. Volume fraction φ=0.05. Scale bars in images represent 25 μm.

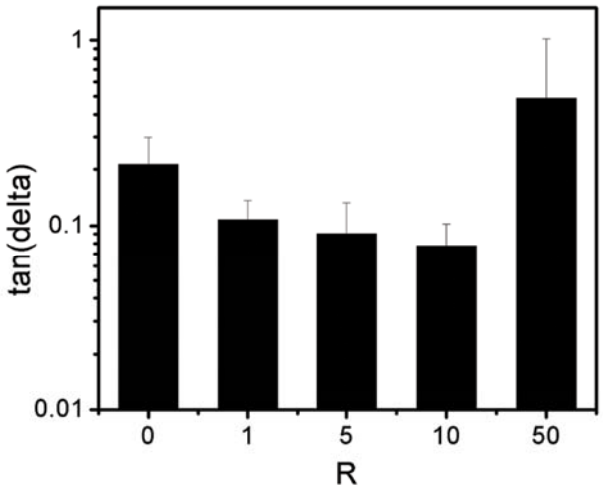

Figure S7. Tan(δ) of the colloidal gels as a function of silica-to-gelatin ratio (R). Volume fraction φ=0.05.

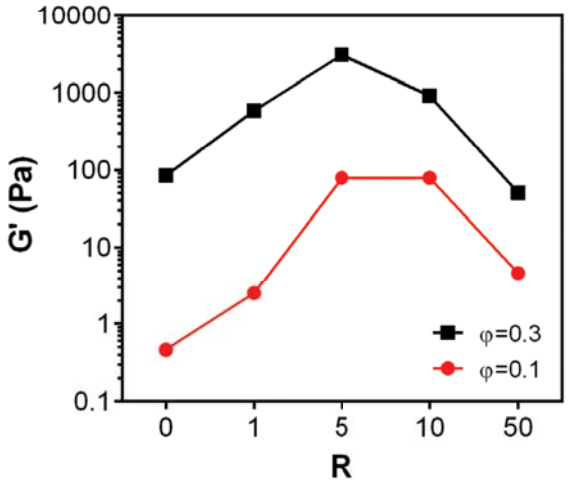

Figure S8. Storage modulus (G') of the colloidal gels as a function of silica-to-gelatin ratio (R) at different volume fractions (φ=0.1 and 0.3).

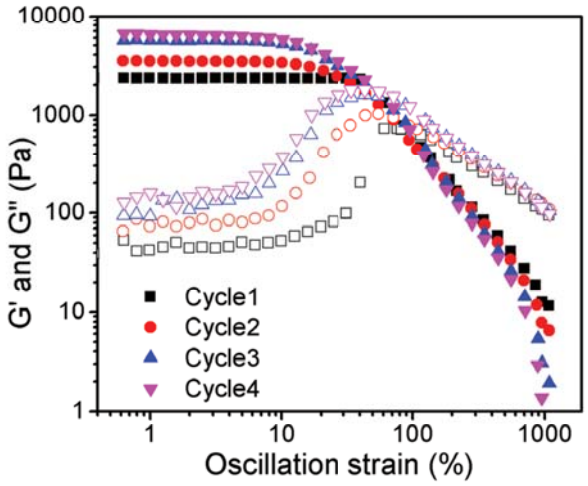

Figure S9. Multiple cycles of strain sweeps for a composite colloidal gel (R=5, and φ=0.3) with 30 min of recovery between each cycle. Solid and open symbols correspond to storage (G') and loss (G'') moduli, respectively.

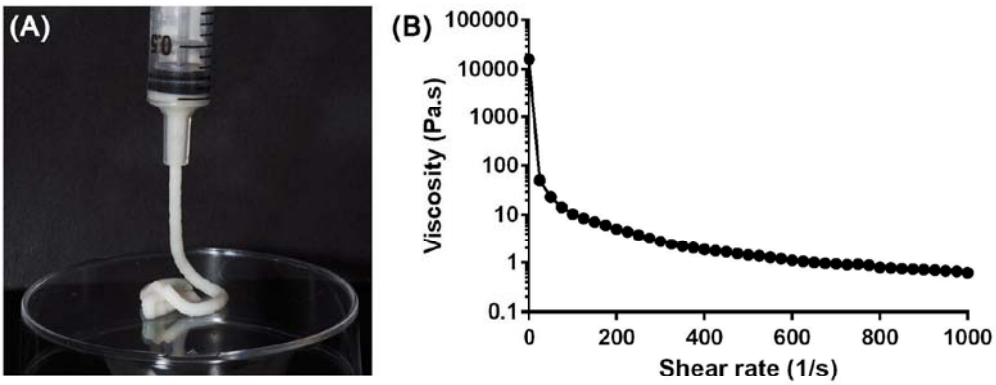

Figure S10. (A) Digital photograph during the injection and (B) shear-thinning behavior of composite colloidal gels with R=5 and φ=0.5.

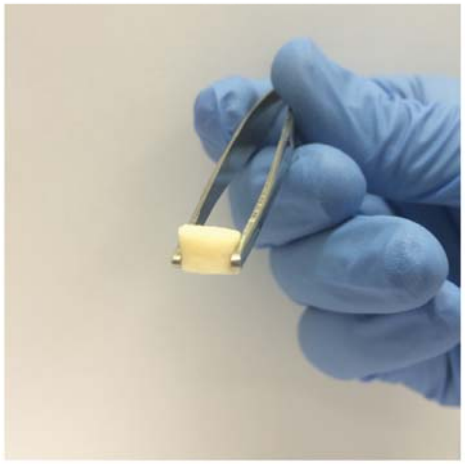

Figure S11. Digital photograph of a molded colloidal gel with R=5 and φ=0.5.

Figure S12. Experimental setup used for destructive shearing of colloidal gels for analysis using confocal microscopy.

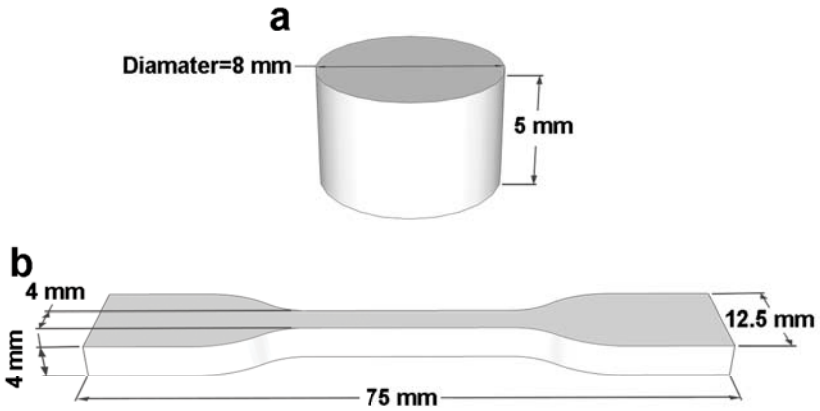

Figure S13. Geometry of a) compression and b) tensile test specimens.

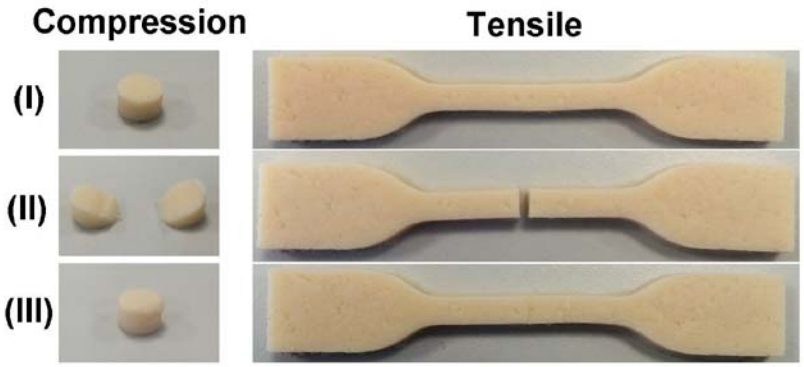

Figure S14. Macroscopic photographs showing composite gel specimens (R=5, φ=1) used for compressiown and tensile tests. I) as prepared, II) after manual cutting, and III) after self-healing by establishing physical contact between the cut surfaces.

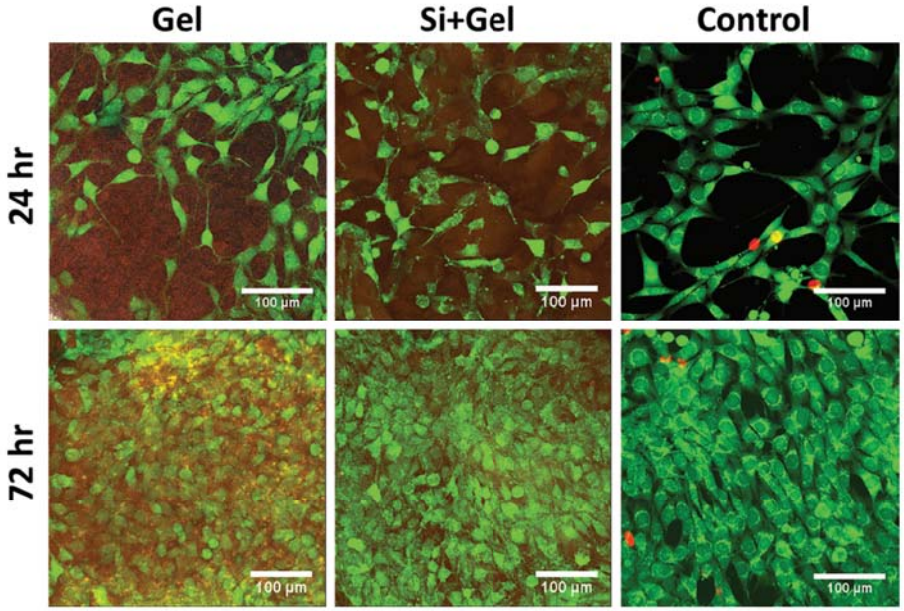

Figure S15. LIVE/DEAD assay of NIH 3T3 fibroblast cells after 24 and 72 h of culture on top of the pure gelatin (φ=0.75, denoted as Gel) and the composite colloidal gels (R=1, φ=0.75, denoted as Si+Gel) and a culture plate as control.

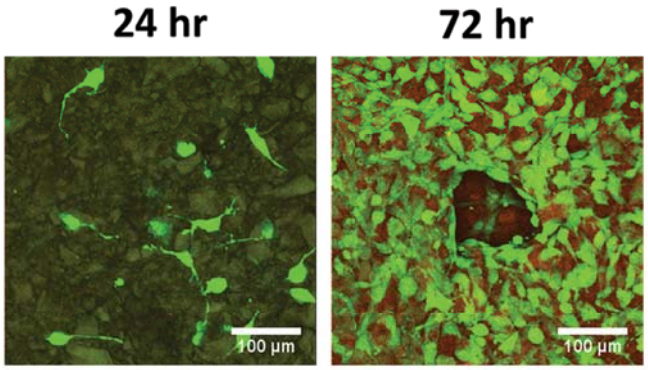

Figure S16. LIVE/DEAD assay of NIH 3T3 fibroblast cells after 24 and 72 h of 3D culture in the composite colloidal gels (R=1, φ=0.75).

3. Supplemental movies

Movie S1. Time-lapse confocal microscopy of a suspension with R=5 and φ=0.05 (with GDL).

Movie S2. Time-lapse confocal microscopy of a suspension with R=5 and φ=0.05 (without GDL).

Movie S3. Time-lapse confocal microscopy of a pure gelatin (R=0) suspension with φ=0.05 (with GDL).

Movie S4. Time-lapse confocal microscopy of a pure silica suspension with φ=0.05 (with GDL).

Movie S5. Time-lapse confocal microscopy of a colloidal dispersion with R=100 and φ=0.05 (with GDL) after overnight equilibration.

Movie S6. Digital video showing the drop of a colloidal gel sample (R=5 and φ=1) in slow motion.

Movie S7. Digital video showing a composite colloidal gel specimen (R=5 and φ=1) during a compression test.

Movie S8. Digital video showing a composite colloidal gel specimen (R=5 and φ=1) during a tensile test.w

4. Supplemental references

[1] W. Thielicke, E. Stamhuis, PIVlab–towards user-friendly, affordable and accurate digital particle image velocimetry in MATLAB, Journal of Open Research Software 2 (2014) e30.

[2] N.A. Hotaling, K. Bharti, H. Kriel, C.G. Simon, DiameterJ: A validated open source nanofiber diameter measurement tool, Biomaterials 61 (2015) 327-338.

Chapter 3

Composite colloidal gels made of bisphosphonate-functionalized gelatin and bioactive glass particles for regeneration of osteoporotic bone defects

This chapter is based on:

M. Diba, W.A. Camargo, M. Brindisi, K. Farbod, A. Klymov, S. Schmidt, M.J. Harrington, L. Draghi, A.R. Boccaccini, J.A. Jansen, J.J.J.P. van den Beucken, and S.C.G. Leeuwenburgh, *Advanced Functional Materials*, (2017) 1703438.

1. Introduction

Bone loss and fracture require effective regenerative treatment, particularly when accompanied by a degenerative condition such as osteoporosis [1]. Currently, the use of autologous bone is still the gold standard in clinical practice for treatment of bone defects [2]. However, disadvantages associated with this treatment modality include donor site morbidity and limited availability. These clinical drawbacks have urged the development of alternative strategies for regeneration of bone tissue [3]. Therefore, extensive research efforts have been dedicated to the development of a wide range of bone regenerative materials [4]. Among these materials, organic-inorganic composites are particularly promising by mimicking the chemical composition of bone, while combining mechanical stability with biocompatibility [5, 6]. In addition, the intraoperative handling properties of bone-substituting biomaterials are crucial for their clinical applicability [7]. Hence, injectable composite biomaterials have recently gained interest for applications in bone regeneration [7, 8]. Colloidal gels are particularly promising injectable biomaterials [9-12]. These gels are solely composed of colloidal particles. Various types of particles can be used as colloidal building blocks, which can be loaded or functionalized with different types of drugs or biomolecules [13-16]. By utilizing reversible, non-covalent interparticle bonds, self-healing colloidal gels can be prepared that recover their mechanical properties after destructive shearing upon extrusion through needles [9]. Furthermore, the dynamic and adaptive nature of colloidal gel networks can provide an excellent microenvironment for tissue ingrowth and cellular activity [9], potentially leading to improved bone regeneration.

We have recently shown [9-11, 14, 15, 17] that gelatin-based colloidal gels are promising materials for applications in bone regeneration. Nevertheless, colloidal gels composed of only soft organic particles are mechanically weak and lack sufficient bioactivity [11, 12]. The performance of these purely organic colloidal systems was enhanced previously by (i) modification of organic particles with functionally and biologically active molecules [15, 16, 18] or (ii) inclusion of bioactive inorganic particles [9, 10]. Regarding strategy (i), we have recently demonstrated [18, 19] that functionalization of gelatin nanoparticles with bisphosphonate molecules enhances their binding affinity toward calcium-containing minerals, i.e., hydroxyapatite, and induces sustained release of bisphosphonates. Regarding strategy (ii), it was

recently shown that the inclusion of inorganic fillers such as bio-inactive silica [9] or hydroxyapatite particles [10] generates colloidal gel composites with superior mechanical performance. By combining both strategies, we hypothesized that composite colloidal gels can be designed that combine mechanical robustness, bone regenerative capacity, and anti-osteoporotic therapeutic efficacy.

Here, we report the development of injectable composite colloidal gels assembled from bisphosphonate-functionalized gelatin and bioactive glass particles (Scheme 1). Gelatin was used to prepare the organic building blocks due to its widespread availability [20], availability of adhesive cell recognition sites [21], and ease of functionalization [18, 19]. 45S5 bioactive glass (Bioglass®) particles were used as the inorganic building blocks since this glass type is the most common type of bioactive glass due to its strong bioactivity and biodegradability [22]. We functionalized the gelatin particles with calcium-binding bisphosphonate groups not only for their capacity to bind to calcium-containing bioactive glasses [23] but also due to their anti-osteoporotic efficacy [24]. We first used a colloidal probe atomic force microscopy (AFM) technique to quantify the effect of the bisphosphonate functionalization of gelatin particles on the interparticle adhesion forces between gelatin and bioactive glass particles. We then prepared colloidal gels from gelatin nanoparticles, with or without bisphosphonates, and bioactive glass particles and studied the viscoelastic properties of the resulting gels. Next, we assessed the *in vitro* performance of these composite gels by quantifying the proliferation and differentiation of osteoblastic cells cultured on top of the gels, and also evaluated the apatite-forming ability of these materials in the presence or absence of cells. Finally, we examined the bone regenerative capability of the composite colloidal gels *in vivo* upon implantation into femoral condyle defects in osteoporotic rats.

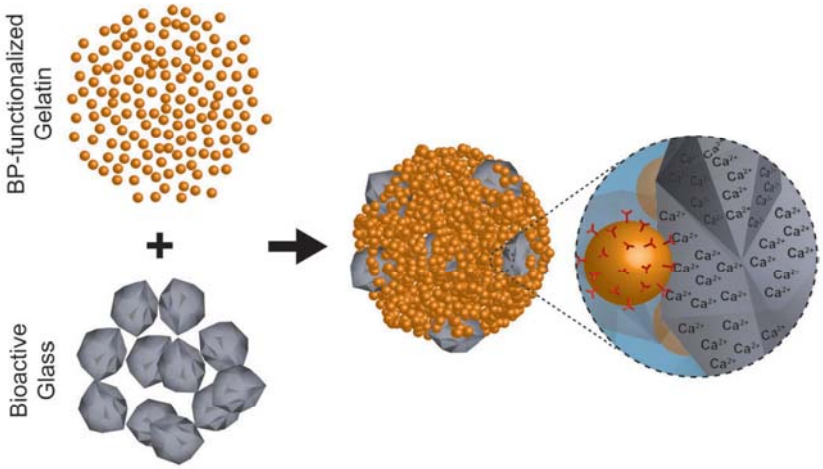

Scheme 1. Schematic illustration of formation of composite colloidal gels composed of bisphosphonate (BP)-functionalized gelatin and bioactive glass particles.

2. Materials and methods

2.1. Materials

Gelatin powder (Type B from bovine skin; 225 Bloom) was purchased from Sigma–Aldrich. Glutaraldehyde solution (25 wt% aqueous solution in water) was obtained from Acros Organics. Alendronic acid (ALN; 4-Amino-1-hydroxybutane-1,1-diphosphonic acid) was purchased from AK Scientific, Inc. (AKSci, Union City, CA, USA). Aldehyde-functionalized (SuperAldehyde) glass slides were purchased from Arrayit Corporation (Sunnyvale, CA, USA). For atomic force microscopy experiments, spherical bioactive glass (45S5 Bioglass®) microparticles with an average diameter of 49 ± 4 μm were obtained from XL Sci-Tech, Inc. (Richland, WA, USA). For hydrogel preparation, commercially available bioactive glass particles of 45S5 composition (Vitryxx®, Schott AG, Mainz, Germany) with a mean particle size of ~2 μm were used. The 45S5 Bioglass® particles used for the force microscopy and hydrogel preparation contained 45 wt% SiO_2, 24.5 wt% CaO, 24.5 wt% Na_2O, and 6 wt% P_2O_5. All other chemicals were reagent grade and used without any purification.

2.2. Synthesis and functionalization of gelatin nanoparticles

2.2.1. Preparation of non-functionalized nanoparticles

Spherical gelatin nanoparticles were produced by a two-step desolvation method [9]. In the first desolvation step, gelatin powder (50 g) was dissolved at 50 °C in 1 L of MilliQ water. Afterward, 1 L of acetone was rapidly added to the

gelatin solution. The mixture was left for 1 h at room temperature to precipitate the gelatin with high molecular weight. Thereafter, the supernatant was removed and the gelatin precipitates were re-dissolved in MilliQ water and freeze-dried for further usage. In the second desolvation step, 3.75 g of the freeze-dried gelatin was dissolved at 50 °C in 75 mL of MilliQ water, after which the pH of the solution was adjusted to 2.5 using HCl (5 M aqueous solution). Thereafter, 225 mL of acetone was added to the gelatin solution at a dripping rate of 12 mL/min using a syringe pump during vigorous stirring (1200 rpm) of the solution at 50 °C. To stabilize the gelatin nanoparticles via cross-linking, glutaraldehyde was used at a molar ratio of 1:1 between glutaraldehyde molecules and amine groups of gelatin. Accordingly, 555 µL of glutaraldehyde solution (25 wt%) was added dropwise to the gelatin dispersion at room temperature and left to react while stirring at 600 rpm for ~16h. In the next day, 300 mL of an aqueous solution of glycine (100 mM) was added to the dispersion of gelatin nanoparticles in order to block unreacted aldehyde groups. After 1 h of reaction, the dispersion was filtered using a nylon mesh (mesh size 100 µm) to remove any gelatin aggregates. Subsequently, the dispersion was washed with MilliQ water through four centrifugation (at 5000 rpm for 1 h) and redispersion steps. Finally, the gelatin nanoparticles were dispersed in a 1:3 (V:V) mixture of acetone:water and freeze-dried for further usage.

2.2.2. Preparation of bisphosphonate-functionalized nanoparticles

Alendronic acid was used as the bisphosphonate compound for functionalization of the gelatin nanoparticles. The preparation of bisphosphonate-functionalized gelatin nanoparticles was carried out according to our previous report [18]. Briefly, the two-step desolvation method was performed as described above. However, after the cross-linking step with glutaraldehyde, unreacted aldehyde groups present in the gelatin nanoparticles were utilized for conjugation to the amine group of alendronate molecules. A molar ratio of 5:1 was used between alendronate and glutaraldehyde molecules added to the dispersion. Accordingly, 1.83 g of alendronic acid was dissolved in 183 mL of MilliQ water (pH was adjusted to 2.7 using NaOH solution). The alendronate solution was added dropwise to the gelatin dispersion instead of glycine solution used for non-functionalized nanoparticles. After ~16h of reaction during stirring at 600 rpm, the nanoparticles were filtered, washed, and freeze-dried as described above.

2.3. Characterization of particles

2.3.1. Scanning Electron Microscopy (SEM)

The morphology of bioactive glass and gelatin particles in dry state was evaluated using a field emission scanning electron microscope (FE-SEM; Sigma 300, Zeiss, Germany). Sample preparation was carried out prior to the imaging by dispersing the particles on a sticky carbon tape and sputter-coating with an electroconductive chromium layer (5 nm thick). The average sizes of bioactive glass and gelatin particles were determined by measuring the size of 50 particles for each particle type in SEM images using ImageJ software.

2.3.2. Dynamic Light Scattering (DLS)

The size and polydispersity of swollen gelatin nanoparticles in aqueous solution were measured by Dynamic Light Scattering (DLS) using a Zetasizer® Nano-S (Malvern Instruments Ltd.). The measurements were carried out in MilliQ water with three repetitions for each particle type.

2.3.3. Elemental analysis

To confirm successful bisphosphonate functionalization of gelatin nanoparticles, their elemental composition was analyzed using Inductively Coupled Plasma-Optical Emission Spectrometry (ICP-OES, iCAP 6300, Thermo Fisher Scientific, USA). Sample preparation was carried out by dissolving the particles in concentrated nitric acid solutions for 24 h at 37 °C. Thereafter, the solutions were diluted with MilliQ water to reach a nitric acid concentration of 1 v/v% for further analysis using ICP-OES.

2.4. Atomic Force Microscopy (AFM)

A colloidal probe atomic force microscopy (AFM) method was used to quantify the interactions between gelatin and bioactive glass particles. The measurements were performed in MilliQ water (pH adjusted to 7 using NaOH solution) and phosphate-buffered saline (PBS) solutions at room temperature using a NanoWizard III AFM instrument (JPK Instruments AG, Germany) equipped with an inverted optical microscope (Olympus IX71, Germany). Force measurements were performed between a bioactive glass microsphere fixed on a cantilever and gelatin nanoparticles fixed on a glass slide. The colloidal probes (Figure S1) were prepared by gluing single Bioglass® microparticles to AFM cantilevers (μMash, CSC38/tipless/No Al)

using an epoxy resin (UHU Plus Schnellfest, UHU GmbH & Co. KG, Germany). Gelatin nanoparticles were fixed to glass slides by covering the reactive side of aldehyde-functionalized glass slides with concentrated suspensions of gelatin nanoparticles for 1h. Subsequently, the substrates were rinsed with MilliQ water to remove unattached gelatin nanoparticles and then immersed in 100 mM glycine solutions for 1 h to block potential unreacted aldehyde groups present on the glass slides. Finally, the substrates were rinsed with MilliQ water to remove residual glycine molecules. Prior to AFM measurements for each substrate or solution type, the colloidal probe was rinsed with MilliQ water and treated for 1 min in an air-plasma cleaner. For each experimental condition, AFM measurements were carried out by performing approach/withdrawal cycles with a velocity of 1 μm/s through force mapping of 35 spots. After each approach step, prior to the withdrawal step, the colloidal probe was kept in contact with the substrate for 5 seconds at constant force of 3.5 nN. The adhesion force value in each force-distance curve was determined as the force difference between the zero deflection point and the maximum adhesion point.

2.5. Preparation of colloidal gels

To prepare the colloidal gels, different ratios of gelatin and bioactive glass powders were added in plastic tubes and thoroughly mixed using a spatula and vortexing. The particle volume fraction in a colloidal gel was defined as the total volume of solid bioactive glass particles and swollen gelatin nanoparticles divided by the total volume of the colloidal gel (i.e., particles plus free water).

By considering a bulk density of 1.4 g/ml for dry gelatin and a 1.6-fold expansion of the gelatin nanoparticle diameter upon complete swelling (corresponding to a fourfold volume increase) as determined by SEM and DLS measurements, we calculated that each gram of dry gelatin nanoparticles would require ~2 mL of water for complete swelling. Depending on the desired particle volume fraction, a specific volume of MilliQ water was added to the powder. The amount of added water included the volume of the water required for the complete swelling of dry gelatin nanoparticles in each composition. After addition of water, the tubes were subjected to 1 min of vortexing. Thereafter, the tubes were centrifuged for 1 min at 5000 rpm to confine the colloidal gels at the bottom of the tubes. Table 1 lists the compositions of colloidal gels prepared in this study.

Table 1. List of colloidal gel samples prepared in this study.

Sample abbreviation	Type of gelatin nanoparticles	Bioglass®/gelatin ratio (w/w)
Gel	Non-functionalized	0
Gel+BG(R)	Non-functionalized	0.1-25
BPGel	Bisphosphonate-functionalized	0
BPGel+BG(R)	Bisphosphonate-functionalized	0.1-25

*R indicates the Bioglass®/gelatin ratio (w/w) of the corresponding sample.

2.6. Rheological characterizations

Rheological properties of the colloidal gels were evaluated using an AR2000 Advanced Rheometer (TA Instruments) with a flat steel plate geometry (8 mm diameter) and gap distance of 500 µm at 25 °C. Frequency sweep measurements (0.1 Hz to 10 Hz) were carried out at a fixed strain of 0.5%. Storage (G') modulus, loss (G'') modulus, and tan(delta) of the colloidal samples were determined by performing a time sweep for 1 min at 0.5% strain and an oscillatory frequency of 1 Hz. The self-healing ability of the gels was evaluated in three consecutive steps by measuring the recovery of G' after shear-induced gel network destruction:

Step 1: Time sweep for 1 min at 0.5% strain and a frequency of 1 Hz.

Step 2: Strain sweep from 0.5% to 1000% strain at a frequency of 1 Hz.

Step 3: Time sweep for 5 min at 0.5% strain and a frequency of 1 Hz.

The recovery of G' was determined using Equation 1:

$$Recovery\ of\ G'\ (\%) = \left(\frac{G'_r}{G'_i}\right) \times 100 \qquad (1)$$

where G'_i is the average of G' values during the time sweep in step 1 and G'_r is the G' at the end of step 3, i.e., after 5 min of recovery. For all measurements, three samples were analyzed for each experimental condition.

2.7. *In vitro* cell culture and mineralization experiments

2.7.1. Sample preparation

Gelatin and bioactive glass particles were disinfected by freeze-drying and exposure to UV radiation (peak wavelength of 365 nm) for 1 h. Thereafter, Gel, BPGel, BPGel+BG(0.1), and BPGel+BG(0.5) samples with a particle volume fraction of 0.4 were prepared by adding sterile MilliQ water to the particles, followed by vortexing and centrifugation as described above. Subsequently, the gels were

transferred to sterile syringes and injected into cylindrical polypropylene molds. Each mold contained around 160 µL of gel. The molds were placed in 24-well cell culture plates (Greiner-BioOne) and stabilized with metal rings to prevent floating. All sample preparation steps were carried out under sterile conditions.

2.7.2. Cell culture experiments

Frozen stocks of osteoblast precursor cells (MC3T3 cell line; LGC Standards, Wesel, Germany) were cultured for 10 days in Alpha Minimum Essential Medium (Alpha MEM) medium supplemented with 10% v/v fetal bovine serum (FBS) at 37 °C, 95% of relative humidity and 5% of CO_2. The medium was refreshed every 3 days of culture. At 70–80% of confluence, cells were washed with PBS, detached using 0.25% w/v Trypsin (0.25% w/v)/EDTA (0.02% w/v) for 2 min, and re-suspended in Alpha MEM medium with 10% v/v FBS. Prior to cell-seeding, each colloidal gel sample was pre-immersed in 1.7 mL of Alpha MEM supplemented with 10% v/v FBS and 1% v/v Penicillin Streptomycin for three days in 24-well plates. During this period, the medium was changed every day. After the pre-immersion step, cells were seeded on top of the gels (surface area ≈ 0.5 cm^3) at a density of 10.000 cells/cm^2 and allowed to attach for 3 h. Subsequently, 1.7 mL of Alpha MEM supplemented with 10% v/v FBS and 1% v/v Penicillin Streptomycin was added to each well in 24-well plates, and the samples were placed in an incubator with 37 °C, 95% relative humidity and 5% CO_2. The medium was refreshed every 3 days during the 30-days culture period to prevent nutrient exhaustion. Similar experiments were performed for up to 30 days without cells. For mineralization and biological assays, samples (n = 4) were washed with PBS after each time point, incubated in 1 mL of MilliQ water, frozen, and thawed twice before analysis. Thereafter, cell lysates were collected for biological assays and the gels were freeze-dried for mineralization tests. For cytological analyses, colloidal gels (n = 3) after 30 days of cell culture were fixed in phosphate-buffered formalin (10%) and dehydrated through a graded ethanol series. All experiments were performed without additional osteogenic supplements.

2.7.3. Mineralization of colloidal gels and dissolution of their bioactive glass content

Fourier Transform Infrared Spectroscopy (FTIR, Spectrum One, Perkin Elmer) was

used to monitor formation and growth of apatite minerals within the freeze-dried gels after each time point with or without cells. The FTIR spectra were measured in Attenuated Total Reflectance
(ATR) mode, with a spectral resolution of 4 cm^{-1}, a scan speed of 0.2 $cm.s^{-1}$, and 10 scans per measurement. Prior to the measurements, a background scan was performed in air at room temperature. Three samples were measured for each experimental group, a representative spectrum of which was used for further analysis. At last, the spectra were normalized and analyzed using Spectrum 10 software (Perkin Elmer, Inc.).

ICP-OES was used for elemental analysis of freeze-dried gels. Sample preparation was carried out by dissolving the samples in concentrated nitric acid solutions for 2 weeks at 37 °C with 10 intervals of ultrasonication (10 min per interval) to assure the dissolution of their inorganic content. Thereafter, the solutions were diluted with MilliQ water to reach a nitric acid concentration of 1 v/v% for further analysis using ICP-OES. The extent of dissolution of bioactive glass particles for each sample was estimated using Equation 2 based on their remaining silicon content:

$$Bioglass^{®}\ dissolution(\%) = \left(1 - \frac{Si_f}{Si_i}\right) \times 100 \qquad (2)$$

where Si_f and Si_i are final and initial silicon contents in each sample, respectively. The amount of calcium deposited on each sample was estimated using Equations 3 and 4:

$$Ca_{BG} = Si \times R \qquad (3)$$

where Ca_{BG} (mg) is the maximum possible calcium content of remaining bioactive glass particles, Si (mg) is the measured silicon content of the sample after the immersion, and R is the Ca/Si weight ratio in the 45S5 Bioglass® composition. Thereafter, the minimum possible amount of calcium deposition was estimated as follows:

$$Deposited\ Ca\ (wt\%) = \left(\frac{Ca_{total} - Ca_{BG}}{W_{total}}\right) \times 100 \qquad (4)$$

where Ca_{total} (mg) and W_{total} (mg) are the total calcium content and total weight of a sample, respectively.

2.7.4. Cell proliferation and osteoblastic activity

Cell proliferation was assessed by measuring the DNA content in each sample solution using a Quantifluor™ dsDNA System (Promega Corporation, USA) according to the instruction of manufacturer, followed by quantification using a Biotek Synergy HT plate reader (485 nm excitation, 528 nm emission). The differentiation of the cultured cells was quantified by assessing the Alkaline Phosphatase (ALP) activity of the cells as an early marker for osteoblastic differentiation. Briefly, standard samples were prepared by serial dilutions of 4-nitrophenol from 25 to 0 nM. Thereafter, 20 mL of buffer solution (0.5M 2-amino-2-methyl-1- propanol) and 80 mL of an experimental or standard sample were added to each well of 96-well plates. Afterward, 100 mL of substrate solution (5 mM P-Nitrophenylphosphate disodium salt) was added into each well. Thereafter, the plates were covered with a lid to prevent evaporation and incubated for 60 min at 37°C. Finally, 100 µl of a stop solution (0.3M NaOH) was added to each well and the ALP concentrations were quantified by performing absorbance measurements at 405 nm using a Biotek Synergy HT plate reader. To determine the ALP activity of the cells for each sample, the ALP concentration was normalized to the DNA content.

2.7.5. Cytological analyses

Each fixated and dehydrated sample was cut in half perpendicular to the cell-seeded surface whereafter each half was embedded in paraffin. Afterward, 6 µm-thick sections were cut perpendicular to the cell seeded surface using a standard microtome (RM 2165; Leica, Germany). For evaluation of the distribution of cells throughout the gels, the sections were stained with hematoxylin/eosin (HE) and assessed with optical microscopy. For evaluation of apatite formation throughout the gels, the sections were sputter-coated with a 10-nm thick chromium layer and assessed using FE-SEM equipped with an energy-dispersive X-ray detector (EDX; XFlash detector 610M, Brucker Nano GmbH, Germany). The distribution of Ca and P throughout the sections was evaluated by EDX mapping of these two elements.

2.8. *In vivo* characterization of colloidal gels

2.8.1. Sample preparation

Gelatin and bioactive glass particles were disinfected by freeze-drying and UV treatment (peak wavelength of 365 nm) for 1 h. Thereafter, Gel, BPGel, and

BPGel+BG(0.5) samples with a particle volume fraction of 0.6 were prepared by adding sterile MilliQ water to the particles, followed by vortexing and centrifugation as described above. Afterward, the gels were transferred to 1 mL sterile syringes.

2.8.2. Surgical procedure

A total of 16 male Wistar rats (12-weeks old, weight of ~250 g) was used for the implantation study. The study protocol was reviewed and approved by the Experimental Animal Committee of the Radboud University (RU-DEC 2015-0036-004) and carried out in accordance with national guidelines concerning care and use of laboratory animals. Initially, the rats were acclimatized for 10 days and randomly housed in pairs using standard macrolon type III cages with sawdust as bedding material. The rats were fed with standard rodent chow and bottled tap water ad libitum. The housing room was maintained under standard laboratory conditions (light-dark cycle: 12:12 h, temperature: 20–22 °C, relative humidity: 45–55%). After acclimatization, the rats underwent an orchidectomy (ORX), as described previously [25], and had free access to water and low-calcium pelleted chow (0.01% Ca and 0.77% P; ssniff Spezialdiäten GmbH, Soest, Germany) to induce osteoporosis. Osteoporotic conditions were confirmed after 6 weeks using an *in vivo* micro-CT imaging system (Inveon; Siemens Medical Solutions, Knoxville, TN) and the animals underwent surgical intervention for the implantation of colloidal gels in both femoral condyles in a randomized manner (Table S1).

After the confirmation of the osteoporotic condition, bilateral frontal femoral condyle bone defects were created (n = 8 per experimental group) and the materials were implanted in the left or right femur of each animal under inhalation anesthesia (2% Isoflurane® by volume). To perform the surgery, the animals were immobilized supine with the knee joint in a maximally flexed position and the hind limbs were shaved, washed and disinfected with 10% povidone iodine. After careful exposure of the knee joint, a 1 mm pilot hole was drilled and the defect was gradually widened using different drills of increasing size using a surgical motor (Elcomed 100, W&H Dentalwerk Burmoos, Austria) at low rotational drilling speed (800 rpm) and continuous external cooling with saline, until a final cylindrical defect of 2.5 mm in diameter and 5 mm in depth was reached. The surgery was performed in both legs of the rats and one defect was created in each condyle. Thereafter, the colloidal gels were injected into the defects using 1 mL disposable syringes and the

wounds were closed with stainless steel wound clips (Becton Dickinson, Franklin Lakes, NJ). For pain control, Rimadyl® (5.0 mg/kg) and Temgesic® (0.02 mg/kg) were used for 2 days postoperatively. During the implantation period, all rats were kept at the low calcium diet.

2.8.3. Explantation and histological processing

Rats were euthanized by CO_2 suffocation, after which the femoral condyles were carefully dissected, cleaned from adhering tissues, and then immediately fixed in neutral buffered formaldehyde for 48 hours. After fixation, samples were kept in 70% ethanol, dehydrated in graded series of ethanol solutions (70–100%) and embedded in poly(methylmethacrylate) (pMMA). Following polymerization, non-decalcified ~10 µm-thick longitudinal sections were made cross-sectional perpendicular on the longitudinal axis of the implanted material (at least three sections per specimen) using a modified sawing microtome technique [26] and stained with methylene blue and basic fuchsin.

2.8.4. Histomorphometrical analysis

Histomorphometrical analysis was carried out using ImageJ software and was based on the combination of histological staining and tissue morphology. The bone area (%) was quantified in each image within a circle of 2500 µm, which was identical to the diameter of the original defect. Peri-implant bone area (%) was measured within a vicinity of 500 µm surrounding the diameter of the original defect. All measurements were performed on three histological sections per femoral condyle.

2.9. Statistics

All values were presented as average ± standard deviation. The statistical analyses were performed using GraphPad Prism® software. AFM and rheological tests were analyzed statistically using an unpaired Student's t-test. A two-way ANOVA with Tukey's multiple comparisons test was used for statistical analysis of the *in vitro* tests. Histomorphometrical results were analyzed statistically using a one-way ANOVA test, followed by Tukey's multiple comparisons test. In all tests, the significance threshold was set at $P < 0.05$.

3. Results

3.1. Characterization of colloidal building blocks

Figure 1A and B show SEM micrographs of bioactive glass and gelatin particles in dry state. The glass particles were irregularly shaped, whereas the gelatin nanoparticles were highly spherical. The gelatin and bioactive glass particles had average sizes of 210 ± 64 nm and 2.0 ± 1.2 µm, respectively. While the rigid glass particles hardly swelled in water, the average diameter of gelatin nanoparticles increased up to ~332 ± 3 nm (PdI = 0.14 ± 0.02) upon swelling in water as measured by means of DLS. Sizes and swelling ratios were similar for non-functionalized and bisphosphonate-functionalized gelatin nanoparticles, as reported previously [18]. Elemental analysis based on quantification of phosphorous content in gelatin nanoparticles indicated that functionalized gelatin nanoparticles contained 2.40 ± 0.01 wt% of bisphosphonate.

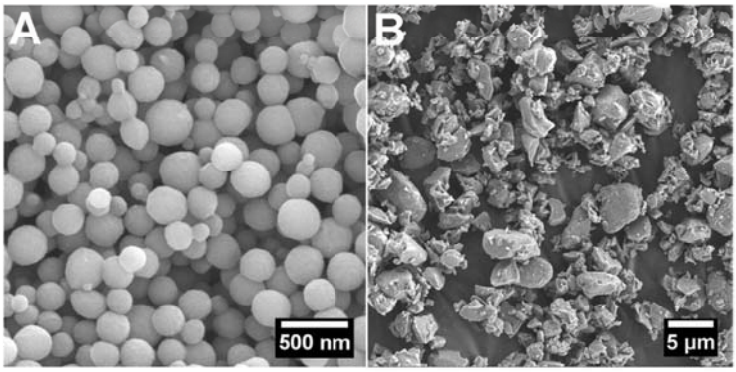

Figure 1. Scanning electron micrographs of A) gelatin and B) bioactive glass particles.

3.2. Atomic force microscopy

Figure 2A illustrates the AFM setup used in this study for the quantification of interactions between gelatin and bioactive glass particles. As shown in Figure 2B, both non-functionalized and bisphosphonate-functionalized gelatin nanoparticles formed strong adhesive bonds with bioactive glass particles, as indicated by multiple adhesion events upon withdrawal of the cantilever. Figure 2C shows the quantified adhesion force values measured in MilliQ water and PBS solution. These quantifications revealed that the bisphosphonate functionalization of gelatin nanoparticles enhanced their binding affinity toward Bioglass® about 1.9 fold. When these measurements were performed in PBS solutions, the measured adhesion forces for non-functionalized and functionalized gelatin nanoparticles decreased as compared to measurements in MilliQ water. Nevertheless, functionalization of gelatin nanoparticles with bisphosphonate groups resulted in a remarkable

3.6-fold enhancement of the adhesion force in PBS, which was significantly higher as compared to measurements performed in MilliQ water.

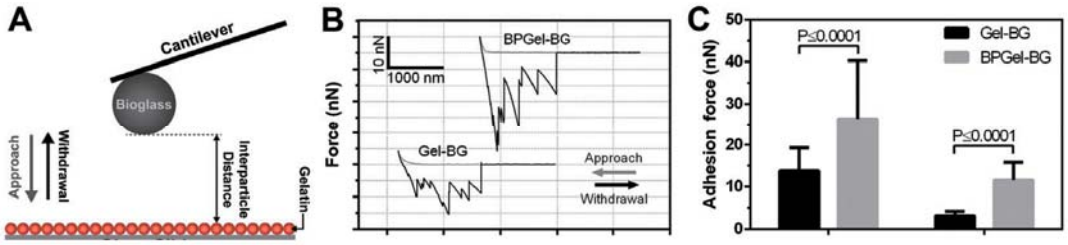

Figure 2. Interparticle adhesion force measurements performed by a colloidal probe AFM technique. A) Schematic illustration of the AFM setup. B) Representative force curves showing interactions of non-functionalized (Gel) or bisphosphonate-functionalized gelatin (BPGel) nanoparticles with bioactive glass (BG) particles in MilliQ water. C) Quantified values of the interparticle adhesion force between gelatin and bioactive glass particles in MilliQ water or PBS solution.

3.3. Viscoelastic properties of colloidal gels

Figure 3 shows the storage modulus (G') and tan(delta) values for colloidal gels composed of non-functionalized or bisphosphonate-functionalized gelatin nanoparticles and different amounts of bioactive glass particles, at a fixed particle volume fraction of 0.25. Importantly, all the colloidal gel compositions exhibited frequency-independent solid-like behavior (Figure S2). The incorporation of bioactive glass particles into colloidal gelatin gels produced more elastic gels as evidenced by the increase of storage modulus and the decrease of the damping factor tan(delta), which was, however, followed by a substantial increase of tan(delta) at Bioglass®/gelatin ratios of >1 (w/w) corresponding to a more viscous behavior for colloidal gels with high inorganic contents. As shown in Figure 3A, pure colloidal gelatin gels composed of bisphosphonate-functionalized gelatin nanoparticles showed significantly lower G' and higher tan(delta) values as compared to gels made entirely from non-functionalized gelatin nanoparticles. Upon Bioglass® incorporation, composite gels containing bisphosphonate-functionalized gelatin nanoparticles exhibited around twofold higher G' values at a Bioglass®/gelatin ratio of 0.1 (w/w), whereas G' values were statistically similar for all other Bioglass®/gelatin ratios.

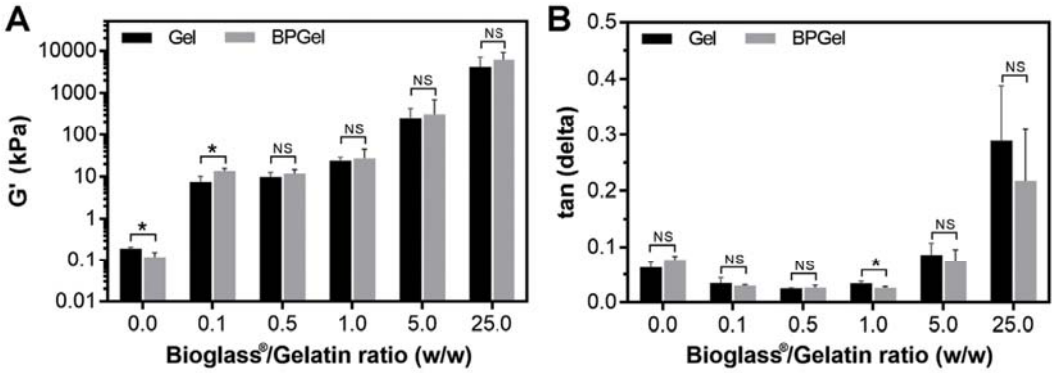

Figure 3. A) Storage modulus (G') and B) tan(delta) of colloidal gels composed of non-functionalized (Gel) or bisphosphonate-functionalized (BPGel) gelatin nanoparticles and various contents of bioactive glass. Measurements were performed at a frequency of 1 Hz. All samples were prepared with particle volume fraction of 0.25. * and NS indicate $P \leq 0.05$ and not statistically significant, respectively.

3

Since the composite colloidal gels with a Bioglass®/gelatin ratio of 0.1 (w/w) displayed the most pronounced increase in storage modulus upon bisphosphonate functionalization, this composition was selected to study the storage modulus of the gels as a function of bisphosphonate functionalization and particle volume fraction. As shown in Figure 4, the G' value of the gels was strongly enhanced by increasing particle volume fraction. More importantly, storage moduli of gels containing bisphosphonate-functionalized gelatin particles were significantly higher for samples with volume fractions of 0.1 (~tenfold increase) and 0.25 (~twofold increase), whereas the effect of bisphosphonate functionalization for samples with a volume fraction of 0.4 was not statistically significant.

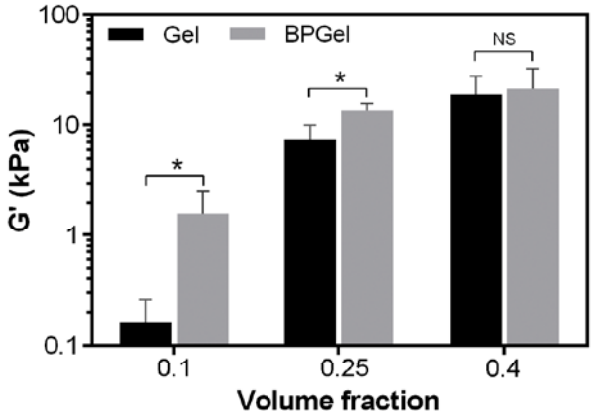

Figure 4. Storage modulus (G') of composite colloidal gels composed of non-functionalized (Gel) or bisphosphonate-functionalized (BPGel) gelatin nanoparticles at a Bioglass®/gelatin ratio of 0.1 (w/w) and different particle volume fractions. Measurements were performed at a frequency of 1 Hz. * and NS indicate $P \leq 0.05$ and not statistically significant, respectively.

Figure 5 shows the recovery of colloidal gels after shear-induced gel network destruction. As shown in Figure 5A, composite gels with a low bioactive glass content (0.1 Bioglass®/gelatin ratio) displayed a liquid-like behaviour upon destructive straining up to 1000% in step (II). Nevertheless, upon removal of this high shear in step (III), these formulations immediately recovered their elasticity. By increasing the glass content, however, the self-healing ability of the composite gels gradually declined; at a Bioglass®/Gelatin ratio of 25 (w/w), the materials could recover only less than 1% of their initial G' value (Figure 5B).

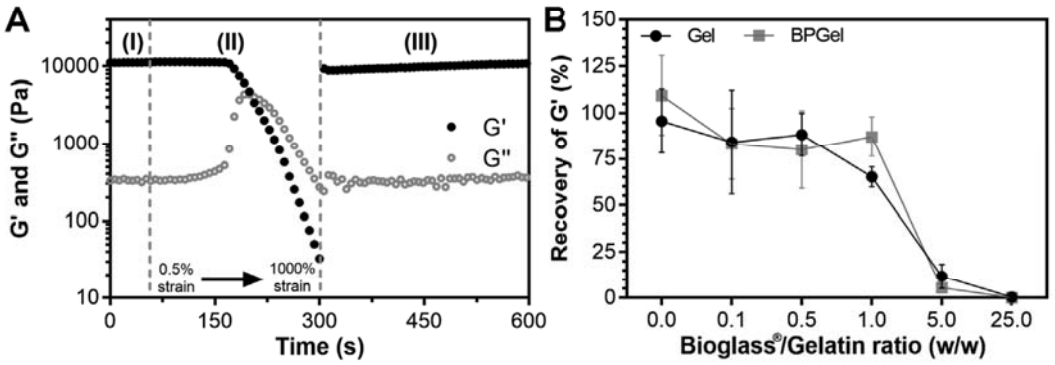

Figure 5. A) Self-healing of a composite colloidal gel (BPGel+BG(0.1)) upon shear-induced failure characterized by rheological tests in three stages: (I) time sweep at 0.5% strain, (II) network destruction by increasing strain from 0.5% to 1000%, and (III) recovery at 0.5% strain. B) Recovery of storage modulus (G') of colloidal gels made with different bioactive glass contents. Measurements were performed at a frequency of 1 Hz. All samples were prepared with a particle volume fraction of 0.25.

3.4. *In vitro* mineralization of colloidal gels

Figures 6A and 6B show the FTIR spectra of freeze-dried colloidal gels after 30 days of incubation in cell culture medium with or without cells. No remarkable differences were observed between the spectra of samples incubated with or without cells. In these spectra, the sharp peaks at ~570 and ~600 cm^{-1} correspond to the ν_4 bending mode of P–O–P bond from the PO_4^{3-} groups of hydroxyapatite [23, 27]. Moreover, the peak at ~871 cm^{-1} is the absorption peak characteristic for CO_3^{2-} group as present in carbonated apatite [27]. Accordingly, no evidence of mineralization was observed for the pure gelatin gels, with or without bisphosphonate functionalization. Similarly, the inclusion of a low amount of bioactive glass particles (0.1 Bioglass®/gelatin ratio (w/w)) also could not induce apatite-formation in bisphosphonate-functionalized gels. Nevertheless, when a higher amount of bioactive glass particles (0.5 Bioglass®/

gelatin ratio (w/w)) was combined with the bisphosphonate-functionalized gelatin nanoparticles, the resulting gels promoted apatite formation within their matrix. The assessment of these composite gels at different incubation time points revealed that the formation of apatite minerals in these samples started within the first 10 days of incubation (Figure S3).

To obtain a more quantitative insight into the mineralization behavior of the colloidal gels, the dissolution of their bioactive glass content and calcium deposition within their matrix were estimated based on their silicon and calcium contents as measured before and after the immersion period. As shown in Figure 6C, when the composite gels contained a low amount of bioactive glass particles (0.1 Bioglass®/gelatin ratio (w/w)), their bioactive glass content was almost completely dissolved during the 30-day incubation period. On the contrary, the colloidal gels with a high bioactive glass content still contained bioactive glass particles after the incubation period. Figure 6D shows the estimated amounts (%) of calcium deposition in the colloidal gels with different compositions. Almost no calcium deposition was observed for the pure gelatin gels without bisphosphonate. Upon bisphosphonate functionalization, a slight increase of calcium deposition was observed for pure gelatin gels. Importantly, the inclusion of bioactive glass particles in the composition of gels strongly stimulated calcium deposition within their matrix. The highest levels of calcium deposition was, in fact, observed for the composite gels with the highest bioactive glass content. However, when comparing these composite gels incubated with or without cells, calcium deposition values were significantly higher for the latter.

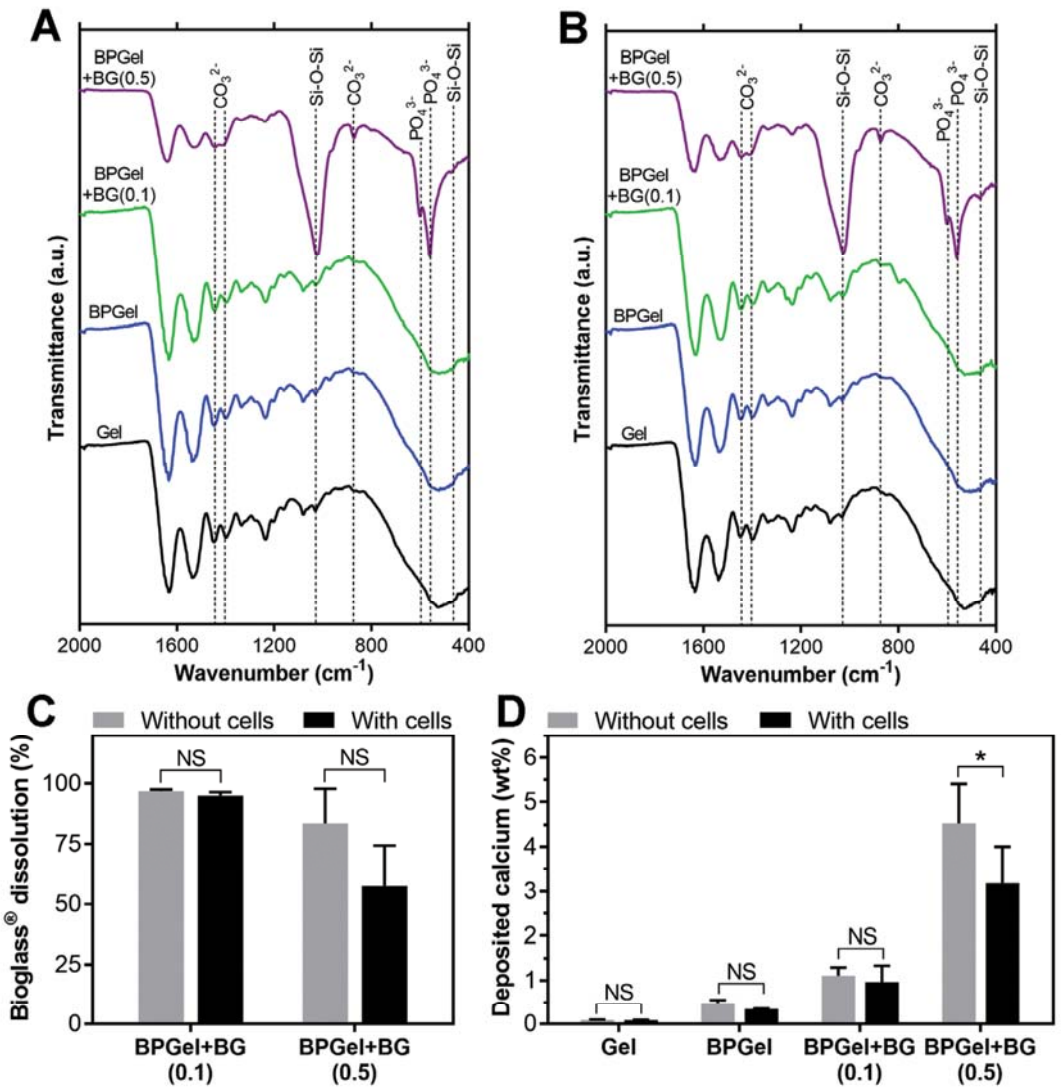

Figure 6. *In vitro* mineralization of colloidal gels. FTIR spectra of the freeze-dried colloidal gels after 30 days of incubation A) without or B) with cells. Estimated percentages of C) dissolved bioactive glass particles and D) deposited calcium within colloidal gels after 30 days of incubation with or without cells.

3.5. Cell proliferation and osteoblastic activity

Figure 7 shows the DNA content and ALP activity of the cells after 10, 20, and 30 days of culture on top of various colloidal gels. At 10 days of cell culture, DNA content and ALP activity for all experimental groups were similar. Most notably, cells seeded on pure gelatin gels without bisphosphonate showed a strong increase of DNA content until day 20, followed by a decline at day 30. However, cells seeded on the composite gels did not show significant variations of DNA content over time.

Concerning the ALP activity of the cells, at 20 days of cell culture, the bisphosphonate-containing groups showed higher ALP activity levels than the bisphosphonate-free group. Nevertheless, while the cells cultured on the bisphosphonate-free gelatin gels showed increased levels of ALP activity at day 30, the cells cultured on the bisphosphonate-containing gels with high bioactive glass content (BPGel+BG(0.5)) showed a peak at day 20 followed by a declined ALP activity at day 30.

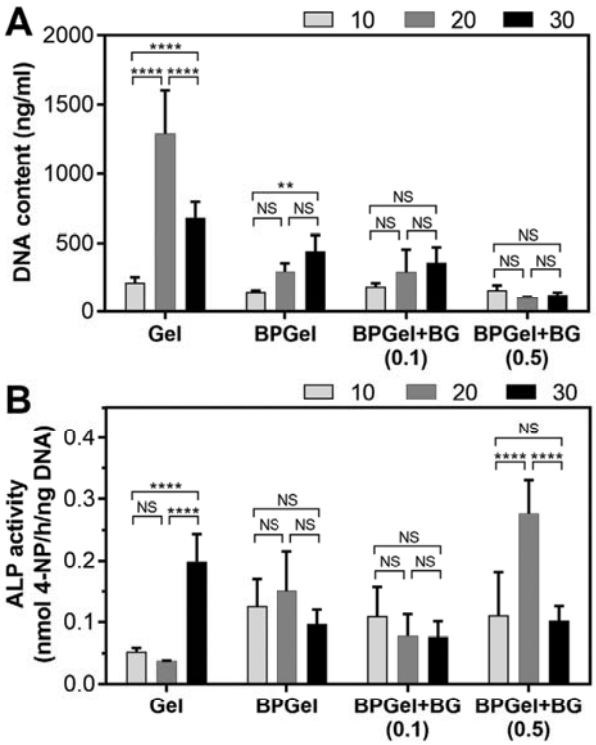

Figure 7. A) DNA content and B) ALP activity of colloidal gel samples during 30 days of cell culture experiments. **, **** and NS indicate $P \leq 0.01$, $P \leq 0.0001$ and not statistically significant, respectively.

Cytological evaluation of the colloidal gels after 30 days of cell culture revealed the formation of continuous cell layers on the surface of bisphosphonate-free gelatin gels (Figure 8A). Interestingly, these results also showed cell ingrowth from the surface of gels toward their interior as deep as ~2.5 mm from the surface (Figure 8B). The presence of cells on and within bisphosphonate-containing samples was less evident. Cytological imaging, combined with SEM and EDX evaluations (Figure 8C-E), revealed the formation of a thick (~100 µm) calcium phosphate layer on the surface of BPGel+BG(0.5) samples. Such a thick inorganic layer was not detected on the surface of the other samples that contained less bioactive glass particles.

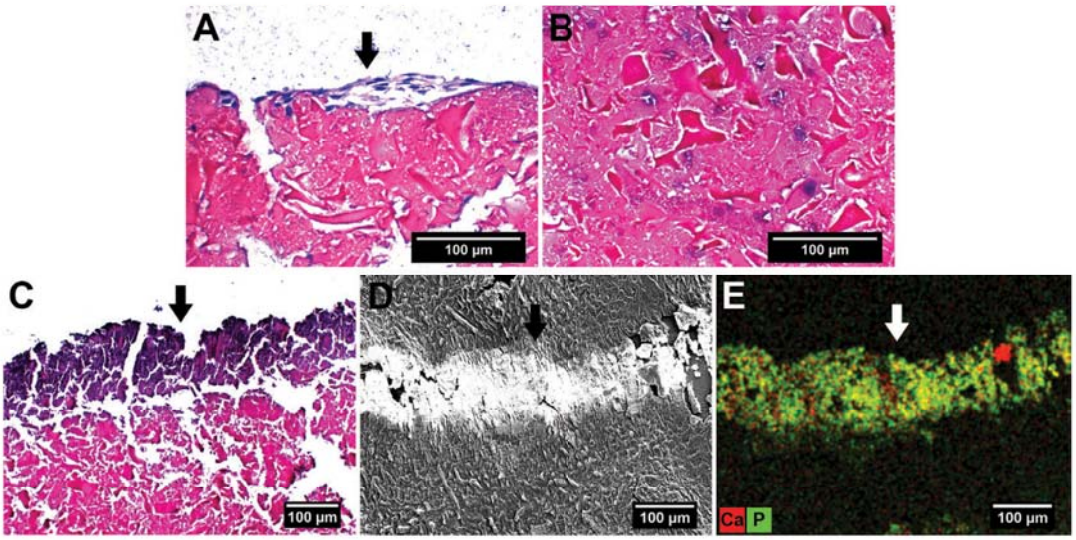

Figure 8. Cross-sectional microscopy images of colloidal gels after 30 days of cell culture. Representative cytological images showing cells A) on top and B) inside Gel samples. Representative C) cytological, D) SEM, and E) EDX mapping images showing extensive calcium phosphate formation on the top surface of BPGel+BG(0.5) samples. Arrows point to the top surface of samples.

3.6. Osteocompatibility of colloidal gels

Figure 9A shows the surgical procedure for implantation of colloidal gels into femoral condyles of osteoporotic rats. After 8 weeks of implantation of the colloidal gels in femoral condyle defects, abundant bone formation was observed inside the original defect area for all colloidal gel compositions (Figures 9B-D), while no inflammatory response was observed for any of the implanted materials. The histological images showed that bone regeneration proceeded from the peripheral bone toward the center of the defect. Importantly, a large number of blood vessel-like structures could be observed throughout the defect area (Figures 9E and 9F), which seemed more apparent for the composite gels. Furthermore, as shown in Figure 9G, numerous cells were present within the bone-free central regions of the original defects.

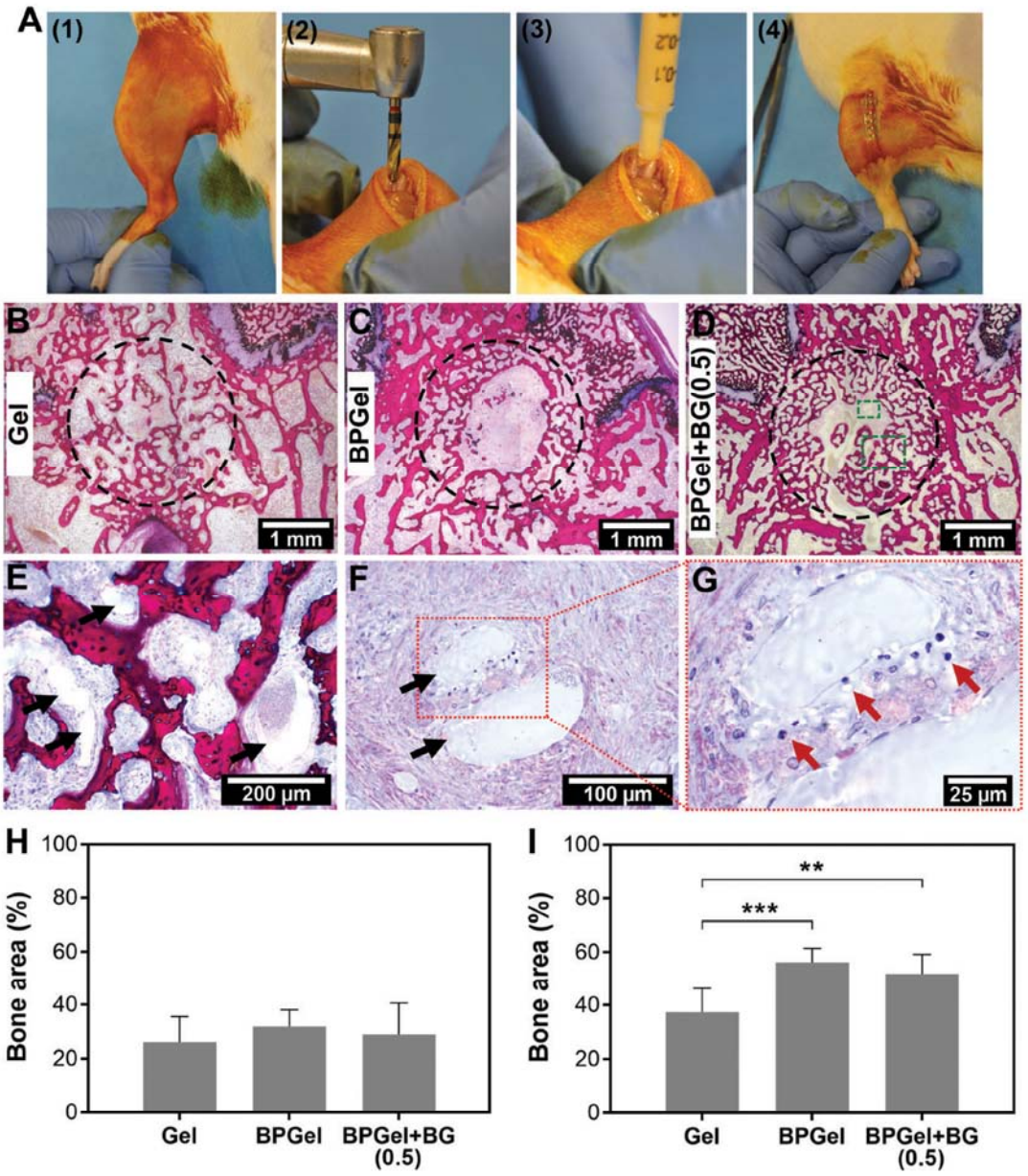

Figure 9. *In vivo* evaluation of colloidal gels. A) Digital photographs showing the surgical procedure for implantation of colloidal gels into femoral condyles of osteoporotic rats. B), C), and D) Representative histological images of different experimental groups after 8 weeks of implantation. The circles indicate the original defect areas. E) and F) show high magnification images of large and small rectangles in D), respectively. G) shows high magnification image of the rectangle in F). Black and red arrows indicate blood vessel-like structures and cells, respectively. Quantified bone area (%) in H) defect and I) peri-implantation regions. ** and *** represent $P \leq 0.01$ and $P \leq 0.001$, respectively.

Quantification of the amount of newly formed bone inside the original defect area indicated a high degree of bone formation for all the experimental groups (average values ranging from 26.0 to 31.8 %). The amounts of new bone formation were statistically similar for all groups (Figure 9H). Nevertheless, the experimental groups that contained bisphosphonate-functionalized gelatin formed significantly more bone than the bisphosphonate-free formulation in the 500 μm area in vicinity to the defect (Figure 9I).

4. Discussion

Annually, around 9 million osteoporotic bone fractures occur worldwide [28], which means a new osteoporotic fracture takes place about every 4 seconds, resulting in various types of bone defects. Consequently, biomaterials that can aid regeneration of bone defects for osteoporotic patients are highly demanded. Although the assembly of biomaterials from colloidal particles was shown to be a promising strategy for the development of injectable and self-healing gels with bone regenerative capability [9, 10, 14, 15], the potential of these colloidal systems for regeneration of osteoporotic bone defects has never been explored before. Hence, the goal of this study was to develop injectable and self-healing composite colloidal gels that combine mechanical robustness with the capacity to regenerate osteoporotic bone through the concerted action of anabolic and anti-catabolic stimuli.

The bulk mechanical properties of colloidal gels are determined by their microstructure, the mechanical properties of each colloidal particle, and the interactions between these particles within a colloidal gel network [9, 11]. We recently found [23] that functionalization of hyaluronan macromers with calcium-binding bisphosphonate groups significantly enhances the binding affinity of this macromer toward calcium-containing Bioglass® particles. In addition, bisphosphonate functionalization of gelatin nanoparticles was recently shown [18] to increase the interparticle adhesion between gelatin and hydroxyapatite particles. Based on these previous results, we hypothesized that strong adhesion forces could also be created between bisphosphonate-functionalized gelatin and Bioglass® particles. This hypothesis was indeed confirmed by means of AFM experiments using a colloidal probe technique (Figure 2A). Nevertheless, we also witnessed adhesive interactions between bisphosphonate-free gelatin and Bioglass® particles, which was similar to previous reports [29, 30] that demonstrated the

existence of adhesive interactions between Bioglass® surfaces and fibrous collagen. Such adhesive interparticle interactions can arise from interparticle van der Waals and hydrophobic forces, as well as from local electrostatic attractions between the carboxyl or amine groups of gelatin and the cations (Na^+ and Ca^{2+}) or silanol groups of bioactive glass particles, respectively [9, 31, 32]. Nonetheless, upon bisphosphonate functionalization of gelatin nanoparticles, the interparticle adhesion forces significantly increased, most likely due to the formation of strong, but reversible, bonds between the bisphosphonate groups of gelatin nanoparticles and calcium ions at the surface of the Bioglass® particle. Since biomaterials are exposed to isotonic biological fluids when implanted *in vivo* [33], we also performed these AFM measurements in PBS solutions with a similar ionic strength as body fluids. Our results showed that the adhesion force values for both groups containing bisphosphonate-free and bisphosphonate-functionalized gelatin decreased when measured in PBS. This decrease is related to screening of interparticle electrostatic interactions at high ionic strengths [34, 35]. Nevertheless, even in PBS, adhesion forces between Bioglass® and gelatin particles were higher after bisphosphonate functionalization of gelatin particles. These findings stress that bisphosphonate-based interparticle bonds are more effective than electrostatic interactions at high ionic strengths such as isotonic body fluids.

After preparation of colloidal gels using gelatin and Bioglass® particles, we studied the viscoelastic properties of these materials by means of rheology. Generally, the storage modulus of these composites increased with increasing bioactive glass content (Figure 3A). These results are in agreement with our previous observations [9, 10] which confirmed that the combination of stiff inorganic particles with soft organic particles results in more elastic gels as compared to the use of organic particles only [11, 12]. However, as shown in Figure 3B, samples with Bioglass®/ gelatin ratios higher than 1 displayed increased tan(delta) values, indicating that viscous behavior became more dominant at such high inorganic contents. Moreover, when immersed in water, these samples lost their integrity within a day (data not shown), indicating that the amount of gelatin particles was insufficient to establish a cohesive composite network. The effect of bisphosphonate functionalization of gelatin nanoparticles on the mechanical properties of colloidal gels was influenced by the composition and the particle volume fraction of these materials (Figures

3A and 4). When the colloidal gels were entirely made of gelatin nanoparticles, bisphosphonate functionalization resulted in inferior mechanical properties (Figure 3A), which can be attributed to repulsive interactions between negatively charged bisphosphonate groups present at the surface of gelatin nanoparticles [18].

Nevertheless, bisphosphonate functionalization of gelatin particles increased the storage modulus of the formulations when bioactive glass particles were included in the colloidal systems. This effect was, however, not statistically significant at the highest bioactive glass contents, possibly due to the excess of bioactive glass particles within the colloidal gel networks at these compositions. Moreover, we found that by increasing the particle volume fraction, the influence of bisphosphonate functionalization on the viscoelastic properties of the composite gels gradually decreased. This decrease might be caused by the transition of the colloidal assembly from a fractal to a more compact morphology [36]. Importantly, all colloidal gels with a Bioglass®/gelatin ratio<1 exhibited an intrinsic ability for self-healing as evidenced by the immediate and substantial recovery of their storage modulus after destructive shearing (Figure 5). Based on these results, we produced composite gels using bisphosphonate-functionalized gelatin nanoparticles at Bioglass®/gelatin ratios of up to 0.5 for further *in vitro* and *in vivo* evaluation.

The evaluation of *in vitro* mineralization of these gels in cell culture media revealed that a minimum Bioglass®/gelatin ratio of 0.5 was essential to stimulate the formation of apatite within the matrix. Mineralization of these composite gels started within the first 10 days of incubation, and by day 30 the majority of bioactive glass particles were replaced by apatite (Figures 6 and S3). The presence of cells on these composites slightly decreased the extent of mineral deposition, possibly due to the formation of a cell layer limiting ion exchange between the gels and surrounding culture media [22]. These results suggest that the mineralization of the composite colloidal gels mainly occurred through a passive route rather than an active route driven by cellular mineralization [37].

Next, we studied the proliferation and osteoblastic activity of MC3T3 cells upon direct contact with the gels in the absence of osteogenic supplements (Figure 7). At 10 days of cell culture, the bisphosphonate functionalization of gelatin and incorporation of bioactive glass particles into the gels did not affect the proliferation and differentiation of cells. Nevertheless, at day 20, the presence of bisphosphonate

in gels stimulated osteoblastic differentiation, which is in line with other reports showing that nitrogen-containing bisphosphonate drugs, such as alendronate, can stimulate osteogenic differentiation of cells [38-40]. Most notably, for bisphosphonate-containing gels with the highest bioactive glass content (Bioglass®/ gelatin ratio = 0.5), osteogenic differentiation of the cells continued to increase up to day 20 before it declined. It is known that during a normal osteogenic differentiation process, the ALP activity reaches a peak level upon osteoblast maturation, followed by a decline upon mineralization [41, 42]. Indeed, the cytological evaluation of these composite gels (BPGel+BG (0.5)) after 30 days of cell culture confirmed the formation of a thick layer of calcium phosphate on their surface (Figure 8), which is in agreement with the mineralization results discussed earlier. Nevertheless, it is important to point out that the *in vitro* osteogenic effects of bioactive glasses depend on the concentration of their dissolution products in cell culture medium [43]. Consequently, these results cannot be translated to *in vivo* conditions, in view of the biologically more complex and perfused nature of animal studies. Therefore, to determine the *in vivo* capacity of the colloidal gels to regenerate defects in osteoporotic bone, we implanted the bioactive composite gels (BPGel+BG (0.5)) as well as bisphosphonate-containing (BPGel) and bisphosphonate-free (Gel) pure gelatin gels into bone defects created in femoral condyles of osteoporotic rats (Figure 9). After 8 weeks, we observed abundant formation of vascularized bone inside the original defect area for all colloidal gel compositions. This vascularization was more apparent for the composite gels, most likely due to the angiogenic effect of Bioglass® particles [43, 44]. Interestingly, similar to the cytological observations (Figure 8B), cells were observed in the central regions of the defects (Figure 9G). We attribute this observation to local adaptation of the gel network through repeated rupture and reformation of interparticle bonds, which allows cell migration into the gels without compromising the bulk integrity of the gels [45]. This behavior differs from that of conventional covalently crosslinked hydrogels that do not allow cell migration due to their static nature [46].

In view of the similarity regarding the amount of bone formation for the various experimental groups (Figure 9H), it was concluded that the bioactive glass particles did not influence the amount of *in vivo* bone regeneration after 8 weeks of implantation, even though the incorporation of bioactive glass particles was highly

beneficial for the mechanical and *in vitro* biological properties of the colloidal gels. Regarding this matter, it is important to consider that our *in vitro* results revealed that the majority of bioactive glass particles of the composite gels were dissolved within a 30-day period. Accordingly, these *in vitro* findings could indicate that the amount of bioactive glass particles incorporated in the composite gels might not be sufficient to facilitate *in vivo* bone regeneration for an 8-week period. Furthermore, the *in vivo* bioactivity of bioactive glass particles might be affected by the low concentration of serum calcium [47], caused by the low calcium diet of the rats [48]. Nonetheless, it should be emphasized that we observed recently in a recent similar animal test (data not published) that femoral condyle defects in osteoporotic rats were regenerated for only 13.8 ± 3.8% after 12 weeks (Figure S4). This observation highlights the strong capacity of the colloidal gels for regeneration of osteoporotic bone.

Finally, we investigated potential anti-osteoporotic effects of our colloidal gels on the peri-defect bone tissue by quantifying the bone area within a vicinity of 500 μm surrounding the defects. These quantifications indicated a significantly enhanced bone regeneration in the surrounding tissue when the colloidal gels were functionalized with bisphosphonate molecules (Figure 9I). This anti-osteoporotic effect can be ascribed to the release of bisphosphonate moieties from the colloidal gels, thereby attaining a therapeutically active bisphosphonate concentration within the peri-implantation region. These results are in agreement with previous reports by Karlsson et al. [49, 50] who showed that after 8 weeks of implantation of alendronate-functionalized implants in rat tibia, released alendronate molecules remained confined within a vicinity of 500 μm surrounding the implants. The highest bone density was observed at a distance of 10–100 μm from the surface of implants, possibly caused by optimal concentrations of released alendronate at this distance. Nevertheless, further investigations are required to determine the stability of the increased bone density caused by the local release of bisphosphonates, particularly in response to the process of bone remodeling over time. Furthermore, given the biological activity of different ions released from bioactive glasses [43], it will be interesting to investigate in future studies the use of other bioactive glass compositions for the preparation of colloidal gels, notably those containing/ releasing strontium ions which might act in synergy with bisphosphonates [51, 52],

leading to an improved treatment of osteoporotic bone defects.

5. Conclusion

We demonstrated successful regeneration of osteoporotic bone defects using bioactive composite colloidal gels made of bisphosphonate-functionalized gelatin and bioactive glass particles. We modified gelatin nanoparticles with bisphosphonate groups to enhance their affinity toward bioactive glass particles and exploit their anti-osteoporotic activity to facilitate bone regeneration under osteoporotic conditions. This modification resulted in enhancement of the interparticle bonds between gelatin and bioactive glass building blocks, which improved the stiffness of specific colloidal gel compositions. By adjustment of the Bioglass®-to-gelatin ratio, composite gels were produced that combined mechanical robustness with self-healing ability. This self-healing capability allowed the recovery of mechanical properties of the gels after shear-induced destruction that can occur during injection of these materials through narrow syringes. The composite gels induced apatite formation and supported proliferation and differentiation of osteoblastic cells *in vitro* without requiring additional osteogenic supplements. *In vivo* evaluation of the regenerative capacity of the composite gels using an osteoporotic rat model demonstrated the ability of the composite gels to promote the formation of vascularized bone inside femoral condyle defects and to enhance the amount of bone formation around these defects. Overall, our results demonstrate that the self-healing composite colloidal gels developed in this study were mechanically robust and stimulated the regeneration of osteoporotic bone, which might open up new therapeutic opportunities for treatment of osteoporotic bone defects.

References

[1] H.S. Alghamdi, R. Bosco, J.J.J.P. van den Beucken, X.F. Walboomers, J.A. Jansen, Osteogenicity of titanium implants coated with calcium phosphate or collagen type-I in osteoporotic rats, Biomaterials 34 (2013) 3747-3757.

[2] H.C. Pape, A. Evans, P. Kobbe, Autologous Bone Graft: Properties and Techniques, Journal of Orthopaedic Trauma 24 (2010) S36-S40.

[3] J.W.M. Vehof, P.H.M. Spauwen, J.A. Jansen, Bone formation in calcium-phosphate-coated titanium mesh, Biomaterials 21 (2000) 2003-2009.

[4] J.D. Kretlow, A.G. Mikos, From Material to Tissue: Biomaterial Development, Scaffold Fabrication, and Tissue Engineering, Aiche Journal 54 (2008) 3048-3067.

[5] K. Rezwan, Q.Z. Chen, J.J. Blaker, A.R. Boccaccini, Biodegradable and bioactive porous polymer/inorganic composite scaffolds for bone tissue engineering, Biomaterials 27 (2006) 3413-3431.

[6] H. Shin, S. Jo, A.G. Mikos, Biomimetic materials for tissue engineering, Biomaterials 24 (2003) 4353-4364.

[7] J.D. Kretlow, S. Young, L. Klouda, M. Wong, A.G. Mikos, Injectable Biomaterials for Regenerating Complex Craniofacial Tissues, Advanced Materials 21 (2009) 3368-3393.

[8] S. Utech, A.R. Boccaccini, A review of hydrogel-based composites for biomedical applications: enhancement of hydrogel properties by addition of rigid inorganic fillers, Journal of Materials Science 51 (2016) 271-310.

[9] M. Diba, H. Wang, T.E. Kodger, S. Parsa, S.C.G. Leeuwenburgh, Highly Elastic and Self-Healing Composite Colloidal Gels, Advanced Materials (2017) 1604672-n/a.

[10] H. Wang, M. Bongio, K. Farbod, A.W.G. Nijhuis, J. van den Beucken, O.C. Boerman, J.C.M. van Hest, Y. Li, J.A. Jansen, S.C.G. Leeuwenburgh, Development of injectable organic/inorganic colloidal composite gels made of self-assembling gelatin nanospheres and calcium phosphate nanocrystals, Acta Biomaterialia 10 (2014) 508-519.

[11] H. Wang, M.B. Hansen, D.W.P.M. Löwik, J.C.M. van Hest, Y. Li, J.A. Jansen, S.C.G. Leeuwenburgh, Oppositely Charged Gelatin Nanospheres as Building Blocks for Injectable and Biodegradable Gels, Advanced Materials 23 (2011) H119-H124.

[12] Q. Wang, L. Wang, M.S. Detamore, C. Berkland, Biodegradable Colloidal Gels as Moldable Tissue Engineering Scaffolds, Advanced Materials 20 (2008) 236-239.

[13] J. Song, J.C.E. Odekerken, D.W.P.M. Löwik, P.M. López-Pérez, T.J.M. Welting, F. Yang, J.A. Jansen, S.C.G. Leeuwenburgh, Influence of the Molecular Weight and Charge of Antibiotics on Their Release Kinetics From Gelatin Nanospheres, Macromolecular Bioscience 15 (2015) 901-911.

[14] J. van der Stok, H. Wang, S. Amin Yavari, M. Siebelt, M. Sandker, J.H. Waarsing, J.A.N. Verhaar, H. Jahr, A.A. Zadpoor, S.C.G. Leeuwenburgh, H. Weinans, Enhanced Bone Regeneration of Cortical Segmental Bone Defects Using Porous Titanium Scaffolds Incorporated with Colloidal Gelatin Gels for Time- and Dose-Controlled Delivery of Dual Growth Factors, Tissue Engineering Part A 19 (2013) 2605-2614.

[15] H. Wang, Q. Zou, O.C. Boerman, A.W.G. Nijhuis, J.A. Jansen, Y. Li, S.C.G. Leeuwenburgh, Combined delivery of BMP-2 and bFGF from nanostructured colloidal gelatin gels and its effect on bone regeneration in vivo, Journal of Controlled Release 166 (2013) 172-181.

[16] H. Wang, O.C. Boerman, K. Sariibrahimoglu, Y. Li, J.A. Jansen, S.C.G. Leeuwenburgh, Comparison of micro- vs. nanostructured colloidal gelatin gels for sustained delivery of osteogenic proteins: Bone morphogenetic protein-2 and alkaline phosphatase, Biomaterials 33 (2012) 8695-8703.

[17] M.V. Priya, A. Sivshanmugam, A.R. Boccaccini, O.M. Goudouri, W. Sun, N. Hwang, S. Deepthi, S.V. Nair, R. Jayakumar, Injectable osteogenic and angiogenic nanocomposite hydrogels for irregular bone defects, Biomedical Materials 11 (2016).

[18] K. Farbod, M. Diba, T. Zinkevich, S. Schmidt, M.J. Harrington, A.P.M. Kentgens, S.C.G. Leeuwenburgh, Gelatin Nanoparticles with Enhanced Affinity for Calcium Phosphate, Macromolecular Bioscience 16 (2016) 717-729.

[19] K. Farbod, A. Curci, M. Diba, T. Zinkevich, A.P.M. Kentgens, M. Iafisco, N. Margiotta, S.C.G. Leeuwenburgh, Dual-functionalisation of gelatine nanoparticles with an anticancer platinum(ii)-bisphosphonate complex and mineral-binding alendronate, Rsc Advances 6 (2016) 113025-113037.

[20] R. Schrieber, H. Gareis, Gelatine handbook: theory and industrial practice, John Wiley & Sons, 2007.

[21] S.-C. Wu, W.-H. Chang, G.-C. Dong, K.-Y. Chen, Y.-S. Chen, C.-H. Yao, Cell adhesion and proliferation enhancement by gelatin nanofiber scaffolds, Journal of Bioactive and Compatible Polymers 26 (2011) 565-577.

[22] J.R. Jones, Review of bioactive glass: From Hench to hybrids, Acta Biomaterialia 9 (2013) 4457-4486.

[23] M. Diba, J. An, S. Schmidt, M. Hembury, D. Ossipov, A.R. Boccaccini, S.C.G. Leeuwenburgh, Exploiting Bisphosphonate-Bioactive-Glass Interactions for the Development of Self-Healing and Bioactive Composite Hydrogels, Macromolecular Rapid Communications 37 (2016) 1952-1959.

[24] H. Fleisch, Bisphosphonates: mechanisms of action, Endocrine reviews 19 (1998) 80-100.

[25] H.S. Alghamdi, J.J.J.P. van den Beucken, J.A. Jansen, Osteoporotic Rat Models for Evaluation of Osseointegration of Bone Implants, Tissue Engineering Part C: Methods 20 (2013) 493-505.
[26] H. Van der Lubbe, C. Klein, K. De Groot, A simple method for preparing thin (10 μm) histological sections of undecalcified plastic embedded bone with implants, Stain technology 63 (1988) 171-176.
[27] M. Mačković, A. Hoppe, R. Detsch, D. Mohn, W.J. Stark, E. Spiecker, A.R. Boccaccini, Bioactive glass (type 45S5) nanoparticles: in vitro reactivity on nanoscale and biocompatibility, Journal of Nanoparticle Research 14 (2012) 966.
[28] O. Johnell, J.A. Kanis, An estimate of the worldwide prevalence and disability associated with osteoporotic fractures, Osteoporosis International 17 (2006) 1726-1733.
[29] R. Oréfice, L. Hench, A. Brennan, Evaluation of the interactions between collagen and the surface of a bioactive glass during in vitro test, Journal of Biomedical Materials Research Part A 90A (2009) 114-120.
[30] L.L. Hench, D. Greenspan, Interactions between Bioactive Glass and Collagen: A Review and New Perspectives, Journal of the Australian Ceramic Society 49 (2013) 1-40.
[31] K. Magyari, L. Baia, O. Popescu, S. Simon, V. Simon, The anchoring of fibrinogen to a bioactive glass investigated by FT-IR spectroscopy, Vibrational Spectroscopy 62 (2012) 172-179.
[32] S. Lin, W. Van den Bergh, S. Baker, J.R. Jones, Protein interactions with nanoporous sol–gel derived bioactive glasses, Acta Biomaterialia 7 (2011) 3606-3615.
[33] T. Kokubo, H. Takadama, How useful is SBF in predicting in vivo bone bioactivity?, Biomaterials 27 (2006) 2907-2915.
[34] R. Perez-Jimenez, R. Godoy-Ruiz, B. Ibarra-Molero, J.M. Sanchez-Ruiz, The efficiency of different salts to screen charge interactions in proteins: A Hofmeister effect?, Biophysical Journal 86 (2004) 2414-2429.
[35] G. Trefalt, T. Palberg, M. Borkovec, Forces between colloidal particles in aqueous solutions containing monovalent and multivalent ions, Current Opinion in Colloid & Interface Science 27 (2017) 9-17.
[36] Z. Shao, A.S. Negi, C.O. Osuji, Role of interparticle attraction in the yielding response of microgel suspensions, Soft Matter 9 (2013) 5492-5500.
[37] T. Kirsch, Biomineralization—An Active or Passive Process?, Connective Tissue Research 53 (2012) 438-445.
[38] E. Boanini, P. Torricelli, M. Gazzano, R. Giardino, A. Bigi, Alendronate–hydroxyapatite nanocomposites and their interaction with osteoclasts and osteoblast-

like cells, Biomaterials 29 (2008) 790-796.
[39] D. Zheng, K.G. Neoh, E.-T. Kang, Immobilization of alendronate on titanium via its different functional groups and the subsequent effects on cell functions, Journal of Colloid and Interface Science 487 (2017) 1-11.
[40] F.P. Koch, C. Merkel, B. Al-Nawas, R. Smeets, T. Ziebart, C. Walter, W. Wagner, Zoledronate, ibandronate and clodronate enhance osteoblast differentiation in a dose dependent manner – A quantitative in vitro gene expression analysis of Dlx5, Runx2, OCN, MSX1 and MSX2, Journal of Cranio-Maxillofacial Surgery 39 (2011) 562-569.
[41] J.E. Aubin, Regulation of Osteoblast Formation and Function, Reviews in Endocrine and Metabolic Disorders 2 (2001) 81-94.
[42] R.A. Thibault, L. Scott Baggett, A.G. Mikos, F.K. Kasper, Osteogenic Differentiation of Mesenchymal Stem Cells on Pregenerated Extracellular Matrix Scaffolds in the Absence of Osteogenic Cell Culture Supplements, Tissue Engineering Part A 16 (2009) 431-440.
[43] A. Hoppe, N.S. Güldal, A.R. Boccaccini, A review of the biological response to ionic dissolution products from bioactive glasses and glass-ceramics, Biomaterials 32 (2011) 2757-2774.
[44] A. Arkudas, A. Balzer, G. Buehrer, I. Arnold, A. Hoppe, R. Detsch, P. Newby, T. Fey, P. Greil, R.E. Horch, A.R. Boccaccini, U. Kneser, Evaluation of Angiogenesis of Bioactive Glass in the Arteriovenous Loop Model, Tissue Engineering Part C: Methods 19 (2012) 479-486.
[45] H. Wang, S.C. Heilshorn, Adaptable Hydrogel Networks with Reversible Linkages for Tissue Engineering, Advanced Materials 27 (2015) 3717-3736.
[46] C.M. Kirschner, K.S. Anseth, Hydrogels in healthcare: From static to dynamic material microenvironments, Acta Materialia 61 (2013) 931-944.
[47] M.R. Filgueiras, G. La Torre, L.L. Hench, Solution effects on the surface reactions of a bioactive glass, Journal of biomedical materials research 27 (1993) 445-453.
[48] I. Wolinsky, K. Guggenheim, Effect of low calcium diet on bone and calcium metabolism in rats and mice—A differential species response, Comparative Biochemistry and Physiology Part A: Physiology 49 (1974) 183-195.
[49] J. Karlsson, A. Martinelli, H.M. Fathali, J. Bielecki, M. Andersson, The effect of alendronate on biomineralization at the bone/implant interface, Journal of Biomedical Materials Research Part A 104 (2016) 620-629.
[50] J. Karlsson, N. Harmankaya, S. Allard, A. Palmquist, M. Halvarsson, P. Tengvall, M. Andersson, Ex vivo alendronate localization at the mesoporous titania implant/bone interface, Journal of Materials Science: Materials in Medicine 26

(2015) 11.
[51] E. Boanini, P. Torricelli, M. Gazzano, E. Della Bella, M. Fini, A. Bigi, Combined effect of strontium and zoledronate on hydroxyapatite structure and bone cell responses, Biomaterials 35 (2014) 5619-5626.
[52] B. Busse, B. Jobke, M. Hahn, M. Priemel, M. Niecke, S. Seitz, J. Zustin, J. Semler, M. Amling, Effects of strontium ranelate administration on bisphosphonate-altered hydroxyapatite: Matrix incorporation of strontium is accompanied by changes in mineralization and microstructure, Acta Biomaterialia 6 (2010) 4513-4521.

Supporting Information

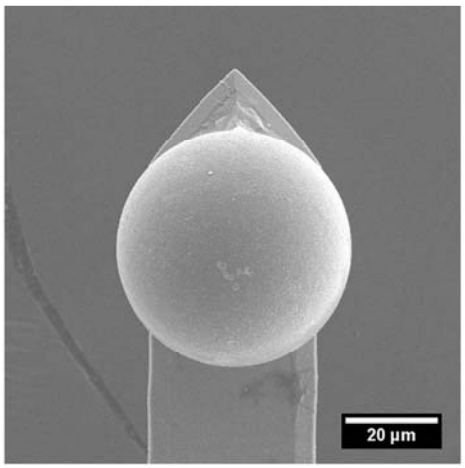

Figure S1. SEM micrograph of a bioactive glass AFM colloidal probe.

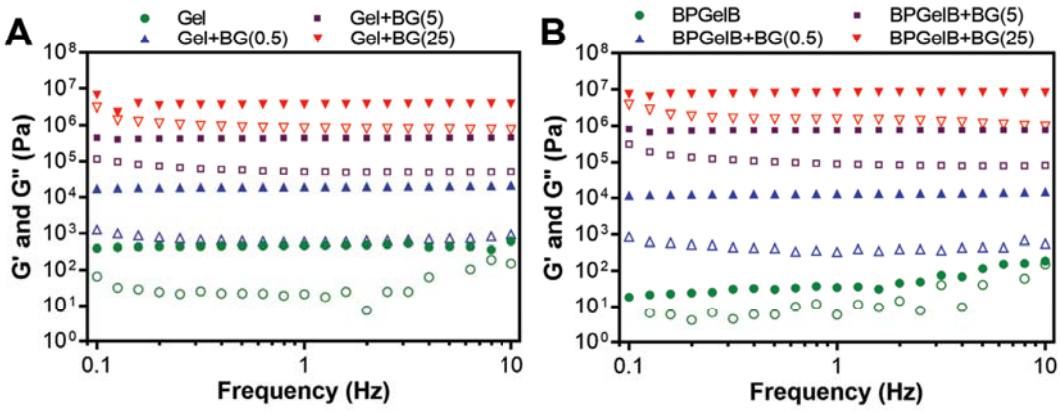

Figure S1. Frequency dependence of storage (solid symbols, G') and loss (open symbols, G'') moduli of colloidal gels prepared with A) non-functionalized or B) bisphosphonate-functionalized gelatin nanoparticles. All samples were prepared with particle volume fraction of 0.25.

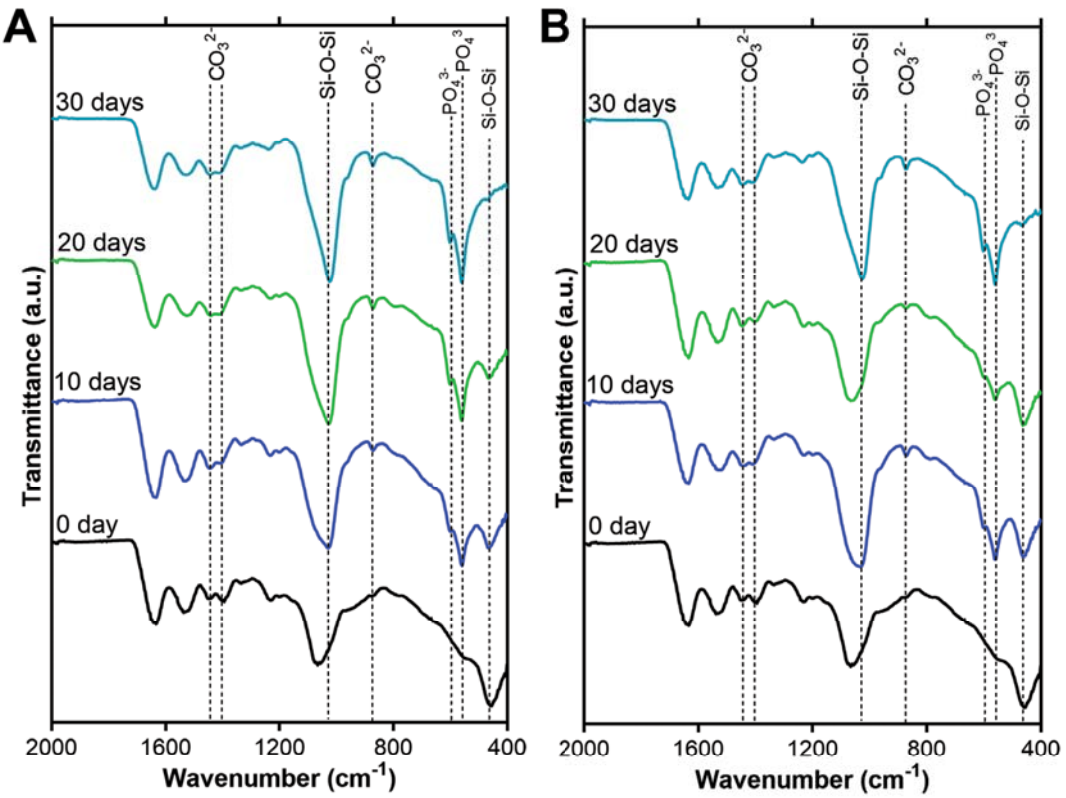

Figure S3. FTIR spectra of freeze-dried BPGel+BG(0.5) colloidal gels at different time points of incubation A) without or B) with cells.

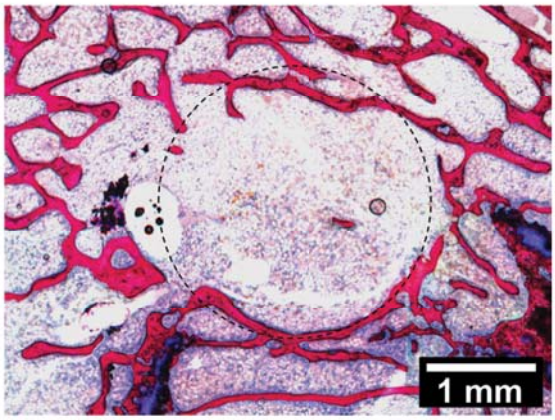

Figure S4. Representative histological image of an empty defect in an osteoporotic femoral condyle of rats 12 weeks after the creation of the defect. The circle indicates the original defect area.

Table S1. Randomized scheme for the implantation of the colloidal gels.

Rat No.	Left femur	Right femur
1		BPGel+BG(0.5)
2	Gel	BPGel
3	BPGel	
4	BPGel+BG(0.5)	Gel
5	Gel	BPGel
6		BPGel+BG(0.5)
7	BPGel+BG(0.5)	Gel
8	BPGel	
9		BPGel
10	BPGel+BG(0.5)	
11	Gel	BPGel+BG(0.5)
12	BPGel	Gel
13	Gel	BPGel+BG(0.5)
14		BPGel
15	BPGel	Gel
16	BPGel+BG(0.5)	

Chapter 4

Exploiting bisphosphonate-bioactive glass interactions for the development of self-healing and bioactive composite hydrogels

This chapter is based on:

M. Diba, J. An, S. Schmidt, M. Hembury, D. Ossipov, A.R. Boccaccini, and S.C.G. Leeuwenburgh, *Macromolecular Rapid Communications*, 37 (2016) 1952-1959.

1. Introduction

Hydrogels are three-dimensional crosslinked networks containing an extensive amount of water [1]. These materials have been widely recognized as promising candidates for various biomedical applications such as tissue engineering and regenerative medicine [2]. Recently, supramolecular hydrogels have gained increasing interest in the biomedical field [3]. In these systems, the reversibility of non-covalent physical bonds not only allows the design of shear-thinning and self-healing materials [4], but also provides an adaptive environment that can be locally adapted to allow cellular activities while keeping its bulk integrity [5]. Although physically cross-linked polymeric gels have been widely studied [4], they are usually mechanically weak and do not mimic the extracellular environment of natural tissues such as bone. The design of composite hydrogels that combine organic and inorganic phases is an emerging strategy to improve the mechanical and biological performance of hydrogels, as well as a possible route to mimic properties of bone tissue [6, 7]. Various types of non-covalent physical interactions, such as electrostatic [8, 9] and coordination [10, 11] bonds have been exploited to develop such composite hydrogel systems. Bisphosphonates (BP) are a class of drugs commonly used for treatment of osteoporosis. Besides their medicinal efficacy, BP groups exhibit a strong binding affinity for the mineral phase of bone, i.e., hydroxyapatite (HAp) [12, 13]. The physical bonds that are formed between BP and HAp are not only strong but also reversible [14], which facilitates the development of self-healing composite biomaterials [10]. Recently, functionalization of polymers with bisphosphonate groups was shown to be a promising strategy for production of composite gels based on BP-HAp interactions [10]. The binding affinity of BP groups for HAp has been attributed to their interaction with calcium ions as present at HAp surfaces [14], which might indicate that BP groups can also bind to other Ca-containing phases. However, although the interaction between bisphosphonates and calcium phosphates (e.g. HAp) has been widely studied [13, 15], interaction of BP with other Ca-containing inorganic phases such as calcium silicates has not been explored extensively yet. Bioactive glasses (BGs) are typically calcium-containing silicate glasses with applications in a wide range of biomedical areas [16, 17]. Specific compositions of these materials (e.g. 45S5 Bioglass®) have been reported to exhibit a superior bone-bonding and regenerative capability as compared to other

bioactive ceramics such as hydroxyapatite [18]. The bone-bonding properties of bioactive glasses are mediated by the formation of a bone-like apatitic layer on their surface. Consequently, the bioactivity of bioactive glasses is often assessed by determining their apatite-forming ability in simulated body fluids [19]. Nevertheless, it is unknown i) to which extent bisphosphonates bind to bioactive glasses as compared to hydroxyapatite, and ii) if this interaction can be exploited for the development of self-healing and bioactive composite hydrogels.

Here, we evaluated the binding affinity of a bisphosphonate-functionalized polymer, hyaluronan, toward a bioactive glass (i.e. 45S5 Bioglass®) using a colloidal probe Atomic Force Microscopy (AFM) technique. We then exploited the interaction between bioactive glass and bisphosphonate-functionalized hyaluronan to develop composite hydrogels and investigated the viscoelastic and self-healing ability of these materials. Finally, we evaluated the stability and apatite-forming behavior of these materials in simulated body fluid as a measure for their bioactivity. Following this approach, we were able to produce injectable and self-healing organic-inorganic composite hydrogels which mineralized abundantly and rapidly in simulated body fluid. These properties render these composite gels suitable for applications in bone tissue engineering.

2. Experimental section

Full experimental details can be found in the Supporting Information. In brief, hyaluronan was functionalized with bisphosphonate groups as described elsewhere [10]. A colloidal probe Atomic Force Microscopy (AFM) technique [20] was used to measure the adhesion forces between inorganic microspheres, composed of 45S5 Bioglass® (BG) or hydroxyapatite (HAp), in aqueous solutions containing hyaluronan with (HYBP) or without (HY) pendant bisphosphonate functional groups. Organic-inorganic dispersions were prepared by addition of a suspension of inorganic particles to HYBP or HY aqueous solutions during vigorous vortexing. The viscoelastic properties and self-healing ability of the dispersions were evaluated using an AR2000 Advanced Rheometer (TA Instruments). The self-healing ability of the hydrogels upon failure induced by cutting was evaluated by performing compression tests using a Zwick Roell Z2.5 instrument (Germany). The *in vitro* mineralization behavior of hydrogel composites was studied by immersing them in simulated body fluid (SBF) [21] at 37 °C after which their apatite-forming ability

was monitored using Fourier Transform Infrared Spectroscopy (FTIR, Spectrum One, Perkin Elmer), Inductively Coupled Plasma-Optical Emission Spectrometry (ICP-OES; iCAP 6300, Thermo Fisher Scientific, USA), and Thermogravimetric Analysis (TGA; Q50 analyzer, TA instruments, USA). A Field Emission Scanning Electron Microscope (FE-SEM; Sigma 300, Zeiss, Germany) equipped with an energy-dispersive X-ray analyzer (EDS; XFlash detector 610M, Brucker Nano GmbH, Germany) was used to evaluate the morphology and composition of lyophilized hydrogels.

3. Results and discussion

3.1. Colloidal probe atomic force microscopy

The colloidal probe AFM technique is a promising strategy to investigate the interactions between polymers and colloidal particles [22]. Here, we used the colloidal probe technique [20] to measure the adhesion forces between two inorganic microspheres, i.e. Bioglass® (BG) or hydroxyapatite (HAp), in aqueous solutions containing different concentrations of hyaluronan with (HYBP) or without (HY) bisphosphonate functional groups. To this end, inorganic microspheres were fixed on glass slides while the colloidal probe was prepared by gluing a single inorganic microsphere on an AFM cantilever. Figure 1A illustrates our hypothesized mechanism for interparticle adhesion based on polymer bridging, while Figure S1 depicts the AFM setup that was used in our study.

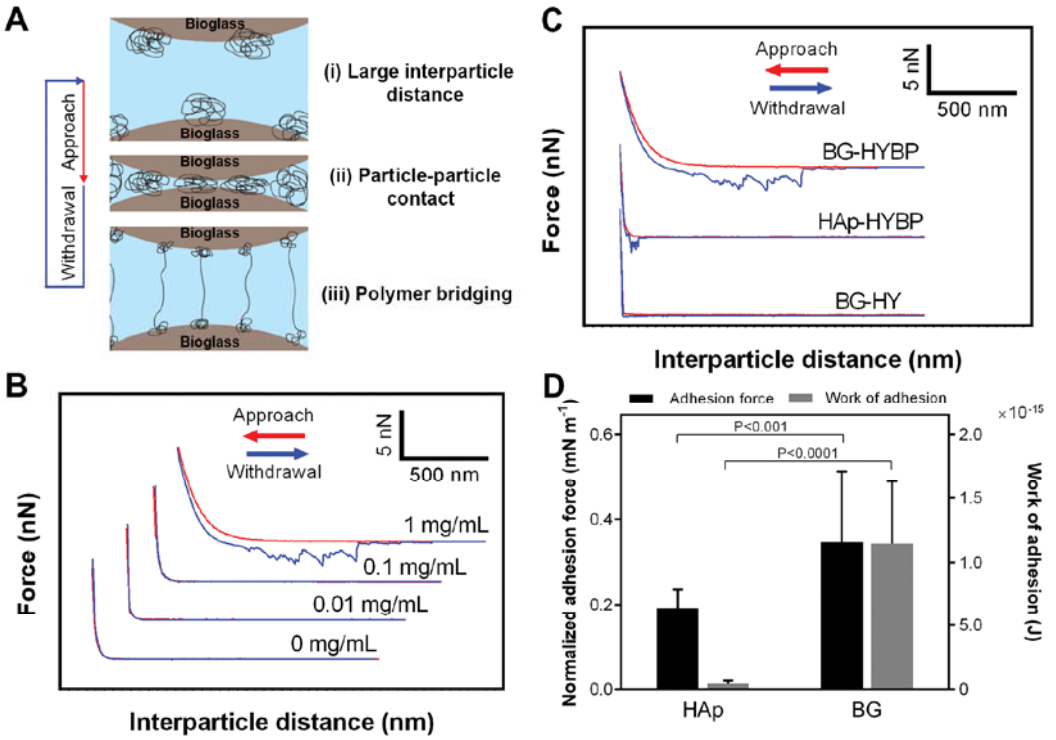

Figure 1. Interparticle adhesion measurements performed by the colloidal probe AFM method. A) Schematic illustration of the bridging phenomena occurring during the AFM measurements. B) Representative adhesion force curves for bioactive glass particles in solutions containing dissolved HYBP polymer at different concentrations. C) Representative adhesion force curves for bioactive glass (BG) or hydroxyapatite (HAp) particles in solutions containing HY or HYBP polymer at a concentration of 1 mg/mL. D) Interparticle adhesion force and work of adhesion for inorganic particles in solutions containing 1 mg/mL of dissolved HYBP polymer.

We first investigated the effects of different concentrations of dissolved HYBP on interparticle forces between BG particles. As shown in Figure 1B, at HYBP concentrations of 0 to 0.1 mg/mL, no adhesion event was observed. However, when the HYBP concentration was increased to 1 mg/mL, the force curve during probe withdrawal revealed a strong and complex adhesion behavior, as reflected by multiple force maxima and minima, corresponding to HYBP bridging two BG particles. The complex nature of the adhesion behavior can be related to interparticle bridging by multiple HYBP chains leading to several dissociation events [23], as shown in Figure 1B. Interestingly, at this concentration, the approach part of the force curves shows only a small slope upon particle contact, whereas the slope is much steeper at the lower HYBP concentrations. Such behavior can be due to the formation of a thin and soft HYBP layer on the surfaces of particles at high polymer concentration.

By increasing the interparticle distance during probe withdrawal, bridged polymer chains between the two particles unfold at small interparticle distances, which gave rise to less interparticle adhesion as compared to the stronger adhesion events observed at larger interparticle distances. Importantly, the interparticle adhesion between the BG particles in the presence of HYBP was observed for several cycles of approach/withdrawal (Figure S5), thereby confirming the reversible nature of the HYBP-BG bonds and their applicability for development of self-healing materials. In addition, we observed the formation of a thick hydrogel layer on the substrate surface at HYBP concentrations higher than 1 mg/mL, which was possibly caused by polymer bridging between multiple BG particles at the substrate preventing AFM measurements. Next, we investigated the interparticle adhesion between HAp or BG particles in solutions containing 1 mg/mL of HYBP or HY in the solution. As shown in Figure 1C, the affinity between HAp particles was lower than the adhesion between BG particles in solutions containing, which reveals that HYBP macromers adhere more strongly to BG than to HAp. Importantly, no adhesion between BG particles was observed in solutions containing hyaluronan without pendant bisphosphonate groups (HY), indicating that the observed adhesion for HYBP was specifically caused by the pendant bisphosphonate groups and not by other groups as present along the hyaluronan chains. Finally, the adhesion force and work of adhesion caused by HYBP interparticle bridging were shown to be ~2 and ~26 times higher for BG particles as compared to HAp particles, respectively (Figure 1D). For these quantifications, we normalized the adhesion force values to the effective radius of the two microparticles used in each single measurement in order to exclude effects of differences in particle size from our results (see Supporting Information for more details). Previous investigations [14, 24, 25] have attributed the binding affinity of BP with calcium phosphates to their interaction with calcium ions as well as their substitution with phosphate ions from calcium phosphate surfaces. It has been observed [14] that more reactive calcium phosphate phases exhibit a strong affinity for BP adsorption as compared to more stable phases, which has been attributed to their strong capacity for ion exchange. Accordingly, these reports suggest that the superior binding affinity of BP groups toward BG surfaces observed in our study is due to the high surface reactivity and ion exchange capability of the 45S5 Bioglass® composition [26]. Further investigations would

be of interest to determine if similar effects would appear when more complex bioactive glass compositions with the capacity to release therapeutic ions (e.g. Sr, B, Cu) would be used.

3.2. Hydrogel formation and viscoelastic properties

Subsequently, we studied the viscoelastic properties of hydrogel composites by means of rheological measurements. First, we investigated the formation of hydrogels as a function of the HYBP polymer (between 1-20 mg/mL) content at a fixed inorganic content of 60 mg/mL BG particles. As shown in Figure 2A, we observed that stable hydrogels (defined as storage modulus (G')> loss modulus (G")) could only be formed for HYBP concentrations higher than 5 mg/mL. The most elastic samples were obtained at a HYBP concentration of 20 mg/mL; these hydrogels showed frequency-independent viscoelastic behavior which indicates an effective bridging flocculation of BG particles with HYBP polymer chains at this concentration. Therefore, this polymer concentration was selected for the further investigations. Figure 2B shows a SEM micrograph with corresponding elemental mapping for silicon of a lyophilized hydrogel, indicating a homogenous distribution of the BG particles throughout the hydrogel. We did not observe gel formation when we used HY instead of HYBP or pure silica instead of BG particles (Figure S6 and S7), which suggest that the gel formation is based on bond formation between BP groups and calcium ions as present on the surface of BG particles. Moreover, hydrogel composites containing HAp particles exhibited ~40% lower storage moduli (G') (Table S1).

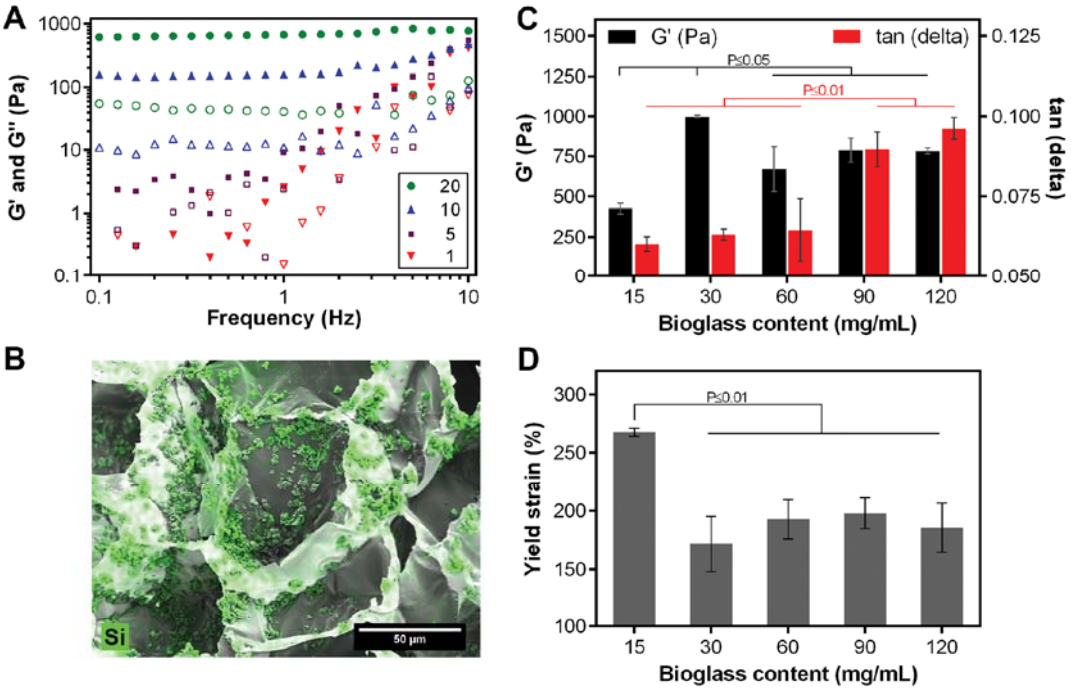

Figure 2. Viscoelastic properties of composite hydrogels. A) Frequency dependence of storage (solid symbols, G') and loss (open symbols, G'') moduli of suspensions containing 60 mg/mL of Bioglass® content and different concentrations (mg/mL) of HYBP. B) SEM micrograph with elemental mapping for silicon of a lyophilized composite hydrogels containing 20 mg/mL of HYBP and 60 mg/mL of the Bioglass® particles. C) Storage modulus (G'), tan (delta) and D) yield strain of composite hydrogels as a function of their Bioglass® content (HYBP concentration=20 mg/mL).

In addition, we studied the viscoelastic properties of hydrogel composites as a function of their inorganic BG content (between 15-120 mg/mL). As shown in Figure 2C, by increasing the BG content from 15 to 30 mg/mL, we observed a significant rise in the G' value, after which the G' value declined. However, further increase of the BG content did not have a significant effect on the G'. In our system, BG particles can influence the elasticity of the hydrogel composites by (i) cross-linking the hydrogel network [27], (ii) reinforcing the hydrogels due to their high stiffness and (iii) increasing the solid volume fraction of the hydrogels [6]. The variations of G' as function of BG content of the hydrogels (Figure 2C) suggest gel elasticity was mainly determined by cross-linking. We also observed an enhanced damping factor tan (delta) in the composite hydrogels at high BG contents (90 and 120 mg/mL), which indicates that viscous behavior (as reflected by G'' values) was more prominent for composite hydrogels with such high inorganic contents. Moreover, by increasing the BG content from 15 to 30 mg/mL, the yield strength of

the hydrogels significantly decreased, which correspond to increased brittleness of the networks. However, further increase of the BG content did not have a significant effect on the yield strength.

3.3. Self-healing capability of hydrogels

Figure 3A demonstrates the self-healing ability of the composite hydrogels upon failure induced by cutting. As shown in this figure, after pressing two cut surfaces of hydrogels together, the hydrogels could recover their cohesiveness almost immediately. No viscous flow through the interface was detected, since colors did not mix, thereby confirming that self-healing was a local interfacial phenomenon. Moreover, the self-healed hydrogels could maintain their integrity when immersed in water (Figure S8). In order to quantify the self-healing ability of the hydrogels upon cutting, we performed compression tests on virgin and self-healed samples. As shown in Figure 3B, these tests revealed that the hydrogels could completely recover their mechanical properties after self-healing. Particularly, no significant differences were observed between the compressive strengths and elastic moduli of the virgin and self-healed samples (Figure 3C).

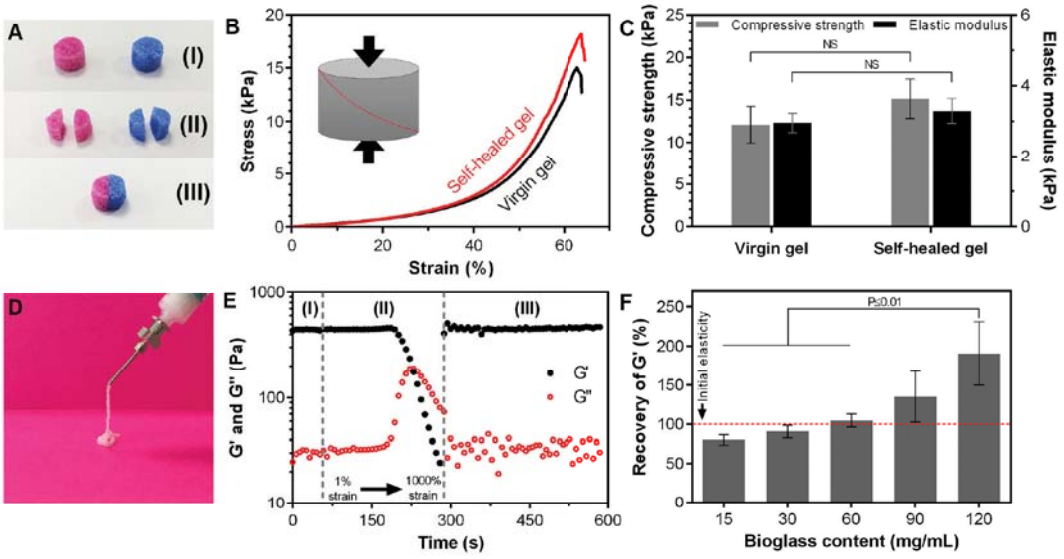

Figure 3. A) Self-healing behavior of composite hydrogels after cutting demonstrated in the digital photographs showing: (I) original composite hydrogels stained with either blue or red dyes, (II) composite hydrogels after cutting, or (III) a composite hydrogel after self-healing. B) Stress-strain curves and C) corresponding mechanical properties of virgin and self-healed gels evaluated through compression tests. The red lines and black arrows in the schematic demonstrate the cut/self-healed interfaces of the hydrogel samples and the direction of applied force, respectively. NS indicates not significant (P>0.1). D) Digital photograph of a composite hydrogel during injection. E) Self-healing behavior of a composite hydrogel upon

shear-induced failure evaluated through rheological tests in three steps: (I) time sweep at 1% strain, (II) network destruction by increasing strain from 1% to 1000%, and (III) recovery at 1% strain. F) Recovery of storage modulus (G') for hydrogels with various bioactive glass contents, 5 min after gel network destruction. The hydrogels used in figures A, B, C, D and E contained 60 mg/mL of Bioglass® particles. All the hydrogels contained 20 mg/mL of HYBP.

The composite hydrogels developed in this study were shear-thinning (Figure S9) and injectable (Figure 3D). Generally, however, extrusion of a material through a narrow needle produces extensive shear forces which can lead to mechanical failure of the material. Consequently, we evaluated the self-healing ability of the composite hydrogels upon failure induced by destructive shearing up to 1000% strain. As shown in Figure 3E, the hydrogel composites showed liquid-like behavior upon shear-induced failure at step (II), but their elasticity recovered completely immediately after reducing the strain at step (III) to 1%. Our experiments demonstrated that the self-healing ability of the hydrogels, characterized by the recovery of G' after damage, increased with increasing BG content (Figure 3F). We propose that the inferior self-healing ability of hydrogel composites containing low amounts of BG (15 and 30 mg/mL) is caused by complete coating of the BG particles with HYBP chains during composite gel destruction (II) and limited re-establishment of the non-covalent polymer bridges between the BG particles during the recovery stage (III). Surprisingly, hydrogels with 120 mg/mL of BG content showed more than 100 % and significantly higher recovery of G' as compared to the other compositions. We expected that the higher elasticity of these composite hydrogels after shear-induced failure was related to fragmentation of brittle glass particles into a large number of smaller particles during the high shear. However, this possibility was ruled out since we did not observe any significant particle size variation after the damage (Figure S10). Nevertheless, elemental mapping for silicon using EDS indicated a more uniform distribution of the BG particles after the high shear (Figure S11), which might explain the recovery values exceeding 100%.

3.4. *In vitro* apatite-forming capacity

In order to evaluate the mineralization behavior of the composite hydrogels, they were immersed in simulated body fluid (SBF) [19, 21] for up to 14 days and their apatite-forming capacity was studied as a measure for their bioactivity. Figure 4A shows the FTIR spectra of the composite hydrogels as-prepared and after immersion in SBF for various periods of time. Within the first 12 hours of immersion, sharp peaks

at ~570 and ~600 cm^{-1} corresponding to the bending mode of ν_4(P–O–P) bond from the PO_4^{3-} groups found in hydroxyapatite [28, 29] were detected, which increased in intensity as a function of immersion time. At ~470 cm^{-1}, a peak associated to the ν_2(P–O–P) bending mode could also be detected, which, however, overlapped with the ν_{sym}(Si–O–Si) band of the Bioglass® (Figure S12) [28]. In addition, upon immersion of the hydrogels in SBF, the intensity of the absorption band at ~930 cm^{-1}, which corresponds to the Si-O bonds of the Bioglass® with one non-bridging oxygen (NBO), declined. This decline has been reported to be caused by ion exchange reactions of the Bioglass® in SBF, resulting in the formation of apatite [28]. As shown in Figure 4B, SEM examination revealed formation of sub-micron needle-shaped crystals throughout the hydrogels. These needle-shaped crystals had an approximate length and width of 307±83 and 59±17 nm, respectively. Moreover, when evaluated by means of EDS, the hydrogels displayed enhanced calcium and phosphorus levels after SBF immersion (Figure S13).

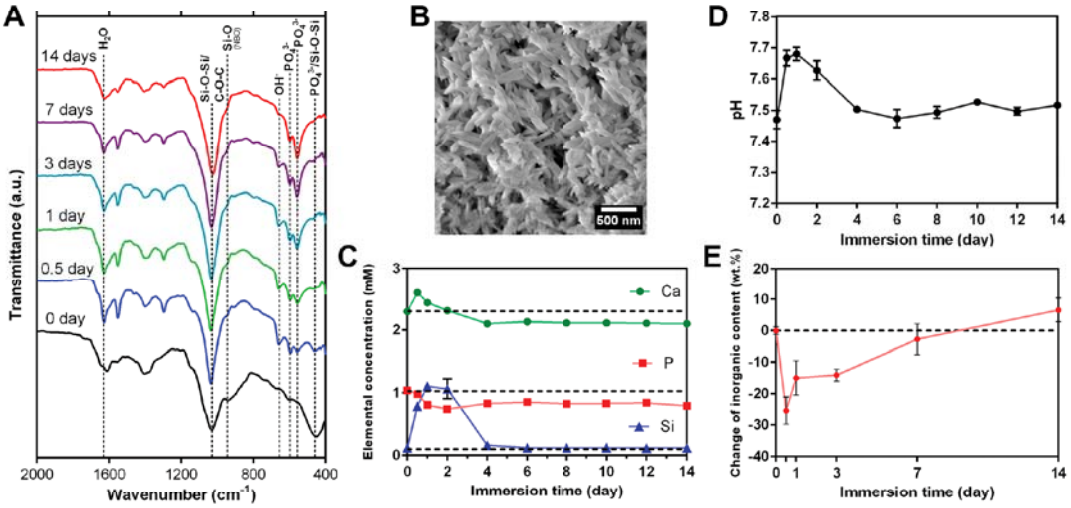

Figure 4. A) FTIR spectra of the composite hydrogels after 0 to14 days of immersion in SBF. B) SEM micrograph showing the needle-shaped crystals formed throughout the hydrogels after immersion in SBF. C) Elemental composition and D) pH of SBF solutions at different time points of immersion. E) Change of inorganic content of the composite hydrogels (as measured using TGA) as a function of immersion time in SBF. All hydrogel composites contained 20 mg/mL of HYBP and 60 mg/mL of Bioglass® particles. Dashed lines in C and E correspond to the initial conditions before the immersion.

In order to improve our understanding of the mechanism and kinetics of apatite formation on the composite hydrogels, we analyzed the elemental composition and pH of the SBF solutions as well as the change of the inorganic content of composite

hydrogels during the immersion in SBF. The ICP-OES results (Figure 4C) showed a rapid increase of calcium concentration in the SBF within the first day of immersion, which is known to be caused by cation exchange between Ca^{2+} ions from the glass and the H^{+} of the solution [17]. This cation exchange leads to formation of silanol groups (Si-OH) on the surface of BG particles and, as can be seen in Figure 4D, increased the pH of solution. The high pH disrupts the silicate network of the BG particles by cleaving Si-O-Si bonds, releasing soluble silica into the solution, as shown by the ICP-OES results (Figure 4C). This step produces more silanol groups on the surface of BG particles, which undergo a polycondensation process and form a silica-rich layer [17]. This silica-rich layer adsorb calcium and phosphate ions from the solution as well as the Bioglass®, and accordingly lead to formation of a calcium phosphate layer [17]. We observed that the release of silica stopped after 4 days of immersion, while the pH returned to neutrality, possibly due to complete coverage of BG surfaces with calcium phosphates. However, the consumption of calcium and phosphate from the solution continued at constant rates, which suggests a continuous mineralization process of calcium phosphates of our hydrogels for at least up to 14 days. Furthermore, analysis of the change of inorganic content using TGA (Figure 4E) was in agreement with the FTIR, ICP-OES and pH measurements and indicated a competition between dissolution of the glass and calcium phosphate mineralization. At the early stage of SBF immersion, the glass dissolution rate was much higher than the mineralization rate, leading to a sudden reduction of the inorganic content during the first 12 hours. Over time, the mineralization caught up and the hydrogels contained more inorganic content than they contained before the immersion by day 14. Since the degradation of hyaluronan is known to be mediated by hyaluronidase and/or by harsh chemical/physical conditions [30], we do not expect that the mild and enzyme-free conditions upon immersion in SBF could cause degradation of the organic hyaluronan matrix. Finally, we evaluated the viscoelastic properties of the hydrogels as a function of imemrsion time in SBF, which revealed that the hydrogels did not loose their mechanical integrity and retained their typical solid-like behavior (Figure S14). It should be emphasized that by dissolution of the BG particles, new apatitic particles are formed within the hydrogel matrix that can take over the cross-linking role of BG particles, thereby retaining the mechanical integrity of the hydrogels. Nevertheless, hydrogels containing low concentrations

of BG particles (5 mg/ml) did not retain their integrity in SBF and dissolved within the first few days of immersion.

4. Conclusions

In conclusion, we introduced a novel class of apatite-forming and self-healing composite hydrogels. Bisphosphonate functionalization of hyaluronan resulted into a strong binding affinity of this polymer for a bioactive silicate glass (45S5 Bioglass®). This binding affinity even exceeded the well-known binding affinity of bisphosphonate groups for hydroxyapatite. Therefore, through bridging flocculation of bioactive glass particles with bisphosphonate-functionalized hyaluronan, organic-inorganic composite hydrogels could be successfully prepared. The reversibility of bisphosphonate-bioactive glass bonds allowed synthesis of injectable composite hydrogels with remarkable self-healing capacity. These composite hydrogels not only could keep their integrity in simulated body conditions, but were also able to mineralize apatitic crystals abundantly within their matrix, demonstrating a strong potential for application in bone regeneration.

References

[1] P.J. Flory, Introductory lecture, Faraday Discussions of the Chemical Society 57 (1974) 7-18.
[2] N.A. Peppas, J.Z. Hilt, A. Khademhosseini, R. Langer, Hydrogels in Biology and Medicine: From Molecular Principles to Bionanotechnology, Advanced Materials 18 (2006) 1345-1360.
[3] M.J. Webber, E.A. Appel, E.W. Meijer, R. Langer, Supramolecular biomaterials, Nat Mater 15 (2016) 13-26.
[4] Z. Wei, J.H. Yang, J. Zhou, F. Xu, M. Zrinyi, P.H. Dussault, Y. Osada, Y.M. Chen, Self-healing gels based on constitutional dynamic chemistry and their potential applications, Chemical Society Reviews 43 (2014) 8114-8131.
[5] H. Wang, S.C. Heilshorn, Adaptable Hydrogel Networks with Reversible Linkages for Tissue Engineering, Advanced Materials 27 (2015) 3717-3736.
[6] S. Utech, A. Boccaccini, A review of hydrogel-based composites for biomedical applications: enhancement of hydrogel properties by addition of rigid inorganic fillers, Journal of Materials Science 51 (2016) 271-310.
[7] J. Zheng, P. Xiao, W. Liu, J. Zhang, Y. Huang, T. Chen, Mechanical Robust and Self-Healable Supramolecular Hydrogel, Macromolecular Rapid Communications (2015) n/a-n/a.
[8] Q. Wang, J.L. Mynar, M. Yoshida, E. Lee, M. Lee, K. Okuro, K. Kinbara, T. Aida, High-water-content mouldable hydrogels by mixing clay and a dendritic molecular binder, Nature 463 (2010) 339-343.
[9] H. Wang, M. Bongio, K. Farbod, A.W.G. Nijhuis, J. van den Beucken, O.C. Boerman, J.C.M. van Hest, Y. Li, J.A. Jansen, S.C.G. Leeuwenburgh, Development of injectable organic/inorganic colloidal composite gels made of self-assembling gelatin nanospheres and calcium phosphate nanocrystals, Acta Biomaterialia 10 (2014) 508-519.
[10] M.R. Nejadnik, X. Yang, M. Bongio, H.S. Alghamdi, J.J.J.P. van den Beucken, M.C. Huysmans, J.A. Jansen, J. Hilborn, D. Ossipov, S.C.G. Leeuwenburgh, Self-healing hybrid nanocomposites consisting of bisphosphonated hyaluronan and calcium phosphate nanoparticles, Biomaterials 35 (2014) 6918-6929.
[11] Y. Lee, H.J. Chung, S. Yeo, C.-H. Ahn, H. Lee, P.B. Messersmith, T.G. Park, Thermo-sensitive, injectable, and tissue adhesive sol-gel transition hyaluronic acid/pluronic composite hydrogels prepared from bio-inspired catechol-thiol reaction, Soft Matter 6 (2010) 977-983.
[12] G.A. Rodan, H.A. Fleisch, Bisphosphonates: mechanisms of action, Journal of Clinical Investigation 97 (1996) 2692-2696.
[13] K. Farbod, M. Diba, T. Zinkevich, S. Schmidt, M.J. Harrington, A.P.M.

Kentgens, S.C.G. Leeuwenburgh, Gelatin Nanoparticles with Enhanced Affinity for Calcium Phosphate, Macromolecular Bioscience 16 (2016) 717-729.
[14] F. Errassifi, S. Sarda, A. Barroug, A. Legrouri, H. Sfihi, C. Rey, Infrared, Raman and NMR investigations of risedronate adsorption on nanocrystalline apatites, Journal of Colloid and Interface Science 420 (2014) 101-111.
[15] M.A. Lawson, Z. Xia, B.L. Barnett, J.T. Triffitt, R.J. Phipps, J.E. Dunford, R.M. Locklin, F.H. Ebetino, R.G.G. Russell, Differences between bisphosphonates in binding affinities for hydroxyapatite, Journal of Biomedical Materials Research Part B: Applied Biomaterials 92B (2010) 149-155.
[16] V. Miguez-Pacheco, L.L. Hench, A.R. Boccaccini, Bioactive glasses beyond bone and teeth: Emerging applications in contact with soft tissues, Acta Biomaterialia 13 (2015) 1-15.
[17] J.R. Jones, Review of bioactive glass: From Hench to hybrids, Acta Biomaterialia 9 (2013) 4457-4486.
[18] Y. Fujishiro, L.L. Hench, H. Oonishi, Quantitative rates of in vivo bone generation for Bioglass® and hydroxyapatite particles as bone graft substitute, Journal of Materials Science: Materials in Medicine 8 (1997) 649-652.
[19] A.L.B. Maçon, T.B. Kim, E.M. Valliant, K. Goetschius, R.K. Brow, D.E. Day, A. Hoppe, A.R. Boccaccini, I.Y. Kim, C. Ohtsuki, T. Kokubo, A. Osaka, M. Vallet-Regí, D. Arcos, L. Fraile, A.J. Salinas, A.V. Teixeira, Y. Vueva, R.M. Almeida, M. Miola, C. Vitale-Brovarone, E. Verné, W. Höland, J.R. Jones, A unified in vitro evaluation for apatite-forming ability of bioactive glasses and their variants, Journal of Materials Science: Materials in Medicine 26 (2015) 1-10.
[20] M. Borkovec, I. Szilagyi, I. Popa, M. Finessi, P. Sinha, P. Maroni, G. Papastavrou, Investigating forces between charged particles in the presence of oppositely charged polyelectrolytes with the multi-particle colloidal probe technique, Advances in Colloid and Interface Science 179–182 (2012) 85-98.
[21] T. Kokubo, H. Takadama, How useful is SBF in predicting in vivo bone bioactivity?, Biomaterials 27 (2006) 2907-2915.
[22] M. Kappl, H.-J. Butt, The Colloidal Probe Technique and its Application to Adhesion Force Measurements, Particle & Particle Systems Characterization 19 (2002) 129-143.
[23] I. Popa, G. Gillies, G. Papastavrou, M. Borkovec, Attractive Electrostatic Forces between Identical Colloidal Particles Induced by Adsorbed Polyelectrolytes, The Journal of Physical Chemistry B 113 (2009) 8458-8461.
[24] S. Mukherjee, Y. Song, E. Oldfield, NMR Investigations of the Static and Dynamic Structures of Bisphosphonates on Human Bone: a Molecular Model, Journal of the American Chemical Society 130 (2008) 1264-1273.

[25] S. Mukherjee, C. Huang, F. Guerra, K. Wang, E. Oldfield, Thermodynamics of Bisphosphonates Binding to Human Bone: A Two-Site Model, Journal of the American Chemical Society 131 (2009) 8374-8375.
[26] L.L. Hench, Bioceramics, Journal of the American Ceramic Society 81 (1998) 1705-1728.
[27] E.A. Appel, M.W. Tibbitt, M.J. Webber, B.A. Mattix, O. Veiseh, R. Langer, Self-assembled hydrogels utilizing polymer–nanoparticle interactions, Nature Communications 6 (2015).
[28] M. Mačković, A. Hoppe, R. Detsch, D. Mohn, W.J. Stark, E. Spiecker, A.R. Boccaccini, Bioactive glass (type 45S5) nanoparticles: in vitro reactivity on nanoscale and biocompatibility, Journal of Nanoparticle Research 14 (2012) 1-22.
[29] S. Koutsopoulos, Synthesis and characterization of hydroxyapatite crystals: A review study on the analytical methods, Journal of Biomedical Materials Research 62 (2002) 600-612.
[30] I. Capila, R.A.M. Sasisekharan, Chapter 2 - Methods for Analysis of Hyaluronan and Its Fragments, Chemistry and Biology of Hyaluronan, Elsevier Science Ltd, Oxford, 2004, pp. 21-40.

Supporting Information

1. Experimental section

1.1. Materials

Hyaluronic acid (molecular weight: 100–150 KDa) was purchased from Lifecore Biomedical (Chaska, The U.S.A). Hydroxyapatite (spherical shape with average diameter of 35 ± 4 µm; CAM Bioceramics BV (Leiden, the Netherlands)) and bioactive glass (45S5 Bioglass®; spherical shape with average diameter of 49 ± 4 µm; XL Sci-Tech, Inc. (Richland, WA, USA)) microparticles were used for atomic force microscopy experiments. For hydrogel preparation, melt-derived 45S5 Bioglass® and hydroxyapatite particles with average particle sizes of ~2 µm were obtained from Schott AG (Mainz, Germany) and CAM Bioceramics BV (Leiden, the Netherlands), respectively. The 45S5 Bioglass® particles, used for the force microscopy and hydrogel preparation, contained 45 wt% SiO_2 , 24.5 wt% Na_2O, 24.5 wt% CaO, and 6 wt% P_2O_5.

1.2. Methods

1.2.1. Synthesis of hyaluronan-bisphosphonate

First, hyaluronan-thiol was synthesized as reported elsewhere [1]. Thereafter, through a thiol–ene photopolymerization, the hyaluronan-thiol was functionalized with amino-bisphosphonate alendronate as described elsewhere [2]. Briefly, acrylated bisphosphonate was added to a 5 mg/mL aqueous solution of hyaluronan–thiol to obtain a bisphosphonate/thiol molar ratio of 4. Thereafter, 8 mg of Irgacure® 2959 was added to the solution and stirred for 10 min under ultraviolet light (36W UV timer lamp, CNC international BV, Netherlands). Finally, the solution was dialyzed and lyophilized. The quality of the obtained polymers was confirmed by nuclear magnetic resonance (NMR) spectroscopy.

1.2.2. Colloidal probe atomic force microscopy

Interparticle adhesion force measurements were performed using an Atomic Force Microscope (AFM; NanoWizard, JPK Instruments AG, Germany) equipped with an inverted optical microscope at room temperature. Figure S1 illustrates the experimental setup that was used to perform the AFM experiments. Colloidal probes

were prepared by gluing single hydroxyapatite or bioactive glass microparticles to an AFM cantilever (μMash, CSC38/No Al) using an epoxy resin (UHU Plus Schnellfest, UHU GmbH & Co. KG, Germany). The substrates were prepared by (i) locating two sheets of aluminum foil with an average thickness of ~16 μm on two sides of a cover glass (60mm×22mm), (ii) spreading of a thin layer of the epoxy glue (thickness: ~16 μm) using the edge of a razor blade on the area between the two aluminum sheets, and (iii) dropping of multiple hydroxyapatite or Bioglass® microparticles on the glue surface. After 30 minutes, the unbonded particles were removed by compressed air and rinsing with distilled water and ethanol. To ensure that the surface of bonded microparticles were air-exposed and not covered by the glue, each substrate was cut into two parts using a diamond pen, and the cross sections were inspected by optical microscopy. Figures S2 and S3 show the scanning electron microscopy (SEM) images of colloidal probes and substrates, respectively. Each substrate was glued to the surface a plastic Petri dish. Prior to each AFM measurement, the Petri dish containing the substrate as well as the cantilever were treated for 1 min in an air-plasma cleaner. Thereafter, the Petri dish was filled with distilled water containing different concentrations of polymers. For each AFM measurement, the microparticle attached to the cantilever was positioned above another microparticle attached to the substrate through manual adjustments of both substrate and cantilever locations based on live images obtained from the inverted optical microscope linked to the AFM. The AFM measurements were carried out by performing approach/retraction cycles with a velocity of 1 μm/s. After each approaching step, prior to the retraction, upon reaching a set point of 10 nN, the microparticles were kept in contact for 3 seconds.

In order to exclude effects of differences in particle size from our results, we normalized the adhesion force values to the effective radius of the two microparticles used in each single measurement. The effective radius R_{eff} of each two particles were calculated using equation S1:

$$R_{eff} = \frac{R_c R_s}{R_c + R_s} \qquad \text{(S1)}$$

where R_c and R_s represent the radii of the microparticles on the cantilever and on the substrate, respectively. R_c and R_s values were measured using optical microscopy images collected from the cantilever and the microparticle on the substrate used

for each force measurement, as shown in Figure S4. We determined the work of adhesion by integrating the area of the retraction force curve under the baseline. In each experimental condition, the average values for adhesion force and work of adhesion were calculated from approach/retraction cycles performed on 10 different microparticles.

1.2.3. Preparation of hydrogels

In order to prepare the hydrogels, polymers were dissolved in MilliQ water with different concentrations. Separately, inorganic particles were suspended in MilliQ water at a concentration of 200 mg/mL. Depending on the polymer and particle concentration in the final sample, a specific volume of the particle suspension was added to a polymer solution under vigorous vortexing. In case of gel formation, the mixture immediately showed solid-like behavior (Figure S6B).

1.2.4. Rheological measurements

An AR2000 Advanced Rheometer (TA Instruments) with an aluminum parallel plate geometry (diameter of 8mm) was used for the rheological evaluation of the samples. Initially, the linear viscoelastic regime of the hydrogels was determined by strain sweep measurements at a frequency of 1 Hz. Frequency sweep measurements (01 Hz to 10 Hz) were carried out at a fixed strain of 1%. The yield strain (%) of the hydrogels was determined as the crossing point of storage (G') and loss (G") moduli during strain sweep measurements (1-1000% strain) at a fixed frequency of 1 Hz. The self-healing ability of the hydrogels upon shearing was evaluated by measuring the recovery of G' after shear-induced gel network destructions in three steps as follows:

Step 1: Time sweep for 1 min at 1% strain and the frequency of 1 Hz.

Step 2: Strain sweep from 1% to 1000% at the frequency of 1 Hz.

Step 3: Time sweep for 5 min at 1% strain and the frequency of 1 Hz.

The recovery of G' was determined using equation S2:

$$Recovery\ of\ G'\ (\%) = \left(\frac{G'_r}{G'_i}\right) \times 100 \qquad \text{(S2)}$$

where G'_i is the average of G' values during the time sweep in step 1 and G'_r is the G' at the end of step 3, i.e., after 5 minutes of recovery. For all measurements, three samples were analyzed for each experimental condition.

1.2.5. Compression tests

Compression tests were performed using a Zwick Roell Z2.5 instrument (Germany). Cylindrical hydrogel specimens were prepared by pressing the hydrogels into cylindrical Teflon molds (diameter: 8 mm, height: 5 mm) and keeping them at 4 °C overnight. Self-healed samples were prepared by the cutting cylindrical hydrogels into two parts through diagonal cuts using a surgical blade and bringing the two sections back together to fuse their cut interfaces. Thereafter, the samples were kept at 4 °C overnight inside cylindrical Teflon molds with similar dimensions as the samples, in order to ensure physical contact between the two sections. The compression tests were carried out at a loading rate of 0.5 mm/min, and the force data were collected using a Xforce P load cell with nominal force of 20 N (Zwick Roell, Germany).

1.2.6. *In vitro* bioactivity

The *in vitro* bioactivity of hydrogels was evaluated by immersion in simulated body fluid (SBF) solutions prepared according to an established protocol [3]. First, hydrogels with a BG content of 60 mg/mL and HYBP concentration of 20 mg/mL were prepared. Cylinder-shaped hydrogel samples were made by pushing the hydrogels into Teflon molds with a height of 3 mm and a diameter of 4 mm. In order to prevent potential damage to the hydrogels when refreshing the SBF solutions, the hydrogel samples were placed inside Falcon™ cell strainers with a mesh size of 100 µm. The cell strainers containing the hydrogels were put inside 6-well plates, and 10 mL of SBF solution was added to each well. The SBF solutions were refreshed each 2 days. After each time point, the cell strainers containing the hydrogels were rinsed in distilled water and then immediately freeze-dried. The rheological characterizations were carried out on hydrogels immediately after each time point, without performing the freeze-drying step.

1.2.6.1. Fourier Transform Infrared Spectroscopy

Fourier Transform Infrared Spectroscopy (FTIR, Spectrum One, Perkin Elmer) was used to monitor formation and growth of apatite within the lyophilized hydrogels after each time point. Three samples were analyzed for each experimental condition.

1.2.6.2. pH and concentration measurements of SBF solutions

After each time point as well as each refreshment of the SBF solution, the solutions

were collected, their pH was measured after which they were stored for further analyses. In order to determine the concentrations of Si, Ca and P in solutions, the solutions were diluted 28 times in 1 v/v% nitric acid and the concentrations were measured by Inductively Coupled Plasma-Optical Emission Spectrometry (ICP-OES; iCAP 6300, Thermo Fisher Scientific, USA). Three samples were analyzed for each experimental condition.

1.2.6.3. Quantification of inorganic content of hydrogels

In order to determine the inorganic contents of the lyophilized hydrogels after each time point, thermogravimetric analysis (TGA) was carried out using a TGA Q50 analyzer (TA instruments, USA). The TGA measurements were performed under nitrogen atmosphere using a heating ramp of 100 °C/min from room temperature up to 500 °C. Subsequently, the temperature was fixed at 500 °C for 10 min to ensure removal of the organic phase. The inorganic content of each sample was calculated based on the initial and final weight of the sample in each TGA measurement. Three samples were analyzed for each experimental condition.

1.2.7. Scanning electron microscopy and energy-dispersive X-ray spectroscopy

A Field Emission Scanning Electron Microscope (FE-SEM; Sigma 300, Zeiss, Germany) equipped with an energy-dispersive X-ray analyzer (EDS; XFlash detector 610M, Brucker Nano GmbH, Germany) was used to evaluate the structure and composition of lyophilized hydrogels. Prior to each SEM/EDS test, the samples were sputter coated with a 10 nm thick gold layer.

2. Supporting figures and tables

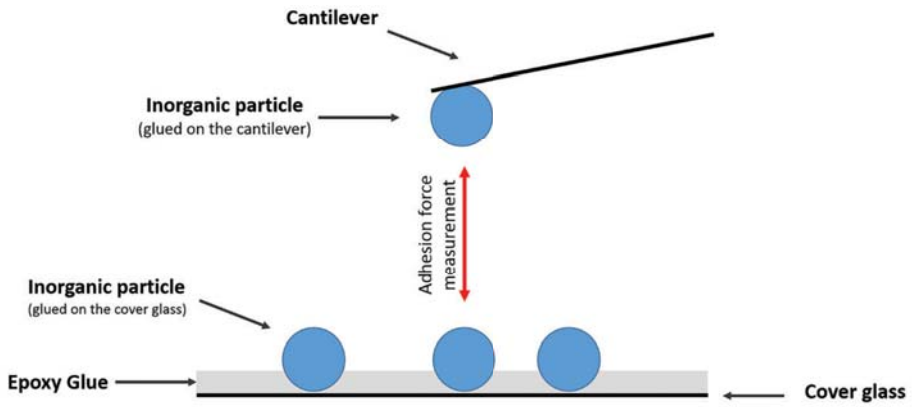

Figure S1. Schematic illustration of the AFM setup.

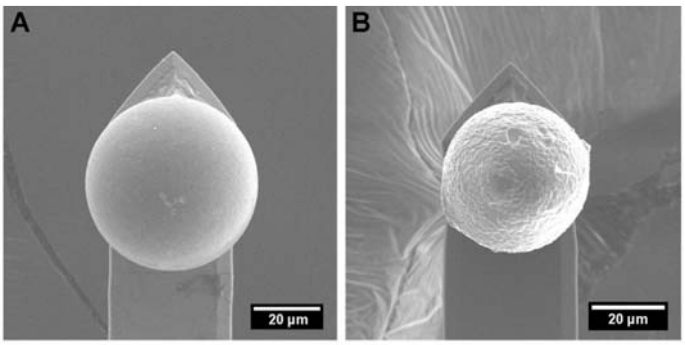

Figure S2. SEM micrographs of A) bioactive glass and B) hydroxyapatite AFM colloidal probes.

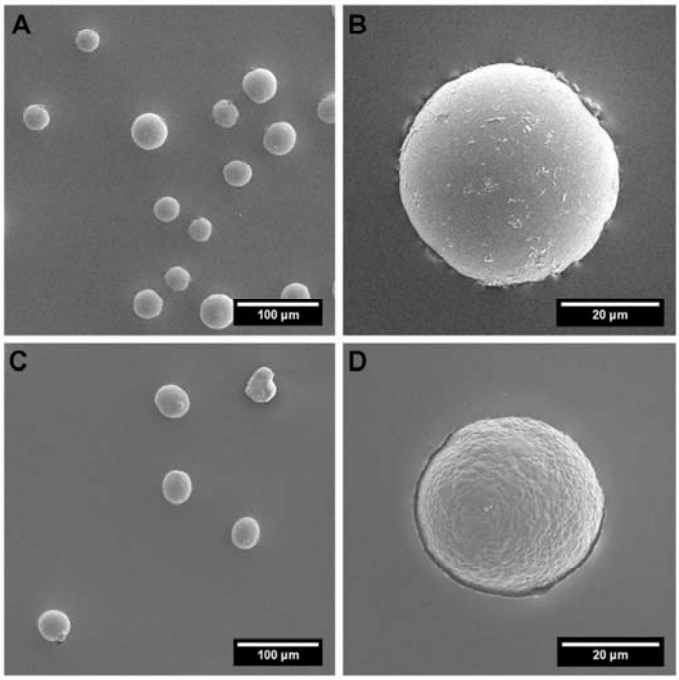

Figure S3. SEM micrographs of A, B) bioactive glass and C, D) hydroxyapatite microparticles glued onto the surface of glass slides.

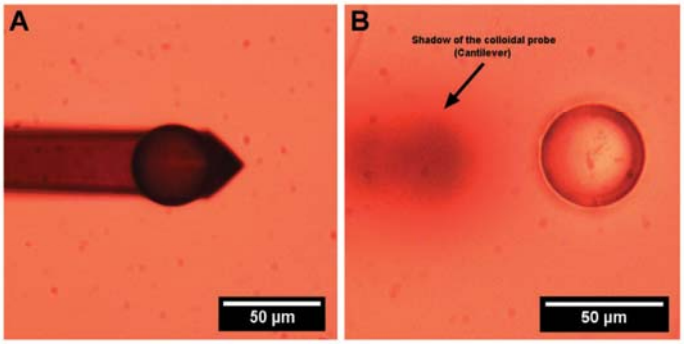

Figure S4. Representative optical microscopy images showing the microparticles on A) the cantilever and B) the substrate.

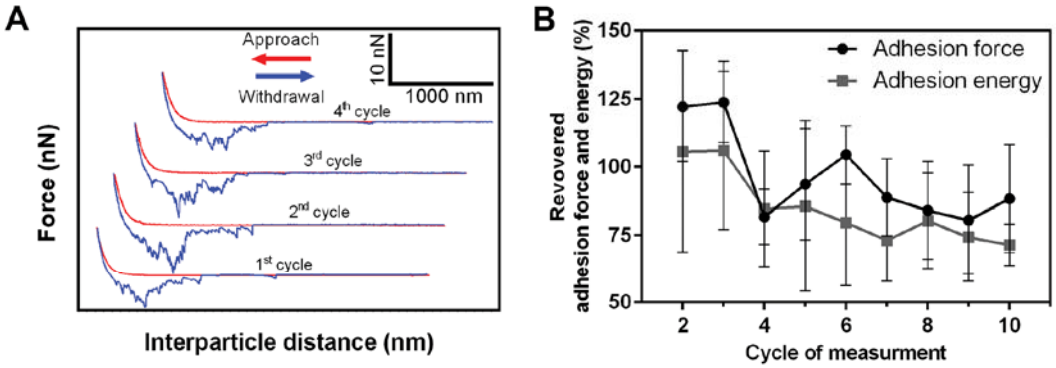

Figure S5. A) Representative force curves and B) average values of recovered adhesion force and energy during multiple cycles of approach-withdrawal between two bioactive glass microparticles at a HYBP polymer concentration of 1 mg/mL. The recovered adhesion force and energy were calculated relative to the initial values measured in the 1st cycle.

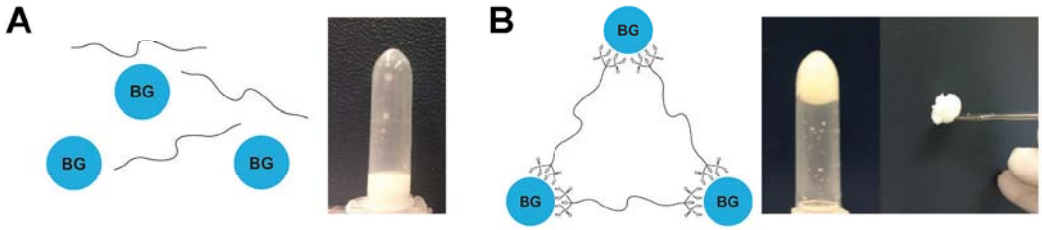

Figure S6. Schematic illustrations and photographs of A) BG+HY and B) BG+HYBP samples.

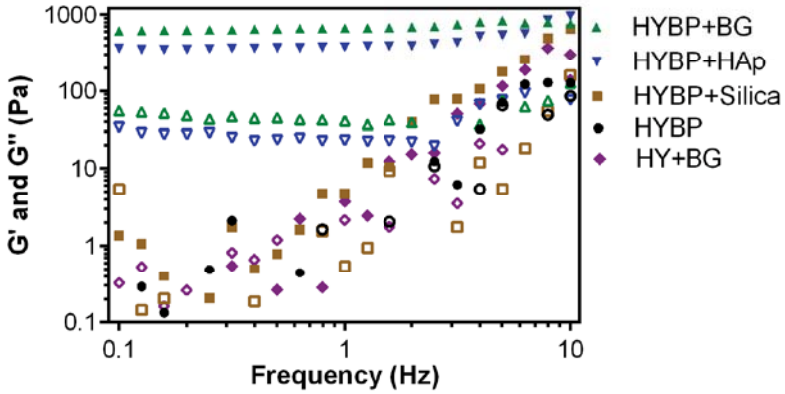

Figure S7. Frequency dependence of storage (solid symbols, G') and loss (open symbols, G'') moduli of various samples with or without inorganic particles. The polymer (HY or HYBP) concentration in all the samples was 20 mg/mL. All the particle-containing samples were with 60 mg/mL of the inorganic particles. The silica particles with an average diameter of 80 nm were synthesized based on an established Stöber method [4].

Table S1. Viscoelastic properties of hydrogels prepared using 60 mg/mL bioactive glass (BG) or hydroxyapatite (HAp) particles, and with 20 mg/mL of HYBP concentration.

Type of hydrogel	G' (Pa)	tan (delta)	Yield strain (%)	Recovery of G' (%)
HYBP+BG	671±139	0.065±0.01	192±17	105± 8.22
HYBP+HAp	391±20	0.054±0.005	316±12	82±19

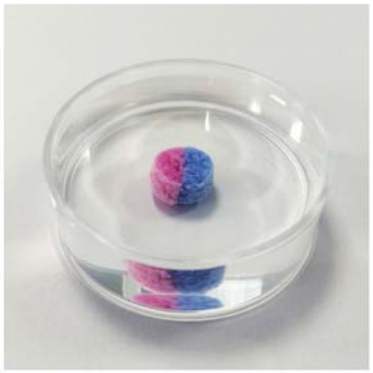

Figure S8. Digital photograph of a hydrogel self-healed after cutting, immersed in water for 10 min. The hydrogel contained 20 mg/mL of HYBP and 60 mg/mL of bioactive glass.

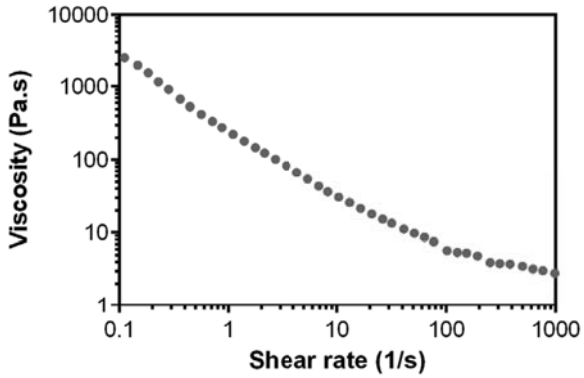

Figure S9. Shear-thinning behavior of composite hydrogels containing 20 mg/mL of HYBP and 60 mg/mL of bioactive glass.

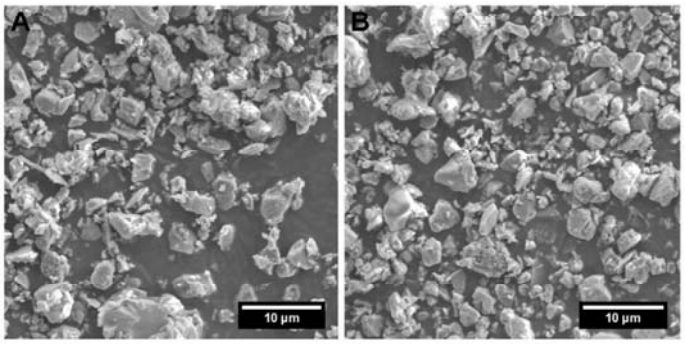

Figure S10. SEM micrographs of bioactive glass particles obtained after removal of the organic phase of the hydrogels at 500 °C A) before or B) after shear-induced network destruction. The hydrogels contained 20 mg/mL of HYBP and 120 mg/mL of the bioactive glass particles.

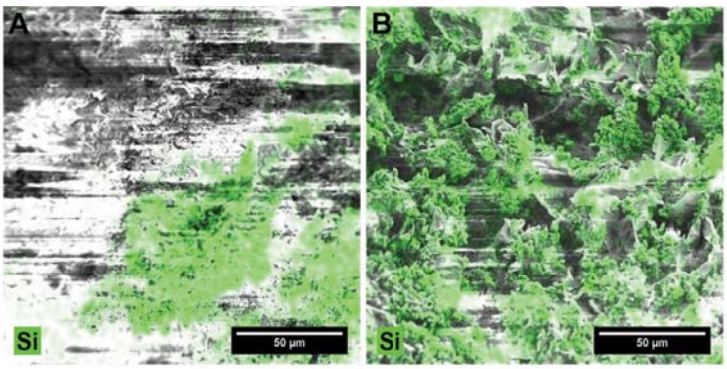

Figure S11. SEM micrographs with overlaid EDS maps of lyophilized hydrogels with 20 mg/mL of HYBP and 120 mg/mL of the bioactive glass particles A) before and B) after shear-induced network destruction.

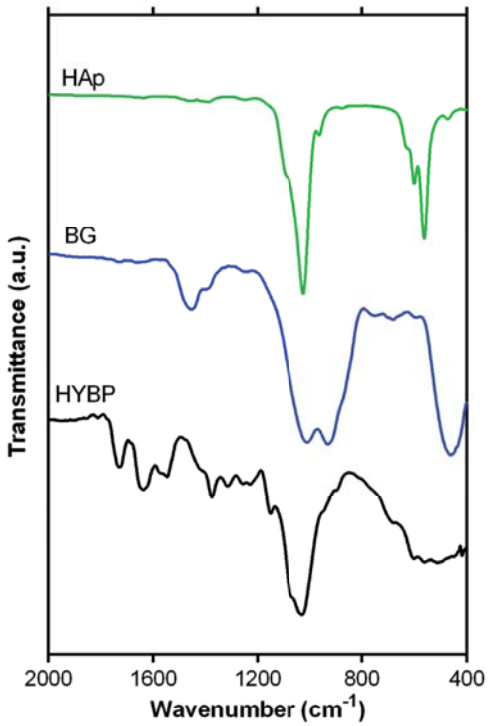

Figure S12. FTIR spectra of hydroxyapatite (HAp), Bioglass® (BG) and bisphosphonate-functionalized hyaluronan (HYBP).

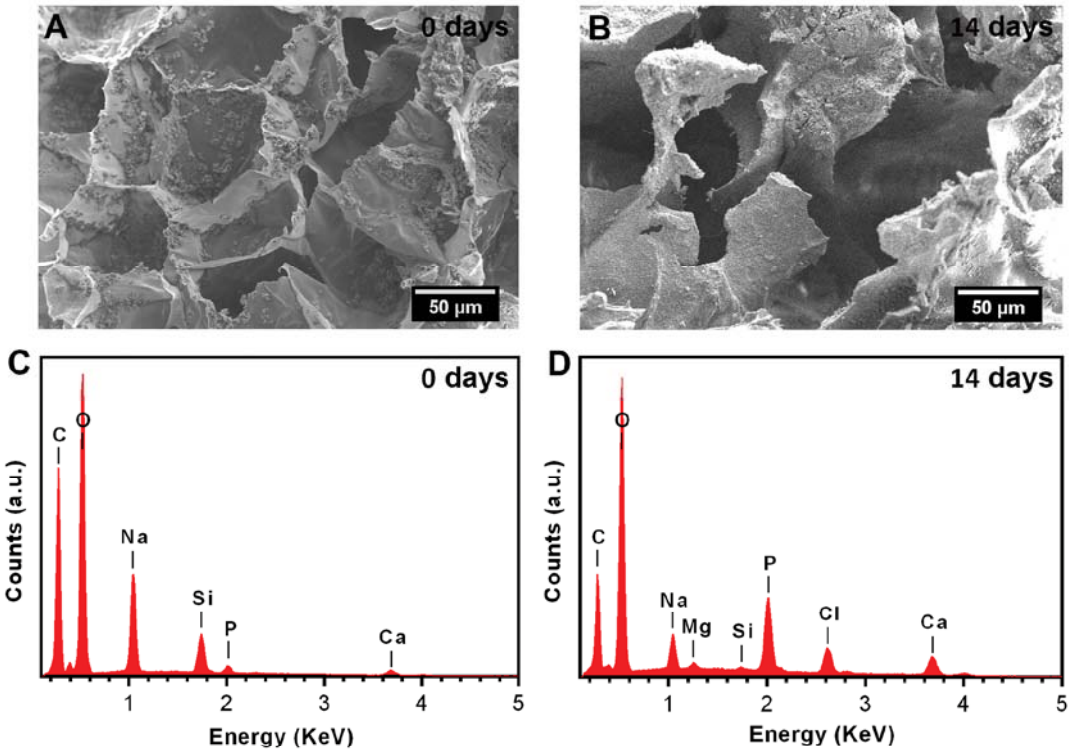

Figure S13. A, B) SEM micrographs and C, D) EDS spectra of composite hydrogels before and after immersion in SBF.

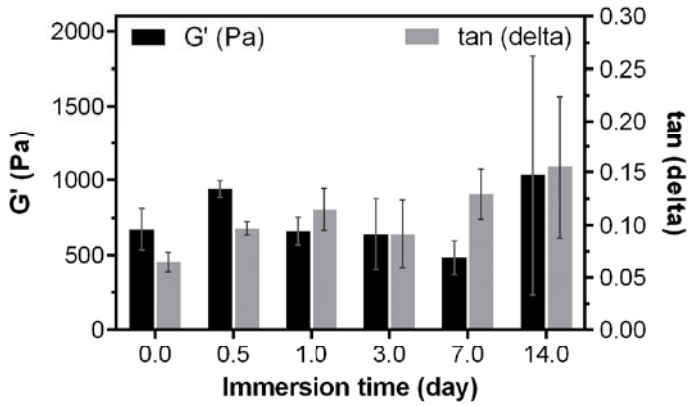

Figure S14. Storage modulus (G') and tan (delta) of the hydrogels as function of immersion time in SBF. The hydrogels contained 20 mg/mL of HYBP and 60 mg/mL of the bioactive glass particles.

3. Supporting references

[1] D.A. Ossipov, S. Piskounova, O.P. Varghese, J. Hilborn, Functionalization of Hyaluronic Acid with Chemoselective Groups via a Disulfide-Based Protection Strategy for In Situ Formation of Mechanically Stable Hydrogels, Biomacromolecules 11 (2010) 2247-2254.

[2] M.R. Nejadnik, X. Yang, M. Bongio, H.S. Alghamdi, J.J.J.P. van den Beucken, M.C. Huysmans, J.A. Jansen, J. Hilborn, D. Ossipov, S.C.G. Leeuwenburgh, Self-healing hybrid nanocomposites consisting of bisphosphonated hyaluronan and calcium phosphate nanoparticles, Biomaterials 35 (2014) 6918-6929.

[3] A.L.B. Maçon, T.B. Kim, E.M. Valliant, K. Goetschius, R.K. Brow, D.E. Day, A. Hoppe, A.R. Boccaccini, I.Y. Kim, C. Ohtsuki, T. Kokubo, A. Osaka, M. Vallet-Regí, D. Arcos, L. Fraile, A.J. Salinas, A.V. Teixeira, Y. Vueva, R.M. Almeida, M. Miola, C. Vitale-Brovarone, E. Verné, W. Höland, J.R. Jones, A unified in vitro evaluation for apatite-forming ability of bioactive glasses and their variants, Journal of Materials Science: Materials in Medicine 26 (2015) 1-10.

[4] W. Stöber, A. Fink, E. Bohn, Controlled growth of monodisperse silica spheres in the micron size range, Journal of Colloid and Interface Science 26 (1968) 62-69.

Chapter 5

Hybrid alendronate-bioactive glass particles for treatment of osteoporotic bone defects

This chapter is based on:

M. Diba, W.A. Camargo*, T. Zinkevich*, Y. Kabiri, A.P.M. Kentgens, A.R. Boccaccini, J.A. Jansen, J.J.J.P. van den Beucken, and S.C.G. Leeuwenburgh, (*In Preparation*).

*These authors contributed equaly to this work.

1. Introduction

Osteoporosis is the most widespread metabolic bone disease, leading to reduced bone mass and an increased risk of bone fracture [1]. Each year around 9 million new osteoporotic bone fractures occur worldwide [2], which imposes a major clinical and public health burden. Nevertheless, currently available medical treatments do not provide long-term solutions for treatment of osteoporotic bone fractures [1]. Consequently, novel biomaterials with a strong capacity to regenerate osteoporotic bone defects are urgently required.

Bisphosphonates are common drugs for treatment of osteoporotic bone. These drugs are usually applied through systemic administration, which is associated with a high risk of side effects, low bioavailability and a lack of site specificity [3]. The anti-osteoporotic action of bisphosphonates mainly involves an inhibitory effect on osteoclastic bone resorption, which is related to their strong affinity to bone tissue as well as their medicinal efficacy. Both properties vary for each type of bisphosphonate drug [4]. Previous research has demonstrated that the amino- or nitrogen-containing side group present in nitrogen-containing bisphosphonates such as alendronate (alendronic acid; ALN) enhances their anti-osteoporotic potency up to 10,000-fold as compared to non–nitrogen-containing bisphosphonates such as clodronate [5].

The bone-bonding capacity of bisphosphonates is mainly caused by the strong affinity of their phosphonate groups toward Ca ions at the bone mineral surface, i.e., hydroxyapatite (HAp) [5]. The interactions between bisphosphonates and calcium phosphate minerals (e.g. HAp) have been widely studied [6-10] and also exploited for development of calcium bisphosphonates [11] and self-healing nanocomposites [12]. Nonetheless, the interaction between bisphosphonates and other Ca-containing inorganic materials such as calcium silicates has been hardly investigated so far. Bioactive glasses (BGs) are typically amorphous calcium-containing silicates that are used in various tissue regeneration and replacement strategies [13, 14]. The most frequently used type of BGs is 45S5 BG, which contains 45 wt% SiO_2, 24.5 wt% CaO, 24.5 wt% Na_2O, and 6 wt% P_2O_5 [13, 15]. 45S5 BG is osteoconductive, osteogenic, and biodegradable [16, 17], but also which are highly favorable properties for application in bone tissue regeneration. Consequently, in view of the anti-osteoporotic and osteopromotive efficacy of bisphosphonate drugs (such as

ALN) and 45S5 BG, respectively, combinations of these compounds are obvious candidates for regeneration of defects in osteoporotic bone. Nevertheless, only a few studies have investigated interactions between BGs and bisphosphonate drugs. In 2007, Srisubut et al. [18] reported that local delivery of ALN together with BG granules (Biogran®) enhanced the osteopromotive efficacy of BG granules when implanted in mandibular bone defects of healthy rats. Nevertheless, this study did not provide any details on the chemical or structural effects of ALN on BG granules. In 2010, Bui et al. [19] developed zoledronate-46S6 BG composites by adsorbing zoledronate onto BG particles. In 2011, Lee et al. [20] reported that osteoblastic differentiation of cells in the presence of a bioactive glass-ceramic was increased when a specific concentration (10^{-7} M) of ALN was added to the cell culture media. In 2013, Rosenqvist et al. [21] studied the interaction between S53P4 BG with clodronate by mixing wet powders of these substances, and reported formation of a calcium clodronate layer on the BG surface. However, the precipitated layer could not be isolated and consequently its exact composition was not determined. Other studies have used physical adsorption [22] or vacuum infiltration [23] methods to achieve local delivery of bisphosphonate drugs from BG nanoparticles or coatings, respectively. Overall, these studies suggest that strong interactions exist between bisphosphonate drugs and BGs. Nevertheless, these interactions have not been investigated in detail so far. In addition, these interactions have not yet been exploited to facilitate the preparation of hybrid bisphosphonate-bioactive glass biomaterials for treatment of osteoporotic bone defects.

Here, we report the formation of a novel class of hybrid particles based on the interaction between ALN and 45S5 BG particles. By immersing the BG particles in ALN solutions at different pH and BG/ALN molar ratios, we form hybrid ALN-BG particles of tunable morphology, composition and chemical structure through a precipitation process. By monitoring the formation of these particles as a function of immersion time using inductively coupled plasma-optical emission spectroscopy and solid-state nuclear magnetic resonance spectroscopy, we obtain in-depth information on this precipitation reaction as well as the interactions between BG and ALN. We then demonstrate that these hybrid particles facilitate differential release of ALN as well as various bioinorganic elements (Ca, Na, Si, and P), and stimulate regeneration of osteoporotic bone *in vivo*. Finally, we conclude that these

novel hybrid particles have potential for the further development of effective bone substitute materials for the treatment of bone defects in osteoporotic patients.

2. Materials and methods

2.1. Materials

BG particles of 45S5 composition with a mean particle size of 2.0±1.2 µm were obtained from Schott AG (Mainz, Germany). Alendronic acid (4-Amino-1-hydroxybutane-1,1-diphosphonic acid) powder was purchased from AK Scientific (Union City, CA, USA). 4-(2-Hydroxyethyl)piperazine-1-ethanesulfonic acid (HEPES; ≥99.5%) and 2-(N-Morpholino)ethanesulfonic acid hydrate (MES hydrate; ≥99.5%)) were obtained from Sigma-Aldrich. Sodium hyaluronate powder (1.01MDa-1.8MDa) was purchased from Lifecore Biomedical (Chaska, MN, USA)99.5%). All other chemicals were reagent grade and used without any purification.

2.2. Immersion procedure

Bisphosphonate solutions were prepared by dissolving 100 mM of ALN powder in MilliQ water and adjusting their pH using NaOH solutions. BG particles were immersed in bisphosphonate solutions (pH 5, 7 or 9) at concentrations of 11.5, 23, and 46 mg/mL corresponding to Ca_{BG}/ALN molar ratios of 0.5, 1, and 2, where Ca_{BG} and ALN correspond to Ca content of BG particles and ALN molecules in solution, respectively. The mixtures were kept at 37 ºC for up to three days. After immersion, the mixtures were centrifuged at 5000 rpm for 5 min. The supernatants were collected for further analysis and the solid sediments were rinsed with MilliQ water through a redispersion and centrifugation (5000 rpm for 5 min) step. Thereafter, the sediments were dried at 65 ºC for 2 h, after which they were kept at room temperature for further analysis.

2.3. Electron microscopy

A Field Emission Scanning Electron Microscope (FE-SEM; Sigma 300, Zeiss, Germany) equipped with an energy-dispersive X-ray detector (EDX; XFlash detector 610M, Brucker Nano GmbH, Germany) was used for morphological evaluation of particles and EDX mapping of Si. For these experiments, sample preparation was carried out by dispersing the particles on a sticky carbon tape and sputter-coating with a conductive chromium layer with a thickness of ~ 5 nm.

A Transmission Electron Microscope (TEM; Titan cubed 60-300) equipped with an EDX detector was used for scanning transmission electron microscopy (STEM) and EDX mapping of single particles at 300 kV. For these experiments, sample preparation was carried out by dispersing 0.02 g of the particles in 2 mL of ethanol using a sonication bath (5 min). Thereafter, 4 µL of the dispersion was drop-casted onto a glow-discharged standard perforated carbon TEM grid (Quantifoil® 200 mesh) and incubated for 1 minute. Finally, the TEM grid was rinsed with MilliQ water, dried and used for the imaging experiments.

2.4. Elemental analysis

The ALN content of the precipitated particles was determined by measuring their nitrogen content using a CN Elemental Analyzer (NA1500, Carlo Erba - Thermo Fisher Scientific, USA). Calcium (Ca), sodium (Na), phosphorus (P) and silicon (Si) contents of the precipitated particles were determined by elemental analysis of the supernatants using Inductively Coupled Plasma-Optical Emission Spectrometry (ICP-OES, iCAP 6300, Thermo Fisher Scientific, USA). To this end, the total elemental composition of the mixture (solution+BG particles) was calculated first based on the composition of the ALN solutions and the total amount of BG particles added to each solution. Accordingly, the composition of precipitated particles was calculated by deducting the mass of each element in the supernatant from the total mass of that element present in the mixture. To determine the mass of P in hybrid particles derived from their BG constituent, the mass of P derived from their ALN content (measured using the CN Elemental Analyzer) was subtracted from the total mass of P present in the particles. Subsequently, the percentage of each element in the hybrid particles was measured relative to the total mass of dry precipitates, and multiplied by 100%.

Sample preparation for the ICP-OES measurements was carried out by diluting all immersion solutions using 2 v/v% nitric acid solutions (both before and after precipitation of the particles). A similar ICP-OES method was used to determine the composition of supernatants at different stages of the immersion process.

2.5. Powder X-ray Diffraction (XRD)

Powder XRD analysis of precipitated particles was carried out using a PANalytical X'Pert^3 Powder X-ray diffractometer with Cu Kα radiation at a voltage of 45kV and a current of 40mA. The measurements were performed from 7° to 47° (2θ) using a

step size of 0.05° and a counting time of 30s per step.

2.6. Solid-State Nuclear Magnetic Resonance (NMR) Spectroscopy

Phosphorous spectra were measured using a Varian NMR spectrometer operating at a proton frequency of 300 MHz. Measurements were performed at a Magic angle spinning (MAS) frequency of 10 kHz, which did not produce spinning sidebands in the region of real NMR-signals. Cross-polarization (CP) measurements were performed for qualitative evaluation of different samples to save experimental time. In these experiments, a proton hard pulse of 100 kHz was applied, which last for 2.5 µs. The resulting phosphorous signal was measured at 75 kHz of ^{1}H decoupling, using a CP-time of 1.75 ms. Direct-polarization (DP) measurements were conducted for a quantitative analysis of phosphonate and phosphate fractions in the various samples. ^{31}P chemical shifts were calculated relative to the known ALN spectrum [24].

Carbon spectra were measured using a Varian NMR spectrometer at a proton frequency of 400 MHz. Measurements were performed at a MAS frequency of 15 kHz. A CP pulse sequence was used with a proton pulse of 91 kHz, which last for 2.75 µs. 75 kHz decoupling power was used to break dipole-dipole interactions between carbons and protons. CP-time was optimized to 2 ms. ^{13}C chemical shifts were referenced to the known chemical shifts of adamantane.

Sodium spectra were recorded by means of a 850 MHz proton frequency Varian NMR spectrometer at a MAS frequency of 35 kHz. The measurements were performed using a 30° pulse, and ^{23}Na signal was obtained by means of a single pulse excitation scheme. The radiofrequency field strength was calibrated by means of the solid-state ^{23}Na resonance of NaCl.

Proton spectra were acquired by means of a 850 MHz Varian NMR spectrometer at a MAS frequency of 35 kHz. The pulse sequence represented a 90° hard pulse (strength of 100 kHz) to excite a single-quantum coherence. Signal acquisition was performed for 50 ms. These measurements were performed at high spinning frequencies and high magnetic field to break homonuclear proton-proton coupling and enhance the spectral resolution.

2.7. Degradation and release behavior of hybrid particles

Degradation of hybrid particles and release of their content were evaluated upon immersion in aqueous solutions for up to 14 days. To investigate the effect of pH

on the degradation of the particles, the immersion process was carried out at pH 7.4 or 5.5 using HEPES- or MES-buffers, respectively. The natural and acidic pH conditions were selected to mimic the local pH of healthy and inflamed tissues, respectively. These buffer solutions were prepared by dissolving 100 mM of HEPES or MES powder in MilliQ water and adjusting the pH using NaOH solutions. Thereafter, 20 mg of hybrid particles were added into 2 mL Eppendorf tubes. The tubes were filled with 2 mL of buffered solutions and incubated at 37 °C on a rotating plate with a rotation rate of 120 rpm. At each time point, the tubes were centrifuged at 12000 rpm for 2 min. Afterwards, the solutions were collected for further analysis, fresh solutions were added into the tubes, and the tubes were put back in the incubator until the next release time point. After the last time point (day 14), the remaining particles were dried at 65 ºC for 2 h and their weight was measured using an analytical balance. The elemental composition of the collected solutions was analyzed by means of ICP-OES. The cumulative release of each element (Ca, Na, P and Si) was expressed relative to its original content in the hybrid powder. The expressed values for P include P derived from both ALN and BG constituents.

2.8. *In vivo* performance of hybrid particles

To assess the *in vivo* performance of hybrid particles, HP1-7 and HP2-7 hybrid particles were selected. In these experiments, pure BG particles were used as positive control.

2.8.1. Sample preparation

Particles were sterilized at 121 ºC for 15 min using a Tuttnauer 2840EL benchtop autoclave. For the ease of handling and to minimize potential leakage of the particles from the bone defects upon implantation, injectable cohesive pastes were prepared by mixing the particles with an aqueous solution of sodium hyaluronate (26 mg/mL). All pastes had a particle content of 75 w/v%. Prior to implantation, the pastes were transferred to 1 mL sterile syringes and kept at 4 ºC overnight.

2.8.2. Surgical procedure

A total number of 12 male Wistar rats (12-weeks old, weight of ~250 g) was used for the *in vivo* study. The study protocol was reviewed and approved by the Experimental Animal Committee of the Radboud University (RU-DEC 2015-

0036-004) and national guidelines regarding care and use of laboratory animals were obeyed. First, the rats were acclimatized for 10 days and randomly housed in pairs using standard macrolon type III cages with sawdust as bedding material. The animals were fed with standard rodent chow and bottled tap water ad libitum. The housing room was kept under standard laboratory conditions (light-dark cycle: 12:12 h, temperature: 20-22°C, relative humidity: 45-55%). After acclimatization, the animals underwent orchidectomy (ORX) surgery to induce an osteoporotic bone condition, as described previously [25], and had free access to water and low calcium pelleted chow (0.01% Ca and 0.77% P; ssniff Spezialdiäten GmbH, Soest, Germany). After 6 weeks, osteoporotic conditions in the femoral condyle trabecular bone of the animals were confirmed using an *in vivo* micro-CT imaging system (Inveon; Siemens Medical Solutions, Knoxville, TN) [25]. Thereafter, bilateral frontal femoral condyle bone defects were made (n=8 per experimental group) and the particles pastes were injected in the left or right femur of each animal under inhalation anesthesia (2% Isoflurane® by volume) in a randomized manner (Table S1). To perform the surgery, the rats were immobilized supine with the knee joint in a maximally flexed position and the hind limbs were shaved, washed and disinfected with povidone iodine (10%). After exposure of the knee joint, a 1 mm pilot hole was drilled and the defect was gradually widened using various drills of increasing size by means of a surgical motor (Elcomed 100, W&H Dentalwerk Burmoos, Austria) at low rotational drilling speed (800 rpm) and continuous external cooling with saline solution, until a cylindrical defect of 2.5 mm in diameter and 5 mm in depth was created. The surgery was carried out in both legs of the animals and one defect was created in each femoral condyle. Thereafter, the pastes were injected into the defects using 1 mL disposable syringes and the wounds were closed with metallic wound clips (Becton Dickinson, Franklin Lakes, NJ). For pain control, Temgesic® (0.02 mg/kg) and Rimadyl® (5.0 mg/kg) were used for 2 days postoperatively. During the implantation period, the rats were fed with the low calcium diet.

2.8.3. Explantation and histological processing

Animals were euthanized by CO_2 suffocation after 8 weeks, after which the femoral condyles were carefully removed, cleaned from adhering tissues, and then immediately fixed in neutral buffered formaldehyde for 2 days. Thereafter, the samples were placed in 70% ethanol solutions, dehydrated in graded series

of ethanol solutions (70% to 100%) and embedded in poly(methylmethacrylate) (pMMA). After the PMMA embedding procedure, non-decalcified ~10 µm-thick sections were made cross-sectional perpendicular on the longitudinal axis of the implanted material (≥ 3 sections per specimen) using a modified sawing microtome method [26] and stained with methylene blue and basic fuchsin.

2.8.4. Histomorphometrical analysis

Histomorphometrical analysis of stained sections was performed using ImageJ software, based on the combination of tissue morphology and histological staining. The bone area (%) inside the original bone defects (a circle of 2500 µm) was quantified in each image. The measurements were performed on three histological sections per femoral condyle.

2.9. Statistics

The statistical analyses were performed with GraphPad Prism® software using a one-way ANOVA test, followed by Tukey's multiple comparisons test. In all tests, $P<0.05$ was considered statistically significant.

3. Results and discussion

Figure 1 illustrates the chemical structures of BG particles and ALN molecules. To assess interactions between these two compounds, we first immersed the BG particles in neutral aqueous solutions with or without 100 mM of dissolved ALN. Upon immersion of BG particles in ALN-free solutions, the particles sedimented and no visual changes were observed during 3 days of incubation. However, BG particles quickly shrank upon immersion in ALN solutions, and precipitates were formed after 3 days of incubation. Consequently, to determine the nature of these hybrid precipitates, we immersed various amounts of BG particles in ALN solutions at different pH values, and studied the properties of resulting precipitates using SEM, TEM, EDX, XRD, solid-state NMR and elemental analysis techniques

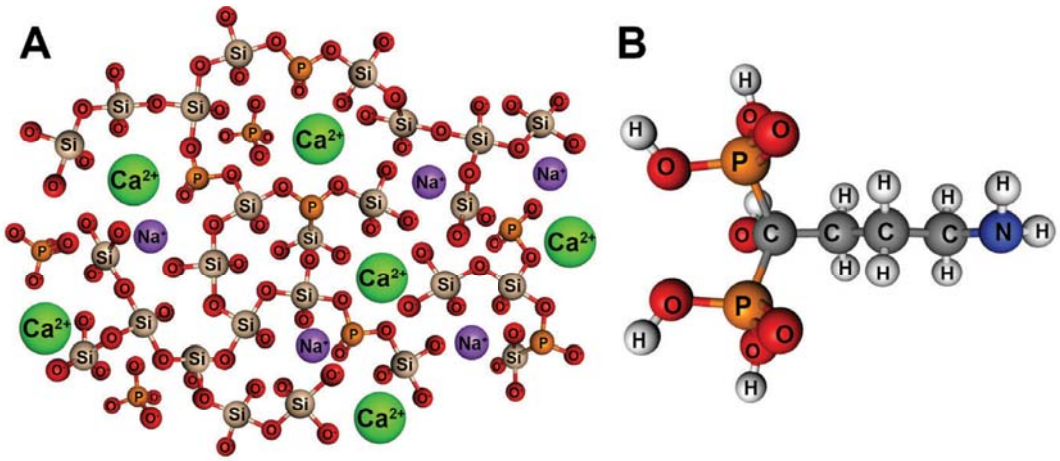

Figure 1. Schematic illustrations of the chemical structures of A) bioactive glass particles and B) alendronic acid molecules.

3.1. Morphology, composition and structure

Figure 2 shows SEM images of hybrid particles formed after immersion of BG particles in ALN solutions. The morphology of the precipitated particles varied depending on the respective Ca_{BG}/ALN ratio (R). While spherical particles were formed at a Ca_{BG}/ALN ratio of 0.5 (Figure 2A+D), discrete needle-like microparticles were formed at ratios of 1 and 2 (Figure 2BCEF). Importantly, samples prepared at a ratio of 2 contained unreacted BG residues as confirmed by EDX mapping (Figure S1). The size and morphology of precipitated particles were also affected by the initial pH of the ALN solution. At a fixed Ca_{BG}/ALN ratio of 0.5, the precipitated clusters exhibited spherulitic structures composed of nanosheets or honeycomb-like morphologies composed of entangled nanofibers (Figure 3) when prepared at pH 7 or 9, respectively. In general, at a basic pH of 9, smaller particles were formed than at a neutral pH of 7. For example, at a Ca_{BG}/ALN ratio of 1, the length of needle-like microparticles was around 9±5 µm or 4±3 µm when prepared at pH 7 or 9, respectively. Nevertheless, the shape of the resulting particles did not depend on the pH at Ca_{BG}/ALN ratios of 1 and 2. This polymorphism resembled the morphological variability as observed in natural structures (e.g. diatoms) where self-assembly occurs between inorganic ions and organic molecules [27]. Indeed, similar processes have also been studied to enable rational design of precipitating microstructures such as carbonate-silica co-precipitates by controlling reaction conditions such as ionic concentration and solution pH [28, 29]. When ALN solutions were acidic (pH 5), the precipitation of hybrid particles was inhibited due to the protonation of

bisphosphonate groups at acidic conditions, reducing their binding affinity for BG surfaces.

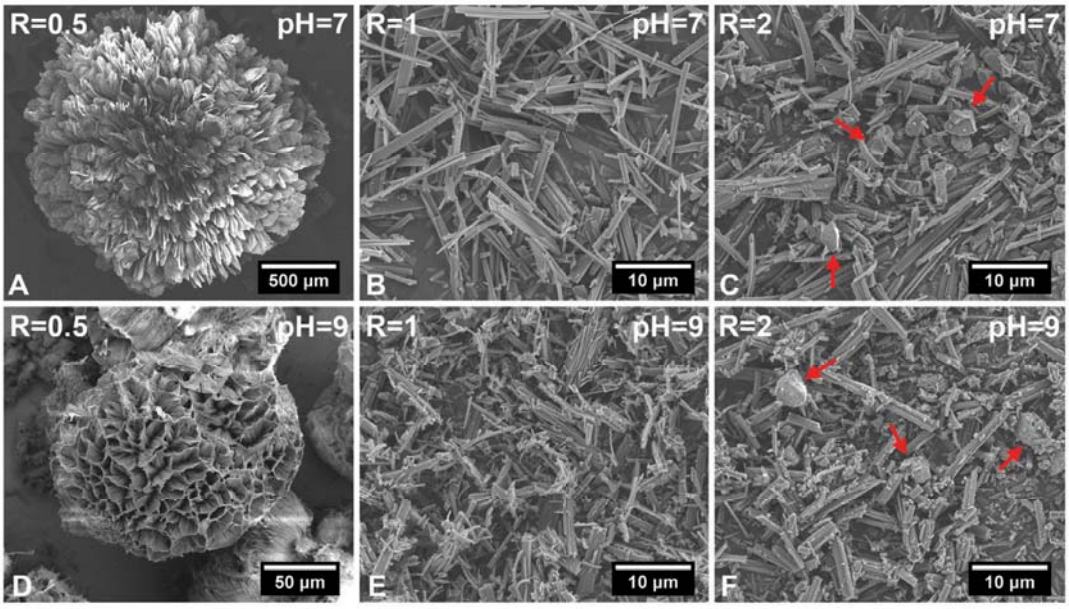

Figure 2. Scanning clcctron micrographs of hybrid ALN-BG particlcs prccipitatcd at different Ca_{BG}/ALN ratios (R) and pH values after 3 days of incubation at 37 ºC. Red arrows indicate bioactive glass residues.

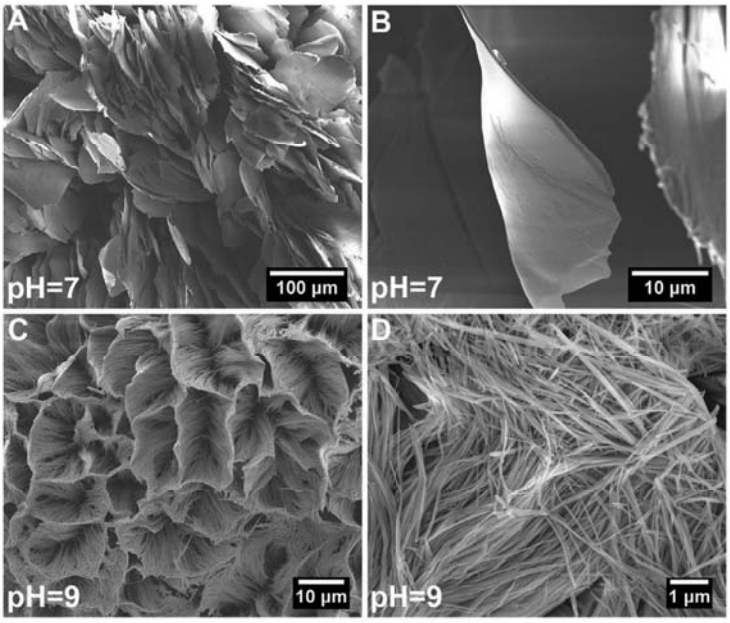

Figure 3. High magnification scanning electron micrographs of hybrid ALN-BG particles precipitated at a Ca_{BG}/ALN ratio of 0.5 and a pH of 7 (A, B) or 9 (C, D).

Table 1 shows the chemical composition of precipitated hybrid particles. Hybrid particles formed at Ca_{BG}/ALN ratios of 0.5 and 1 both contained ~55-70 wt% of ALN.

At a Ca_{BG}/ALN ratio of 2, the ALN content of particles decreased significantly. At this ratio, the particles also contained higher amounts of Si and P (unrelated to ALN; see Materials and Methods) which was attributed most likely to BG residues. Due to the compositional similarity of samples prepared at pH 7 or 9, further investigations were focused on hybrid particles formed using ALN solutions at an initial pH of 7.

Table 1. Chemical composition of hybrid ALN-BG particles precipitated at different conditions after 3 days of incubation at 37 ºC.

Sample abbreviation	Immersion conditions		Final composition (wt%)				
	Ca_{BG}/ALN ratio	pH	ALN	Ca	Na	Si	P*
HP0.5-7	0.5	7	69.3±0.5	11.5±0.0	11.9±0.0	<2	<1
HP1-7	1	7	62.3±0.6	11.4±0.0	12.8±0.0	<2	<1
HP2-7	2	7	25.5±9.8	16.7±0.3	34.7±0.0	7.3±0.3	9.9±0.2
HP0.5-9	0.5	9	68.6±0.2	10.5±0.0	10.7±0.0	<2	<1
HP1-9	1	9	55.6±2.5	10.1±0.3	10.8±0.0	<2	<1
HP2-9	2	9	25.6±4.4	11.3±0.4	20.5±0.0	5.8±0.3	4.3±0.2

EDX elemental mapping combined with STEM imaging of single hybrid particles revealed a uniform distribution of elements throughout each particle (Figure 4A). Figure 4B shows powder XRD spectra of various particle types. ALN powder was highly crystalline, whereas the BG particles were fully amorphous. Interestingly, the hybrid particles exhibited crystalline structures that depended on the Ca_{BG}/ALN ratio used in the incubation step. The particles precipitated using a ratio of 2 exhibited a less crystalline structure as compared to particles containing lower amounts of BG (prepared at ratios of 0.5 and 1). Nevertheless, XRD peaks could not be identified using available crystallographic databases and literature, indicating the formation of novel crystalline phases that were not reported before to the best of our knowledge. Similar to novel metal-organic frameworks [30], structural determination of these hybrid particles was challenging. Our attempts to use single-crystal XRD and electron diffraction techniques were not successful due to the small size and electron-beam sensitivity of the hybrid particles, respectively.

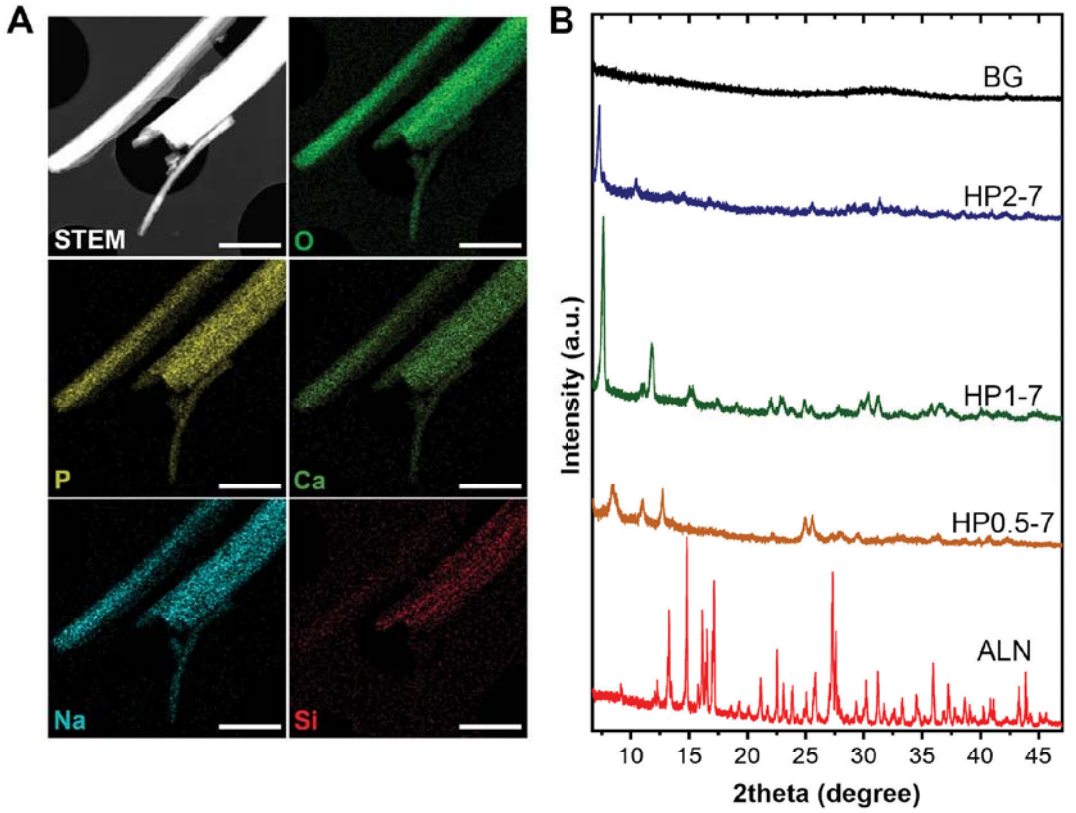

Figure 4. A) STEM image and EDX elemental maps of single HP1-7 particles. B) Powder XRD spectra of different particle types. Scale bars in images correspond to 1 μm.

Therefore, we used solid-state NMR spectroscopy to gain a deeper insight into the chemical structure of these hybrid particles. Figure 5 shows solid-state NMR spectra of different types of particles. As shown in Figure 5A, the ^{13}C spectra of hybrid particles showed pronounced peak broadening and shifts as compared to the peaks of pure ALN, indicating that hybrid particles are less crystalline and contain coordination complexes, respectively [24, 31-33]. The ^{13}C spectrum of HP0.5-7 consisted of four broad signals. In this sample, the largest peak shift ($\Delta\delta$=4.6 ppm) occurred for the peak at ~72 ppm corresponding to the carbon closest to the phosphonate groups of ALN (see Figure S2 for the peak assignment). The two peaks at ~40 and ~32 ppm corresponded to the CH_2 groups and shifted with 3.2 ppm, suggesting a large conformational change for ALN molecules [33]. The smallest shift was observed for the peak located at ~24 ppm ($\Delta\delta$=0.9 ppm), indicating that the amine-linked CH_2 group was affected least. Interestingly, by increasing the Ca_{BG}/ALN ratio, the ^{13}C spectra became narrower and revealed different features. Particularly, for HP1-7 and HP2-7, the amine-linked CH_2 signal showed a larger

shift ($\Delta\delta \approx 4$ ppm) as compared to HP0.5-7, indicating that the amine group also participated in the complex formation when higher Ca_{BG}/ALN ratios were used.

In general, the ^{31}P spectra (Figure 5B) displayed similar trends as the ^{13}C spectra. The spectrum of HP0.5-7 showed a broad featureless peak positioned at 20 ppm, corresponding to the presence of heterogeneous microenvironments around the phosphonate groups at this composition. The ^{31}P spectrum of HP1-7 exhibited a more narrow peak shifted upfield for 17.8 ppm, corresponding to a more homogeneous microenvironment surrounding the ALN molecules. Moreover, the ^{31}P of HP2-7 displayed two intense narrow signals, which suggest the presence of well-ordered domains at this composition. These sharp peaks resembled the sharp peaks present in the ^{31}P spectrum of pure ALN, but displayed a shift which might be caused by complexation with Ca^{2+} [31, 34]. Importantly, this spectrum also revealed the existence of a signal from residual BG, which is in agreement with our previous SEM observations. Nevertheless, this peak showed a slight upfield shift which indicates that the microenvironment surrounding BG residues in the HP2-7 sample was different from the one in pure BG sample (Figure S3). Integration of phosphonate (10 to 27 ppm) and phosphate (-2 to 9 ppm) regions of ^{31}P DP spectra of HP2-7 indicated that ~96% of all phosphorous in this sample was derived from ALN molecules, while the remaining phosphorus (4%) was attributed to BG residues. We also observed a similarity between ^{23}Na spectra of the HP2-7 and pure ALN particles (Figure 5C). However, the HP2-7 particles contained a larger variety of Na microenvironments as compared to our pure ALN. Figure 5D presents the ^{1}H spectra of pure ALN and hybrid particles. The most important feature observed for all hybrid particles was the absence of low field signals ($\delta_H > 10$ ppm) that were present for pure ALN. These signals correspond to the phosphonate groups of ALN and their absence indicates deprotonation of these groups and therefore a high degree of coordination complex formation [31, 35].

Overall, the presented results indicate: (i) formation of ALN-cation coordination complexes within the hybrid particles and (ii) a strong dependence of the chemical structure of the hybrid particles on the preparation conditions. Particularly, XRD analyses show that the hybrid particles become less crystalline when a high amount of BG particles (Ca_{BG}/ALN ratio=2) is used during preparation.

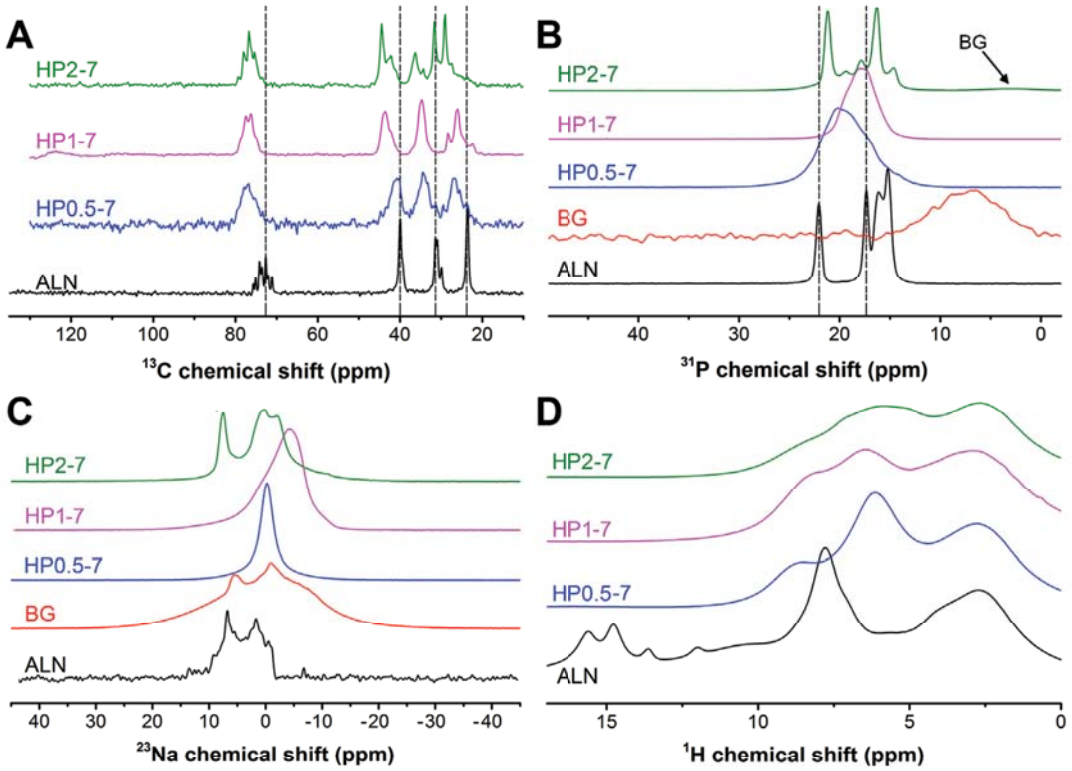

Figure 5. Solid-state CP-MAS NMR spectra of different types of particles.

3.2. Precipitation kinetics

To study the precipitation mechanism of hybrid particles and the interaction between BG and ALN, we selected HP1-7 particles and studied their formation at different time points during the immersion process by means of pH and elemental analyses of the supernatants and the evaluation of particles using mass measurements, SEM imaging and NMR spectroscopy (Figure 6). As shown in Figures 6A, BG particles rapidly dissolved immediately after their immersion in the ALN solution; within the first minute of immersion, ~20 wt% of BG particles dissolved causing a pH rise from 7 to 10. Until 200 min of immersion, the dissolution of BG particles resulted in a continuous release of Ca, Na and Si into the supernatant, while the P content of the supernatant remained almost constant (Figure 6B). After 200 min of the immersion, a sharp drop of Ca, Na and P contents of the supernatant occurred which coincided with a remarkable mass gain of the particles (Figure 6A), corresponding to the formation of precipitates containing these three specific elements. Nevertheless, the Si concentration in the supernatant continued to rise until almost the entire silica content of the original BG particles was released into the supernatant after 1000 min of immersion, revealing that the released Si ions did not play a dominant role

in the formation of the precipitates. On the contrary, only around half of the Ca content of the original BG particles was released into the supernatant after 200 min of immersion, confirming that Ca is actively involved in the precipitation process. Importantly, the solid mass as well as the pH and ionic concentrations of the supernatant stabilized after 1000 min, indicating that the reaction reached an equilibrium state. These results were in agreement with the SEM images of the particles (Figure 6C), which revealed the presence of needle-like microparticles at 200 min and the formation of precipitates with identical morphology to the final HP1-7 particles (Figure 2B) after 1000 min of immersion.

Next, we studied ^{31}P and ^{23}Na NMR spectra of precipitated particles as a function of immersion time. As shown in Figure 6D, both phosphate and phosphonate fractions were already identified from an early stage of the immersion process (5 min). Over time, the phosphonate fraction increased while the phosphate fraction gradually declined until its complete disappearance after 200 min (Figure 6E). These results suggest that the formation of precipitates was driven by substitution of phosphate groups of BG particles by phosphonate groups of ALN molecules, which is similar to previously reported mechanisms on the interaction of bisphosphonate drugs with calcium phosphate minerals [10, 33]. Considering the constant concentration of P in the supernatant for the first 200 min (Figure 6B), we propose that this reaction occurs by release of ~2 phosphate groups per ALN substitution. The substitution reaction proceeded without affecting the microenvironment of remaining phosphates in BG particles, since the phosphate peak did not shift largely from its initial position until its disappearance (intensity<4%) from the spectrum at 200 min (Table S2). Importantly, the phosphonate peak showed a significant change from 100 to 200 min, which resulted in an abrupt shift and narrowing of the signal. At this time point, similar changes were observed in the ^{23}Na spectrum of the particles (Figure 6F).

Overall, these results suggest that the precipitation of HP1-7 particles proceeded through complexation of ALN with Ca/Na cations as present in BG particles. This complexation process occurred by means of substitution of phosphate groups in BG particles by ALN molecules, leading to disruption of the BG silicate network and release of Si, Ca and Na. The reaction between ALN and BG almost completely disrupted the BG structure around 200 min after the immersion. This disruption was

followed by a rapid precipitation and growth of hybrid ALN-BG particles, which stopped after 1000 min of the immersion.

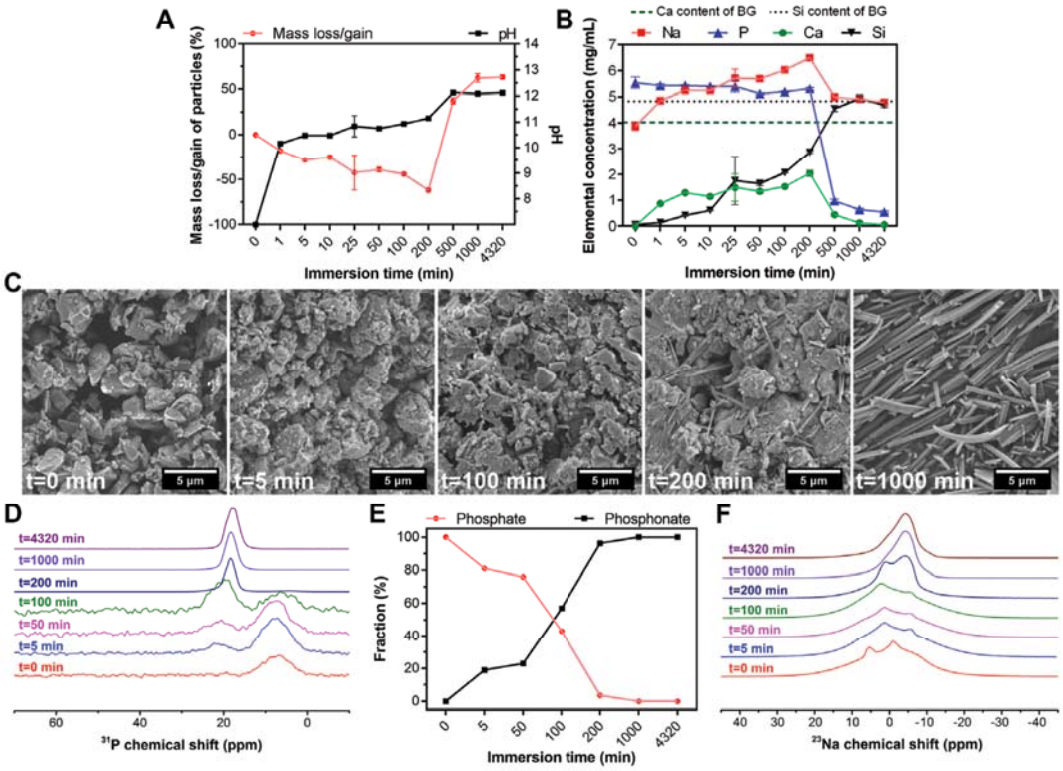

Figure 6. Precipitation of HP1-7 particles as a function of immersion time. A) Mass loss/gain of particles and pH of supernatants. B) Elemental composition of supernatants during the immersion period. C) Scanning electron micrographs, D) solid-state DP ^{31}P NMR spectra, E) phosphate and phosphonate weight fractions, and F) solid-state CP-MAS ^{23}Na NMR spectra of particles at various time points. In A) and B), values are presented as average ± standard deviation for n=3 per experimental condition. In E), values represent the fractions calculated based on the NMR spectra shown in D).

3.5. Degradation and release behavior

To study the applicability of the hybrid particles for regenerative medicine, we studied their *in vitro* degradation and release behavior at two different pH values. In addition to neutral pH (7.4), these experiments were carried out at an acidic pH of 5.5 in order to mimic acidosis [36]. These acidic testing conditions were also selected since the interaction of ALN with BG was shown to depend on the pH (see section 3.1).

Figure 7 shows the weight loss of hybrid particles after 14 days of immersion in buffered solutions, revealing that all types of hybrid particles were degradable. While the weight loss of HP0.5-7 and HP1-7 particles was similar (~30%), HP2-7 particles

were degraded for ~45% after 14 days of immersion in neutral pH. Degradation of HP0.5-7 and HP1-7 particles did not depend on the pH of the immersion medium, whereas the degradation of HP2-7 particles was significantly enhanced to ~70% at acidic pH. As described previously, the bisphosphonate groups of ALN molecules were deprotonated and involved in complexation with BG-derived cations. Nevertheless, upon immersion of hybrid particles in acidic solutions, their bisphosphonate groups become protonated which might compromise their complexation with BG-derived cations. In combination with the lower crystallinity of HP2-7 particles, this phenomenon can explain the enhanced degradation of these particles upon the acidification.

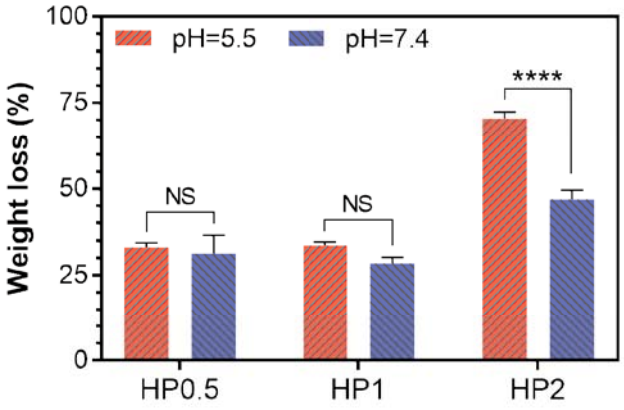

Figure 7. Weight loss (%) of hybrid ALN-BG particles after 14 days of immersion in solutions with acidic or neutral pH. NS and **** indicate no statistical difference and statistical difference with $P<0.0001$, respectively. All values are presented as average ± standard deviation for n=3 per experimental condition.

Figure 8 demonstrates the cumulative release (expressed relative to the original content) of various inorganic elements from hybrid particles upon their immersion in solutions with acidic (5.5) or neutral (7.4) pH conditions. In general, HP2-7 particles released more calcium than HP0.5-7 and HP2-7 particles, but retained their sodium content, whereas HP0.5-7 and HP2-7 showed an opposite trend by releasing less calcium but more sodium than HP2-7. At neutral pH, P release from all particle types was similar. The released P from the particles can originate from both ALN and BG. Nevertheless, based on the composition of hybrid particles (Table 1), the P released from HP0.5-7 and HP1-7 corresponds almost entirely to ALN, whereas P release from HP2-7 particles is related to a more even mixture of constituents. Despite the low Si content of HP0.5-7 and HP1-7 particles (Table 1), their Si release

was more pronounced than Si release from HP2-7 particles, suggesting that the minor trace of Si was not well integrated in the structure of HP0.5-7 and HP1-7.
As expected, acidification of solutions affected the release behavior of the hybrid particles. An enhancement of Ca release was observed for all particle types upon acidification. Na release from HP0.5-7 and HP1-7 particles was also increased at acid pH, but Na release from HP2-7 was hardly affected by the acidification, suggesting that Na played a more dominant role in complex formation in HP0.5-7 and HP1-7 than in HP2-7 particles. A strong enhancement of P release upon acidification was only observed for HP2-7 particles, which is in agreement with the degradation results discussed previously.

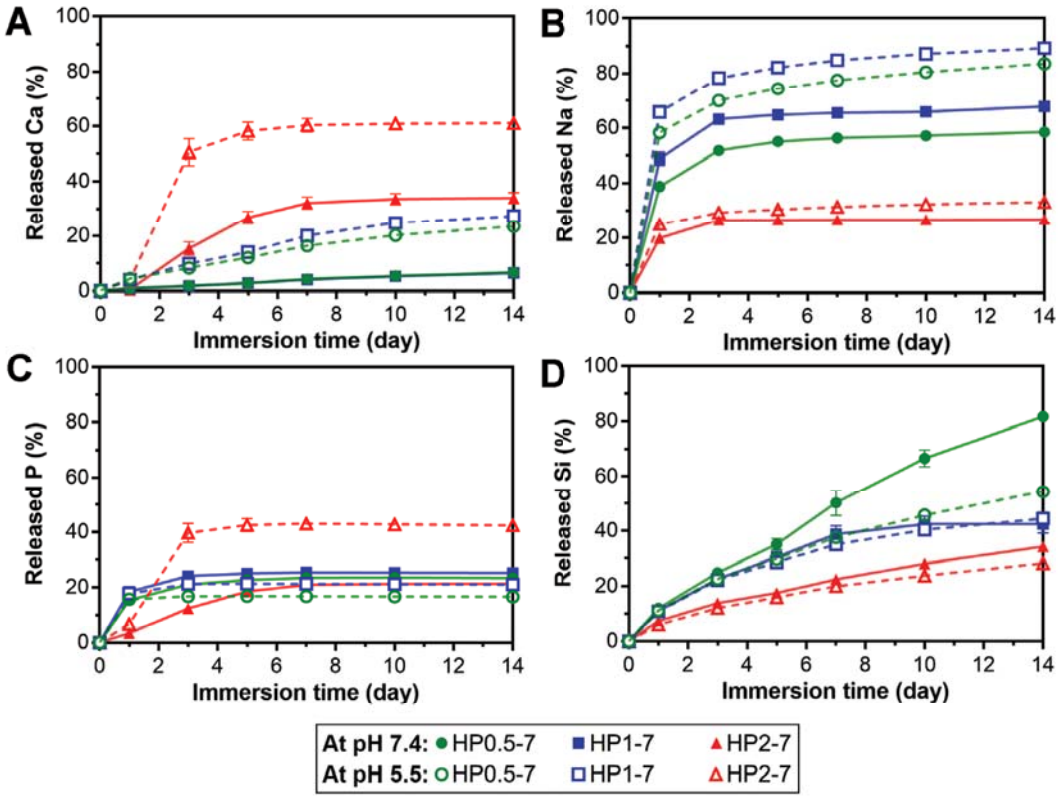

Figure 8. Cumulative release profiles of different elements from hybrid ALN-BG particles into buffered solutions at acidic (open symbols) or neutral pH (closed symbols). The release of each element was expressed relative to its original content in the hybrid powder. All values are presented as average ± standard deviation for n=3 per experimental condition.

Overall, these results indicate that the hybrid ALN-BG particles are degradable, which facilitates their application in bone tissue regeneration, since biomaterials should degrade to allow for replacement by newly formed bone tissue [37]. In addition, anti-osteoporotic ALN molecules and BG-derived inorganic ions were

released in a controllable manner. Inorganic ions are known to affect the regeneration of bone tissue *in vivo* [38]. For example, specific concentrations of Ca ions were shown to stimulate proliferation and differentiation of osteoblastic cells and induce mineralization of the extracellular matrix [39]. In addition, phosphate ions can promote the expression of matrix Gla protein (MGP) which is a key regulator for bone formation [40]. Furthermore, Si is an important factor for bone formation [41] which can affect the precipitation of hydroxyapatite [42]. Nevertheless, it should be stressed that the biological effects of ALN and bioinorganic ions depend on their concentration in the extracellular matrix. However, our *in vitro* results cannot be translated directly to highly perfused *in vivo* conditions, which necessitates more detailed studies on the *in vivo* release kinetics of both ALN molecules and inorganic ions.

3.6. *In vivo* performance

In view of the similarity between HP0.5-7 and HP1-7 particles, we selected HP1-7 and HP2-7 for an *in vivo* implantation study under osteoporotic conditions, while 45S5 BG particles were used as control in view of their well-known osteopromotive capacity. As shown in Figure 9A, after 8 weeks of implantation of HP1-7 particles in osteoporotic rats, abundant bone formation was observed inside the original defect area without any visible inflammatory response, similar to the control BG group (Figure 9C). However, the defects filled with HP2-7 particles showed low amounts of bone formation and contained residual material after the implantation period (Figure 9B). We postulate that these material remnants are clusters of partially degraded HP2-7 particles that are high in sodium and more stable than the original HP2-7 composition.

As shown in Figure 9D, quantification of new bone formation inside the original defects indicated that the HP1-7 particles could facilitate bone formation at level similar to 45S5 BG particles, whereas the amount of newly formed bone was much lower upon implantation of HP2-7 particles. Such remarkable difference between the *in vivo* behavior of HP1-7 and HP2-7 particles can be attributed to the differences between their composition, structure and degradation behavior. For instance, upon implantation of biomaterials, the local pH of bone tissue drops from ~ 7.4 to ~5.5 due to a physiological inflammatory response [43]. As described in Section 3.5, such local acidification leads to the release of significantly higher amounts of Ca ions

and ALN for HP2-7 particles as compared to HP1-7 particles. As shown in previous reports [39, 44, 45], such high concentrations of Ca and/or ALN might be cytotoxic for bone-forming osteoblast cells, thereby impeding *in vivo* bone regeneration. Although HP1-7 and 45S5 BG particles both stimulated the formation of bone tissue, the underlying stimulatory mechanism is different for both types of particles. For example, while 45S5 BG particles can induce bone formation owing to their apatite-forming ability and osteogenic effects caused by their ionic dissolution products [13, 38], HP1-7 particles can assist bone regeneration by inhibiting bone resorption through the release of ALN and promoting bone formation by releasing inorganic ions with osteogenic efficacy [39]. Nevertheless, a more detailed investigation is required to determine the mechanism by which HP1-7 particles are able to support bone formation.

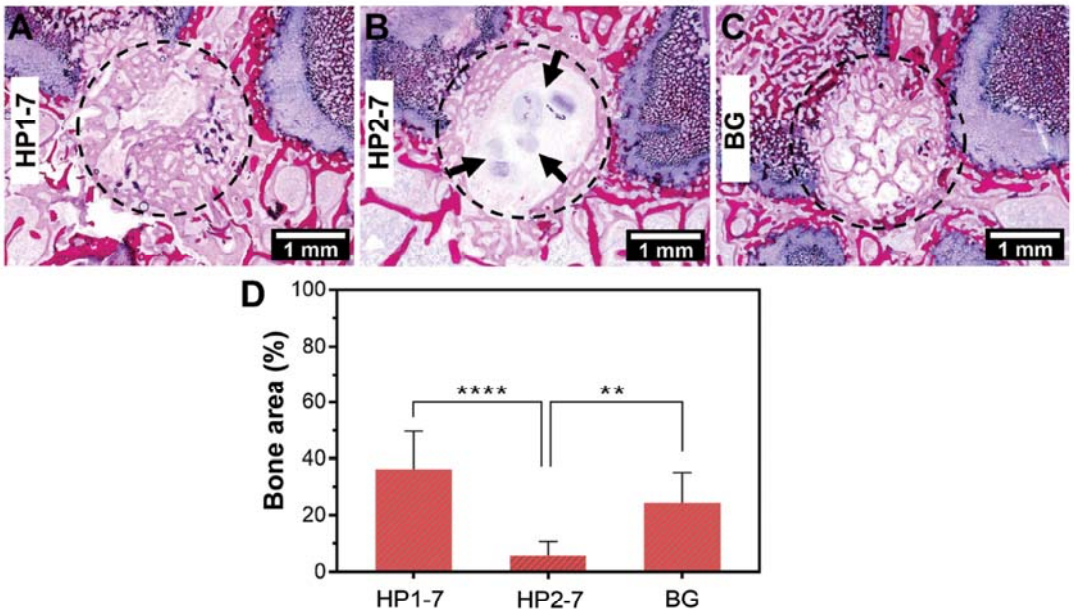

Figure 9. *In vivo* evaluation of hybrid ALN-BG particles. A, B, C) Representative histological images and D) quantified bone area (%) of different experimental groups after 8 weeks of implantation. Circles and arrows indicate the original defect area and remaining materials, respectively. ** and **** indicate $P<0.005$ and $P<0.0001$, respectively.

4. Conclusion

We have shown the facile preparation of a novel class of hybrid alendronate-bioactive glass (ALN-BG) particles. By immersing 45S5 BG particles in ALN solutions, phosphate ions of BG were substituted by ALN molecules, thereby forming ALN-cation coordination complexes. This process resulted in dissolution of BG particles and precipitation of novel hybrid ALN-BG particles. By varying the

immersion conditions (i.e., BG concentration and pH), the morphology, composition, and chemical structure of precipitated hybrid particles could be tuned. *In vitro* investigations showed that these hybrid particles were degradable, which facilitated their application in bone tissue regeneration. In addition, anti-osteoporotic ALN molecules and BG-derived inorganic ions were released in a controllable manner. *In vivo* evaluation of the hybrid particles revealed their strong capacity to facilitate regeneration of bone defects in an osteoporotic rat model. Consequently, this novel class of hybrid particles is appealing for the further development of effective bone substitute materials for bone defect regeneration in osteoporotic patients. Moreover, the presented approach using 45S5 BG can be applicable to other BG compositions, especially those containing strontium ions which can assist regeneration of osteoporotic bone defects.

References

[1] A. Klibanski, L. Adams-Campbell, T. Bassford, S.N. Blair, S.D. Boden, K. Dickersin, D.R. Gifford, L. Glasse, S.R. Goldring, K. Hruska, S.R. Johnson, L.K. McCauley, W.E. Russell, N.I.H.C.D.P. Osteopor, Osteoporosis prevention, diagnosis, and therapy, Jama-Journal of the American Medical Association 285 (2001) 785-795.

[2] O. Johnell, J.A. Kanis, An estimate of the worldwide prevalence and disability associated with osteoporotic fractures, Osteoporosis International 17 (2006) 1726-1733.

[3] S.B. Woo, J.W. Hellstein, J.R. Kalmar, Systematic review: Bisphosphonates and osteonecrosis of the jaws, Annals of Internal Medicine 144 (2006) 753-761.

[4] H. Fleisch, Bisphosphonates: Mechanisms of Action, Endocrine Reviews 19 (1998) 80-100.

[5] M.T. Drake, B.L. Clarke, S. Khosla, Bisphosphonates: Mechanism of action and role in clinical practice, Mayo Clinic Proceedings 83 (2008) 1032-1045.

[6] E. Puljula, P. Turhanen, J. Vepsäläinen, M. Monteil, M. Lecouvey, J. Weisell, Structural Requirements for Bisphosphonate Binding on Hydroxyapatite: NMR Study of Bisphosphonate Partial Esters, ACS Medicinal Chemistry Letters 6 (2015) 397-401.

[7] G.H. Nancollas, R. Tang, R.J. Phipps, Z. Henneman, S. Gulde, W. Wu, A. Mangood, R.G.G. Russell, F.H. Ebetino, Novel insights into actions of bisphosphonates on bone: Differences in interactions with hydroxyapatite, Bone 38 (2006) 617-627.

[8] P. Pascaud, P. Gras, Y. Coppel, C. Rey, S. Sarda, Interaction between a Bisphosphonate, Tiludronate, and Biomimetic Nanocrystalline Apatites, Langmuir 29 (2013) 2224-2232.

[9] P. Pascaud, F. Errassifi, F. Brouillet, S. Sarda, A. Barroug, A. Legrouri, C. Rey, Adsorption on apatitic calcium phosphates for drug delivery: interaction with bisphosphonate molecules, Journal of Materials Science-Materials in Medicine 25 (2014) 2373-2381.

[10] F. Errassifi, S. Sarda, A. Barroug, A. Legrouri, H. Sfihi, C. Rey, Infrared, Raman and NMR investigations of risedronate adsorption on nanocrystalline apatites, Journal of Colloid and Interface Science 420 (2014) 101-111.

[11] E. Boanini, P. Torricelli, M. Gazzano, M. Fini, A. Bigi, Crystalline Calcium Alendronate Obtained by Octacalcium Phosphate Digestion: A New Chance for Local Treatment of Bone Loss Diseases?, Advanced Materials 25 (2013) 4605-4611.

[12] M.R. Nejadnik, X. Yang, M. Bongio, H.S. Alghamdi, J. Van den Beucken,

M.C. Huysmans, J.A. Jansen, J. Hilborn, D. Ossipov, S.C.G. Leeuwenburgh, Self-healing hybrid nanocomposites consisting of bisphosphonated hyaluronan and calcium phosphate nanoparticles, Biomaterials 35 (2014) 6918-6929.
[13] J.R. Jones, Review of bioactive glass: From Hench to hybrids, Acta Biomaterialia 9 (2013) 4457-4486.
[14] V. Miguez-Pacheco, L.L. Hench, A.R. Boccaccini, Bioactive glasses beyond bone and teeth: Emerging applications in contact with soft tissues, Acta Biomaterialia 13 (2015) 1-15.
[15] L.L. Hench, R.J. Splinter, W.C. Allen, T.K. Greenlee, Bonding mechanisms at the interface of ceramic prosthetic materials, Journal of Biomedical Materials Research 5 (1971) 117-141.
[16] A.K. Miri, N. Muja, N.O. Kamranpour, W.C. Lepry, A.R. Boccaccini, S.A. Clarke, S.N. Nazhat, Ectopic bone formation in rapidly fabricated acellular injectable dense collagen-Bioglass hybrid scaffolds via gel aspiration-ejection, Biomaterials 85 (2016) 128-141.
[17] L.L. Hench, J.M. Polak, Third-Generation Biomedical Materials, Science 295 (2002) 1014-1017.
[18] S. Srisubut, A. Teerakapong, T. Vattraphodes, S. Taweechaisupapong, Effect of local delivery of alendronate on bone formation in bioactive glass grafting in rats, Oral Surgery, Oral Medicine, Oral Pathology, Oral Radiology, and Endodontology 104 (2007) e11-e16.
[19] X.V. Bui, H. Oudadesse, Y. Le Gal, A. Mostafa, P. Pellen, G. Cathelineau, Chemical reactivity of biocomposite glass-zoledronate, Journal of the Australian Ceramic Society 46 (2010) 24-28.
[20] J.H. Lee, K.M. Lee, S.J. Jang, H.S. Lee, H.R. Baek, Effects of Bisphosphonate-Treated Bioactive Ceramic Grafts for the Proliferation and Osteoblastic Differentiation of Human Bone Marrow Mesenchymal Stem Cells, Tissue Engineering and Regenerative Medicine 8 (2011) 69-77.
[21] K. Rosenqvist, S. Airaksinen, S.J. Fraser, K.C. Gordon, A.M. Juppo, Interaction of bioactive glass with clodronate, International Journal of Pharmaceutics 452 (2013) 102-107.
[22] E. Boanini, S. Panseri, F. Arroyo, M. Montesi, K. Rubini, A. Tampieri, C. Covarrubias, A. Bigi, Alendronate Functionalized Mesoporous Bioactive Glass Nanospheres, Materials 9 (2016) 135.
[23] S. Ray, R. Acharya, S. Saha, A. Islam, S. Dey, S.K. Nandi, T.K. Mandal, G. Banerjee, J. Chakraborty, Role of a nitrogenous bisphosphonate (local delivery) incorporated vitreous coating (with/without polymer) on surgical grade SS316L implant material to improve fixation at the damaged tissue site, RSC Advances 6

(2016) 89467-89483.
[24] M.S. Ironside, M.J. Duer, D.G. Reid, S. Byard, Bisphosphonate protonation states, conformations, and dynamics on bone mineral probed by solid-state NMR without isotope enrichment, European Journal of Pharmaceutics and Biopharmaceutics 76 (2010) 120-126.
[25] H.S. Alghamdi, J.J.J.P. van den Beucken, J.A. Jansen, Osteoporotic Rat Models for Evaluation of Osseointegration of Bone Implants, Tissue Engineering Part C: Methods 20 (2013) 493-505.
[26] H.B.M. van der Lubbe, C.P.A.T. Klein, K. de Groot, A Simple Method for Preparing Thin (10 μm) Histological Sections of Undecalcified Plastic Embedded Bone with Implants, Stain Technology 63 (1988) 171-176.
[27] S. Weiner, L. Addadi, Design strategies in mineralized biological materials, Journal of Materials Chemistry 7 (1997) 689-702.
[28] W.L. Noorduin, A. Grinthal, L. Mahadevan, J. Aizenberg, Rationally Designed Complex, Hierarchical Microarchitectures, Science 340 (2013) 832-837.
[29] C.N. Kaplan, W.L. Noorduin, L. Li, R. Sadza, L. Folkertsma, J. Aizenberg, L. Mahadevan, Controlled growth and form of precipitating microsculptures, Science 355 (2017) 1395-1399.
[30] F. Gandara, T.D. Bennett, Crystallography of metal-organic frameworks, Iucrj 1 (2014) 563-570.
[31] E. Alvarez, A.G. Marquez, T. Devic, N. Steunou, C. Serre, C. Bonhomme, C. Gervais, I. Izquierdo-Barba, M. Vallet-Regi, D. Laurencin, F. Mauri, P. Horcajada, A biocompatible calcium bisphosphonate coordination polymer: towards a metal-linker synergistic therapeutic effect?, CrystEngComm 15 (2013) 9899-9905.
[32] G. Grossmann, A. Grossmann, G. Ohms, E. Breuer, R. Chen, G. Golomb, H. Cohen, G. Hägele, R. Classen, Solid-state NMR of bisphosphonates adsorbed on hydroxyapatite, Magnetic Resonance in Chemistry 38 (2000) 11-16.
[33] S. Mukherjee, Y. Song, E. Oldfield, NMR Investigations of the Static and Dynamic Structures of Bisphosphonates on Human Bone: a Molecular Model, Journal of the American Chemical Society 130 (2008) 1264-1273.
[34] M.W.G. Lockyer, D. Holland, R. Dupree, NMR investigation of the structure of some bioactive and related glasses, Journal of Non-Crystalline Solids 188 (1995) 207-219.
[35] E. Boanini, P. Torricelli, M. Gazzano, R. Giardino, A. Bigi, Alendronate–hydroxyapatite nanocomposites and their interaction with osteoclasts and osteoblast-like cells, Biomaterials 29 (2008) 790-796.
[36] T.R. Arnett, Acidosis, hypoxia and bone, Archives of Biochemistry and Biophysics 503 (2010) 103-109.

[37] K. Rezwan, Q.Z. Chen, J.J. Blaker, A.R. Boccaccini, Biodegradable and bioactive porous polymer/inorganic composite scaffolds for bone tissue engineering, Biomaterials 27 (2006) 3413-3431.
[38] A. Hoppe, N.S. Güldal, A.R. Boccaccini, A review of the biological response to ionic dissolution products from bioactive glasses and glass-ceramics, Biomaterials 32 (2011) 2757-2774.
[39] S. Maeno, Y. Niki, H. Matsumoto, H. Morioka, T. Yatabe, A. Funayama, Y. Toyama, T. Taguchi, J. Tanaka, The effect of calcium ion concentration on osteoblast viability, proliferation and differentiation in monolayer and 3D culture, Biomaterials 26 (2005) 4847-4855.
[40] M. Julien, S. Khoshniat, A. Lacreusette, M. Gatius, A. Bozec, E.F. Wagner, Y. Wittrant, M. Masson, P. Weiss, L. Beck, D. Magne, J. Guicheux, Phosphate-Dependent Regulation of MGP in Osteoblasts: Role of ERK1/2 and Fra-1, Journal of Bone and Mineral Research 24 (2009) 1856-1868.
[41] E.M. Carlisle, Silicon: A requirement in bone formation independent of vitamin D1, Calcified Tissue International 33 (1981) 27-34.
[42] J.J.M. Damen, J.M. Ten Cate, Silica-induced Precipitation of Calcium Phosphate in the Presence of Inhibitors of Hydroxyapatite Formation, Journal of Dental Research 71 (1992) 453-457.
[43] J.B. Park, Biomaterials: an introduction, Plenum Publishing Corporation, 1979.
[44] J. Sun, F.Y. Song, W.P. Zhang, B.E. Sexton, L.J. Windsor, Effects of alendronate on human osteoblast-like MG63 cells and matrix metalloproteinases, Archives of Oral Biology 57 (2012) 728-736.
[45] E.W.H. Bodde, R.S.Z. Kowalski, P.H.M. Spauwen, J.A. Jansen, No increased bone formation around alendronate or omeprazole loaded bioactive bone cements in a femoral defect, Tissue Engineering Part A 14 (2008) 29-39.

Supporting Information

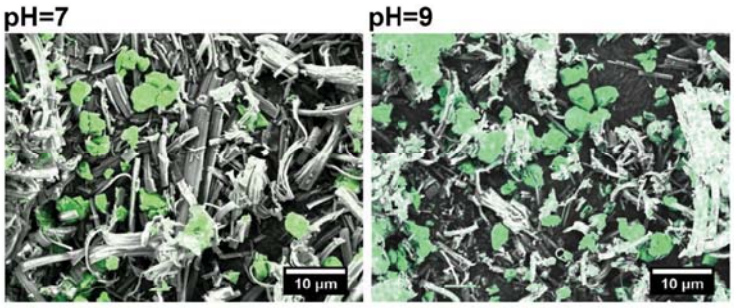

Figure S1. SEM micrographs with overlaid EDX maps of HP2-7 and HP2-9 particles. The green color corresponds to silicon distribution.

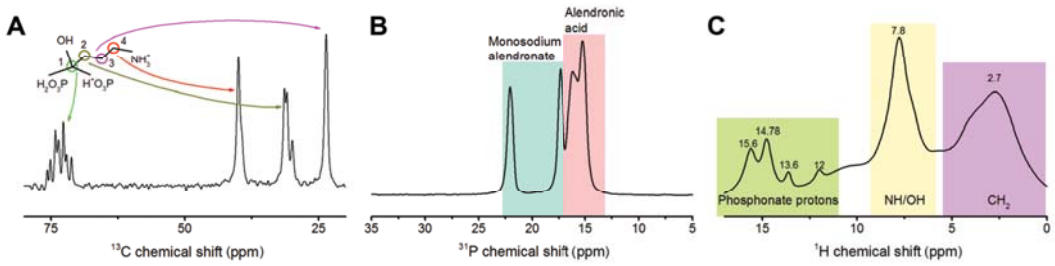

Figure S2. A) ^{13}C, B) ^{31}P and C) ^{1}H solid-state NMR spectra of pure ALN powder.

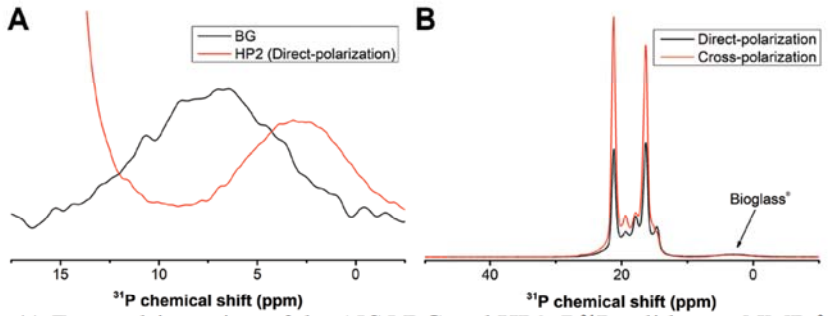

Figure S3. A) Zoomed-in region of the 45S5 BG and HP2-7 ^{31}P solid-state NMR ^{3}spectra. B) Direct- and cross-polarization ^{31}P solid-state NMR spectra of HP2-7 particles.

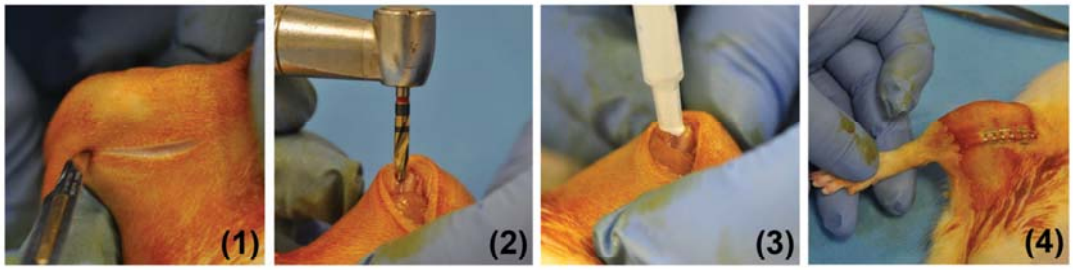

Figure S4. Digital photographs showing the surgical procedure for implantation of particle pastes into femoral condyles of osteoporotic rats.

Table S1. Randomized scheme for the implantation of the particle pastes.

Rat No.	Left femur	Right femur
1	45S5 BG	HP1-7
2	HP2-7	45S5 BG
3	45S5 BG	HP1-7
4	HP1-7	45S5 BG
5	HP2-7	HP1-7
6	HP1-7	45S5 BG
7	HP1-7	HP2-7
8	45S5 BG	HP2-7
9	HP2-7	HP1-7
10	45S5 BG	HP2-7
11	HP1-7	HP2-7
12	HP2-7	45S5 BG

Table S2. Solid-state DP ^{31}P NMR chemical shifts of phosphate and phosphonate peaks during the formation of HP1-7 particles.

Time (min)	Phosphate chemical shift (ppm)	Phosphonate chemical shift (ppm)
5	7.7	21.6
50	7.7	20.8
100	6.6	20.4
200	4.2	18.4
1000	Not observable anymore	18.2
4320	Not observable anymore	17.8

Chapter 6

Fiber-reinforced colloidal gels as injectable and moldable biomaterials for regenerative medicine

This chapter is based on:

M. Diba, A. Polini*, D.G. Petre*, Y. Zhang, and S.C.G. Leeuwenburgh, (*Submitted*).

*These authors contributed equaly to this work.

1. Introduction

Hydrogels are the preferred material choice for various strategies in regenerative medicine [1]. These materials can mimic the structure and properties of natural tissues [2], and offer several possibilities to deliver cells [3] as well as various biomolecules such as drugs [4] and growth factors [5]. Recently, injectable hydrogels have gained interest in the biomedical field due to their applicability for minimally invasive treatments [6] and the production of complex hydrogel structures at room or body temperature using techniques such as 3D printing [7] and injection molding [8]. Nevertheless, due to their high water content and soft nature, these hydrogels are often mechanically weak, which limits their applicability for biomedical applications considerably [9]. To this end, reinforcement of hydrogels with fibers has been explored as a method to produce mechanically more robust biomedical hydrogels [10-12]. This strategy is based on fiber-based reinforcement mechanisms as observed in nature for tissues such as articular cartilage, the mechanical properties of which are directly correlated with fiber content [13]. Incorporation of fibers can increase the stiffness of hydrogels [12], but also enhance their toughness through crack bridging mechanism [14]. However, the majority of synthetic fiber-reinforced hydrogels are made of continuous interconnected fiber meshes or constructs, which hampers their injectability or moldability [11, 15, 16]. Attempts to reinforce hydrogels using discrete fibers are still scarce [11, 17-19]. Recently, Poveda-Reyes et al. [11] used short polymeric microfibers to reinforce gelatin gels. Although these microfibers effectively reinforced the non-injectable chemically cross-linked gels, reinforcement of injectable gels using these microfibers was not achieved [11]. Other injectable hydrogel systems which have been reinforced with fibers were only injectable prior to their gelation, requiring a post-injection photo-polymerization [17, 18] or chemical cross-linking [19] step to achieve mechanical stability. Therefore, it remains a challenge to produce injectable fiber-reinforced hydrogels.

To this end, colloidal gels are an interesting class of hydrogels in view of their particulate nature [20-24]. These gels assemble into solid-like interconnected networks [25], but they possess injectable, adaptive and self-healing features due to the reversibility of their physical interparticle bonds [20, 23]. Nevertheless, similar to other physically cross-linked hydrogels, polymeric colloidal gels suffer

from weak mechanical properties [20, 22, 24]. Although mechanical reinforcement of colloidal gels with inorganic nanoparticles was shown to be effective, these nanocomposite gels are still too weak to resist compressive loading [21] or display brittle fracture under compression [23]. Moreover, various applications such as soft tissue engineering often require biomaterials that are fully organic and biodegradable [26-28]. These requirements necessitate a new strategy for the development of fully organic colloidal gels that are not only injectable, but also are mechanically robust. Here, we report the development of fully organic fiber-reinforced colloidal gels for applications in regenerative medicine. We used gelatin nanoparticles as colloidal building blocks, which can assemble into colloidal gel networks, and reinforced the colloidal gels with discrete sub-micron poly-L-lactic acid (PLLA) fibers of various lengths in order to achieve mechanically strong hydrogels. Following this strategy, we were able to produce fully organic colloidal gels which were cytocompatible, injectable/moldable and mechanically strong.

2. Materials and methods

2.1. Materials

Gelatin type B (from bovine skin, gel strength ~225 g Bloom) and glycine were purchased from Sigma-Aldrich (Steinheim, Germany). PLLA pellets (PURASORB PL 65) were provided by Corbion Purac (Gorinchem, The Netherlands). Dulbecco Modified Eagle Medium (DMEM) and fetal calf serum (FCS) were obtained from Gibco (Eggenstein, Germany) and Sigma-Aldrich (Steinheim, Germany), respectively. All other chemicals were of reagent grade and were used without any purification.

2.2. Synthesis of gelatin nanoparticles

Gelatin nanoparticles were synthesized using a two-step desolvation method [20]. In the first step, 50 g of gelatin powder was dissolved in 1 L of distilled water at 50 °C. Afterward, 1 L of acetone was rapidly added to the gelatin solution and the mixture was left at room temperature for 1h to precipitate high molecular weight gelatin. Thereafter, the supernatant was discarded and the gelatin precipitates were dissolved in 800 mL of distilled water and lyophilized for further usage. In the second step, 3.75 g of the lyophilized gelatin was dissolved in 75 mL of distilled water and the pH of solution was set to 2.5 by adding hydrochloric acid. Thereafter,

225 mL of acetone was slowly added to the gelatin solution at 50 °C using a syringe pump with a dripping rate of 12 mL/min during vigorous stirring of the solution at 1000 rpm. To cross-link the gelatin nanoparticles, 555 µL of glutaraldehyde solution (25 wt%) was added dropwise to the gelatin dispersion at room temperature and left to react overnight while stirring at 600 rpm. In the next day, 300 mL of a 0.1M aqueous solution of glycine was added to the gelatin dispersion to block unreacted aldehyde groups. After 1 h of stirring, the dispersion was filtered with a nylon mesh (100 µm mesh size). Subsequently, the dispersion was washed with distilled water through four centrifugation (each at 5000 rpm for 90 min) and redispersion steps. Thereafter, the nanoparticles were dispersed in aceone:water (1:3; V:V) solutions, frozen with liquid nitrogen, and lyophilized for further use.

2.3. Processing of PLLA into fibers

PLLA pellets were dissolved in 1,1,1,3,3,3-hexafluoro-2-propanol at a concentration of 2.5 wt% and subsequently loaded in a syringe connected to a 21 gauge nozzle. Consequently, sub-micron PLLA fibers were obtained by means of an electrospinning apparatus (Fuence Co., Wako, Japan). Electrospinning was performed at a voltage of 20 kV, a flow rate of 5 µL/h and an air gap of 20 cm. Solidified fiber meshes were collected on an aluminum foil and placed in the chemical fume hood for 24h in order to remove any residual solvents. Thereafter, the electrospun fiber meshes were aminolyzed by immersion of the meshes in a 5% ethylenediamine solution in isopropanol at 37 ºC for 3, 4 or 6h [29]. After the aminolysis procedure, the suspension of nanofibers was centrifuged and washed two times with distilled water followed by a one minute sonication step at 100% amplitude and 50% duty cycle using a sonication probe (UP100H, Hielscher Ultrasonics, Teltow, Germany) in order to facilitate the fragmentation of the fiber. Thereafter, the fibers were freeze dried before further use.

2.4. Preparation of hydrogels

Hydrogels with a solid content of 10 w/v% (~30% particle volume fraction) were prepared by adding water or an aqueous dispersion of fibers (with 0-500 mM of dissolved sodium chloride) to the lyophilized gelatin nanoparticles. Thereafter, the solution/dispersion and nanoparticles were thoroughly mixed using a spatula and vortexing (1 min). Thereafter, the samples were centrifuged at 5000 rpm for 1 min to obtain bulk gels.

2.5. Dynamic Light Scattering (DLS)

DLS measurements were performed using a Zetasizer® Nano-S instrument (Malvern Instruments Ltd., UK) to determine the hydrodynamic size of gelatin nanoparticles and PLLA fibers. The measurements were performed using MilliQ water as the dispersion medium and each test was carried out at 25 °C for 60 seconds (n=3).

2.6. Zeta potential

Zeta potential measurements were performed using a Zetasizer® Nano-S instrument (Malvern Instruments Ltd.) to determine the net surface charge of gelatin nanoparticles and PLLA fibers. The measurements were performed at 25 °C, and HEPES buffer (5 mM, pH =7) was used as the dispersion medium. Zeta potential values were calculated by the Zetasizer software based on the measured mobility of nanoparticles according to the Smoluchowski equation (n=3).

2.7. Scanning Electron Microscopy (SEM)

A Field Emission Scanning Electron Microscope (FE-SEM; Sigma 300, Zeiss, Germany) was used to evaluate the morphology of lyophilized nanoparticles, fibers and gels. All electron microscopy samples were prepared by fixing the samples on a sticky carbon tape and sputter-coating with a conductive 10 nm thick chromium layer.

2.8. Mechanical evaluation of hydrogels

Rheology tests: An AR2000ex rheometer (TA instruments, UK) with a flat steel plate geometry (20 mm diameter) was used for rheological evaluation of the hydrogels. The measurements were performed at 25 °C with an operating gap of 500 µm. Each hydrogel was first characterized by means of frequency sweeps (0.1-10 Hz; at 1 % strain), followed by a time sweep (1 min, 1 Hz and 1 % strain), a strain sweep (1-1000 % strain, and 1 Hz) and a time sweep (1 min, 1 Hz and 1 % strain) step. The storage modulus (G') of the gels was defined as the average G' during the first time sweep step. The yield strain of the gels was determined as the strain at which G' and G'' were equal. The self-healing capability of hydrogels after shear-induced destruction was evaluated by quantifying the recovery (%) of their storage modulus (G'). The recovery of G' (%) was determined as the ratio between the storage modulus 1 min after strain sweep-induced gel network destruction (0.01-1000 strain %) relative to their original storage modulus. The shear-thinning

behavior of the gels was determined through steady flow experiments by measuring their viscosity while varying the shear rate from 0.1 to 100 s^{-1}.

Compression tests: Compression tests were performed using an LS1 (Lloyd Instruments, UK) universal testing machine equipped with a 10 N load cell. Cylindrical hydrogel specimens were prepared by injecting the hydrogels into cylindrical Teflon molds (diameter: 8 mm, height: 5 mm) and keeping them at 4 °C overnight. The compression tests were carried out at a loading rate of 0.5 mm/ min. The elastic modulus of the samples was calculated from the average slope of the initial part (0 to 10 % strain) of their stress-strain curves. Three samples were measured for each experimental condition (n=3).

Nanoindentation tests: Mechanical properties of the hydrogels at the microscopic level were measured using a PIUMA nanoindentation instrument (Optics11, The Netherlands). The measurements were carried out using a spherical nanoindentation probe with a stiffness of 0.492 N/m and a radius of 45 µm. The hydrogel samples were filled into cylindrical plastic molds which were fixed on plastic petri dishes using epoxy glue. The petri dishes were filled with MilliQ water and indentations were made in these wet conditions at room temperature with a probe displacement velocity of 9 µm/s at three different spots (n=3) on the surface of each type of hydrogel. Elastic moduli were calculated by the Piuma software using the method provided by Oliver and Pharr for spherical indenters [30, 31].

2.9. *In vitro* cytocompatibility

The cytocompatibility of the hydrogels was assessed by culturing mouse fibroblastic NIH 3T3 cells on the gel surface and performing an alamarBlue® assay to assess the metabolic activity of the cultured cells. The nanoparticles and fibers were sterilized by acetone/ethanol rinsing followed by a freeze-drying step. The hydrogels were prepared inside a fume hood using autoclaved MilliQ water and injected into cylindrical plastic molds (diameter: 6 mm, height: 4 mm), which were placed with molds inside a 48 well plate. 1×10^4 fibroblasts were seeded on the top surface of each hydrogel sample and cultured for up to 7 days. As cell culture medium, we used DMEM supplemented with 10% FCS, penicillin (100 U/mL) and streptomycin (10 µg/mL). At each time point, an alamarBlue® stock solution (0.1 mg/mL in PBS) was 10 times diluted with serum-free DMEM. This solution was transferred to each well at a final volume of 1 mL and then incubated at 37 °C for 4h in the dark. Thereafter,

the optical density of the solutions was measured at 570 nm and 600 nm (reference wavelength) using a multi-mode spectrophotometer (Biotek, Winooski, USA). Four samples of each group were analyzed for the experiment. The metabolic activity of cells in each sample was calculated according to the assay protocol (BIO-RAD, Veenendaal, Netherlands) using cell-free medium as negative control and the cells cultured on pure gelatin gels as positive control.

2.10. Statistics

All values were presented as average ± standard deviation. The statistical analyses were carried out using GraphPad Prism 7 software (GraphPad Software Inc., San Diego, CA, USA). Statistical differences between experimental groups were determined by one-way ANOVA with Tukey's multiple comparisons test. $P<0.05$ was considered as significantly different.

3. Results and discussion

Particles as basic building blocks of colloidal gels play a key role in determining the properties of these materials [25]. Therefore, the physicochemical properties of the individual particles were characterized in more detail. Figure 1 shows the scanning electron micrographs of the particulate building blocks that we used in this study as well as a schematic depiction of our methodology to prepare the colloidal hydrogels. The gelatin nanoparticles had an average diameter of 210±64 nm (Figure 1a), which upon swelling increased to ~332±3 nm (PdI= 0.14±0.02) as measured by means of DLS. Previous studies [20, 23] have shown that despite their electrostatic long-range repulsion (Zeta potential of -23 ±2 mV at pH 7), the gelatin nanoparticles are able to form interparticle bonds when they are in close proximity. Such bonds arise from short-range hydrophobic and ionic interactions between the dangling gelatin chains on the surface of nanoparticles and can lead to the formation of colloidal gel networks. We hypothesized that these dangling chains would also interact with the amine and remaining carboxyl groups of aminolyzed PLLA fibers [29], leading to the formation of physical crosslinks between these fibers and gelatin nanoparticles. As shown in Figure 1(b-d), the PLLA fibers produced in this study exhibited an average diameter of 795±78 nm and average lengths of 2.2±0.7, 7.1±3.2 and 19.1±12.1 μm when aminolyzed for 6, 4 and 3h, respectively.

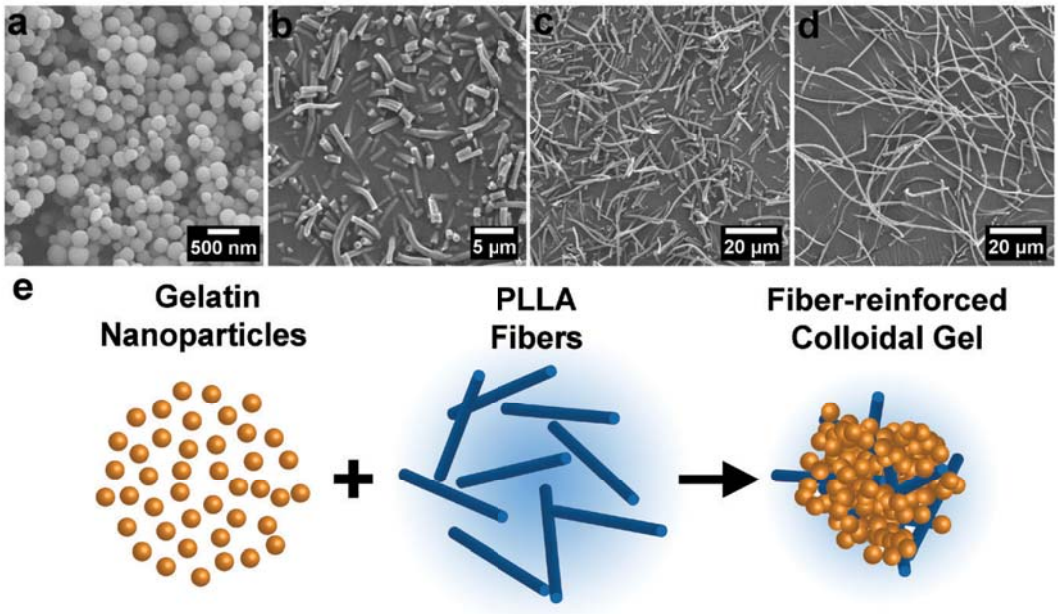

Figure 1. Building blocks and formation of colloidal gels. Scanning electron micrographs of (a) gelatin nanoparticles, and PLLA fibers aminolyzed for (b) 3h, (c) 4h and (d) 6h. Schematic illustration of the formation of fiber-reinforced gels is shown in (e).

To assess the distribution of PLLA fibers within the hydrogels, we lyophilized the hydrogels and evaluated their morphology by electron microscopy. Figure 2 shows the scanning electron micrographs of various types of lyophilized colloidal gels. These images reveal a homogeneous dispersion of the fibers throughout the hydrogels for all compositions. Nevertheless, in samples prepared with long PLLA fibers (aminolyzed for 3h), the fibers appeared to protrude from the hydrogel matrix (Figure 2f). Importantly, imaging of the samples at high magnification showed that the PLLA fibers were covered with spherical gelatin nanoparticles (Figure 2c), which indeed suggests a high affinity between the fibers and the gelatin nanoparticles.

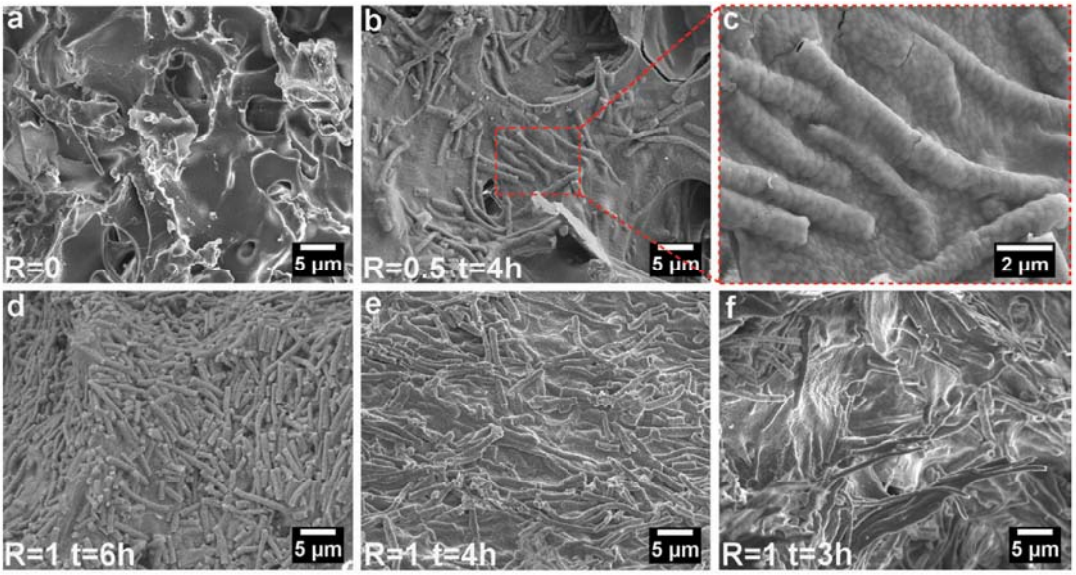

Figure 2. Scanning electron micrographs of lyophilized gelatin-PLLA colloidal hydrogels containing different amounts of PLLA fibers with different lengths (controlled by the aminolysis time). R and t correspond to fiber/gelatin (w/w) ratio and the aminolysis time of fibers, respectively.

Subsequently, we investigated the effects of fiber incorporation on the viscoelastic properties of the hydrogels (Figure 3). Importantly, all hydrogels showed frequency-independent solid-like behavior (Figure S1). The rheological measurements revealed a significant reinforcement of the hydrogels upon incorporation of the fibers, as evidenced by a 15-fold increase of the storage modulus (G') of the gels upon fiber incorporation. The strongest reinforcement effect was observed for hydrogels reinforced with fibers aminolyzed for 4h, which showed significantly higher storage moduli as compared to the other groups at a fiber/gelatin ratio (w/w) of 1, indicating that the average length of 7.1±3.2 µm of these fibers was optimal for reinforcement of the colloidal gels. However, the lowest tan(delta) and highest yield strain were observed for hydrogels reinforced with the shortest fibers (2.2±0.7 µm after aminolysis for 6h). This effect might be caused by a more uniform distribution of these small fibers throughout the gels and a stronger interaction with gelatin nanoparticles as a result of their higher specific surface area. In order to assess the self-healing ability of the hydrogels, we quantified the recovery of the storage modulus after destructive shearing up to 1000% strain. As shown in Figure 3d, these experiments indicated that the reinforcement of colloidal gels with the PLLA fibers aminolyzed for 4 or 6h negatively affected their self-healing capacity;

upon incorporation of these fibers in the colloidal gels, the recovery of the storage modulus decreased from around 70% to as low as 40%. However, the reinforcement of colloidal gels with longer fibers (19.1±12.1 μm after aminolysis for 3h) did not compromise their self-healing capacity since the recovery of the storage modulus remained statistically similar after the incorporation of fibers. These results indicate that the effect of fiber-reinforcement on the self-healing properties of colloidal gels depends on the fiber dimensions. The reduction of self-healing capacity upon incorporation of shorter fibers might result from their stiffer and less flexible behavior which compromised the dynamic nature of colloidal gelatin gels. As a consequence, the restoration of a uniform colloidal network after destructive shearing was hindered.

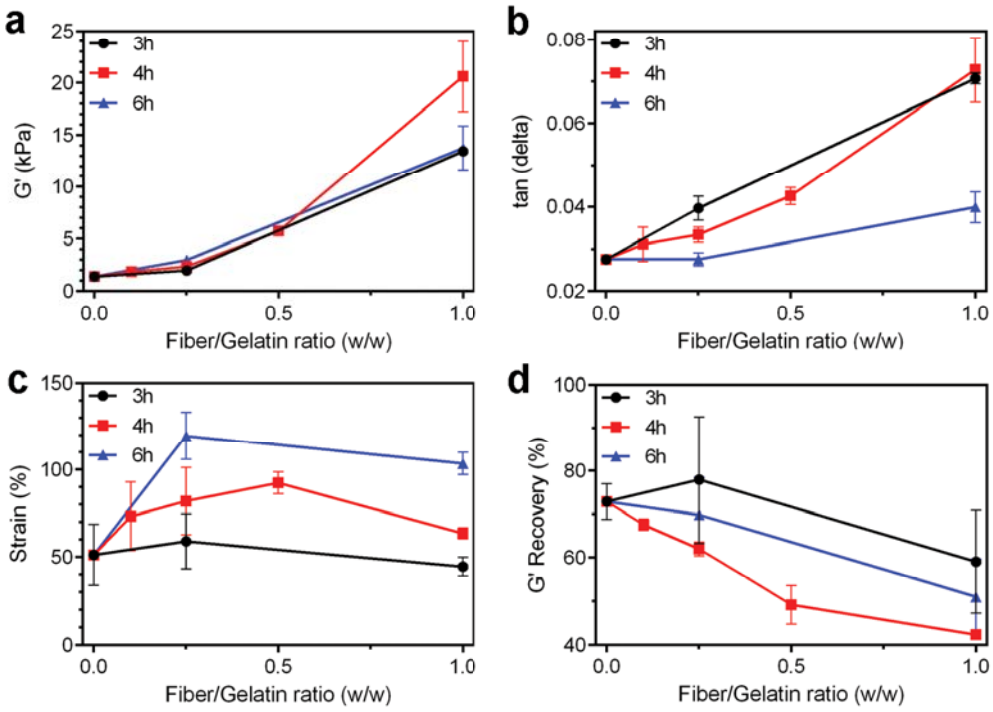

Figure 3. (a) Storage modulus (G'), (b) damping factor (tan (delta)), (c) yield strain, and (d) recovery of G' after destructive-shearing, for hydrogels reinforced with different amounts of fibers aminolyzed for 3, 4 or 6h.

Since the most effective reinforcement of hydrogels was observed upon incorporation of fibers aminolyzed for 4 hours, we selected the hydrogels prepared with these fibers for a more detailed study. To validate the applicability of the fiber-reinforced gels in biological fluids of high ionic strength, we studied the effect of ionic strength on the viscoelastic properties of the hydrogels by dissolving different concentrations

of sodium chloride in the solutions used for the hydrogel preparation. As shown in Figure 4, the increase of ionic strength up to 500mM did not compromise the viscoelastic properties of the hydrogels, as no statistical difference was observed between viscoelastic parameters at different ionic strengths. Since electrostatic interactions are screened at high ionic concentrations [21], these results indicate that other interactions such as hydrophobic and Van der Waals forces can also be responsible for the formation of interparticle bonds in our gels. In the absence of such hydrophobic and Van der Waals interactions, other polymeric colloidal gels [32] were shown to lose their mechanical integrity at high ionic concentrations.

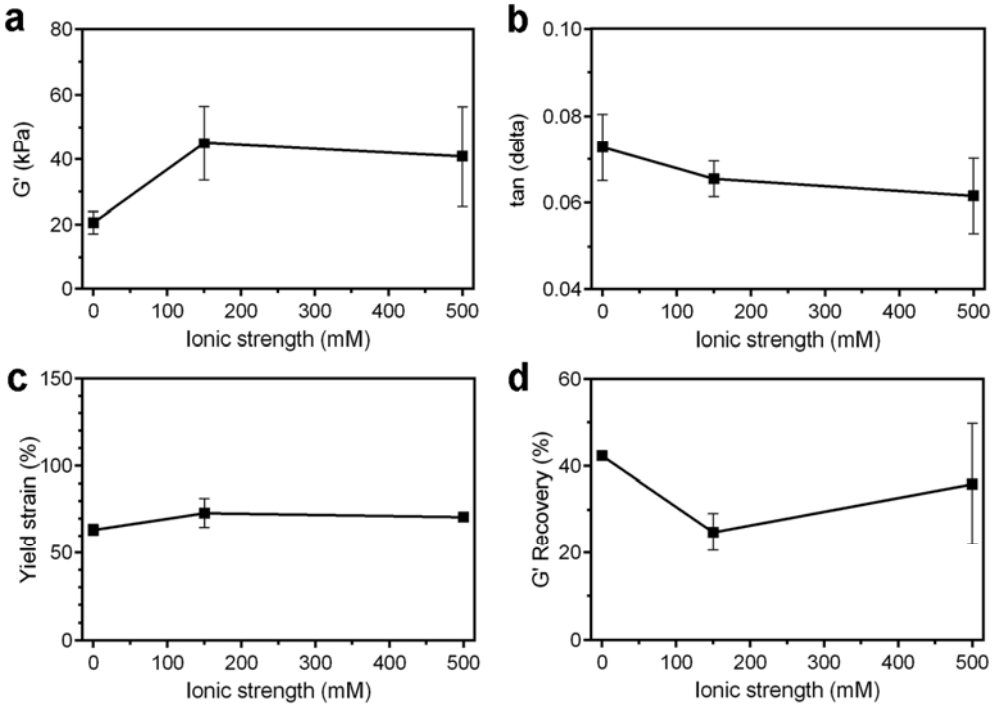

Figure 4. (a) Storage modulus (G'), (b) damping factor (tan (delta)), (c) yield strain, and (d) recovery of storage modulus (G') after destructive shearing of fiber-reinforced colloidal gels of different ionic strength. All hydrogels were prepared from PLLA fibers aminolyzed for 4h and a fiber/gelatin (w/w) ratio of 1.

Importantly, as shown in Figure 5a and Movie S1, the reinforcement of the gels with PLLA fibers did not compromise the injectability of these materials; the fiber-reinforced fibers showed shear-thinning behavior similar to fiber-free gels (Figure 5b). This unique combination of fiber reinforcement and injectability was obtained owing to a sufficient amount of reversible interactions between the gelatin nanoparticles and PLLA fibers, as previous attempts [12] could not simultaneously achieve reinforcement and injectability upon incorporation of PLLA fibers into

polymeric hydrogels. In addition to their injectability, the fiber-reinforced hydrogels also showed excellent moldability (Figure 5c), which enabled the evaluation of their mechanical properties under compressive loading. As shown in Figure 5d, these tests demonstrated that the fiber-reinforcement strategy significantly improved the mechanical resistance of the colloidal gels against compressive loading. Upon fiber incorporation, the elastic modulus of the hydrogels was increased almost tenfold from 2.4±0.2 to 23.1±2.1 kPa. The fiber-reinforced gels showed a linear elastic behavior for up to around 20% strain, after which crack formation and propagation occurred and the deformation proceeded plastically (Movie S2). Nevertheless, such visible fracture event was not observed for the fiber-free gels.

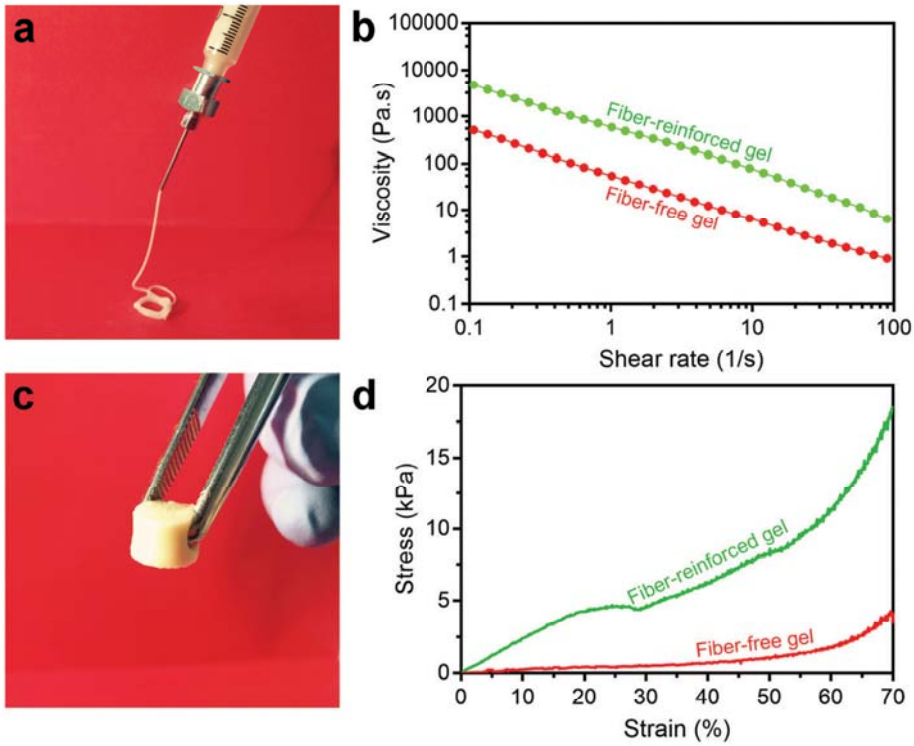

Figure 5. (a) Digital photograph of a fiber-reinforced colloidal gel during extrusion from a syringe. (b) Shear-thinning behavior of fiber-reinforced and fiber-free colloidal gels. (c) Digital photograph of a fiber-reinforced colloidal gel after molding. (d) Stress–strain curves of fiber-reinforced and pure gelatin colloidal gels during compressive loading. The fiber-reinforced gels were prepared at a fiber/gelatin (w/w) ratio of 1, using 4h aminolyzed fibers.

Rheological and compression tests describe the bulk mechanical behavior of hydrogels, but direct cell-biomaterial interactions occur at microscale. Therefore, we performed nanoindentation tests on our hydrogels using a micron-size spherical probe to elucidate the effect of fiber incorporation on mechanical properties of

hydrogels at microscale. As shown in Figure 6, upon incorporation of the fibers in the gels, the elastic modulus increased more than 150-fold. Importantly, the microscopic mechanical reinforcement effect caused by the fibers occurred uniformly throughout the gel matrix, since standard deviations were low. These results clearly indicate that the fiber reinforcement effect is not limited to the macroscopic level but also occurs at the microscale. This considerable change of elasticity at the microscopic scale can be sensed by cells and direct cellular behavior such as differentiation [33]. For example, Engler et al. [131] have shown that the elasticity of biomaterials can influence the phenotype of mesenchymal stem cells, since matrices with elastic moduli of 0.1–1 kPa, 8–17 kPa, or 25–40 kPa were neurogenic, myogenic, or osteogenic, respectively. These elasticities were in the same range as our colloidal gels, which highlights the potential applicability of our fiber reinforcement strategy for engineering of various tissue types. Nevertheless, more detailed biological studies are required to elucidate the effect of elasticity of fiber-reinforced colloidal gels on cellular behavior.

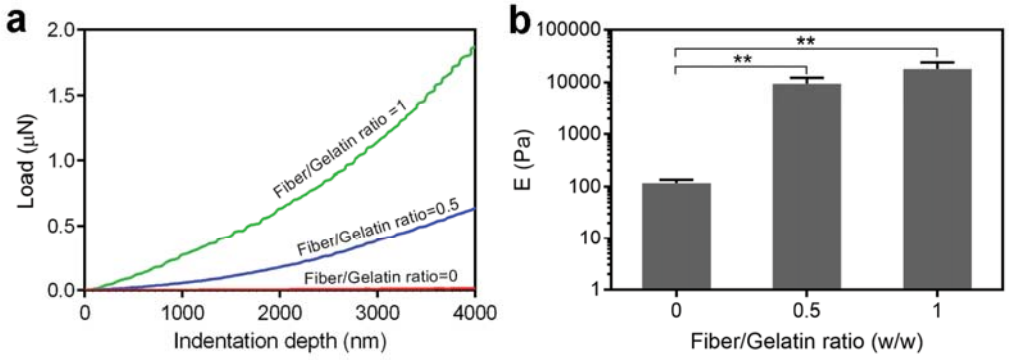

Figure 6. (a) Load-displacement curves and (b) elastic modulus (E) of hydrogels with different fiber contents, measured by nanoindentation tests. ** indicates statistical difference ($P<0.005$).

Although the cytocompatibility of pure gelatin colloidal gels has been shown previously [21, 23, 34], the effect of incorporation of PLLA fibers on the cytocompatibility of these materials has not been studied yet. Therefore, we cultured fibroblastic NIH 3T3 cells on our colloidal gelatin-PLLA gels. As shown in Figure 7a, the alamarBlue® assay indicated that the fiber-reinforced colloidal gels were highly cytocompatible. Moreover, the rheological evaluation of the hydrogels

after 7 days of cell culture showed that these materials retained their mechanical integrity during the cell culture period, which proves that the reinforcement of the gels with fibers was still effective after the cell culture period (Figure 7b). The cytocompatibility and mechanical stability of fiber-reinforced colloidal gels suggest a great potential for the use of these materials for applications in tissue engineering and regenerative medicine.

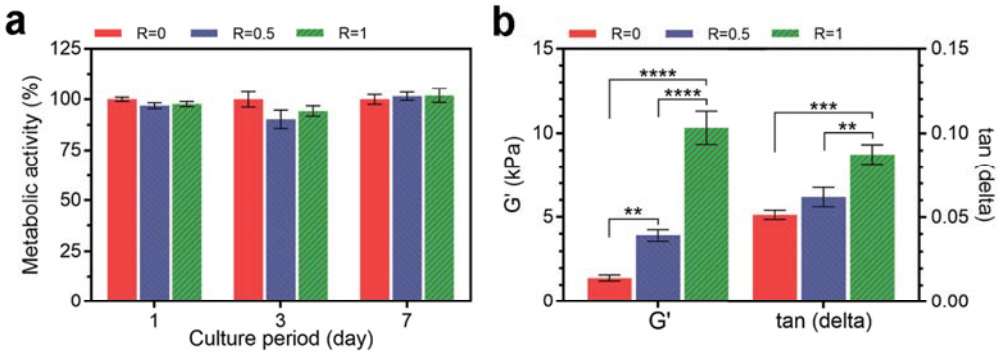

Figure 7. (a) Metabolic activity of fibroblast cells seeded on the hydrogels at different time points of cell culture, and (b) viscoelastic properties of the hydrogels after 7 days of cell culture. R indicates fiber/gelatin ratio (w/w). *, **, ***, and **** indicate statistical difference with $P<0.05$, $P<0.01$, $P<0.001$ and $P<0.0001$, respectively.

4. Conclusions

This study demonstrated successful mechanical reinforcement of colloidal gels using PLLA fibers. This reinforcement strategy did not compromise the injectability of these materials, and facilitated the preparation of moldable gels that were mechanically robust. Importantly, the fiber reinforcement of gels was effective at both macroscopic and microscopic levels. Finally, these fully organic gels were cytocompatible and could retain their mechanical integrity under physiological conditions for up to one week. Consequently, these materials exhibit a strong potential for applications in tissue engineering and regenerative medicine.

References

[1] N. Annabi, A. Tamayol, J.A. Uquillas, M. Akbari, L.E. Bertassoni, C. Cha, G. Camci-Unal, M.R. Dokmeci, N.A. Peppas, A. Khademhosseini, 25th anniversary article: rational design and applications of hydrogels in regenerative medicine, Advanced Materials 26 (2014) 85-124.

[2] H. Geckil, F. Xu, X.H. Zhang, S. Moon, U. Demirci, Engineering hydrogels as extracellular matrix mimics, Nanomedicine 5 (2010) 469-484.

[3] S. Utech, R. Prodanovic, A.S. Mao, R. Ostafe, D.J. Mooney, D.A. Weitz, Microfluidic generation of monodisperse, structurally homogeneous alginate microgels for cell encapsulation and 3D cell culture, Advanced Healthcare Materials 4 (2015) 1628-1633.

[4] T.R. Hoare, D.S. Kohane, Hydrogels in drug delivery: Progress and challenges, Polymer 49 (2008) 1993-2007.

[5] R. Censi, P. Di Martino, T. Vermonden, W.E. Hennink, Hydrogels for protein delivery in tissue engineering, Journal of Controlled Release 161 (2012) 680-692.

[6] L. Yu, J.D. Ding, Injectable hydrogels as unique biomedical materials, Chemical Society Reviews 37 (2008) 1473-1481.

[7] R.A. Barry, R.F. Shepherd, J.N. Hanson, R.G. Nuzzo, P. Wiltzius, J.A. Lewis, Direct-write assembly of 3D hydrogel scaffolds for guided cell growth, Advanced Materials 21 (2009) 2407-2410.

[8] S.C. Chang, J.A. Rowley, G. Tobias, N.G. Genes, A.K. Roy, D.J. Mooney, C.A. Vacanti, L.J. Bonassar, Injection molding of chondrocyte/alginate constructs in the shape of facial implants, J Biomed Mater Res 55 (2001) 503-11.

[9] S. Utech, A.R. Boccaccini, A review of hydrogel-based composites for biomedical applications: enhancement of hydrogel properties by addition of rigid inorganic fillers, Journal of Materials Science 51 (2016) 271-310.

[10] B. Lu, F. Lin, X. Jiang, J. Cheng, Q. Lu, J. Song, C. Chen, B. Huang, One-pot assembly of microfibrillated cellulose reinforced PVA–borax hydrogels with self-healing and pH-responsive properties, Acs Sustainable Chemistry & Engineering 5 (2017) 948-956.

[11] Y.W. Huang, D.R. King, T.L. Sun, T. Nonoyama, T. Kurokawa, T. Nakajima, J.P. Gong, Energy-dissipative matrices enable synergistic toughening in fiber reinforced soft composites, Advanced Functional Materials 27 (2017) 1605350.

[12] S. Poveda-Reyes, L.R. Mellera-Oglialoro, R. Martínez-Haya, T.C. Gamboa-Martínez, J.L. Gómez Ribelles, G. Gallego Ferrer, Reinforcing an injectable gelatin hydrogel with PLLA microfibers: Two routes for short fiber production, Macromolecular Materials and Engineering 300 (2015) 977-988.

[13] P. Calvert, Hydrogels for soft machines, Advanced Materials 21(7) (2009) 743-

756.
[14] X. Zhao, Multi-scale multi-mechanism design of tough hydrogels: building dissipation into stretchy networks, Soft Matter 10 (2014) 672-687.
[15] A. Agrawal, N. Rahbar, P.D. Calvert, Strong fiber-reinforced hydrogel, Acta Biomaterialia 9 (2013) 5313-5318.
[16] C.-D. Young, J.-R. Wu, T.-L. Tsou, High-strength, ultra-thin and fiber-reinforced pHEMA artificial skin, Biomaterials 19 (1998) 1745-1752.
[17] A.C. Borges, P.E. Bourban, D.P. Pioletti, J.A.E. Månson, Curing kinetics and mechanical properties of a composite hydrogel for the replacement of the nucleus pulposus, Composites Science and Technology 70 (2010) 1847-1853.
[18] A. Khoushabi, A. Schmocker, D.P. Pioletti, C. Moser, C. Schizas, J.A. Manson, P.E. Bourban, Photo-polymerization, swelling and mechanical properties of cellulose fibre reinforced poly(ethylene glycol) hydrogels, Composites Science and Technology 119 (2015) 93-99.
[19] O. Regev, C.S. Reddy, N. Nseir, E. Zussman, Hydrogel reinforced by short albumin fibers: mechanical characterization and assessment of biocompatibility, Macromolecular Materials and Engineering 298 (2013) 283-291.
[20] H. Wang, M.B. Hansen, D.W.P.M. Löwik, J.C.M. van Hest, Y. Li, J.A. Jansen, S.C.G. Leeuwenburgh, Oppositely charged gelatin nanospheres as building blocks for injectable and biodegradable gels, Advanced Materials 23 (2011) H119-H124.
[21] H. Wang, M. Bongio, K. Farbod, A.W.G. Nijhuis, J. van den Beucken, O.C. Boerman, J.C.M. van Hest, Y. Li, J.A. Jansen, S.C.G. Leeuwenburgh, Development of injectable organic/inorganic colloidal composite gels made of self-assembling gelatin nanospheres and calcium phosphate nanocrystals, Acta Biomaterialia 10 (2014) 508-519.
[22] Q. Wang, L. Wang, M.S. Detamore, C. Berkland, Biodegradable colloidal gels as moldable tissue engineering scaffolds, Advanced Materials 20 (2008) 236-239.
[23] M. Diba, H. Wang, T.E. Kodger, S. Parsa, S.C.G. Leeuwenburgh, Highly elastic and self-healing composite colloidal gels, Advanced Materials 29 (2017) 1604672.
[24] J. Gu, Y. Zhao, Y. Guan, Y. Zhang, Effect of particle size in a colloidal hydrogel scaffold for 3D cell culture, Colloids and Surfaces B: Biointerfaces 136 (2015) 1139-1147.
[25] P.J. Lu, D.A. Weitz, Colloidal particles: crystals, glasses, and gels, in: J.S. Langer (Ed.), Annual Review of Condensed Matter Physics, Vol 42013, pp. 217-233.
[26] Q.-Z. Chen, S.E. Harding, N.N. Ali, A.R. Lyon, A.R. Boccaccini, Biomaterials in cardiac tissue engineering: Ten years of research survey, Materials Science and Engineering: R: Reports 59 (2008) 1-37.

[27] T.H. Qazi, D.J. Mooney, M. Pumberger, S. Geißler, G.N. Duda, Biomaterials based strategies for skeletal muscle tissue engineering: Existing technologies and future trends, Biomaterials 53 (2015) 502-521.
[28] S. MacNeil, Biomaterials for tissue engineering of skin, Materials Today 11 (2008) 26-35.
[29] A. Polini, D.G. Petre, M. Iafisco, S. de Lacerda Schickert, A. Tampieri, J. van den Beucken, S.C.G. Leeuwenburgh, Polyester fibers can be rendered calcium phosphate-binding by surface functionalization with bisphosphonate groups, Journal of Biomedical Materials Research Part A (2017). doi:10.1002/jbm.a.36077
[30] W.C. Oliver, G.M. Pharr, An improved technique for determining hardness and elastic modulus using load and displacement sensing indentation experiments, Journal of Materials Research 7 (2011) 1564-1583.
[31] W.C. Oliver, G.M. Pharr, Measurement of hardness and elastic modulus by instrumented indentation: Advances in understanding and refinements to methodology, Journal of Materials Research 19 (2011) 3-20.
[32] S.R. Van Tomme, M.J. van Steenbergen, S.C. De Smedt, C.F. van Nostrum, W.E. Hennink, Self-gelling hydrogels based on oppositely charged dextran microspheres, Biomaterials 26 (2005) 2129-2135.
[33] M. Ahearne, Introduction to cell–hydrogel mechanosensing, Interface Focus 4 (2014) 20130038.
[34] H. Wang, Q. Zou, O.C. Boerman, A.W.G. Nijhuis, J.A. Jansen, Y. Li, S.C.G. Leeuwenburgh, Combined delivery of BMP-2 and bFGF from nanostructured colloidal gelatin gels and its effect on bone regeneration in vivo, Journal of Controlled Release 166 (2013) 172-181.

Supporting Information

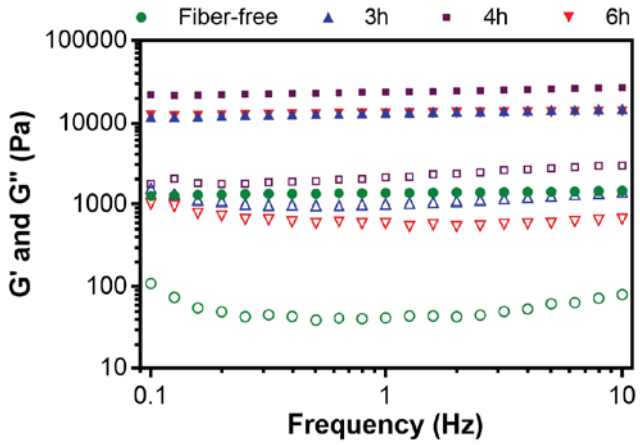

Figure S1. Frequency dependence of storage (solid symbols, G') and loss (open symbols, G") moduli of fiber-free or fiber-reinforced gels. All fiber-reinforced gels contained a fiber/gelatin (w/w) ratio of 1, and were prepared using fibers aminolyzed for 3, 4 or 6h.

Movie S1. Digital video showing the extrusion of a fiber-reinforced colloidal gel through a 28-gauge needle. The gel was prepared at a fiber/gelatin (w/w) ratio of 1, using 4h aminolyzed fibers.

Movie S2. Digital video showing a fiber-reinforced colloidal gel specimen during a compression test (playback speed=20x). The gel was prepared at a fiber/gelatin (w/w) ratio of 1, using 4h aminolyzed fibers.

Chapter 7

Nanostructured raspberry-like gelatin microspheres for local delivery of multiple biomolecules

This chapter is based on:

M. Diba, B. Pape, A. Klymov, Y. Zhang, J. Song, D. Löwik, H. Seyednejad, and S.C.G. Leeuwenburgh, *Acta Biomaterialia*, 58 (2017) 67-79.

1. Introduction

In nature, materials and organisms owe their functions to their hierarchical and complex structure [1-3]. Various studies [4] have aimed to mimic these natural structures to produce materials with advanced functionalities. The preparation of multicompartment particles has become a particularly promising biomimetic strategy during the past decade to improve the functionality [5, 6]. In these particles, each individual compartment can act as a carrier for a different compound. Consequently, their multicompartmental structure can facilitate simultaneous and differential delivery of several biomolecules [7, 8]. This capacity for multiple delivery of biomolecules is highly attractive for applications in pharmaceutics, cosmetics, agriculture, and food products. Various methods such as self-assembly, phase separation, and microfluidics have been employed for the production of such multicompartment particles [6]. Nevertheless, these methods are often complex and only offer small-scale production. Techniques based on the use of supercritical carbon dioxide (CO_2) have been widely exploited for large-scale synthesis and processing of materials [9]. These technologies have been applied for production of particles [10] and porous structures [11], and also utilized as a method for drying [12], sterilization [13] and encapsulation [14] of various compounds. Moreover, as opposed to conventional spray-drying techniques [15] which require high temperatures, supercritical CO_2 spray-drying can be performed at low temperatures allowing production of particles containing temperature-sensitive polymers and biomolecules [16, 17]. Different types of biodegradable polymeric particles, such as poly lactic-co glycolic acid (PLGA), polycaprolactone (PCL), and polylactic acid (PLA), have been produced by means of supercritical CO_2 spray-drying [18]. Nevertheless, although the application of this technique for the production of particles from polymer solutions [10, 18] or polymer-nanoparticle mixtures [19-21] has been widely studied, production of multicompartment particles from colloidal particles only has not been reported yet using this technique.

Here, we report the formation of raspberry-like gelatin (RLG) microparticles composed of gelatin nanoparticles as colloidal building blocks through supercritical CO_2 processing. We show that these RLG microparticles exhibit a high stability upon dispersion in aqueous media without requiring any chemical cross-linking. We investigate simultaneous incorporation of small and large model compounds,

i.e. vancomycin and dextran, into the RLG microparticles and study their corresponding release kinetics. While vancomycin (MW=1.5 kDa) used as a model therapeutic drug, dextran (MW=20 kDa) is utilized as a model compound for growth factors. We further use two cell lines to assess the cytocompatibility of the RLG microparticles for biomedical applications. Based on these cytotoxicity and release studies, we reveal that these microparticles are cytocompatible and allow for differential release of multiple biomolecules. These results not only demonstrate the potential application of the RLG microparticles as vehicles for local delivery of multiple compounds, but can also pave the way for industrial production of various multicompartment particles using the supercritical CO_2 processing technique.

2. Experimental section

2.1. Materials

Gelatin A (from porcine skin, 300 Bloom), Glycine (≥99.0%), fluorescein isothiocyanate–dextran (FITC–Dextran; 20 kDa), vancomycin hydrochloride hydrate (potency ≥900 $\mu g \cdot mg^{-1}$), and alkaline phosphatase (ALP; lyophilized powder from bovine intestinal mucosa, ≥10 DEA units/mg solid) were purchased from Sigma–Aldrich. All other chemicals were of reagent grade and were used without any purification.

2.2. Synthesis of gelatin nanoparticles

Spherical gelatin nanoparticles were synthesized by a two-step desolvation method [22]. As the first step, 50 g of gelatin powder was dissolved in 1 L of MilliQ water at 50 °C. Thereafter, 1 L of acetone was added to the gelatin solution and the mixture was left for 1 h at room temperature to precipitate high molecular-weight gelatin. Afterward, the supernatant was discarded, the gelatin precipitates were dissolved in MilliQ water and lyophilized until further usage. For the second step, 3.75 g of the freeze-dried gelatin was dissolved in 75 mL of MilliQ water and the pH of solution was set to 2.5 using hydrochloric acid (5 M). Thereafter, 225 mL of acetone was added to the gelatin solution at 40 °C using a syringe pump with a dripping rate of 12 mL/min during vigorous stirring of the solution at 1000 rpm. In order to stabilize the gelatin nanoparticles by cross-linking, an excessive amount of 25 wt% glutaraldehyde solution (2 mL) was added to the gelatin dispersion at room temperature and left to react for ~16h while stirring at 600 rpm. Thereafter, 300

mL of a 100 mM aqueous solution of glycine was added to the gelatin dispersion to block unreacted aldehyde groups. After 1 h of stirring, the dispersion was filtered with a nylon mesh (100 μm mesh size). Subsequently, the dispersion was washed with distilled water through four centrifugation (at 5000 rpm for 1h) and redispersion steps. At last, the nanoparticles were dispersed in a 1:3 (V:V) mixture of acetone:water at a concentration of 8 mg/ml, and stored at 4 ºC for further processing.

2.3. Production of RLG microspheres

A supercritical fluid spray-drying process [17] was used for processing of the suspensions of gelatin nanoparticles. In this process, supercritical CO_2 was used as an antisolvent for the gelatin nanoparticles and extraction medium for the solution. Considering the low miscibility of supercritical CO_2 and water, acetone was included in the solution to enhance the drying process. A scheme of the experimental setup has been illustrated in Figure 1. The process was carried out by spraying of the suspension of gelatin nanoparticles into a high pressure vessel through the inner tube of a coaxial nozzle at a flow rate of 0.5 ml/min. Prior to the spraying of the suspension, the vessel was pressurized with CO_2 to 150 bar and its temperature was set to 40 ºC. During the process, supercritical CO_2 was injected into the vessel at a flow rate of 30 kg/h through the outer tube of the coaxial nozzle. The pressure and temperature of the vessel were kept at 150 bar and 40 ºC, respectively, and the produced particles were collected on top of a paper filter mounted at the bottom of the vessel. After spraying the suspension, the vessel was flushed for 30 minutes with fresh CO_2 to remove any remaining solvent and slowly depressurized to atmospheric pressure before opening and collecting the particles. Samples were stored at 4 °C in the dark before and after processing.

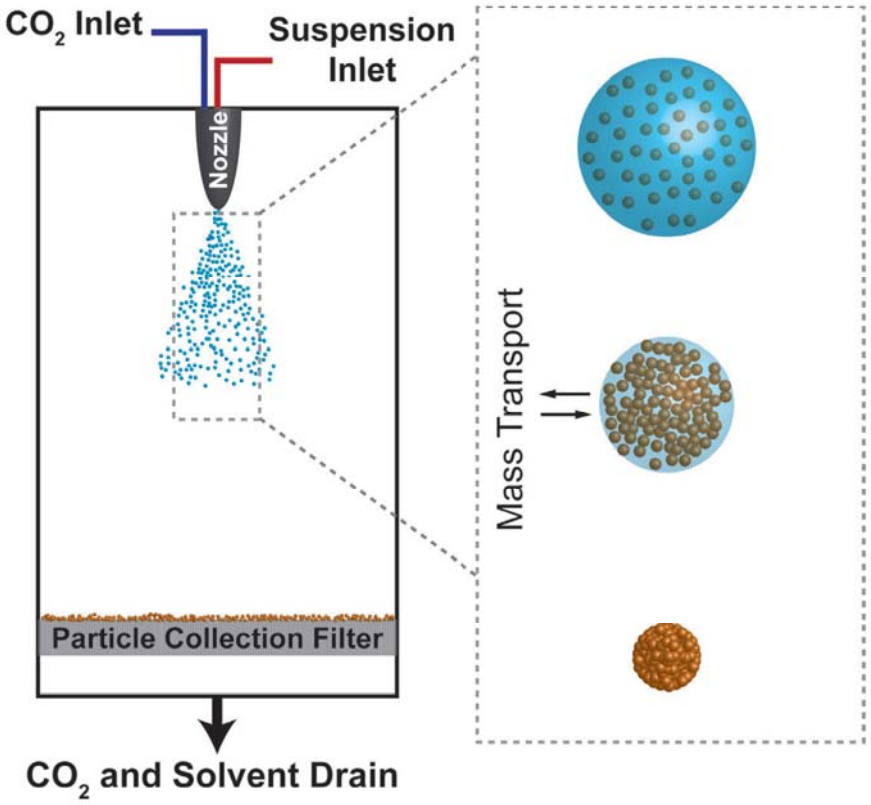

Figure 1. Schematic illustration of the production setup and formation mechanism of the RLG microparticles.

2.4. Incorporation of biomolecules into RLG microspheres

In order to incorporate vancomycin and FITC-dextran into the RLG microparticles, these compounds were dissolved in the suspension of gelatin nanoparticles prior to supercritical CO_2 processing. To assess the effect of supercritical CO_2 processing on the bioactivity of biomolecules, RLG microparticles containing ALP were prepared by dissolving ALP powder in the suspension used for the processing. Table 1 presents an overview of the composition of the suspensions used for the processing.

Table 2. List and contents of suspensions used for supercritical CO_2 processing.

Gelatin content (mg/mL)	Vancomycin content		FITC-Dextran content		ALP content	
	(µg/ml)	(wt%)*	(µg/ml)	(wt%)*	(µg/ml)	(wt%)*
8	0	0	0	0	0	0
8	40	0.5	0	0	0	0
8	40	0.5	0.8	0.01	0	0
8	40	0.5	16	0.2	0	0
8	0	0	0	0	16	0.2

* Relative to the solid gelatin content.

2.5. Particle size and morphology evaluation

A Field Emission Scanning Electron Microscope (FE-SEM; Sigma 300, Zeiss, Germany) was used to evaluate the morphology of particles. The inner structure of RLG microparticles was evaluated though cross-sectional etching using a focused ion beam (FIB) (FEI, NOVALAB 600 dual beam machine) by applying a beam current of 9.0 pA and a dwell time of 100ns. For each test, a microparticle was partially etched using the FIB and an image was captured using a FE-SEM linked to the FIB. All electron microscopy samples were prepared by dispersing the particles on a sticky carbon tape and sputter-coating with a conductive 5 nm thick chromium layer. The size of swollen nanoparticles in water was measured via Dynamic Light Scattering (DLS) using a Zetasizer Nano-S instrument (Malvern Instruments Ltd.). The DLS measurements were performed at 25 ºC for 60 seconds (n=3). A confocal laser scanning microscope (Olympus FV1000) was utilized to study the distribution of FITC-dextran throughout RLG microparticles. The size of gelatin nanoparticles and RLG microparticles was determined using scanning electron microscopy by measuring the diameter of 100 and 150 particles, respectively. Similar measurements were performed using FE-SEM images of FIB-etched microparticles to determine the size of their inner pores through measuring the size of 100 pores in 5 different FIB-etched microparticles. For morphological evaluation of particles during the stability and release experiments, at each time point, the tube containing the dispersion of particles was centrifuged at 10000 rpm for 2 min and the supernatant was discarded. Thereafter, 1 ml of acetone/water mixed solution (3/1; V/V) was added into the tube, the particles were redispersed by vortexing, and the suspension was freeze-dried to obtain dry particles.

2.6. Stability tests

Stability of RLG microparticles were assessed by their immersion in distilled water. Around 5 mg of microparticles were added in a 2 ml Eppendorf tube. 2 mL of MilliQ water was added to the tube and the microparticles were dispersed in the liquid by 1 min of vortexing. Subsequently, the tube was left at room temperature for 1 week. Thereafter, the particles were freeze-dried for SEM evaluation as explained above. Moreover, a similar test was performed where the immersion step included 10 min of ultra-sonication of the tube in an ultra-sonication bath.

2.7. *In vitro* release and degradation studies

5 mg of RLG microparticles were added in 1.5 ml Eppendorf tubes (n=5) and 1 ml of PBS, with or without collagenase (400 ng), was added to each tube. Collagenase-containing solutions also contained 0.001 w/v% of sodium azide in order to eliminate potential microbial growth. Thereafter, the tubes were incubated at 37 °C on a rotating plate with a rotation rate of 90 rpm. At each time point, the tubes were centrifuged at 10000 rpm for 2 min, the supernatants were collected for further analysis, fresh solutions were added into the tubes, the microparticles were redispersed by vortexing, and the tubes were put back in the incubator until the next release time point. The experiments were performed for up to 14 days.

2.8. Quantification of vancomycin release

A reverse phase high-performance liquid chromatography (RP-HPLC) using a Hitachi HPLC instrument was utilized to determine the concentration of released vancomycin in the solutions. The HPLC setup consisted of a LiChrospher RP-18 endcapped column (125 mm × 4.0 mm, particle size 5 µm), a Hitachi L-2400 UV detector, a Hitachi L-2130 pump, and a Hitachi L-2200 auto-sampler. For each sample an injection volume of 30 µl was used. A 90:10 (V/V) mixture of ammonia phosphate buffer (50mM; pH 3, adjusted with H_3PO_4) and acetonitrile was used as the mobile phase, which was applied with a flow rate of 1 ml/min. To quantify the vancomycin concentrations without interference from collagenase and gelatin degradation products, the wavelength of the UV detector was set at 198 nm and 240 nm for collagenase-free and collagenase-containing solutions, respectively. A calibration curve was prepared using a range of vancomycin solutions with concentrations between 0.1–40 µg/mL. The amount of released vancomycin was plotted as percentage of the initial vancomycin dissolved in the gelatin suspensions prior to the supercritical CO_2 processing.

2.9. Quantification of dextran release

The concentration of released FITC-dextran molecules in solutions was determined by measuring the fluorescence intensity using a Biotek Synergy HT plate reader (485 nm excitation, 528 nm emission). The amount of released dextran was plotted as percentage of the initial dextran dissolved in the gelatin suspensions prior to the supercritical CO_2 processing.

2.10. Quantification of gelatin degradation

The degradation of gelatin particles was quantified by measuring the amount of proteins released into the supernatant at various time points. The amount of released gelatin in the supernatants was measured using a bicinchoninic acid (BCA) assay. The effect of enzymatic degradation of gelatin on the release profile of dextran was assessed by plotting the amount of enzymatically released dextran versus enzymatic degradation of gelatin at different time points. These values were calculated by deducting the mean values of dextran or soluble gelatin in collagenase-free solutions from their released contents in solutions containing collagenase.

2.11. Quantification of ALP activity

To determine the bioactivity of the ALP proteins after the supercritical CO_2 processing, 15 mg of ALP-free or ALP-containing RLG microparticles were added in 1.5 ml Eppendorf tubes, and 0.5 ml of MilliQ water was added to each tube. Thereafter, the tubes were incubated at room temperature on a rotating plate with a rotation rate of 120 rpm. After 3 days, the tubes were centrifuged at 10000 rpm for 2 min and the supernatants were collected for further analysis. The concentration of proteins, i.e., soluble gelatin and ALP, released from ALP-free or ALP-containing RLG microparticles was determined by analyzing their supernatants using a BCA assay. The concentration of released ALP was calculated by deducting the concentration of released proteins (soluble gelatin) for ALP-free microparticles from the concentration of released proteins (soluble gelatin and ALP) for ALP-containing microparticles. Thereafter, an ALP activity assay was used to analyze the ALP-containing supernatants (10 times diluted) and aqueous solutions of ALP (n=3). Briefly, standard samples were prepared by serial dilutions of 4-nitrophenol (25 to 0 nM). Afterward, 20 µL of buffer solution (0.5M 2-amino-2-methyl-1- propanol) and 80 µL of a standard or experimental sample were added to each well in a 96-well plate. Thereafter, 100 µL of substrate solution (5 mM P-Nitrophenylphosphate disodium salt) was added into each well. Subsequently, the plate was covered with a lid to prevent evaporation and was incubated at 37°C for 1 h. Finally, 100 µl of a stop solution (0.3M NaOH) was added to each well, and the ALP activity was determined by performing absorbance measurements at 405 nm using a Biotek Synergy HT plate reader. ALP activities were normalized to the amount of ALP for each sample.

2.12. *In vitro* cell culture

Prior to cell culture experiments, RLG microparticles were UV-treated for 10 min as a precautionary disinfection step. Cell culture experiments were performed using mouse fibroblastic NIH 3T3 or human osteoblastic MG63 cells. These two cell types were chosen since they are commonly used for cytotoxicity tests of biomaterials and cover a wide range of biomedical application areas. Dulbecco's Modified Eagle's Medium (DMEM, Gibco, Invitrogen Corp., Paisley, Scotland) and α-Minimal Essential Medium (αMEM; Gibco, Invitrogen Corp., Paisley, Scotland) were used as cell culture medium for NIH 3T3 and MG63 cells, respectively. Both medium types were supplemented with 10% fetal calf serum (FCS; Sigma F7524, Taukirchen, Germany), penicillin (100 U/mL) and streptomycin (10 µg/mL).

2.12.1. Cell viability

The cells were seeded in 96-well plates at a density of 10^4 cells per well and incubated for 24 h with 200 µL of the relevant medium. Thereafter, the medium was removed and replaced with fresh medium containing different concentrations of RLG microparticles (25-400 µg/mL). Cells cultured in medium without microparticles or with 10 v/v% dimethylsulfoxide (DMSO) were used as negative and positive controls, respectively. After 24 h, the viability of cells was determined by measuring their metabolic activity using an alamarBlue® assay. Briefly, 20 µL of alamarBlue® reagent were added into each well containing 200 µL of growth medium and incubated at 37 °C for 3 h in the dark. Thereafter, the well plates were centrifuged for 5 min at 2000 rpm, and 100 µL of solution of each well were transferred into a new well in order to avoid potential interference of gelatin microparticles with the alamarBlue® reaction product. Thereafter, the optical absorbance of the solutions was measured at 570 nm, using 600 nm as a reference wavelength, by means of a Biotek Synergy HT plate reader. 6 samples were analyzed for each experimental group. The alamarBlue® reduction by cells in each sample was calculated according to the assay protocol (Thermo Fisher Scientific, Rockford, IL). The cell viability (%) for different microparticle concentrations was expressed relative to the cell viability for the negative and positive control groups, which were considered as 100% and 0%, respectively.

2.12.2. Cell attachment and morphology

The microparticles were dispersed on the surface of circular cover glasses each of

which was fixed in between two stainless steel rings located inside standard cell culture plates. The cells were dispersed in cell-culture medium and seeded on top of the microparticles. After one day of incubation, LIVE/DEAD assay (Molecular Probes, Leiden, the Netherlands) was carried out according to the manufacturer's manual. After staining, the cells were washed with phosphate-buffered saline solution (PBS) and imaging was performed using a fluorescence microscope (Axio Imager Microscope Z1, Carl Zeiss Micro Imaging GmbH, Göttingen, Germany). For scanning electron microscopy, the substrates were washed with PBS, fixated for 5 min in 0.1 M sodium-cacodylate solution containing 2% glutaraldehyde, and washed with 0.1 M sodium-cacodylate. Thereafter, the substrates were dehydrated in a graded series of ethanol/water solutions. Subsequently, a droplet of tetramethylsilane (Sigma) was added on their surface and air dried at room temperature. Finally, the substrates were sputter-coated with a 10 nm thick gold layer and evaluated by scanning electron microscopy (JEOL 6310, Jeol, Tokyo, Japan).

2.13. Statistics

All values were presented as average ± standard deviation. The statistical analyses were carried out using GraphPad Prism software. Statistical differences between experimental groups were determined using a one-way ANOVA (release of vancomycin) or an unpaired Student's t-test (release of dextran and ALP activity), respectively. In both tests, $P<0.05$ was considered as significantly different.

3. Results and discussions

3.1. Formation

In order to assess the size and dispersibility of gelatin nanoparticles prior to the supercritical CO_2 processing, we evaluated these particles in wet and dry state using DLS and SEM techniques, respectively. As shown in Figure 2a, the DLS profile displayed only one sharp peak indicating that the nanoparticles were stable in suspension and did not form aggregates; the average diameter of swollen gelatin nanoparticles was around 478 nm (PdI=0.038). Upon freeze-drying, the nanoparticles did not form clusters and appeared as separated single particles in the SEM micrograph (Figure 2b); the average diameter of freeze-dried gelatin nanoparticles was around 224±55 nm.

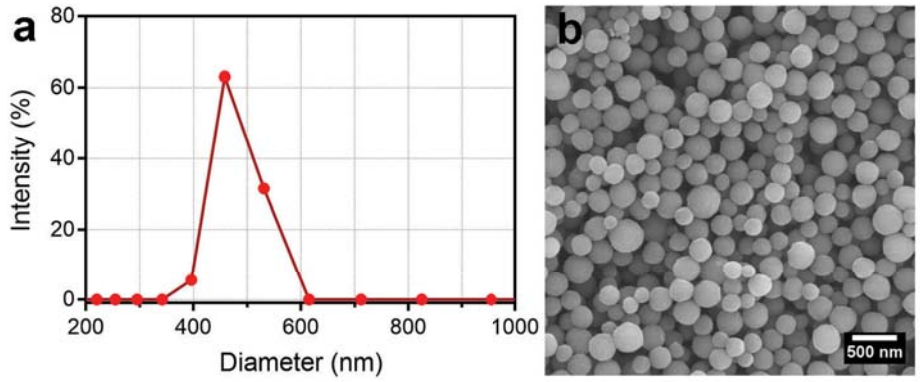

Figure 2. (a) DLS profile of gelatin nanoparticles in aqueous suspension. (b) SEM micrograph of freeze-dried gelatin nanoparticles.

Upon supercritical CO_2 processing of suspensions of gelatin nanoparticles, the nanoparticles were assembled into spherical microparticles displaying a raspberry-like morphology (Figure 3a and 3b). These microparticles had an average diameter of 1.4±0.8 µm, while their diameter increased ~twice when dispersed in water (Figure S1). Remarkably, the gelatin nanoparticles within the RLG microparticles were about 20% smaller (diameter 182±23nm) than the freeze-dried nanoparticles before the supercritical CO_2 processing. To evaluate the interior of the RLG microparticles, we studied their cross-section through FIB-etching. As shown in Figure 3c, their interior was mainly composed of highly packed gelatin nanoparticles, although some nano-pores with an average size of 52±27 nm were randomly distributed inside the microparticles. It should be noted that owing to the flexible nature of gelatin nanoparticles much higher packing densities can be obtained for RLG microparticles (Figure 3c) than for random close packing of monodisperse hard spheres (~0.64) [23, 24]. In general, the mechanism of particle formation by means of supercritical CO_2 processing is known to be a complex process which involves various factors such as hydrodynamics, phase behaviour, mass transport and precipitation kinetics [25]. As illustrated in Figure 1, we propose that atomization of the suspension in the nozzle leads to formation of droplets containing the nanoparticles. Subsequently, CO_2 is absorbed into the droplets, the solvent is gradually extracted, and the nanoparticles are concentrated in the droplets. Ultimately, this process leads to the saturation of nanoparticles inside the droplets, complete extraction of the liquid phase, and assembly of the gelatin nanoparticles into spherical raspberry-like structures [17, 26]. Moreover, the CO_2 also acts as an antisolvent for the biomolecules [27] that are dissolved in the liquid phase of

the gelatin suspension, i.e., vancomycin and dextran, leading to their incorporation into the raspberry-like microspheres. The reduced size and the high packing density of gelatin nanoparticles inside the RLG microparticles can be caused by attractive interparticle capillary forces which arise during the extraction of solvent from the droplets [28]. By assuming a packing density of 100%, we estimate that a single RLG microparticle of average size is composed of around 460 gelatin nanoparticles.

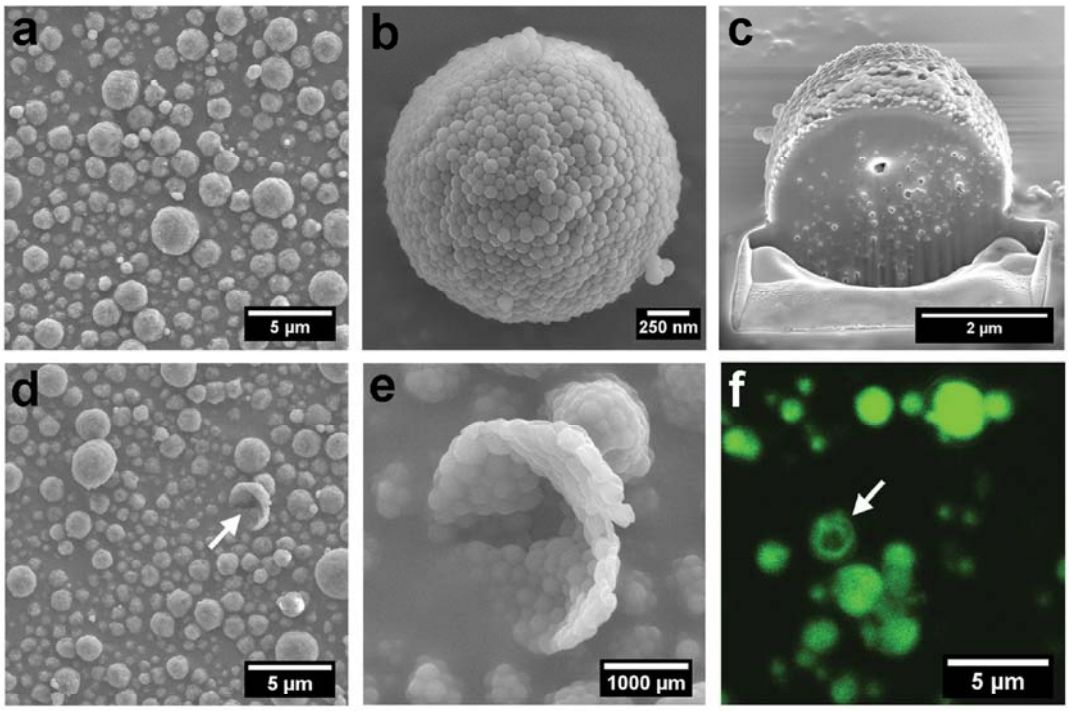

Figure 3. SEM micrographs of (a,b) the RLG microparticles and (c) the cross-section of a RLG microparticle after FIB etching. (d,e) SEM and (f) confocal florescent microscopy images showing rare cases of hollow RLG microparticles formed during the supercritical CO2 processing. The microparticles in (f) contained FITC-Dextran to visualize the hollowness of the microparticles. Arrows indicate hollow microparticles.

Although our observations showed that the vast majority of the RLG microparticles were highly compacted particles, we also occasionally observed hollow microparticles (Figure 3d-f). Based on Figures 3e and 3f, we estimate that a hollow microparticle contains only around 35% of the number of nanoparticles as present in dense RLG microparticle. The formation of hollow microparticles has been commonly reported for particles produced by conventional spray-drying methods, which can be considered as a three-dimensional analogue of the coffee-stain effect [29]. Alternatively, Hao et al. [30] previously observed formation of hollow poly(ethylene glycol) (PEG) microparticles when using a supercritical CO_2 process,

i.e., PGSS (Particles from Gas-Saturated Solutions). The authors postulated that the hollow structure is generated by expansion of entrapped CO_2 bubble inside the microparticles during the spraying. It is not clear yet which mechanism is involved in the formation of these hollow microparticles in our study. Therefore, further studies are required to elucidate the mechanism behind this phenomenon and enable large-scale production of hollow RLG microcapsules.

3.2. Stability

The stability of RLG microspheres depends strongly on the interactions between their colloidal building blocks, i.e., gelatin nanoparticles. Although spherical droplets can form during the atomization process, the microparticles would fall apart into separate nanoparticles upon drying when attractive interactions between the colloidal building blocks would not be sufficiently strong. We observed this condition when we used suspensions of hard and repulsive silica nanoparticles as the initial reagent for the supercritical CO_2 processing (Figure S2). Gelatin not only contains hydrophobic groups, but this macromere also contains, as a natural polyampholyte, both anionic and cationic groups along its chain. Consequently, the dangling gelatin chains on their surface can interact with each other at intermolecular level when the gelatin nanoparticles are in close proximity, leading to formation of stable interparticle bonds through electrostatic and hydrophobic interactions [22, 24]. Moreover, the high packing density of gelatin nanoparticles inside the RLG microparticles causes an increased contact area between the nanoparticles, which can contribute to the stability of the RLG microparticles.

Accordingly, we propose that in order to realize a successful production of stable microparticles from colloidal nanoparticles based on our strategy, long-range repulsions and short-range attractions should co-exist [31] between these nanoparticles in sufficient amounts. In such system, the long-range repulsive forces allow preparation of a stable suspension of the nanoparticles, whereas the short-range attractive forces ensure sufficient bonding between these nanoparticles during the microparticle assembly process. These requirements can be met by using a suitable material for nanoparticle synthesis (e.g. amphiphilic polymers), adjustment of the suspension conditions (e.g. type of solvent, pH, ionic concentration), and/or surface modification of the nanoparticles.

Although these interactions were sufficient to maintain the stability of RLG

microparticles upon drying, in order to realize practical applications of these microparticles, it was necessary to assess their stability upon dispersion in an aqueous media. Therefore, we dispersed the RLG microparticles in distilled water by vortexing (~ 1 min), and kept the dispersion at room temperature for one week. Figures 4a and 4b show the SEM micrographs of lyophilized microparticles after the immersion process. To our surprise, we observed that without the need of any additional chemical cross-linker, these microparticles were stable and could maintain their integrity even after vortexing, soaking, and freeze-drying. On the other hand, when the microparticles were subjected to 10 min of sonication during the immersion process, some of the microparticles were partially de-assembled into separated gelatin nanoparticles (Figures 4c and 4d). This sonication-induced de-assembly can be potentially exploited to facilitate controlled release upon external sonication, thereby allowing to control the time and degree of disintegration of microparticles.

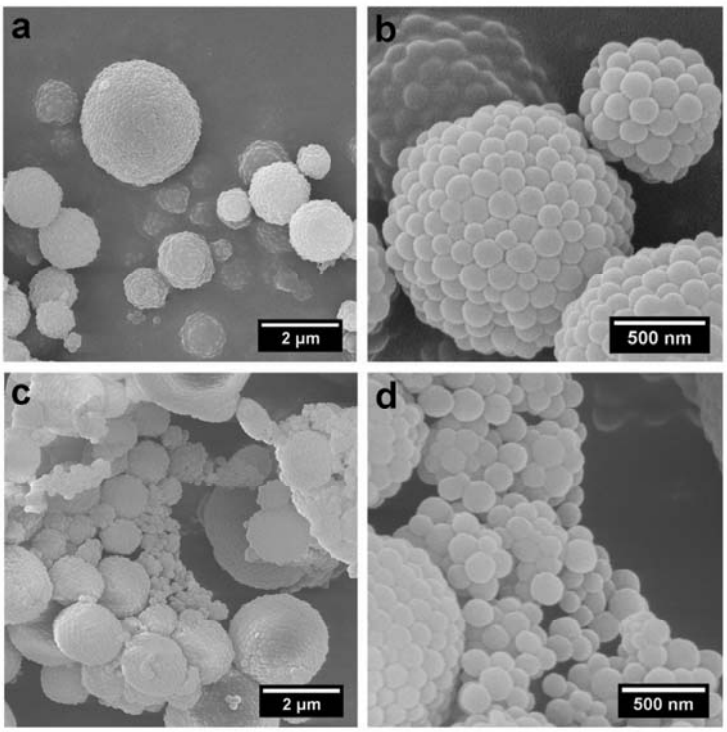

Figure 4. SEM micrographs of RLG microparticles after one week of immersion in water, (a,b) without and (c,d) with sonication.

3.3. Release and degradation

The incorporation of vancomycin and FITC-dextran into RLG microparticles did not influence the size and morphology of the resulting RLG microparticles (Figure S3). The release of vancomycin from the microparticles into the solutions occurred in a sustained manner (Figures 5a and 5b). All vancomycin molecules were released from the microparticles into the solutions within a week. The incorporation of dextran into the microparticles did not affect the vancomycin release profile, as no statistical difference was observed between the vancomycin release profiles of samples with different dextran contents. Importantly, the release of vancomycin was independent from the presence of collagenase in the release medium. Fitting the data for the initial release of vancomycin into to the Ritger–Peppas Equation ($\frac{M_t}{M_\infty} = kt^n$) [32] revealed that the vancomycin release from the RLG microparticles occurs by Fickian diffusion (n≈0.43 and k≈0.19 h^{-n}).

Figures 5c and 5d demonstrate the release profiles of dextran from RLG microparticles containing vancomycin and loaded with low (0.01 wt%) or high (0.2 wt%) dextran contents. For the microparticles containing a low dextran content, around 50% of the dextran was released within the first 6 hours of immersion (Figure 5c). This initial burst release of dextran was increased to around 75% for microparticles loaded with a high dextran content of 0.2 wt% (Figure 5d).

Nevertheless, despite the initial burst release at the first time point, during the rest of the immersion period (up to 14 days), the dextran showed a sustained release profile. Moreover, as confirmed by statistical analysis, the presence of collagenase in the soaking media enhanced the release rate of the dextran, suggesting that the mechanism of dextran release is associated with enzymatic degradation of RLG microparticles, which is in contrast to the profiles observed for vancomycin release. Previous literature [33, 34] showed that the conditions used for supercritical processing of our RLG microparticles do not deactivate biomolecules such as growth factors. These observations were also confirmed by additional tests which showed that the activity of the enzyme ALP was maintained for up to around 80% after inclusion in the RLG microparticles using our encapsulation process (Figure S4).

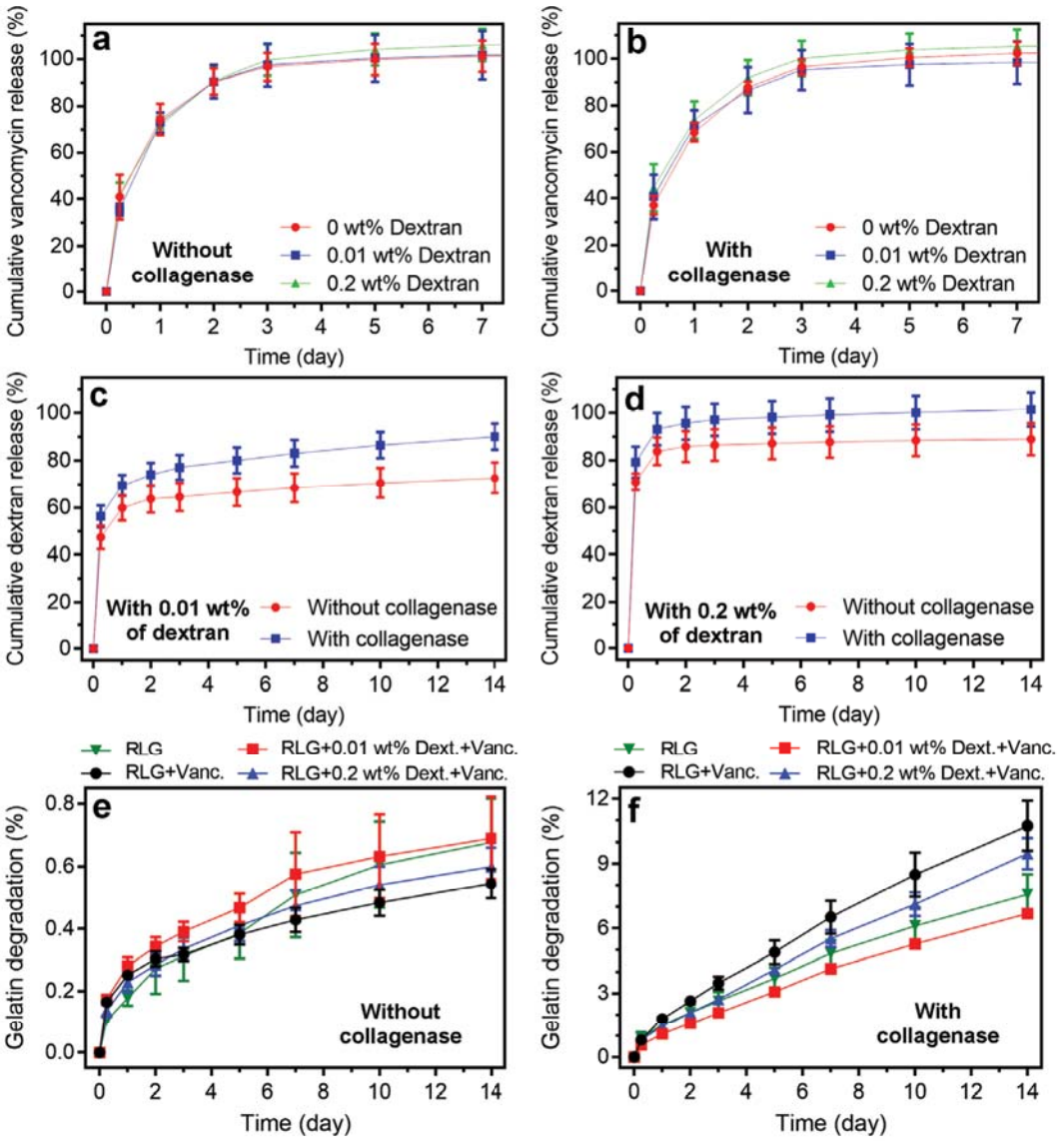

Figure 5. Release kinetics of (a,b) vancomycin, (c,d) dextran, and (e,f) soluble gelatin from RLG microparticles. The microparticles in (a-d) were loaded with 0.5 wt% of vancomycin. All values are presented as average ± standard deviation for n=5 per experimental condition.

In order to obtain more insight into the degradation kinetics of RLG microparticles, we quantified the kinetics of gelatin degradation from RLG microparticles of different composition in the absence or presence of collagenase. Without collagenase (Figure 5e), the amount of released gelatin was negligible (<1 wt%). However, as shown in Figure 5f, when collagenase was present in the solution, gelatin degraded in a linear manner up to 6-12 wt% depending on the type and amount of loaded biomolecules. Surprisingly, incorporation of vancomycin appeared to enhance the degradation of RLG microparticles (Table S1). Such enhancement of the rate of

gelatin degradation might be caused by a reduction in the attractive forces between gelatin nanoparticles upon incorporation of positively charged vancomycin molecules, thereby favoring diffusion of collagenase into the gradually degrading RLG microparticles. Nevertheless, electron microscopy imaging of the RLG microparticles did not reveal any detectable differences between disintegration of these particles with and without vancomycin. Therefore, more studies should be performed to elucidate this phenomenon in more detail.

In order to elucidate the relationship between enzymatic degradation of gelatin and the release of dextran, we plotted the cumulative amount of dextran released into collagenase-containing solutions as a function of enzymatic degradation of gelatin. As shown in Figure 6, a linear relationship between dextran release and gelatin degradation was observed at enzymatic degradation contents higher than 1.5 wt%, indicating that release of dextran was controlled by enzymatic degradation of gelatin. To obtain a deeper understanding of the interplay between RLG microparticle disintegration, degradation and biomolecule release, we studied the morphology of microparticles at different time points.

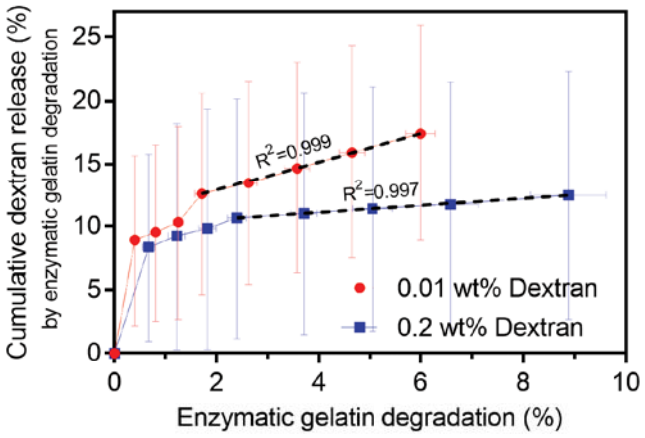

Figure 6. Release of dextran driven by enzymatic degradation of gelatin. The plotted values were calculated using data from figure 5 by deducting the mean values of dextran or soluble gelatin in solutions without collagenase from their released contents in solutions containing collagenase. The dashed lines represent linear regression trend lines. All values are presented as average ± standard deviation for n=5 per experimental condition.

As shown in Figure 7, SEM evaluation of the RLG microparticles revealed that a large number of microparticles retained their integrity up to 14 days of immersion in solutions without collagenase. On the contrary, the microparticles gradually lost their morphological features in solutions containing collagenase, confirming that

RLG microparticles can be degraded enzymatically.

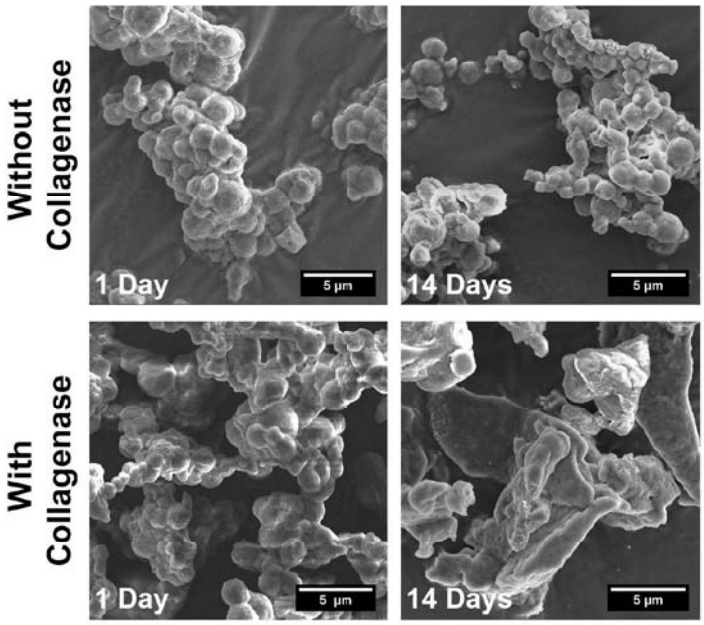

Figure 7. SEM micrographs of the RLG microparticles after 1 and 14 days of immersion in solutions with or without collagenase.

Investigation of the morphology of microparticles at intermediate time points revealed that the disintegration of the microparticles occurred in a gradual manner (Figure 8). The microparticles disintegrated by means of physical separation between the nanoparticles in the absence of collagenase, whereas the disintegration of the microparticles in the presence of collagenase occurred by a combination of physical separation and enzymatic degradation.

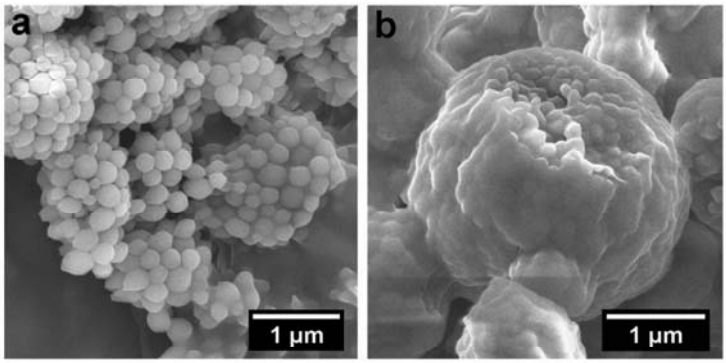

Figure 8. SEM micrographs showing disintegration of the microparticles upon 7 days of immersion in solutions (a) without or (b) with collagenase.

Based on the presented above-mentioned results, Figure 9 proposes a schematic representation of the structure of raspberry-like microparticles and the release mechanism of loaded biomolecules. In general, for both vancomycin and dextran, we observed an incorporation efficiency of near 100% relative to their initial concentrations in the suspensions used for supercritical CO_2 processing. While both of these compounds are polar and therefore fully soluble in the water-acetone solution (3:1; V:V), their insolubility in non-polar CO_2 [27] can lead to their inclusion into RLG microparticles. Considering their smaller size, the vancomycin molecules are likely to be absorbed into the gelatin nanoparticles, whereas the larger dextran molecules are more likely to be incorporated between and on the surface of the gelatin nanoparticles through polyion complexation with gelatin. Our results show that the release of vancomycin from RLG microparticles depends on diffusion rather than enzymatic degradation of the gelatin carriers, which points to the fact that the molecular interactions between vancomycin and gelatin macromers in the RLG microparticles were weak. We expect that slower release kinetics can be achieved for small biomolecules by loading biomolecules with stronger affinity toward the gelatin carriers (e.g. colistin) [35].

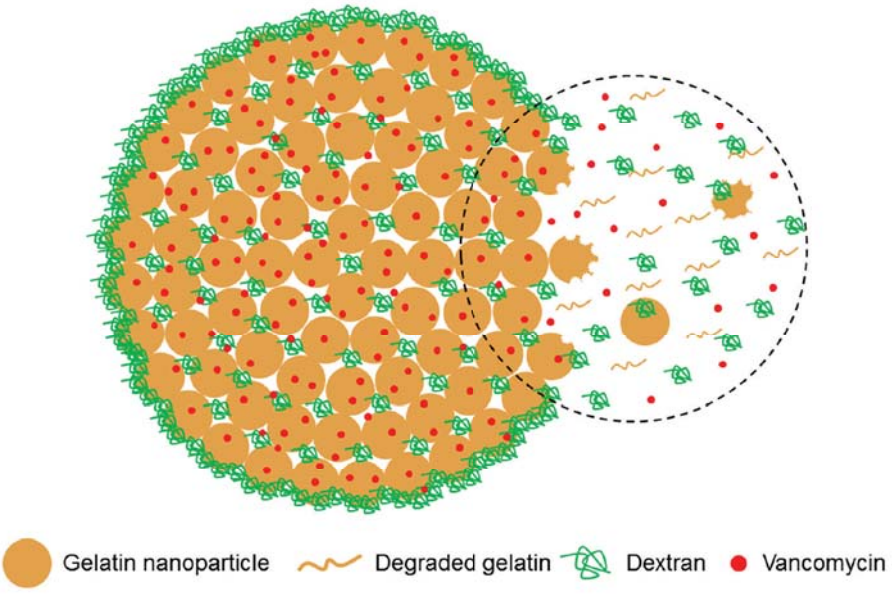

Figure 9. Schematic illustration of the structure of a swollen raspberry-like gelatin microsphere. The black circle shows the release processes.

While vancomycin release was diffusion-controlled and independent from degradation and disintegration of the RLG microparticles, dextran release was

influenced by enzymatic degradation of gelatin, which indicates that molecular interactions are formed between dextran and the gelatin macromers [36-38]. The profile of dextran release, characterized by an initial burst release followed by a subsequent phase of sustained release, is in agreement with previously reported results which show that the release of dextran from collagen matrices depends on swelling, diffusion and erosion processes [39].

In our case, we propose that the initial burst release of dextran was caused by:

(i) desorption of loosely bound dextran molecules from the surface of RLG microparticles;

(ii) release of unbound dextran molecules through the nanopores of swollen RLG microparticles.

During the formation of RLG microparticles, mass transport and removal of liquid phase (Figure 1) occurs at the surface of droplets, which can lead to local increase of dextran concentration closer to the droplets interface and presence of higher concentrations of dextran molecules on the surface of RLG microparticles, leading to adsorption of dextran onto the surface of RLG microparticles. Furthermore, upon swelling of RLG microparticles, their packing density can potentially decrease. Assuming a random close-packing for gelatin nanoparticles inside swollen RLG microparticles, the microparticles can exhibit interparticle pores of ~200 nm, which can provide an open route for unbound dextran molecules (average Stokes radius of 3.3 nm according to the supplier) to diffuse away from the microparticles.

After the initial burst release, the remaining amount of bound dextran was released in a sustained manner caused by disintegration of RLG microparticles and enzymatic degradation of gelatin nanospheres. While the enzymatic degradation leads to a linear release of dextran at prolonged immersion times (Figure 6), it also boosts the release of dextran at earlier stages by accelerating the disintegration of RLG microparticles into separate gelatin nanoparticles. Consequently, the release kinetics can be significantly altered by varying the size of dextran or other biomolecules, For example, Metzmacher et al. [39] demonstrated that enzymatic release of FITC-Dextran could be extended from 5 h to 6 days by increasing the molecular weight from 20 to 70 kDa. At last, our results demonstrate that the linear enzymatic degradation of RLG microparticles (Figure 5f) offers the possibility to obtain sustained long-term release of covalently attached biomolecules such as

bisphosphonates [40].

For comparison, we also assessed the release kinetics of vancomycin and dextran from separate gelatin nanoparticles prepared by simple freeze-drying of their suspensions (Figure S5). While the nanoparticles displayed a similar diffusion-controlled release profile for vancomycin, they were unable to attain a sustained release for dextran. In contrast to the RLG microparticles, the gelatin nanoparticles showed burst release of dextran regardless of the amount of loaded dextran molecules. In the absence of collagenase, more than 80% of the loaded dextran was released from the nanoparticles within the first day of their immersion in PBS solutions, and the remaining amount was completely released in less than 7 days. The difference between the dextran release profiles of gelatin nanoparticles and RLG microparticles was particularly more evident for particles loaded with 0.01 wt% of dextran. This difference highlights the strong influence of the densely packed raspberry-like structure on the release kinetics of dextran from RLG microparticles.

3.4. Cytocompatibility

To evaluate the cytocompatibility of RLG microparticles, the metabolic activity of fibroblastic NIH 3T3 and osteoblastic MG63 cells cultured in the presence of different concentrations of the microparticles for a period of 24 hours was evaluated using an alamarBlue® assay. As shown in Figure 10, the RLG microparticles displayed excellent cytocompatibility with both cell types since cell viabilities exceeded 90% irrespective of the concentration of gelatin microparticles.

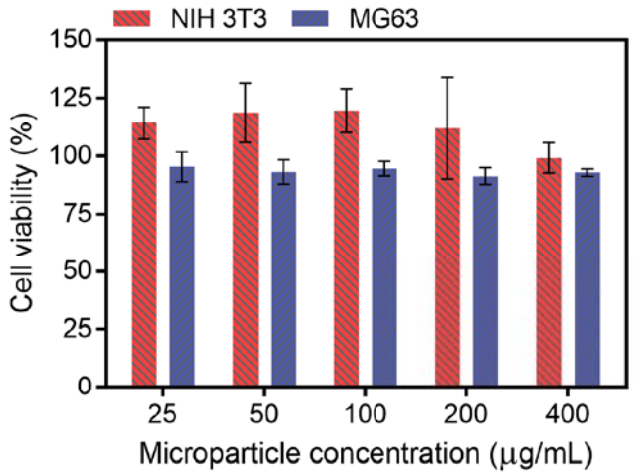

Figure 10. AlamarBlue® assay for different concentrations of RLG microparticles. All values are presented as average ± standard deviation (n=6).

The cytocompatibility of RLG microparticles was also confirmed qualitatively when the cells were stained using a LIVE/DEAD assay (Figure 11), as most of the cells stained green, corresponding to viable cells. Nevertheless, the MG63 cells showed different morphologies depending on the area of the substrate they were attached to. Cells cultured on top of dispersed RLG microparticles exhibited a spread morphology. On the contrary, cells cultured on RLG aggregates (>25 μm) generally did not spread and retained a round shape (Figure S6).

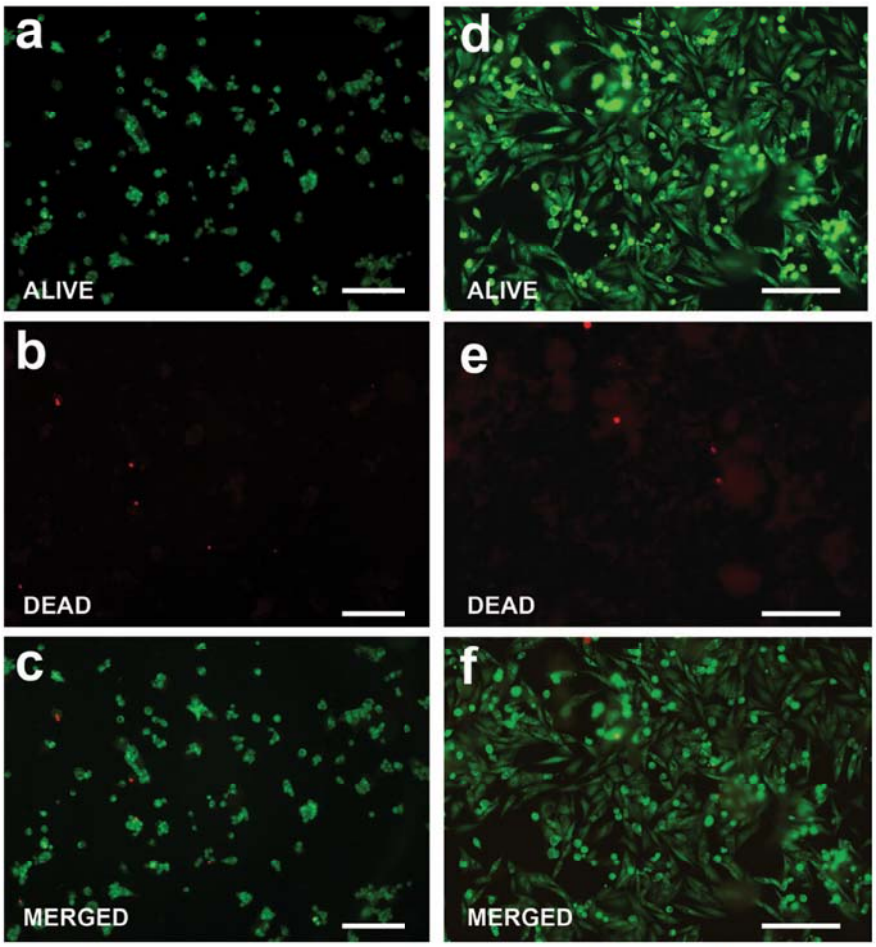

Figure 11. LIVE/DEAD staining of (a-c) NIH 3T3 and (d-f) MG63 cells after 24 h of culture on top of RLG microparticles. Scale bars correspond to 200 μm.

A more detailed evaluation of the MG63 cells by a combination of bright-field and fluorescence microscopy (Figure 12) revealed that cells and particles co-localized, as shown by co-localization between microparticles and green cytosol staining (indicated by red arrows) and co-localization between microparticles and dark unstained vesicle-like structures inside the cells (indicated by white arrows). These observations suggest that microparticles were potentially internalized.

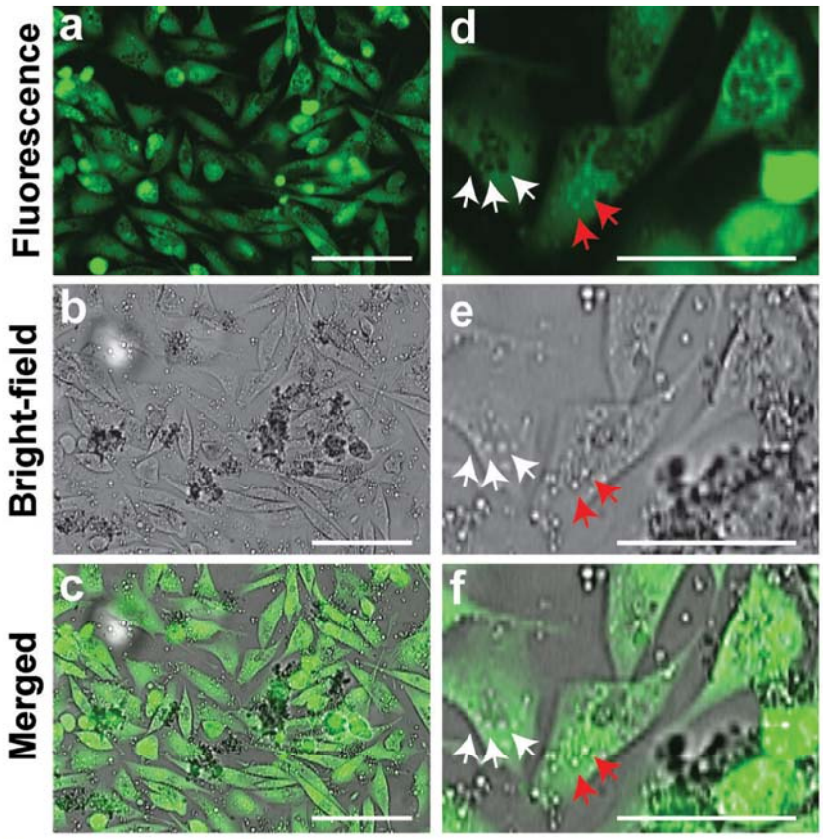

Figure 12. (a-c) Low and (d-f) high magnification images obtained by fluorescence and bright-field microscopy showing co-localization of MG63 cells and RLG microparticles. Scale bars in a-c and d-f correspond to 100 and 50 µm, respectively. In d-f, red and white arrows indicate co-localization of microparticles with cytosol (stained green) and vesicle-like unstained features within cells, respectively.

The SEM analysis (Figure 13) confirmed the observations made by light and fluorescence microscopy. The RLG microparticles were mainly covered by cells. The microparticle morphology could still be recognized despite the fact that the majority of the raspberry-like microparticles were covered by overgrown cells. Moreover, non-aggregated single RLG microspheres could still be observed by means of SEM.

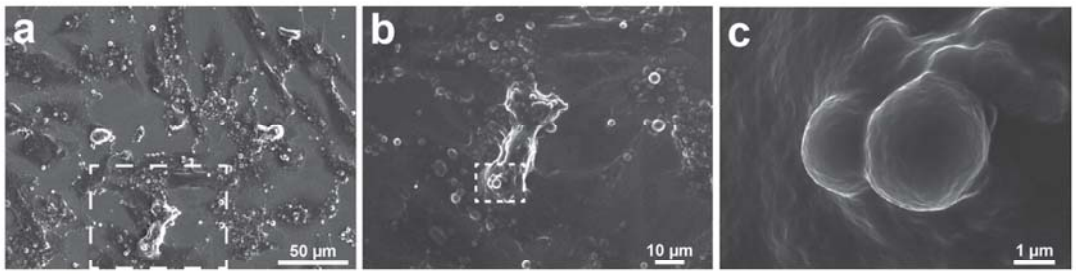

Figure 13. SEM micrographs of MG63 cells after 24 h of culture on top of the RLG microparticles. b and c are high magnification images of white squares in a and b, respectively.

4. Conclusions and outlook

We have demonstrated that nanostructured raspberry-like gelatin microspheres can be successfully produced by supercritical CO_2 processing of suspensions of gelatin nanoparticles. These microparticles are composed of highly packed gelatin nanoparticles, which are bound together through non-covalent interparticle interactions. These interactions are sufficiently strong to hold the microparticles together during immersion in aqueous media and buffers for several days without requiring any covalent cross-linking. Furthermore, we have demonstrated the application of these raspberry-like microspheres for differential release of multiple biomolecules. Release of loaded biomolecules proceeded by means of three different mechanisms, i.e., (i) diffusion-controlled release of unbound small molecules (e.g. vancomycin), (ii) erosion-controlled release of large biomolecules (e.g. dextran), and (iii) degradation-controlled release of biomolecules bound to gelatin macromers through enzymatic degradation. Moreover, cell culture studies revealed that the RLG microparticles were cytocompatible. Therefore, these multicompartment raspberry-like microparticles offer new opportunities for differential delivery of multiple compounds for biomedical applications. The strategy presented here can be utilized as a cost-effective route for production of various types of multicompartment particles using colloidal particles with suitable interparticle interactions.

References

[1] P. Fratzl, R. Weinkamer, Nature's hierarchical materials, Progress in Materials Science 52 (2007) 1263-1334.

[2] T. Speck, I. Burgert, Plant Stems: Functional Design and Mechanics, in: D.R. Clarke, P. Fratzl (Eds.), Annual Review of Materials Research, Vol 41, Annual Reviews, Palo Alto, 2011, pp. 169-193.

[3] B. Alberts, A. Johnson, J. Lewis, M. Raff, K. Roberts, P. Walter, The compartmentalization of cells, (2002).

[4] U.G.K. Wegst, H. Bai, E. Saiz, A.P. Tomsia, R.O. Ritchie, Bioinspired structural materials, Nature Materials 14 (2015) 23-36.

[5] M. Delcea, A. Yashchenok, K. Videnova, O. Kreft, H. Möhwald, A.G. Skirtach, Multicompartmental Micro- and Nanocapsules: Hierarchy and Applications in Biosciences, Macromolecular Bioscience 10 (2010) 465-474.

[6] J. Du, R.K. O'Reilly, Anisotropic particles with patchy, multicompartment and Janus architectures: preparation and application, Chemical Society Reviews 40 (2011) 2402-2416.

[7] E.T. Kisak, B. Coldren, C.A. Evans, C. Boyer, J.A. Zasadzinski, The vesosome - A multicompartment drug delivery vehicle, Current Medicinal Chemistry 11 (2004) 199-219.

[8] W.-F. Lai, A.S. Susha, A.L. Rogach, Multicompartment Microgel Beads for Co-Delivery of Multiple Drugs at Individual Release Rates, ACS Applied Materials & Interfaces 8 (2016) 871-880.

[9] G. Brunner, Applications of Supercritical Fluids, in: J.M. Prausnitz, M.F. Doherty, R.A. Segalman (Eds.), Annual Review of Chemical and Biomolecular Engineering, Vol 1, Annual Reviews, Palo Alto, 2010, pp. 321-342.

[10] Z. Knez, E. Weidner, Particles formation and particle design using supercritical fluids, Current Opinion in Solid State and Materials Science 7 (2003) 353-361.

[11] L. Diaz-Gomez, A. Concheiro, C. Alvarez-Lorenzo, C.A. García-González, Growth factors delivery from hybrid PCL-starch scaffolds processed using supercritical fluid technology, Carbohydrate Polymers 142 (2016) 282-292.

[12] A. Bušić, A. Vojvodić, D. Komes, C. Akkermans, A. Belščak-Cvitanović, M. Stolk, G. Hofland, Comparative evaluation of CO_2 drying as an alternative drying technique of basil (Ocimum basilicum L.) — The effect on bioactive and sensory properties, Food Research International 64 (2014) 34-42.

[13] M. Kamihira, M. Taniguchi, T. Kobayashi, Sterilization of Microorganisms with Supercritical Carbon Dioxide, Agricultural and Biological Chemistry 51 (1987) 407-412.

[14] L.N. Hassani, F. Hindre, T. Beuvier, B. Calvignac, N. Lautram, A. Gibaud, F.

Boury, Lysozyme encapsulation into nanostructured $CaCO_3$ microparticles using a supercritical CO_2 process and comparison with the normal route, Journal of Materials Chemistry B 1 (2013) 4011-4019.
[15] K. Okuyama, M. Abdullah, I. Wuled Lenggoro, F. Iskandar, Preparation of functional nanostructured particles by spray drying, Advanced Powder Technology 17 (2006) 587-611.
[16] O.R. Davies, A.L. Lewis, M.J. Whitaker, H. Tai, K.M. Shakesheff, S.M. Howdle, Applications of supercritical CO_2 in the fabrication of polymer systems for drug delivery and tissue engineering, Advanced Drug Delivery Reviews 60 (2008) 373-387.
[17] N. Jovanović, A. Bouchard, G.W. Hofland, G.-J. Witkamp, D.J.A. Crommelin, W. Jiskoot, Stabilization of Proteins in Dry Powder Formulations Using Supercritical Fluid Technology, Pharmaceutical research 21 (2004) 1955-1969.
[18] R. Ghaderi, P. Artursson, J. Carlfors, Preparation of biodegradable microparticles using solution-enhanced dispersion by supercritical fluids (SEDS), Pharmaceutical research 16 (1999) 676-681.
[19] P. Chattopadhyay, R.B. Gupta, Supercritical CO_2 Based Production of Magnetically Responsive Micro- and Nanoparticles for Drug Targeting, Industrial & Engineering Chemistry Research 41 (2002) 6049-6058.
[20] M. Bahrami, S. Ranjbarian, Production of micro- and nano-composite particles by supercritical carbon dioxide, The Journal of Supercritical Fluids 40 (2007) 263-283.
[21] K. Matsuyama, K. Mishima, K.-i. Hayashi, R. Ohdate, Preparation of Composite Polymer-SiO_2 Particles by Rapid Expansion of Supercritical Solution with a Nonsolvent, Journal of Chemical Engineering of Japan 36 (2003) 1216-1221.
[22] H. Wang, M.B. Hansen, D.W.P.M. Löwik, J.C.M. van Hest, Y. Li, J.A. Jansen, S.C.G. Leeuwenburgh, Oppositely Charged Gelatin Nanospheres as Building Blocks for Injectable and Biodegradable Gels, Advanced Materials 23 (2011) H119-H124.
[23] D.A. Weitz, Packing in the Spheres, Science 303 (2004) 968-969.
[24] M. Diba, H. Wang, T.E. Kodger, S. Parsa, S.C.G. Leeuwenburgh, Highly Elastic and Self-Healing Composite Colloidal Gels, Advanced Materials 29 (2016) 1604672.
[25] Y. Pérez de Diego, H.C. Pellikaan, F.E. Wubbolts, G. Borchard, G.J. Witkamp, P.J. Jansens, Opening new operating windows for polymer and protein micronisation using the PCA process, The Journal of Supercritical Fluids 36 (2006) 216-224.
[26] A. Martín, A. Bouchard, G.W. Hofland, G.J. Witkamp, M.J. Cocero, Mathematical modeling of the mass transfer from aqueous solutions in a supercritical fluid during particle formation, The Journal of Supercritical Fluids 41 (2007) 126-

137.
[27] Y. Pérez, F.E. Wubbolts, G.J. Witkamp, P.J. Jansens, T.W. de Loos, Improved PCA process for the production of nano- and microparticles of polymers, AIChE Journal 50 (2004) 2408-2417.
[28] A.B.D. Nandiyanto, K. Okuyama, Progress in developing spray-drying methods for the production of controlled morphology particles: From the nanometer to submicrometer size ranges, Advanced Powder Technology 22 (2011) 1-19.
[29] Y. Li, Q. Yang, M. Li, Y. Song, Rate-dependent interface capture beyond the coffee-ring effect, Scientific Reports 6 (2016) 24628.
[30] J.Y. Hao, M.J. Whitaker, G. Serhatkulu, K.M. Shakesheff, S.M. Howdle, Supercritical fluid assisted melting of poly(ethylene glycol): a new solvent-free route to microparticles, Journal of Materials Chemistry 15 (2005) 1148-1153.
[31] Y. Liu, Colloidal systems with both a short-range attraction and a long-range repulsion, Chemical Engineering & Process Techniques 1 (2013) 1010.
[32] P.L. Ritger, N.A. Peppas, A simple equation for description of solute release II. Fickian and anomalous release from swellable devices, Journal of Controlled Release 5 (1987) 37-42.
[33] S.M. Howdle, M.S. Watson, M.J. Whitaker, V.K. Popov, M.C. Davies, F.S. Mandel, J.D. Wang, K.M. Shakesheff, Supercritical fluid mixing: preparation of thermally sensitive polymer composites containing bioactive materials, Chemical Communications (2001) 109-110.
[34] R.A. Quirk, R.M. France, K.M. Shakesheff, S.M. Howdle, Supercritical fluid technologies and tissue engineering scaffolds, Current Opinion in Solid State and Materials Science 8 (2004) 313-321.
[35] J. Song, J.C.E. Odekerken, D.W.P.M. Löwik, P.M. López-Pérez, T.J.M. Welting, F. Yang, J.A. Jansen, S.C.G. Leeuwenburgh, Influence of the Molecular Weight and Charge of Antibiotics on Their Release Kinetics From Gelatin Nanospheres, Macromolecular Bioscience 15 (2015) 901-911.
[36] Y.A. Antonov, O.M. Zubova, Phase state of aqueous gelatin–polysaccharide (1)–polysaccharide (2) systems, International Journal of Biological Macromolecules 29 (2001) 67-71.
[37] L. Stobinski, E. Polaczek, K. Rebilas, J. Mazurkiewicz, R. Wrzalik, H.M. Lin, P. Tomasik, Dextran complexes with single-walled carbon nanotubes, Polimery 53 (2008) 571-575.
[38] Y.A. Antonov, I.L. Zhuravleva, R. Cardinaels, P. Moldenaers, Structural studies on the interaction of lysozyme with dextran sulfate, Food Hydrocolloids 44 (2015) 71-80.
[39] I. Metzmacher, F. Radu, M. Bause, P. Knabner, W. Friess, A model describing

the effect of enzymatic degradation on drug release from collagen minirods, European Journal of Pharmaceutics and Biopharmaceutics 67 (2007) 349-360.
[40] K. Farbod, M. Diba, T. Zinkevich, S. Schmidt, M.J. Harrington, A.P.M. Kentgens, S.C.G. Leeuwenburgh, Gelatin Nanoparticles with Enhanced Affinity for Calcium Phosphate, Macromolecular Bioscience 16 (2016) 717-729.

Supporting Information

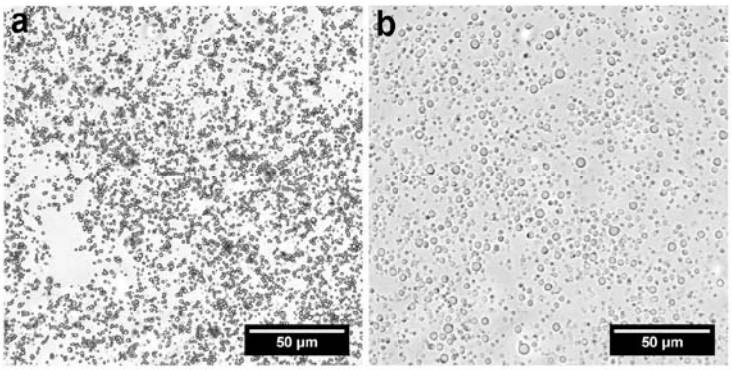

Figure S1. Bright-field optical microscopy images of the RLG microparticles (a) as prepared (in dry state) and (b) dispersed in water.

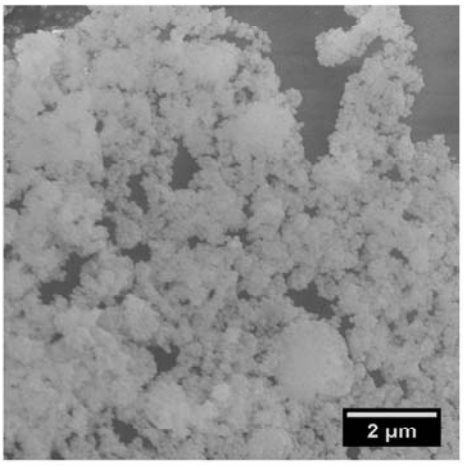

Figure S2. SEM micrograph of supercritical CO_2 processed silica nanoparticles.

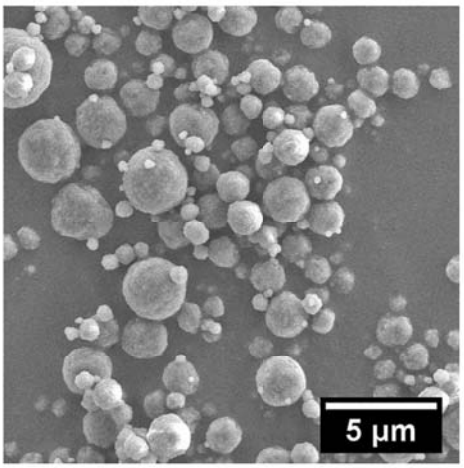

Figure S3. SEM micrograph showing the RLG microparticles containing vancomycin and FITC-Dextran (0.2 wt%).

Table S1. Statistical analysis for the results presented in Figure 5f. "Yes" indicates statistical difference.

Groups	Immersion time (day)							
	0.5	1	2	3	5	7	10	14
RLG+Vanc. vs. RLG+0.01 wt% Dext.+Vanc.	No	Yes	Yes	Yes	Yes	Yes	Yes	Yes
RLG+Vanc. vs. RLG+0.2 wt% Dext.+Vanc.	No	No	Yes	Yes	Yes	Yes	Yes	No
RLG+Vanc. vs. RLG	No	No	Yes	Yes	Yes	Yes	Yes	Yes
RLG+0.01 wt% Dext.+Vanc. vs. RLG	Yes	Yes	Yes	Yes	No	No	No	No
RLG+0.2 wt% Dext.+Vanc. vs. RLG	No	No	No	No	No	No	No	Yes

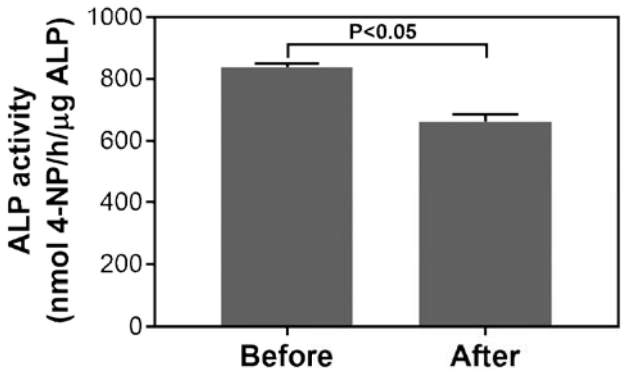

Figure S4. Activity of Alkaline Phosphatase (ALP) enzymes before and after their inclusion in the RLG microparticles using supercritical CO_2 spray-drying. The values are presented as average ± standard deviation for n=3 per experimental condition. Values are presented as average ± standard deviation for n=3 per experimental condition.

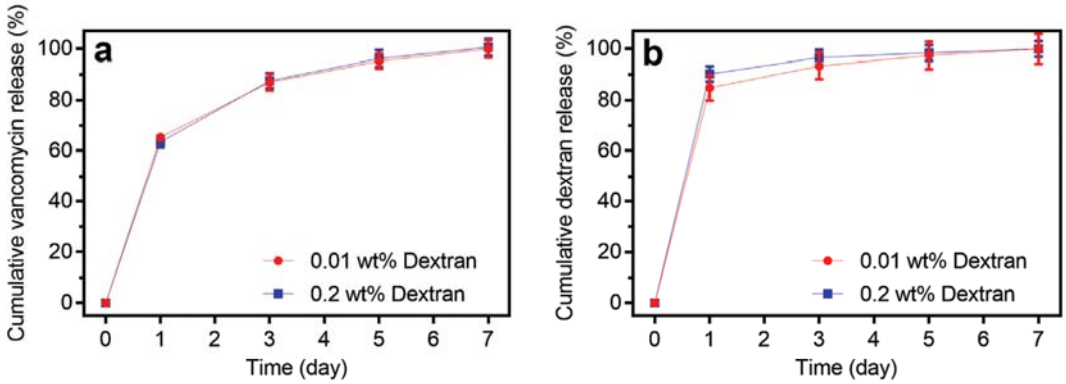

Figure S5. Release kinetics of (a) vancomycin and (b) dextran from freeze-dried gelatin nanoparticles, in PBS solutions without collagenase. The nanoparticles in (a) were loaded with 0.5 wt% of vancomycin. All values are presented as average ± standard deviation for n=5 per experimental condition.

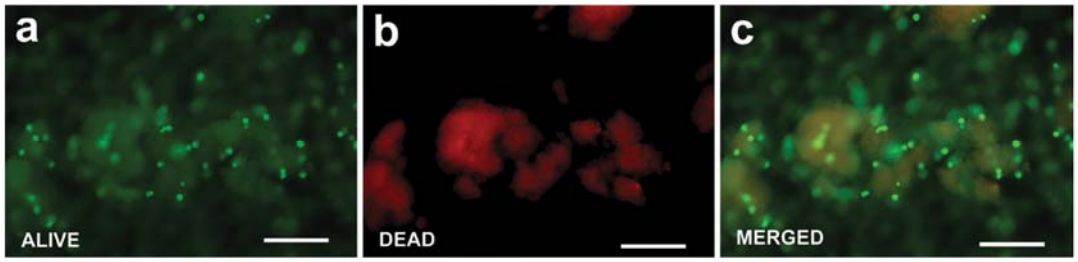

Figure S6. Live/dead staining of MG63 cells after 24 h of culture on top of aggregated RLG microparticles. Large red/green clusters are autofluorescent RLG aggregates. Scale bars correspond to 200 μm.

Figure S7. Higher magnification images from live/dead staining of NIH 3T3 cells after 24 h of culture on top of RLG microparticles. Scale bars correspond to 100 μm.

Chapter 8

Summary, closing remarks
and future perspectives

1. Summary

Colloidal gels are defined as continuous networks of aggregated particles in a liquid phase. This type of gels can form by self-assembly of particles as colloidal building blocks. Traditional application areas of colloidal gels include ceramic and glass processing, paint and coating production, food products, and cosmetics. Colloidal gels are particularly appealing in view of their fascinating viscoelastic properties. By exploiting the reversibility of non-covalent interparticle interactions, colloidal gels can be rendered self-healing. Consequently, self-healing colloidal gels are increasingly considered for biomedical applications such as regenerative medicine. Previously developed self-healing colloidal gels consisted of polymeric particles and were mechanically weak. However, for practical application of self-healing gels, both mechanical robustness and self-healing ability are required. To overcome this mechanical weakness, organic colloidal gels can be reinforced by stiff inorganic nanoparticles, which unfortunately reduced the self-healing capacity dramatically. Nevertheless, such composite colloidal gels that can resist compressive and tensile loads had not been reported before. Furthermore, due to the weak mechanical properties of colloidal gels, their self-healing ability had only been demonstrated by rheological tests. **Chapter 2** presents novel composite colloidal gels which combine high mechanical robustness, by resisting substantial compressive and tensile loads, with a strong capacity for self-healing upon both shear- or cutting-induced failure. This unprecedented combination of mechanical properties and self-healing capacity is enabled by: i) careful control of particle assembly, ii) fundamental understanding of the mechanism of gel network formation, and iii) precise tuning of composition and structure of the resulting gel networks. Amphoteric soft gelatin nanoparticles and negatively charged hard silica nanoparticles are used as the organic and inorganic colloidal building blocks, respectively. To prevent uncontrollable aggregation resulting from direct mixing of attractive binary colloids, electrostatic assembly of the nanoparticles into homogeneous binary networks is facilitated by controlling the pH of the colloidal system. These homogeneous gels exhibit a remarkable self-healing capacity, as evidenced by immediate recovery of gel elasticity upon destructive shearing to values which even exceed initial gel elasticity. Accordingly, this chapter provides new critical insight into the structural and mechanical properties of composite colloidal gels and, more importantly, opens up a new

horizon for applications of colloidal gel systems.

For successful realization of application of self-healing composites in regenerative medicine, these materials should be able to facilitate tissue regeneration *in vivo*. Therefore, **Chapter 3** describes the development of injectable composite colloidal gels for regeneration of osteoporotic bone defects through a bottom-up assembly from bisphosphonate-functionalized gelatin and bioactive glass particles. In this chapter, gelatin is used to prepare the organic building blocks due to its widespread availability, availability of adhesive cell recognition sites, and ease of functionalization. 45S5 bioactive glass (Bioglass®) particles are used as the inorganic building blocks since this glass type is the most common type of bioactive glass due to its strong bone-bonding capacity and biodegradability. Upon bisphosphonate functionalization, gelatin nanoparticles show superior adhesion toward bioactive glass particles, resulting into elastic composite gels. By tuning their composition, these composite colloidal gels combine mechanical robustness with self-healing ability. The composite colloidal gels support cell proliferation and differentiation *in vitro* without requiring any osteogenic supplement. *In vivo* evaluation of the composite colloidal gels reveal a strong capacity to regenerate osteoporotic bone defects. Furthermore, the bisphosphonate modification of gelatin induces a therapeutic effect on the peri-implantation region by enhancing the bone density of the osteoporotic bone tissue. Consequently, these composite colloidal gels offer new therapeutic opportunities for treatment of osteoporotic bone defects.

In **Chapter 4**, the binding affinity of a bisphosphonate-functionalized polymer (i.e. hyaluronan) toward a bioactive glass (i.e. 45S5 Bioglass®) is evaluated using force-distance measurements performed by means of atomic force microscopy. These results show that the bisphosphonate functionalization of hyaluronan results into a strong binding affinity of this polymer for Bioglass®, which even exceeds the well-known binding affinity of bisphosphonate groups for hydroxyapatite. The force microscopy measurements also reveal that bisphosphonate-functionalized polymer chains can establish a polymeric bridge between two adjacent bioactive glass particles. Consequently, the strong and reversible bisphosphonate-bioactive glass interactions are successfully exploited for bridging flocculation of multiple bioactive glass particles, which results into formation of self-healing composite gels. Following this approach, injectable, bioactive and self-healing organic–inorganic

composite hydrogels are produced, which retain their mechanical integrity and mineralize abundantly and rapidly in simulated body fluid. These properties render these composite gels suitable for applications in bone-tissue engineering.

In order to evaluate if the above-mentioned interactions between bioactive glasses and bisphosphonates can be exploited to synthesize novel biomaterials, **Chapter 5** focuses on the formation of hybrid bisphosphonate-bioactive glass particles prepared from amino-bisphosphonate alendronate and Bioglass® particles. To this end, Bioglass® particles are immersed in alendronate solutions at different pH and molar ratios, which results in the formation of novel hybrid particles with various morphologies, compositions and structures based on a precipitation mechanism. By monitoring the formation of these particles as a function of immersion time, in-depth information on this precipitation reaction as well as the interactions between Bioglass® and alendronate are obtained. These hybrid particles facilitate differential release of alendronate drug as well as various inorganic elements (Ca, Na, Si, and P), and stimulate regeneration of osteoporotic bone *in vivo*. Finally, the presented results indicate that these novel hybrid particles represent a great potential for the development of effective treatments for bone defects in osteoporotic patients.

Although organic-inorganic composites are attractive biomaterials for bone tissue regeneration, various biomedical applications such as soft tissue regeneration require biomaterials that are fully organic and biodegradable but also mechanically robust. Therefore, **Chapter 6** describes the development of fully organic fiber-reinforced colloidal gels. In this chapter, gelatin-based colloidal gels are reinforced with discrete sub-micron poly-L-lactic acid (PLLA) fibers of various lengths in order to achieve mechanically strong hydrogels. This reinforcement strategy does not compromise the injectability of these materials, and facilitates the preparation of moldable gels that are mechanically robust. Importantly, the reinforcement of gels using discrete polyester fibers is effective at both macroscopic and microscopic levels, as confirmed by rheological, compression and nanoindentation tests. Finally, these fully organic gels are cytocompatible and can retain their mechanical integrity under physiological conditions for at least one week. Consequently, these materials exhibit a strong potential for applications in soft tissue regeneration.

Materials and organisms in nature owe their functionality to their hierarchical and complex structure. Accordingly, colloidal biomaterials with advanced functionality

can be developed through a hierarchical assembly of smaller particles into complex building blocks. Practical applications of such colloidal biomaterials, however, require large-scale production of their complex building blocks. Supercritical carbon dioxide (CO_2) processing is an industrial technology widely used for large-scale synthesis and processing of materials. Nevertheless, the application of this technology for production of complex particles from smaller colloidal particles had not previously been explored. To this end, **Chapter 7** describes the formation of raspberry-like gelatin (RLG) microparticles composed of gelatin nanoparticles as colloidal building blocks through supercritical CO_2 processing of suspensions of gelatin nanoparticles. These RLG microparticles exhibit a high stability upon dispersion in aqueous media without requiring chemical cross-linking. Owing to the complex and multicompartment structure of the RLG microparticles, two model compounds of different sizes are simultaneously incorporated and released in a controlled manner upon immersion of RLG microparticles in aqueous media. Moreover, cell culture experiments reveal that the RLG microparticles do not impose any cytotoxic effect on fibroblastic and osteoblastic cells. These results not only demonstrate the potential applicability of the RLG microparticles as vehicles for local delivery of multiple compounds, but also pave the way for industrial production of other complex multicompartment particles using the supercritical CO_2 processing technique.

2. Closing remarks and future perspectives

This thesis described the development of self-healing biomaterials using organic and inorganic particles as building blocks. Several strategies were investigated based on the use of reversible physical interactions to develop injectable and self-healing composite gels with suitable mechanical properties and biological functionality to facilitate applications in tissue engineering and regenerative medicine. Several types of particle-based biomaterials were synthesized which surpassed the functional properties of previously developed systems [1-6] in terms of mechanical properties, self-healing and bioactivity. Specifically, the results obtained herein have opened new avenues for further development in the field of composite colloidal biomaterials. Based on these promising results, several directions for future research can be proposed.

2.1. Existing literature

Although the application of colloidal gels as injectable and self-healing biomaterials is a new area of research, scientific literature concerning colloidal gels is vast. The process of colloidal gel formation has been used for synthesis of materials as early as the mid-1800s [7, 8]. Nevertheless, the majority of research in this area has focused on the synthesis of glasses and ceramics [9]. Furthermore, in a conventional sol-gel synthesis procedure, colloids are formed in the same liquid that undergoes a sol-gel transition [9, 10]. Consequently, in these systems, the choice of building blocks is limited due to reaction conditions, and the resulting gels are often not suitable for direct biomedical application due to the cytotoxicity of the liquid phase or reaction byproducts. However, existing literature on sol-gel chemistry can be highly beneficial for further advancement of the research on self-healing colloidal gels for biomedical applications. For example, a wealth of information is already available on sol-gel transition kinetics [11] or the microstructure of colloidal gel networks [12], which can be used for the development of biomedical colloidal gels with improved mechanical properties. Similarly, experimental physicists often use colloidal particles as tools to study the fundamental behavior of condensed matter, for instance by studying the collective phase behavior of the particles to model the behavior of solid materials at the molecular or atomic scale [13]. This information can also be very valuable for the design of novel colloidal biomaterials of improved functionality.

2.2. Material selection

2.2.1. Inorganic particles

The presented results in this thesis revealed that silicate (nano)particles are suitable inorganic materials for the development of composite colloidal gels with self-healing capacity. Although these results showed promising effects of 45S5 Bioglass® particles for bone tissue regeneration, the biological effect of this glass composition can be improved by doping it with therapeutic ions such as silver, strontium, magnesium, boron and/or copper [14]. Nevertheless, further studies are required to determine if these dopants influence the interaction of bioactive glass particles with organic components, particularly those functionalized with bisphosphonates. Moreover, future studies should identify the optimal size of both inorganic and organic particles to maximize both the mechanical properties and

biological functionality (e.g. degradation/release behavior) of the resulting colloidal composites.

2.2.2. Organic particles

With respect to the synthesis of organic nanoparticles, gelatin offers great advantages such as its widespread availability, presence of adhesive cell recognition sites, and ease of functionalization. Nevertheless, batch-to-batch variability complicates the use of gelatin for the synthesis of nanoparticles with reproducible properties and the up-scaling of nanoparticle production for practical applications. For instance, gelatin producers often blend various gelatin sources to reach comparable gel strength (Bloom number), which leads to variations in terms of molecular weight and amino acid composition [15]. Therefore, future studies would benefit from a more consistent gelatin source or well-defined synthetic polymers (preferably containing cell-binding peptides) with a biological performance comparable to gelatin.

2.2.3. Complex particles

A hierarchical assembly strategy based on the use of complex particles assembled from smaller particles [16] can possibly be the basis for development of a next generation of colloidal biomaterials with improved mechanical performance and capacity to deliver multiple biomolecules. For instance, as described in Chapter 7, organic nanoparticles can be first assembled into larger multicompartment particles which could be used subsequently as building blocks for complex colloidal biomaterials. Furthermore, future studies should investigate the combination of organic and inorganic constituents into a single particle type, thereby combining the benefits of both phases in terms of mechanical and biological functionality. Such composite particles might be synthesized by addition of inorganic nanoparticles into the gelatin solution prior to the formation of gelatin nanoparticles, or by combining organic and inorganic particles in suspensions used for supercritical CO_2 processing of microparticles (Chapter 7).

2.3. Functionalization of particles

As shown in Chapter 3, the functionalization of gelatin nanoparticles with bisphosphonate groups enhances their binding affinity toward bioactive glass particles, while also inducing therapeutic effects. Nevertheless, this functionalization did not improve the mechanical properties of colloidal gels at high particle volume

fractions. Therefore, future studies should focus on the effects of other functional groups, such as mineral-binding peptides [17] or hydrophobic alkyl chains [18] for functionalization of the organic building blocks of composite colloidal gels. These alternative functional groups will be particularly interesting for applications where the medicinal effects of bisphosphonates are undesired. Furthermore, future studies should investigate the effects of these novel functionalization strategies on the long-term cohesion of composite gels upon their contact with physiological fluids in view of potential leakage into surrounding tissues.

2.4. Assembly process

With respect to the assembly of colloidal biomaterials, the preparation method and kinetics of gel network formation are of crucial importance. An ideal preparation method should minimize uncontrolled aggregation and allow for tight control over interparticle interactions and their assembly into colloidal networks. In Chapter 2, glucono delta-lactone (GDL) was proven to be an effective reagent for controlled acidification of colloidal suspensions and the induction of gel network formation. Nevertheless, limitations such as the pH-dependent acidification rate make the use of GDL time-consuming, and the control over the kinetics of network formation challenging. Therefore, different acidification strategies or alternative gelation-inducing mechanisms could be investigated to obtain improved control over the assembly kinetics.

2.5. Self-healing and its characterization

The results presented in this thesis demonstrated the benefits of the self-healing capability of colloidal biomaterials for potential use in tissue engineering and regenerative medicine. In particular, the self-healing feature was shown to allow the recovery of mechanical properties of the developed materials upon shear- or cutting-induced mechanical failure, which is highly advantageous for applications such as minimally invasive treatments, three-dimensional printing and injection molding. Moreover, the dynamic and adaptive nature of developed self-healing biomaterials could provide a suitable microenvironment for tissue ingrowth and cellular activity, potentially contributing to the strong tissue regenerative capability of these materials (Chapter 3). Nevertheless, a systematic study is required in order to fully understand the effects of dynamic, adaptive materials on processes such as cell and tissue infiltration. These studies can be performed using both *in vitro* and

in vivo models that monitor the migration, proliferation and differentiation of cells as function of the self-healing capability of biomaterials.

With respect to the evaluation of self-healing capability of biomaterials, a major issue is the lack of standard protocols for mechanical characterizations measuring the self-healing efficacy. Generally, different investigations have used different experimental variables for the mechanical characterization of self-healing properties, which makes the comparison between the reported results difficult. Moreover, it is not yet clear if there is a relationship between the self-healing attained after shear- and cutting-induced failures. Accordingly, a systematic study is essential in order to clarify these issues and establish standard protocols for the mechanical evaluation of self-healing of hydrogels. Such protocols would enable improved understanding of self-healing properties of current and future self-healing gels and will allow direct comparison between reported results in the literature.

The combination of confocal microscopy and rheological results presented in Chapter 2 increased our understanding of the self-healing mechanism of colloidal gels. However, a preferred method to study self-healing mechanisms of hydrogels would be in situ observation of the gel structure during the destruction and reformation processes. Such evaluations could be performed by extruding a colloidal gel inside a microfluidic device while monitoring the gel structure using a confocal microscope.

2.6. Further *in vivo* characterizations

In vivo studies reported in Chapters 3 and 5 employed only one time-point (8 weeks) to evaluate the bone regenerative capability of the materials developed in this thesis. Therefore, further *in vivo* investigations should be carried out using more time-points (both shorter and longer than 8 weeks) to determine the kinetics of bone regeneration as a function of relevant material parameters such as their degradability. Particularly, in view of the promising observation related to the increased bone density of peri-implantation osteoporotic bone upon application of bisphosphonate-functionalized materials (Chapter 3), it should be investigated if this approach provides a permanent solution for local treatment of osteoporotic bone, or if additional systemic administration of bisphosphonate drugs is still requested to maintain this effect. In addition, specific immunohistochemical stains, such as tartrate-resistant acid phosphatase (TRAP), should be used to elucidate the

mechanism of bone regeneration in response to implantation of bisphosphonate-containing colloidal biomaterials in more detail.

References

[1] H. Wang, O.C. Boerman, K. Sariibrahimoglu, Y. Li, J.A. Jansen, S.C.G. Leeuwenburgh, Comparison of micro- vs. nanostructured colloidal gelatin gels for sustained delivery of osteogenic proteins: Bone morphogenetic protein-2 and alkaline phosphatase, Biomaterials 33 (2012) 8695-8703.

[2] H. Wang, M. Bongio, K. Farbod, A.W.G. Nijhuis, J. van den Beucken, O.C. Boerman, J.C.M. van Hest, Y. Li, J.A. Jansen, S.C.G. Leeuwenburgh, Development of injectable organic/inorganic colloidal composite gels made of self-assembling gelatin nanospheres and calcium phosphate nanocrystals, Acta Biomaterialia 10 (2014) 508-519.

[3] H. Wang, M.B. Hansen, D.W.P.M. Löwik, J.C.M. van Hest, Y. Li, J.A. Jansen, S.C.G. Leeuwenburgh, Oppositely Charged Gelatin Nanospheres as Building Blocks for Injectable and Biodegradable Gels, Advanced Materials 23 (2011) H119-H124.

[4] Q. Wang, Z. Gu, S. Jamal, M.S. Detamore, C. Berkland, Hybrid Hydroxyapatite Nanoparticle Colloidal Gels are Injectable Fillers for Bone Tissue Engineering, Tissue Engineering Part A 19 (2013) 2586-2593.

[5] Q. Wang, L. Wang, M.S. Detamore, C. Berkland, Biodegradable Colloidal Gels as Moldable Tissue Engineering Scaffolds, Advanced Materials 20 (2008) 236-239.

[6] S.R. Van Tomme, M.J. van Steenbergen, S.C. De Smedt, C.F. van Nostrum, W.E. Hennink, Self-gelling hydrogels based on oppositely charged dextran microspheres, Biomaterials 26 (2005) 2129-2135.

[7] M. Ebelmen, On the synthesis of silica gels from alkoxides, Annales de chimie et de physique, 1846, p. 129.

[8] T. Graham, XXXV.-On the properties of silicic acid and other analogous colloidal substances, Journal of the Chemical Society 17 (1864) 318-327.

[9] L.L. Hench, J.K. West, The sol-gel process, Chemical Reviews 90 (1990) 33-72.

[10] J.E. Martin, D. Adolf, The sol-gel transition in chemical gels, Annual Review of Physical Chemistry 42 (1991) 311-339.

[11] J.C. Gimel, T. Nicolai, D. Durand, 3D Monte Carlo simulations of diffusion limited cluster aggregation up to the sol-gel transition: Structure and kinetics, Journal of Sol-Gel Science and Technology 15 (1999) 129-136.

[12] K. Nakanishi, Pore Structure Control of Silica Gels Based on Phase Separation, Journal of Porous Materials 4 (1997) 67-112.

[13] P.J. Lu, D.A. Weitz, Colloidal Particles: Crystals, Glasses, and Gels, Annual Review of Condensed Matter Physics 4 (2013) 217-233.

[14] A. Hoppe, N.S. Güldal, A.R. Boccaccini, A review of the biological response to ionic dissolution products from bioactive glasses and glass-ceramics, Biomaterials 32 (2011) 2757-2774.

[15] R. Schrieber, H. Gareis, Gelatine handbook: theory and industrial practice, John Wiley & Sons, 2007.
[16] G.J.d.A.A. Soler-Illia, C. Sanchez, B. Lebeau, J. Patarin, Chemical Strategies To Design Textured Materials: from Microporous and Mesoporous Oxides to Nanonetworks and Hierarchical Structures, Chemical Reviews 102 (2002) 4093-4138.
[17] K. Farbod, M.R. Nejadnik, J.A. Jansen, S.C.G. Leeuwenburgh, Interactions Between Inorganic and Organic Phases in Bone Tissue as a Source of Inspiration for Design of Novel Nanocomposites, Tissue Engineering Part B: Reviews 20 (2013) 173-188.
[18] T. Aewsiri, S. Benjakul, W. Visessanguan, A.B. Encarnacion, P.A. Wierenga, H. Gruppen, Enhancement of Emulsifying Properties of Cuttlefish Skin Gelatin by Modification with N-hydroxysuccinimide Esters of Fatty Acids, Food and Bioprocess Technology 6 (2013) 671-681.

Chapter 9

Samenvatting, slotopmerkingen
en toekomstperspectieven

1. Samenvatting

Colloïdale gels bestaan uit continue netwerken van geaggregeerde deeltjes in een vloeibare matrixfase. Dit soort gels kunnen worden gevormd door zelfassemblage van deeltjes als colloïdale bouwstenen. Traditionele toepassingsgebieden van colloïdale gels omvatten de productie van keramiek, glas, verf, coatings, voedingsmiddelen en cosmetica. Colloïdale gels zijn vooral aantrekkelijk vanwege hun fascinerende viscoelastische eigenschappen. Door gebruik te maken van de reversibiliteit van niet-covalente interacties tussen de deeltjes kunnen colloïdale gels zelfs zelfhelend worden gemaakt. Dientengevolge worden zelfhelende colloïdale gels steeds meer onderzocht voor mogelijke biomedische toepassingen zoals bijvoorbeeld in de regeneratieve geneeskunde.

Eerder ontwikkelde zelfhelende colloïdale gels bestaan uit polymere deeltjes en zijn mechanisch zwak. Voor praktische toepassing van dergelijke zelfhelende gels zijn zowel mechanische robuustheid als een zelfherstellend vermogen vereist. Om de mechanische eigenschappen te verbeteren kunnen organische colloïdale gels worden versterkt met stijve anorganische nanodeeltjes, maar deze strategie vermindert de zelfhelende capaciteit van dergelijke materialen helaas aanzienlijk. Colloïdale composiet-gels die bestand zijn tegen zowel druk- en trekbelastingen zijn derhalve nog niet beschikbaar. Bovendien is het zelfhelende vermogen van deze composieten tot dusver alleen aangetoond door middel van rheologische testen. In **Hoofdstuk 2** wordt een nieuwe type colloïdale composiet-gel beschreven die mechanische robuustheid (blijkens een relatief hoge weerstand tegen trek- en drukbelasting) combineert met een sterke zelfhelende capaciteit. Deze unieke combinatie van mechanische eigenschappen werd mogelijk gemaakt door: i) zorgvuldige controle over de assemblage van de deeltjes, ii) fundamenteel begrip van het mechanisme waarmee de colloïdale netwerken gevormd worden, en iii) nauwkeurige controle over de samenstelling en structuur van de resulterende colloïdale netwerken. Amfotere zachte gelatine nanodeeltjes en negatief geladen en harde silica nanodeeltjes werden gebruikt als de organische respectievelijk anorganische colloïdale bouwstenen. Om oncontroleerbare aggregatie te voorkomen als gevolg van vermenging van deze bouwstenen werd de pH van de colloïdale gel zorgvuldig ingesteld. Deze homogene gels vertonen een opmerkelijke zelfhelende capaciteit, zoals blijkt uit het feit dat de elasticiteit van de gels na destructieve

schuifbelasting hoger was dan voor de beschadiging van de gels. Concluderend kan worden gesteld dat Hoofdstuk 2 met name kritisch inzicht geeft in de structurele en mechanische eigenschappen van colloïdale composiet-gels, waarmee nieuwe toepassingsgebieden mogelijk gemaakt kunnen worden.

Voor een succesvolle toepassing van zelfhelende composieten in de regeneratieve geneeskunde zouden deze materialen *in vivo* weefselregeneratie dienen te vergemakkelijken. Daarom beschrijft **Hoofdstuk 3** de ontwikkeling van injecteerbare colloïdale composiet-gels op basis van bisfosfonaat-gefunctionaliseerde gelatine en bioactieve glasdeeltjes ten behoeve van de regeneratie van osteoporotische botdefecten 45S5 bioactieve glas (Bioglass®) deeltjes worden gebruikt als anorganische bouwstenen omdat dit type glas het ermogen heeft om aan bot te binden en biologisch afbreekbaar is. Na functionalisatie van de nanodeeltjes met bisfosfonaat groepen vertonen de gelatine nanodeeltjes een sterke hechting aan bioactieve glasdeeltjes, wat resulteert in elastische composiet-gels. Door afstemming van hun samenstelling kunnen deze colloïdale composiet-gels mechanische robuustheid combineren met een zelfhelend vermogen. De colloïdale composiet-gels ondersteunen zowel de *in vitro* proliferatie als differentiatie van cellen zonder dat hiervoor osteogene supplementen gebruikt dienen te worden. In een proefdierstudie blijkt de colloïdale gels in staat te zijn om osteoporotische botdefecten te regenereren. Bovendien heeft de modificatie van gelatine met bisfosfonaat groepen een positief therapeutisch effect op de dichtheid van het osteoporotisch bot rondom het aangebrachte implantaat. Deze nieuwe colloïdale composiet-gels bieden derhalve nieuwe therapeutische mogelijkheden voor de behandeling van osteoporotische botdefecten.

In **Hoofdstuk 4** is de bindingsaffiniteit van een bisfosfonaat-functionaliseerd polymeer (hyaluronan) met bioactief glas (45S5 Bioglass®) gekarakteriseerd met behulp van atomic force microscopie (AFM). Deze resultaten tonen aan dat de functionalisatie van hyaluronan met bisfosfonaat leidt tot een verbeterde affiniteit met Bioglas®, waarbij de bindingsaffiniteit met Bioglas® zelfs sterker is dan de binding emt hydroxyapatiet. De AFM metingen onthullen ook dat bisfosfonaat-functionaliseerde polymeerketens een brug kunnen vormen tussen twee aangrenzende bioactieve glasdeeltjes. Dankzij deze sterke en reversibele interacties kunnen injecteerbare, bioactieve en zelfhelende organisch-anorganische

composiet-gels gefabriceerd worden met een gunstige mechanisch gedrag behouden en de capaciteit om te mineraliseren in een simulerende lichaamsvloeistof. Deze eigenschappen maken deze composiet-gels zeer aantrekkelijk voor toepassing in de regeneratie van botweefsel.

Om te beoordelen of de hierboven beschreven interacties tussen bioactieve glasdeeltjes en bisfosfonaten kunnen worden gebruikt om nieuwe biomaterialen te synthetiseren, richt **Hoofdstuk 5** zich op de vorming van hybride deeltjes bereid uit amino-bisfosfonaat alendronaat en Bioglas® deeltjes. Daartoe worden Bioglas® deeltjes ondergedompeld in alendronaat-oplossingen bij verschillende pH-waarden en molaire verhoudingen. Deze methode resulteert in de vorming van nieuwe hybride deeltjes met variabele morfologie, samenstelling en structuur. Door de vorming van deze deeltjes te bestuderen als functie van de onderdompelingstijd, is nuttige informatie verkregen over deze neerslagreactie en de interacties tussen Bioglas® en alendronaat. Deze hybride deeltjes maken het mogelijk om zowel alendronaat als anorganische elementen af te geven (Ca, Na, Si en P), waarmee de regeneratie van osteoporotisch bot *in vivo* versneld kan worden. De resultaten van Hoofdstuk 5 tonen daarmee aan dat deze nieuwe hybride deeltjes veelbelovend zijn voor de ontwikkeling van een effectieve behandelingen van botdefecten in osteoporotische patiënten.

Hoewel organische-anorganische composieten aantrekkelijke biomaterialen zijn voor het regenereren van botweefsel, kunnen anorganische bouwstenen dikwijls niet worden toegepast bij biomedische toepassingen zoals de regeneratie van zachte weefsels. Desondanks dienen materialen voor regeneratie van zachte weefsels in veel gevallen ook mechanisch sterk te zijn. Daarom beschrijft **Hoofdstuk 6** de ontwikkeling van volledig organische, vezelversterkte colloïdale gels. In dit hoofdstuk worden gelatine-gebaseerde colloïdale gels versterkt met discrete sub-micron poly-L-melkzuurvezels om mechanisch sterke hydrogelen te vervaardigen. Deze strategie belemmert de injecteerbaarheid van deze materialen niet, en vergemakkelijkt de bereiding van mechanisch robuuste gels. De versterking van gels met behulp van discrete polyestervezels is effectief op zowel macroscopische als microscopische schaal, zoals blijkt uit rheologische, druk- en nanoindentatie testen. Deze volledig organische gels zijn cytocompatibel en behouden hun mechanische integriteit gedurende minstens een week onder fysiologische omstandigheden.

Deze materialen zijn derhalve veelbelovend voor toepassingen op het gebied van regeneratie van zachte weefsels.

Materialen en organismen in de natuur ontlenen hun functionaliteit aan hun hiërarchische en complexe structuur. Vanuit deze gedachte kunnen colloïdale biomaterialen met geavanceerde functionaliteit worden ontwikkeld door kleinere deeltjes op hiërarchische wijze te assembleren tot complexe bouwstenen. Praktische toepassingen van dergelijke colloïdale biomaterialen vereisen echter productietechnologieën die opschaling mogelijk maken. Superkritische kooldioxide (CO_2) wordt op industriële schaal toegepast in diverse technologieën om materialen te vervaardigen en te verwerken. Toch is de toepassing van deze technologie voor de productie van complexe deeltjes uit kleinere colloïdale deeltjes niet eerder onderzocht. Daartoe beschrijft **Hoofdstuk 7** de vorming van framboosachtige gelatine (RLG) microdeeltjes uit gelatine nanodeeltjes met behulp van superkritisch CO_2. Deze RLG microdeeltjes zijn stabiel in waterige media zonder verdere chemsiche crosslinking. Dankzij de complexe structuur van de RLG microdeeltjes kunnen twee modelverbindingen van verschillende moleculaire afmetingen op een gecontroleerde wijze ingebouwd en afgegeven worden. Bovendien laten celkweek experimenten zien dat de RLG microdeeltjes geen cytotoxisch effect op fibroblastische en osteoblastische cellen hebben. Deze resultaten tonen de mogelijke toepasbaarheid van de RLG microdeeltjes aan voor lokale afgifte van meerdere geneesmiddelen. Daarnaast toont dit hoofdstuk aan dat complexe deeltjes op industriele schaal vervaardigd kunnen worden door gebruik te maken van superkritisch CO_2.

2. Slotopmerkingen en toekomstperspectieven

Dit proefschrift beschrijft de ontwikkeling van zelfhelende biomaterialen op basis van organische en anorganische deeltjes. Diverse strategieën zijn onderzocht om injecteerbare en zelfhelende composiet-gels met geschikte mechanische en biologische eigenschappen te ontwikkelen voor toepassingen in tissue engineering en regeneratieve geneeskunde. Verscheidene soorten biomaterialen zijn gesynthetiseerd met betere functionele eigenschappen dan eerder ontwikkelde systemen [1-6] qua mechanische eigenschappen, zelfheling en bioactiviteit. De beschreven resultaten hebben nieuwe mogelijkheden geopend voor verdere ontwikkeling op het gebied van colloïdale composiet biomaterialen. Op basis van deze veelbelovende resultaten

zijn diverse richtingen voor toekomstig onderzoek mogelijk.

2.1. Bestaande literatuur

Hoewel de toepassing van colloïdale gels als injecteerbare en zelfhelende biomaterialen een nieuw onderzoeksgebied behelst, is de hoeveelheid wetenschappelijke literatuur over colloïdale gels groot. Het proces van colloïdale gelvorming is al sinds het midden van de negentiende eeuw gebruikt voor synthese van materialen [7, 8]. De meerderheid van deze literatuur is echter gericht op de synthese van glas en keramiek [9]. Bovendien worden in een conventionele sol-gel synthese colloïden gevormd in dezelfde matrixvloeistof die vervolgens een sol-gel overgang ondergaat [9, 10]. Dientengevolge is in deze systemen de selectie van bouwstenen beperkt door de reactieomstandigheden, en de resulterende gels zijn vaak niet geschikt voor directe biomedische toepassingen door de cytotoxiciteit van de vloeibare fase en/of reactiebijproducten. Bestaande literatuur over sol-gel chemie kan echter zeer nuttig zijn voor verder onderzoek naar zelfhelende colloïdale gels voor biomedische toepassingen. Zo is er al veel informatie beschikbaar over de kinetiek van de hierboven beschreven sol-gel overgang [11] of de microstructuur van colloïdale gelnetwerken [12]. Deze kennis kan worden gebruikt voor de ontwikkeling van biomedische colloïdale gels met verbeterde mechanische eigenschappen. Op dezelfde manier gebruiken experimentele fysici vaak colloïdale deeltjes als hulpmiddel om het fundamentele gedrag van gecondenseerde materie te bestuderen, bijvoorbeeld door het collectieve fase-gedrag van de deeltjes te bestuderen om de eigenschappen van vaste materialen op moleculaire- of atomaire schaal te modelleren [13]. Deze informatie kan ook zeer waardevol zijn voor het ontwerpen van nieuwe colloïdale biomaterialen met verbeterde functionaliteit.

2.2. Materiaalselectie

2.2.1. Anorganische deeltjes

De gepresenteerde resultaten in dit proefschrift hebben aangetoond dat silicaat (nano)deeltjes geschikte anorganische materialen zijn voor de ontwikkeling van colloïdale composiet-gels met zelfhelende capaciteit. Hoewel het effect van 45S5 Bioglas® deeltjes op de regeneratie van botweefsel positief was, kan het biologische effect van dit type bioactief glas worden verbeterd door dotering met ionen zoals zilver, strontium, magnesium, boor en/of koper [14]. Desalniettemin

zijn verdere studies nodig om te bepalen of deze elementen de interactie van bioactieve glasdeeltjes met (bisfosfonaat-gemodificeerde) organische componenten beïnvloeden. Bovendien dienen toekomstige studies de optimale grootte van zowel anorganische en organische deeltjes te identificeren om zowel de mechanische eigenschappen als de biologische functionaliteit van de resulterende colloïdale composieten te maximaliseren.

2.2.2. Organische deeltjes

Voor de synthese van organische nanodeeltjes biedt gelatine grote voordelen aangezien gelatine makkelijk verkrijgbaar is, hechting van cellen mogelijk maakt en makkelijk te functionaliseren is. Toch compliceert de batch-to-batch variabiliteit het gebruik van gelatine voor de synthese van nanodeeltjes met reproduceerbare eigenschappen en de schaalbaarheid van de productie van nanodeeltjes voor praktische toepassingen. Producenten van gelatine mengen vaak verschillende typen gelatine om een vergelijkbare gelsterkte te bereiken (uitgedrukt als Bloom-sterkte), wat leidt tot variaties in termen van molecuulgewicht en aminozuur samenstelling [15]. Daarom zouden toekomstige studies gebaat zijn bij een meer consistente bron van gelatine of zelfs synthetische (bio-)polymeren met een biologische gedrag dat vergelijkbaar is met gelatine.

2.2.3. Complexe deeltjes

Een hiërarchische assemblage-strategie gebaseerd op de vorming van complexe deeltjes uit kleinere bouwstenen [16] kan mogelijk dienen als basis voor de ontwikkeling van een nieuwe generatie colloïdale materialen met zowel verbeterde mechanische eigenschappen als de capaciteit om meerdere biomoleculen af te geven. Zoals beschreven in Hoofdstuk 7 kunnen organische nanodeeltjes eerst worden geassembleerd tot grotere deeltjes met meerdere compartimenten, die vervolgens als bouwstenen voor complexe colloïdale biomaterialen kunnen worden gebruikt. Bovendien dienen toekomstige studies de combinatie van organische en anorganische bestanddelen in een enkel deeltje te onderzoeken, waardoor de voordelen van beide fasen kunnen worden gecombineerd. Dergelijke composiet-deeltjes kunnen worden gesynthetiseerd door toevoeging van anorganische nanodeeltjes in de gelatineoplossing voorafgaand aan de vorming van gelatine nanodeeltjes, of door organische en anorganische deeltjes in suspensies combineren die gebruikt worden voor superkritische CO_2 verwerking van microdeeltjes

(Hoofdstuk 7).

2.3. Functionalisatie van deeltjes

Zoals getoond in Hoofdstuk 3 verbetert de functionalisatie van gelatine nanodeeltjes met bisfosfonaatgroepen hun bindingsaffiniteit met bioactieve glasdeeltjes, terwijl deze groepen ook een therapeutisch efect kunnen sorteren. Toch verbetert deze functionalisatie de mechanische eigenschappen van colloïdale gels bij een hoog vastestof-percentage niet. Daarom dienen toekomstige studies de effecten van andere functionele groepen te onderzoeken, zoals bijvoorbeeld mineraal-bindende peptiden [17] of hydrofobe alkylketens [18] voor de functionalisatie van de organische bouwstenen van colloïdale composiet-gels. Deze alternatieve functionele groepen kunnen bijzonder interessant zijn voor toepassingen waarin het gebruik van bisfosfonaten ongewenst is. Bovendien moeten de effecten van deze nieuwe functionalisatie-strategieën op de cohesie van composiet-gels worden onderzocht om lekkage in omliggende weefsels te voorkomen.

2.4. Assemblageproces

Voor de assemblage van colloïdale biomaterialen zijn de bereiding en kinetiek van netwerkvorming van cruciaal belang. Een ideale bereidingstechniek moet aggregatie minimaliseren en de controle over interacties tussen de deeltjes alsmede hun assemblage tot colloïdale netwerken mogelijk maken. In Hoofdstuk 2 is glucono delta-lactone (GDL) gebruikt als een effectief middel voor gecontroleerde verzuring van colloïdale suspensies als basis voor de vorming van colloïdale netwerken. De snelheid van verzuring is echter pH-afhankelijk, wat de controle over de kinetiek van netwerkvorming uitdagend maakt. Daarom kunnen verschillende verzuringstrategieën of alternatieve mechanismen worden onderzocht om verbeterde controle over de assemblagekinetiek te verkrijgen.

2.5. Zelfheling en zijn karakterisering

De resultaten die in dit proefschrift worden beschreven hebben de voordelen aangetoond van het zelfhelende vermogen van colloïdale biomaterialen voor potentieel gebruik in tissue engineering en regeneratieve geneeskunde. In het bijzonder werd het proces van zelfheling onderzocht na mechansiche beschadiging. Dergelijk zelfhelend gedrag is zeer voordelig voor toepassingen zoals minimaal invasieve behandelingen, 3D-printen en spuitgieten. Bovendien kan het dynamisch

en adaptief karakter van de ontwikkelde zelfhelende biomaterialen een geschikte micro-omgeving vormen ingroei van cellen en weefsels, wat potentieel kan bijdragen aan het weefselregeneratieve vermogen van deze materialen (Hoofdstuk 3). Desondanks is een systematische studie nodig om de effecten van dynamische, adaptieve materialen op processen zoals cel- en weefselinfiltratie volledig te begrijpen. Deze studies kunnen worden uitgevoerd met behulp van zowel *in vitro* als *in vivo* modellen die de migratie, proliferatie en differentiatie van cellen kunnen bestuderen als functie van het zelfhelende vermogen van biomaterialen. Voor de evaluatie van het zelfhelende vermogen van biomaterialen is een belangrijk probleem het gebrek aan standaardprotocollen voor mechanische karakterisering van dit zelfherstellend vermogen. Verschillende onderzoeken rapporteren verschillende experimentele variabelen voor de mechanische karakterisering van zelfhelende eigenschappen, wat de vergelijking tussen de gerapporteerde resultaten bemoeilijkt. Een systematische studie is derhalve van essentieel belang om deze problemen op te lossen en standaardprotocollen voor de mechanische evaluatie van zelfhelende hydrogels vast te leggen. Dergelijke protocollen dienen een beter begrip van zelfhelende eigenschappen te geven en directe vergelijking tussen gerapporteerde resultaten in de literatuur mogelijk te maken. De combinatie van confocale microscopie en rheologische karakterisatie zoals beschreven in Hoofdstuk 2 heeft het begrip van het zelfhelende mechanisme van colloïdale gels verbeterd. Meer inzicht in de zelfhelende mechanismen van hydrogelen zou kunnen worden verkregen door in situ bestudering van de gelstructuur tijdens het proces van mechanische beschadiging en het eropvolgende herstel. Dergelijke studies zouden kunnen worden uitgevoerd door een colloïdale gel in een microfluïdische opstelling aan te brengen waardoor de gelstructuur met confocale microscopie bestudeerd kan worden.

2.6. Verdere *in vivo* studies

De *in vivo* studies die in Hoofdstuk 3 en 5 zijn gerapporteerd, rapporteren slechts één tijdspunt (8 weken) om de het regeneratieve vermogen van de in dit proefschrift ontwikkelde materialen te evalueren. Daarom dient verder *in vivo* onderzoek plaats te vinden met meer tijdstippen (zowel korter als langer dan 8 weken) om de kinetiek van botregeneratie te bestuderen als een functie van relevante materiaalparameters zoals hun biologische afbreekbaarheid. Gezien de positieve

effecten van bisfosfonaat-gefunctionaliseerde materialen op de regeneratie van osteoporotisch bot (Hoofdstuk 3) kan worden onderzocht of deze aanpak een permanente oplossing biedt voor de lokale behandeling van osteoporotisch bot, of dat additionele systemische toediening van bisfosfonaten alsnog nodig is om een effect op de lange termijn te garanderen. Daarnaast moeten specifieke kleuringen zoals bijvoorbeeld voor tartraat-resistente zure fosfatase (TRAP) worden toegepast om het mechanisme van botregeneratie als reactie op implantatie van bisfosfonaat-houdende colloïdale biomaterialen in meer detail te kunnen verklaren.

Referenties

[1] H. Wang, O.C. Boerman, K. Sariibrahimoglu, Y. Li, J.A. Jansen, S.C.G. Leeuwenburgh, Comparison of micro- vs. nanostructured colloidal gelatin gels for sustained delivery of osteogenic proteins: Bone morphogenetic protein-2 and alkaline phosphatase, Biomaterials 33 (2012) 8695-8703.

[2] H. Wang, M. Bongio, K. Farbod, A.W.G. Nijhuis, J. van den Beucken, O.C. Boerman, J.C.M. van Hest, Y. Li, J.A. Jansen, S.C.G. Leeuwenburgh, Development of injectable organic/inorganic colloidal composite gels made of self-assembling gelatin nanospheres and calcium phosphate nanocrystals, Acta Biomaterialia 10 (2014) 508-519.

[3] H. Wang, M.B. Hansen, D.W.P.M. Löwik, J.C.M. van Hest, Y. Li, J.A. Jansen, S.C.G. Leeuwenburgh, Oppositely Charged Gelatin Nanospheres as Building Blocks for Injectable and Biodegradable Gels, Advanced Materials 23 (2011) H119-H124.

[4] Q. Wang, Z. Gu, S. Jamal, M.S. Detamore, C. Berkland, Hybrid Hydroxyapatite Nanoparticle Colloidal Gels are Injectable Fillers for Bone Tissue Engineering, Tissue Engineering Part A 19 (2013) 2586-2593.

[5] Q. Wang, L. Wang, M.S. Detamore, C. Berkland, Biodegradable Colloidal Gels as Moldable Tissue Engineering Scaffolds, Advanced Materials 20 (2008) 236-239.

[6] S.R. Van Tomme, M.J. van Steenbergen, S.C. De Smedt, C.F. van Nostrum, W.E. Hennink, Self-gelling hydrogels based on oppositely charged dextran microspheres, Biomaterials 26 (2005) 2129-2135.

[7] M. Ebelmen, On the synthesis of silica gels from alkoxides, Annales de chimie et de physique, 1846, p. 129.

[8] T. Graham, XXXV.-On the properties of silicic acid and other analogous colloidal substances, Journal of the Chemical Society 17 (1864) 318-327.

[9] L.L. Hench, J.K. West, The sol-gel process, Chemical Reviews 90 (1990) 33-72.

[10] J.E. Martin, D. Adolf, The sol-gel transition in chemical gels, Annual Review of Physical Chemistry 42 (1991) 311-339.

[11] J.C. Gimel, T. Nicolai, D. Durand, 3D Monte Carlo simulations of diffusion limited cluster aggregation up to the sol-gel transition: Structure and kinetics, Journal of Sol-Gel Science and Technology 15 (1999) 129-136.

[12] K. Nakanishi, Pore Structure Control of Silica Gels Based on Phase Separation, Journal of Porous Materials 4 (1997) 67-112.

[13] P.J. Lu, D.A. Weitz, Colloidal Particles: Crystals, Glasses, and Gels, Annual Review of Condensed Matter Physics 4 (2013) 217-233.

[14] A. Hoppe, N.S. Güldal, A.R. Boccaccini, A review of the biological response to ionic dissolution products from bioactive glasses and glass-ceramics, Biomaterials 32 (2011) 2757-2774.

[15] R. Schrieber, H. Gareis, Gelatine handbook: theory and industrial practice, John Wiley & Sons, 2007.
[16] G.J.d.A.A. Soler-Illia, C. Sanchez, B. Lebeau, J. Patarin, Chemical Strategies To Design Textured Materials: from Microporous and Mesoporous Oxides to Nanonetworks and Hierarchical Structures, Chemical Reviews 102 (2002) 4093-4138.
[17] K. Farbod, M.R. Nejadnik, J.A. Jansen, S.C.G. Leeuwenburgh, Interactions Between Inorganic and Organic Phases in Bone Tissue as a Source of Inspiration for Design of Novel Nanocomposites, Tissue Engineering Part B: Reviews 20 (2013) 173-188.
[18] T. Aewsiri, S. Benjakul, W. Visessanguan, A.B. Encarnacion, P.A. Wierenga, H. Gruppen, Enhancement of Emulsifying Properties of Cuttlefish Skin Gelatin by Modification with N-hydroxysuccinimide Esters of Fatty Acids, Food and Bioprocess Technology 6 (2013) 671-681.

Acknowledgments

List of publications

Awards and honors

Vitae

Acknowledgments

The first time that I encountered the city of Nijmegen was in December 2010 when I was checking the train routes to figure out how my friends and I could go from Cologne to Amsterdam. I was puzzled how to pronounce "Nijmegen" when I needed to ask about our train connections at the information desk. I clearly remember that I looked at Nijmegen on the map and I said to myself, "Who would live in such an unknown place?!" Around two years later, I ended up living in that place, which turned out to be one of the greatest experiences of my life! But certainly, it was not the name of Nijmegen which brought me to this town. I remember that it was summer of 2012, while I was checking an online scientific database for highly ranked scientists in the field of biomaterials, that I got to know Prof. John Jansen and his department at Radboud University Medical Center in Nijmegen. A few months later, I came across an advertisement for a PhD position in this department, and I immediately applied. The decision to move was not at all an easy one, but it opened many new doors in my professional and personal life, for which I am highly grateful. Indeed, I am greatly indebted to many people without whom this journey could not have started and come to a successful end.

First and foremost, my deepest appreciation goes to Prof. John Jansen and Dr. Sander Leeuwenburgh. Dear John, I would like to thank you for establishing and directing this amazing department. I am very grateful for the opportunity to carry out my PhD studies in your group and I want to thank you for all your guidance and insightful comments during my PhD. Dear Sander, since the beginning of my PhD, every day I realized more and more how fortunate I was to carry out my PhD under your supervision. I truly enjoyed the opportunity to work with you, not only from an academic perspective, but also on a personal level. Thank you for giving me the scientific freedom to enjoy my research and thank you very much for guiding me to focus and finalize my project. In addition to benefiting from your scientific knowledge, I also greatly benefited from your supportive and encouraging approach which enabled me to realize my goals. I vividly remember that once during a challenging period, you told me "what doesn't kill you makes you stronger;" indeed, this proved to be totally true!

I would like to acknowledge the Netherlands Enterprise Agency for funding my PhD

project. My special thanks goes to Prof. Sybrand van der Zwaag and Mrs. Annette Steggerda. Dear Sybrand, thank you so much for establishing and directing the IOP (Innovatiegericht Onderzoeksprogramma) Self-Healing Materials Program. Dear Annette, thank you very much for your efforts to coordinate such a well-organized program. The symposiums, courses, summer schools and annual meetings greatly benefited my scientific knowledge and research project, and also widened my perspective, for which I would like to thank you both.

I owe my deepest gratitude to Prof. Aldo Boccaccini. Dear Prof. Boccaccini, the opportunity to work under your supervision and to attend your classes and research seminars during my master's degree studies in Erlangen was a priceless experience which equipped me with the knowledge and skills required to pursue my PhD studies. In addition, the opportunity to collaborate with you during my PhD highly benefited my research and manifested in several scientific publications. I am indeed very thankful for your prompt feedback and invaluable advice amidst your busy schedule. I would also like to express my special appreciation to Prof. Robin Klupp Taylor. Dear Robin, thank you so much for training me on the synthesis and surface modification of nanoparticles during my master's studies in Erlangen. The knowledge and skills that I gained during my M.Sc. mini-project and thesis in your lab were highly beneficial for my PhD research. I am indeed deeply grateful to the Elite Master's Program of Advanced Materials and Processes (MAP) which provided me with an extensive theoretical and practical background to perform interdisciplinary research. I would like to show my greatest appreciation to the MAP office, faculty and all the MAP fellows for such an amazing and unforgettable experience. My special thanks goes to my dear friends Burcu, Felipe, Gokhan, Johann, Ana Maria, Minghui, Neriman, Parisa, Paul, Rajesh, Rooja, Shiva, Taimoor, Wolfram, and Yoones, for making me feel at home in Erlangen during my first experience living abroad.

I would like to express my deepest appreciation to Prof. Mohammadhossein Fathi who introduced me to the field of biomaterials and supervised my bachelor's thesis, which led to my first scientific publications. Dear Prof. Fathi, I am deeply grateful for the opportunity to have worked with you. Thank you so much for your warm encouragement and invaluable advice. My special thanks also goes to Prof. Mahshid

Kharaziha who co-supervised my bachelor's thesis.

I would also like to express my gratitude to Prof. Peter Fratzl, Dr. Matthew Harrington, Dr. Stephan Schmidt, and Dr. Manav Mehta. Dear Peter, thank you so much for supporting my proposal for the ICSHM 2013 travel award in Ghent, for providing me with the opportunity to perform research in your department, and for introducing me to Matt and Manav. The discussion that I had with you during our boat trip back from Self-Healing Materials Summer School in Vlieland was a great help for me to decide between an academic or industrial career. Dear Matt and Stephan, my interactions with you have been a great asset for my PhD, as manifested in three chapters of this thesis. I am highly grateful for your generous support as well as insightful comments and suggestions. Dear Manav, thank you so much for taking the time to share with me about your experiences in academia and industry. I highly benefited from your valuable insight. I would like to also thank the organizers of ICSHM 2013 for the financial support which allowed my research stays at the Max Planck Institute of Colloids and Interfaces.

I would like to offer my special thanks to Prof. David Weitz, Prof. Huanan Wang, Dr. Thomas Kodger, and Dr. Shima Parsa. Dear Dave, thank you very much for providing me with the opportunity to carry out research in your laboratory. I greatly benefited from your insightful comments and suggestions. Dear Huanan, I received generous support from you, particularly during my research stays in the Weitz lab. In addition to all of our scientific discussions, I really enjoyed those times we spent together outside the lab including lunches at the law school, dinners, going to the outlets, and even seeing a Red Sox game together. I wish you all the best in your new professorship position in China and look forward to more opportunities to work together in the future. Dear Tom, your meticulous comments and suggestions were an enormous help to me. Thank you so much for your availability and all your support. Dear Shima, thank you very much for your generous support in analyzing my confocal data. I wish the best for you and your family. Indeed, my stays in the Weitz lab would not have been as pleasant and productive without the insightful suggestions, great help and positive attitude of Weitz lab members including Adrian, Alireza, Aria, Benjamin, Carlos, Christoph, David, Dirk, Elizabeth, Hee Sun, Helen, Ilke, Jing, Jinrong, John, Jordan, Liangliang, Liheng, Liyuan, Liz,

Manis, Max, Maximilian, Sanne, Stefanie, Vincent, Zach, and Zsolt.
I would like to express my gratitude to Prof. Jan van Hest and Dr. Dennis Löwik. Thank you so much for all the support, discussions and suggestions during my PhD. I am also very grateful for your providing me with access to various equipment in your facility, which was essential for my research. My sincere gratitude goes to Prof. Alan Rowan who served as my mentor during my PhD and provided me with his invaluable advice. I am also highly grateful to Prof. Arno Kentgens and Dr. Tatiana Zinkevich for generously providing their resources and expertise for solid-state NMR analyses of materials presented in Chapter 5 of this thesis. Dear Tatiana, thank you so much for all of your input and insightful discussions. I would like to offer my gratitude to FeyeCon Company for providing their facilities for the production of microparticles presented in Chapter 7 of this thesis. My special thanks goes to Dr. Hajar Seyednejad and Dr. Bram Pape for their generous support and valuable input. I would like to thank Dr. Tina Vermonden, Dr. Mathew Hembury, and Mr. Mies van Steenbergen for providing their equipment and assistance for thermogravimetric analyses of materials that I developed during this PhD project. I would like to thank Dr. Lorenza Draghi for our collaboration and valuable discussions. Dear Lorenza, the exchange of students with your group indeed greatly benefited my PhD research. I would also like to thank Mariateresa Brindisi, Marianna Barbuto, Eri Shima, Lianne Tan and Anouk Dekker for assisting me with different parts of my PhD research.
Additionally, I have deep gratitude to Dr. Jeroen van den Beucken, Dr. Frank Walboomers, Dr. Joop Wolke, and Dr. Fang Yang. Dear Jeroen, I am highly thankful for all your feedback and support, particularly concerning the *in vivo* experiments that are presented in this thesis. Dear Frank, thank you so much for all your constructive comments and warm encouragement which certainly helped me to choose an academic career. Dear Joop, thank you very much for all your helpful and detailed comments. I wish you lots of happy and fulfilling moments in this new phase of your life. Dear Fang, I am definitely not the only person in our department who enjoys your pleasant and warm character. Thank you so much for your positive vibe and constructive scientific comments.
I would like to offer my special thanks to all the technicians of the Department of

Biomaterials. Dear Monique, thank you very much for your availability to answer my questions regarding cell culture experiments. Dear Natasja, thank you so much for assisting me with the histological and cytological experiments of my project. Dear Martijn, thank you very much for all the instructions and trainings you gave me during my PhD. Dear Vincent, your wonderful personality and great character is admired by every single PhD student in our lab. Thank you so much for all of your support during my PhD.

I am highly grateful to all PhD students, postdocs and visiting students of the Department of Biomaterials who made this journey a wonderful experience. My special thanks goes to Alessandra, Alessandro, Alexey, Alex, Ali, Angela, Antonio, Arnold, Astghik, Aysel, Bart, Bing, Carla, Claire, Cristina, Daniel, Daniela, Dimitris, Doris, Eline, Erica, Eva, Gerry, Hamdan, Hongbo, Imran, Irene, Jan Willem, Jiamian, Jiankang, Jie, Jing, Jinling, Jinlong, Jinmeng, Johnny, Kambiz, Kelly, Kemal, Laury, Ljupcho, Luis, Manuela, Marcel, Maria, Muhanad, Na, Nathan, Nehar, Paola, Paula, Paulo, Pedro, Raffaella, Reza, Robin, Roel, Rosa, Ruggerro, Shinji (Take), Simone, Simon, Sonia, Steven, Wanxun, Wei, Weihua, Winston, Xian, Xiangzhen, Xinjie, Yang, and Yue. Dear Alessandro, it was a great pleasure to have you in our department and to work with you, which I hope we will continue to do in the future as well. Dear Alexey, Thank you for everything. I was indeed very lucky that I shared an office with you from the first day of my PhD. Dear Ali, you are one the kindest people that I have ever met and indeed every time I met with you was a great opportunity for me to express myself in Farsi! Dear Angela, thank you for reminding me at the end of the long working days that I shouldn't forget to eat and sleep! Having you in our department was wonderful and I hope we can meet again soon. Dear Antonio, being your housemate was a real blast, especially your exceptional cooking skills! Oh man, we have so many good memories together, so many trips, so many parties and so many long working days… Indeed, many hard days coming back home and talking about different topics was a pleasant routine that I will never forget! Dear Dana and Mihai, ia cu paine! :D I am very happy that I met you both during my PhD and I wish you the best in every aspect of your life! Special thanks to Dana for her "positive" temperament and to Mihai for his amazing hospitality. Dear Erica, thank you for all your kindness and positivity! Dear Gerry.

thank you for your warm encouragement and constructive comments. Dear Imran, it was always nice to see you and talk to you in the lab. Thank you for being such a nice and honest colleague. Dear Irene, thank you for trying to take over my "flex spot" which made me start my days in the lab earlier to keep my "flexible" territory! Dear Jiankang, thank you for introducing me to a new level of labeling skills and helping me with HPLC measurements! I am looking forward to being your colleague again! :) Dear Jinlong, thank you for being a great source of photography skills! Dear Kambiz, listen, I am telling you, I feel so fortunate to have had a colleague like you during my PhD! Oh man, I will never forget our never-ending discussions with Alexey and unlimited inside jokes! Thank you and Farahnaz for being such amazing and lovely friends! Dear Kemal, thank you for being such a fun and amusing friend and colleague. I will never forget the time that we spent together in San Francisco. Dear Laury, Thank you for improving my Spanish skills! Dear Luis, the weekly messages that you sent us were truly inspirational! Wishing you best of luck in this new phase of your life. Dear Manuela, thank you for being such a kind and wonderful person. I also truly enjoyed meeting you again in Toronto. Dear Nate, I am writing this now as you sit in front of me in Würzburg! Thank you and Armine for all the good moments including trips and parties! I hope our amazing bike rides will continue! Dear Nehar, thank you for being such a lovely friend and colleague. Dear Paula, it was wonderful to have you and Ricardo here in Nijmegen. I wish you both all the best and hope to see you again soon. Dear Robin, it was a great pleasure to have such a nice person and committed researcher like you as my colleague. I look forward to all of your upcoming scientific achievements. Dear (Mr.) Simone, I am leavviiinnggg! Thank you for all the positivity and Italian warmth that you brought to our lab. Hanging out with you and Giuliana was indeed a wonderful experience! Dear Sonia, thank you for all your generosity with sharing your wonderful cooking skills with us. I truly enjoyed all the parties and dinners at your place, for which I should also thank Irene! Dear Wanxun and Arnold, thank you for making me feel welcomed in this department when I started my PhD. Dear Winston and Kelly, it was a great pleasure spending time with you both in this city. I cannot wait to meet you both in Ireland. Special thanks also goes to Winston for his generous support particularly for the *in vivo* experiments of this thesis. Dear Yang, dear Mr. President,

thank you for all your help with the cell culture experiments presented in this thesis. Spending time with you inside and outside the lab was truly enjoyable and fun!

My heartfelt appreciation goes to my parents for raising me and helping me to realize my own potential. Dear Mom and Dad, all the support that you have provided me throughout my life has been the greatest gift. Dear Mom, you have been a true role model for me to push the boundaries and move forward amidst all the ups and downs in life. I cannot express enough how grateful I am for everything you have done for me and I will never forget all of the sacrifices that you have made to raise me. Dear Dad, your passion and appreciation for education, science and industry have defined who I am. I am deeply grateful for everything you have done for me. Without your support and encouragement, I could not have achieved my goals. I am deeply grateful to my brother Nima without whom this long journey would never have started. Dear Nima, thank you so much for being an inspiration and allowing me to believe in myself. I would also like to thank my uncle for being a great support. Dear Uncle, thank you so much for your kindness and generous support during these years.

One of the most challenging phases of this journey was the ultimate period of finalization of this thesis. A completion of one task meant starting to catch up with the deadline of another task. I could not have overcome this demanding period without the encouragement of those who supported me...

به پایان آمد این دفتر،
حکایت همچنان باقیست. -سعدی شیرازی

This chapter has come to an end,
(but) the story yet remains. -*Saadi Shirazi*

List of publications

Publications related to this thesis:

- M. Diba, H. Wang, S.C.G. Leeuwenburgh, "Development of self healing gels based on reversible cohesive interaction between self-assembling organic and inorganic nanoparticles", In "Self Healing Materials—Pioneering Research in the Netherlands", edited by S. Van der Zwaag and E. Brinkman, Delft University Press, (2015) 37-46.
- M. Diba, J. An, S. Schmidt, M. Hembury, D. Ossipov, A.R. Boccaccini, S.C.G. Leeuwenburgh, "Exploiting bisphosphonate–bioactive-glass interactions for the development of self-healing and bioactive composite hydrogels", *Macromolecular Rapid Communications*, 37 (2016) 1952-1959.
- M. Diba*, H. Wang*, T.E. Kodger, S. Parsa, S.C.G. Leeuwenburgh, "Highly elastic and self-healing composite colloidal gels", *Advanced Materials*, 29 (2017) 1604672.
- M. Diba, B. Pape, A. Klymov, Y. Zhang, J. Song, D. Löwik, H. Seyednejad, S.C.G. Leeuwenburgh, "Nanostructured raspberry-like gelatin microspheres for local delivery of multiple biomolecules", *Acta Biomaterialia*, 58 (2017) 67-79.
- M. Diba, W.A. Camargo, M. Brindisi, K. Farbod, A. Klymov, S. Schmidt, M.J. Harrington, L. Draghi, A.R. Boccaccini, J.A. Jansen, J.J.J.P. van den Beucken, S.C.G. Leeuwenburgh, "Composite colloidal gels made of bisphosphonate-functionalized gelatin and bioactive glass particles for regeneration of osteoporotic bone defects", *Advanced Functional Materials*, (2017) 1703438.
- M. Diba, A. Polini*, D.G. Petre*, Y. Zhang, S.C.G. Leeuwenburgh, "Fiber-reinforced colloidal gels as injectable and moldable biomaterials for regenerative medicine" (*Submitted*).
- M. Diba, W.A. Camargo*, T. Zinkevich*, Y. Kabiri, A.P.M. Kentgens, A.R. Boccaccini, J.A. Jansen, J.J.J.P. van den Beucken, S.C.G. Leeuwenburgh, "Hybrid alendronate-bioactive glass particles for treatment of osteoporotic bone defects" (*In preparation*).

Other publications:

Peer-reviewed articles

- M. Diba, M.H. Fathi, M. Kharaziha, "Novel forsterite/polycaprolactone nanocomposite scaffold for tissue engineering applications", *Materials Letters*, 65 (2011) 1931-1934.
- M. Diba*, M. Kharaziha*, M.H. Fathi, M. Gholipourmalekabadi, A. Samadikuchaksaraei, "Preparation and characterization of polycaprolactone/ forsterite nanocomposite porous scaffolds designed for bone tissue regeneration", *Composites Science and Technology*, 72 (2012) 716-723.
- M. Diba, F. Tapia, A.R. Boccaccini, L.A. Strobel, "Magnesium-containing bioactive glasses for biomedical applications", *International Journal of Applied Glass Science*, 3 (2012) 221-253.
- M. Diba, A. Garcia-Gallastegui, R.N. Klupp Taylor, F. Pishbin, M.P. Ryan, M.S.P. Shaffer, A.R. Boccaccini, "Quantitative evaluation of electrophoretic deposition kinetics of graphene oxide", *Carbon*, 67 (2014) 656-661.
- M. Diba, O.M. Goudouri, F. Tapia, A.R. Boccaccini, "Magnesium-containing polycrystalline bioactive ceramics and glass-ceramics for biomedical applications", *Current Opinion in Solid State and Materials Science*, 18 (2014) 147-167.
- S. Naseri, M. Diba, S. Golkar, A.R. Boccaccini, R.N. Klupp Taylor, "Fabrication of gold-nanoshell/polycaprolactone composite films with high electrical conductivity", *Materials Letters*, 130 (2014) 164-167.
- A.L. Metze, F. Pishbin, M.P. Ryan, S. Seuss, M. Diba, M.S. Shaffer, A.R. Boccaccini, "Electrophoretic co-deposition of chitosan and graphene oxide results in antibacterial coatings for medical applications", *Key Engineering Materials*, 654 (2015) 176-182.
- K. Farbod, M. Diba, T. Zinkevich, S. Schmidt, M.J. Harrington, A.P.M. Kentgens, S.C.G. Leeuwenburgh, "Gelatin nanoparticles with enhanced affinity for calcium phosphate", *Macromolecular Bioscience*, 16 (2016) 717-729.
- J. Song, Q. Chen, Y. Zhang, M. Diba, E. Kolwijck, J. Shao, J.A. Jansen, F. Yang, A.R. Boccaccini, S.C.G. Leeuwenburgh, "Electrophoretic deposition of chitosan coatings modified with gelatin nanospheres to tune the release of antibiotics", *ACS Applied Materials & Interfaces*, 8 (2016) 13785-13792.

- M. Diba*, D.W.H. Fam*, A.R. Boccaccini, M.S.P. Shaffer, "Electrophoretic deposition of graphene-related materials: A review of the fundamentals", *Progress in Materials Science*, 82 (2016) 83-117.
- K. Farbod, A. Curci, M. Diba, T. Zinkevich, A.P.M. Kentgens, M. Iafisco, N. Margiotta, S.C.G. Leeuwenburgh, "Dual-functionalisation of gelatine nanoparticles with an anticancer platinum (ii) bisphosphonate complex and mineral-binding alendronate", *RSC Advances*, 6 (2016) 113025-113037.

Book chapters

- M. Diba, A.R. Boccaccini, "Silver-containing bioactive glasses for tissue engineering applications", In "Precious metals for biomedical applications", edited by N. Baltzer and T. Copponnex, Woodhead Publishing, (2014) 177-211.
- M. Diba, A.R. Boccaccini, "Electrophoretic deposition of graphene-based materials and their energy-related applications", In "Handbook of Graphene Science. Vol 1: Fabrication Methods", edited by M. Aliofkhazari, N. Ali, W.I. Milne, C.S. Ozkan, S. Mitura, and J.L. Gervasoni, CRC Press, (2016) 173-186.

**These authors contributed equally to this work.*

Awards and honors

- **2011:** MAP educational grant for attending the 2nd International Conference on Multifunctional, Hybrid and Nanomaterials, Strasbourg, France.
- **2013:** Travel award for attending the the NSF Workshop for Micro- and Nanotechnologies for Medicine, Cambridge, USA.
- **2013:** Travel award from the 4th International Conference on Self-Healing Materials to perform a research stay at the Max Planck Institute of Colloids and Interfaces, Potsdam, Germany.
- **2014:** Poster award from the New Frontiers Symposium on Regenerative Medicine, Nijmegen, The Netherlands.
- **2015:** Nominated and sponsored by the Elite Network of Bavaria (Bavarian State Ministry of Education, Science and the Arts, Germany) to attend the 65th Lindau Nobel Laureate Meeting, Lindau, Germany.
- **2015:** Selected to attend the 65th Lindau Nobel Laureate Meeting, Lindau, Germany.
- **2017:** Poster award from the 6th International Conference on Self-Healing Materials, Friedrichshafen, Germany.

Vitae

Mani Diba was born in 1986 in Tehran, Iran. He received a B.Sc. degree in 2010 in Materials Engineering from Isfahan University of Technology (Iran). He conducted his B.Sc. thesis in the area of nanocomposite scaffolds for bone tissue engineering applications. In 2012, he received a M.Sc. (Hons.) degree in Advanced Materials and Processes from University of Erlangen-Nuremberg (Germany). He performed his M.Sc. thesis at University of Erlangen-Nuremberg and Imperial College London (UK) focusing on the electrophoretic deposition of nanomaterials. In 2013, he started his PhD degree in the Department of Biomaterials at Radboud University Medical Center (The Netherlands) focusing on the development of self-healing biomaterials. During his PhD studies, he was a visiting researcher at Harvard University (USA) and Max Planck Institute of Colloids and Interfaces (Germany). In October 2017, he started working as a postdoctoral researcher in the Department of Biomedical Engineering and the Institute for Complex Molecular Systems at Eindhoven University of Technology (The Netherlands).